Εθνικό Μετσόβιο Πολυτεχνείο

Σχολή Πολιτικών Μηχανικών

Τομέας Γεωτεχνικής

National Technical University of Athens

School of Civil Engineering

Geotechnical Division

Διπλωματική εργασία

ΚΑΡΑΠΙΠΕΡΗ ΚΩΝΣΤΑΝΤΙΝΟΥ

Επιβλέπων:
Λέκτορας Ν. Γερόλυμος

ΕΜΒΑΘΥΝΣΗ ΣΤΗΝ ΑΡΙΘΜΗΤΙΚΗ ΠΡΟΣΟΜΟΙΩΣΗ ΤΗΣ ΕΓΚΑΡΣΙΑΣ ΑΠΟΚΡΙΣΗΣ ΦΡΕΑΤΩΝ ΘΕΜΕΛΙΩΣΗΣ ΥΠΟ ΣΤΑΤΙΚΗ ΚΑΙ ΑΝΑΚΥΚΛΙΖΟΜΕΝΗ ΦΟΡΤΙΣΗ

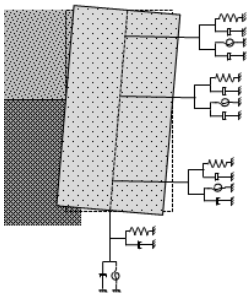

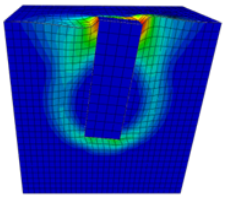

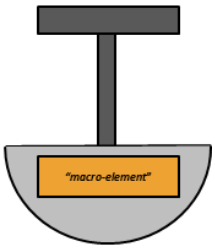

INSIGHT TO THE NUMERICAL MODELING OF THE LATERAL RESPONSE OF CAISSON FOUNDATIONS TO STATIC AND CYCLIC LOADING

Diploma Thesis by

KARAPIPERIS KONSTANTINOS

Supervised by
Lecturer N. Gerolymos

Αθήνα, Οκτώβριος 2012

Athens, October 2012

Acknowledgements

Upon completing my diploma thesis, I feel the need to thank the people that supported and encouraged me throughout my work.

First of all, I would like to express my deepest appreciation and gratitude to Professor G. Gazetas, for his valuable guidance throughout my studies. He has been an endless source of inspiration and has greatly contributed to the love that I have developed towards Engineering in general and Geotechnical Engineering in particular.

This thesis would not have been possible without the guidance, help and patience of my supervisor, Lecturer N. Gerolymos, to whom I owe my respectful gratitude. His contribution to solving the challenging obstacles that arised throughout this thesis was considerable.

I would also like to thank the doctoral students and post-doctoral researchers of the Geotechnical Department for their kind embrace as well as my fellow students and friends for the experiences we shared.

Finally, above all, I feel the need to thank my family for their consistent support and encouragement.

TABLE OF CONTENTS

CHAPTER 1

Introduction

1.1. Scope

In this thesis, the response of rigid caisson foundations under combined axial, horizontal and moment loading is investigated. The first part deals with the extraction and analytical representation of the failure envelopes that govern their response, while emphasis is given to the effect of geometric nonlinearities at the soil – caisson interface on the latter. This could serve as a basis for the development of a plasticity – based "macro-element", a mathematical tool similar to those already developed by researchers in the case of shallow foundations. In the second part of this thesis, a sophisticated Winkler – based constitutive model is extensively calibrated against numerous Finite Element experiments and is validated for static monotonic and cyclic loading. Both approaches are driven by the lack of complete tools that can effectively capture the behaviour of embedded foundations under combined loading and that would enhance the cooperation of structural and geotechnical engineers. In the following sections we provide a layout of the thesis as well as a short review of the literature regarding the analysis of deeply embedded foundations.

1.2. Layout

The second chapter deals with the modeling of the soil – foundation system using the commercial Finite Element code ABAQUS. The geometrical characteristics and constitutive laws adopted in the models are analyzed in detail.

In the third chapter, we describe the methods for the conduction of the numerical analyses and present the results in terms of ultimate capacities and failure envelopes. We provide analytical expressions for the complete representation of the above and assess their ability to effectively capture all major trends. In addition, we provide insight to the different types of soil resisting mechanisms deployed. Throughout this chapter, the two different types of soil – caisson interface considered ("bonded" and "nonlinear") are continuously compared.

The fourth chapter introduces the reader to the second part of this thesis by analyzing the sophisticated BWGG Winkler model developed by Gerolymos and Gazetas, on which the remaining of this thesis is based. Finally, this model, which is essentially a Winkler – based macro-element model is briefly compared to the recently developed plasticity – based macro – element model by Gerolymos and Souliotis.

In the fifth chapter, we analyze the complete methodology followed for the calibration of the Winkler model against numerical experiments, while emphasis is given to the uncoupling of the mechanisms that govern the response of caisson foundations. The model's ability to capture all major aspects of the lateral monotonic and cyclic response for various embedment ratios is assessed and some design considerations are provided.

In the last chapter, the basic conclusions derived from this thesis are summed up and further research recommendations are given.

1.3. Use of deeply embedded foundations

Fig 1.1 presents a rough categorization of the types of foundations that are generally used in order to support structural systems. Surface or shallow embedded foundations are distinguished by small slenderness ratios, while pile foundations are generally more slender elements. Caisson foundations lie somewhere in between in terms of slenderness or embedment; yet their limits are vague. The compressibility of the soil and the structural element should also be taken into consideration for a more realistic distinction of different foundation types.

Caisson foundations have been widely used on both soft and hard soils in order to support major structures, especially bridges. Characteristic examples include:

- the Tagus bridge in Portugal
- the San-Francisco-Oakland bay bridge
- the Williamsburg and Verrazano Narrows bridges in New York
- the Port island and Nishinomiya-ko bridges in Japan

Despite their large dimensions, caisson foundations have been shown not to be immune to seismic loading as it was believed for many years. This was confirmed in the Kobe (1995) earthquake, which caused many structures founded on caissons to suffer severe damage.

Deeply embedded foundations have also been consistently used in major offshore structures, where the study of their response under combined vertical, shear and moment loading is of great importance.

1.4. Caisson Foundations under lateral loading

Although a great deal of research has been done on the response of surface or shallow foundations under lateral loading and as a result numerous methods have been introduced, there is still a relatively small number of studies concerning the response of

deeply embedded foundations and especially caissons. In crudely chronological order [*Gerolymos and Gazetas, 2006*], previous work on caisson foundations include: the analytical solution of Tajimi [*1969*] for a cylindrical foundation embedded in a stratum and bearing on bedrock; the versatile approximate analytical solutions of Novak and Beredugo [*1972*]; the 'consistent-boundary' finite element formulations of Kausel and Roesset [*1975*] for circular foundations in layered deposits over bedrock; the boundary element solution for rectangular foundations in a halfspace by Dominguez [*1978*]; the semi-numerical formulation of Tassoulas [*1981*] applied to embedded cylindrical foundations with variable sidewall heights; the time-domain boundary element method of Karabalis and Beskos [*1986*]; the hybrid boundary-element and finite element solution of Mita and Luco [*1989*] for square foundations embedded in a halfspace; and the 'flexible-volume' substructuring technique of Tajirian and Tabatabaie [*1981*]. Harada [*1981*] developed an approximate analytical solution for cylindrical foundations combining Tajimi's and Novak's concepts. One of the most comprehensive studies on the seismic response of flexible and rigid caissons was conducted by Saitoh [*2001*], who extended Tajimi's approximation to account for caisson flexibility and for soil and interface nonlinearities (separation and gapping of the caisson from the soil). He showed that Novak's plane strain approximation, logical as it may be, leads to inaccurate results. Most of the above methods refer to cylindrical foundations. Finally, a sophisticated and versatile Winkler model has been recently developed by Gerolymos and Gazetas [*2006*], which involves 4 types of nonlinear springs and is able to realistically simulate various foundation shapes, soil profiles, loading conditions and may also account for interface nonlinearities. This model is analyzed extensively in the second part of this thesis.

A comprehensive series of studies on the static and dynamic response of embedded rigid foundations having various plan shapes (ranging from rectangular of any aspect ratio to triangular) have been published by Gazetas, and co-workers [*Gazetas, Dobry, Tassoulas 1985; Gazetas, Tassoulas 1987(a) και 1987(b); Fotopoulou, Kotsanopoulos, Gazetas, Tassoulas 1989*].]. Utilizing an efficient boundary-element method, and numerous results from the published literature, they developed closed-form semi-analytical expressions and charts for stiffnesses and damping of horizontally and rotationally loaded arbitrarily-shaped rigid foundations embedded in homogeneous

soil. Incomplete contact between the foundation vertical walls and the surrounding soil were taken into account in a crude way. Ample confirmation of the basic validity of some of the main concepts and results in these publications were recently provided by Gadre and Dobry [*1998*] through centrifuge modeling.

However, the above-mentioned analytical expressions and charts cannot directly apply to multi-layered soils. Furthermore, it would be impossible to even crudely extend them for use with nonlinearly behaving soils, or to model realistically phenomena such as separation (gapping) and uplifting that may take place under strong static and seismic excitation. On the other hand, the widely available commercial finite-element and finite-difference computer codes, while in principle capable of treating soil nonlinearities, are not yet an easy solution when rectangular caissons are studied (requiring a 3D mesh), embedded in deep soil deposits and subjected to seismic shaking (both requiring special and very distant boundaries), and undergoing strong oscillations with the aforementioned interface nonlinearities (requiring special interface elements).

This has led researchers to approach the response of deeply embedded foundations on the basis of “failure envelopes” or “interaction diagrams”, namely the locus of points that lead a foundation system to failure under combined *M*-*Q*-*N* loading [*Zaharescu 1961; Ticof 1977*]. Various studies have been published that deal with the capacity of –mainly- lightly embedded or surface foundations in the above sense [*Roscoe and Schofield 1957; Bransby and Randolph 1998; Taiebat and Carter 2000; Gourvenec and Randolph 2003; Gourvenec 2004, 2007, 2008; Randolph and Gourvenec 2011, Ukritchon et al. 1998; Martin and Houlsby 2001;*]

In a typical caisson foundation, the vertical component of loading originates from the weight of the supported structure as well as the self-weight of the foundation, which is of considerable importance in contrast to shallow foundations. Regarding the horizontal force and the overturning moment, the general approach so far has been that of a sDoF oscillator, where a force F is applied at a height h above the head of the caisson. This translates into a horizontal force $H = F$ as well as an overturning moment $M = F \cdot h$ at the head of the caisson. Typical loading conditions involve a small vertical component of loading (far from inducing failure in terms of vertical bearing capacity),

while the combination of the two other load components *M*-*Q* is usually critical for the foundation.

The “interaction diagram” approach introduced by Zaharescu and Ticof has been adopted by many researchers and has considerably facilitated the design of foundations through an analytical expression of their “pure” capacities and their interaction law. However, researchers have not yet agreed upon a fixed reference point for the load components, a fact that affects the shape of the interaction diagram as will be displayed throughout this thesis.

Figures

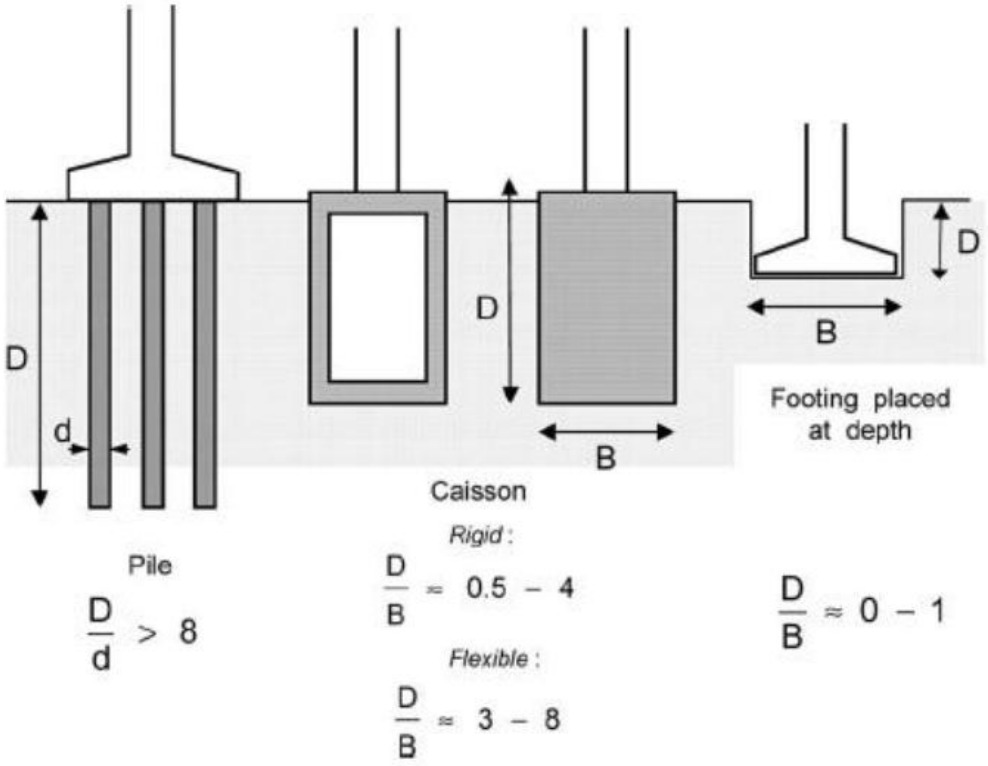

Figure 1.1 *An rough categorization of different foundation types based on their slenderness or embedment ratio D/B. From the left to the right we can distinguish (a) piles, (b) deeply embedded foundations and (c) shallow foundations.*

Figure 1.2 *The Tagus River Bridge in Portugal, founded on a 88 – m high caisson.*

Figure 1.3 *The Nishinomiya-ko bridge in Kobe, Japan*

Figure 1.4 *The Akashi-kaikyo bridge in Kobe, Japan founded on two massive 80-m diameter caissons.*

CHAPTER 2
Finite Element Modeling

2.1. Introduction

This chapter focuses on the characteristics of the 3D Finite Element model that was utilized for the numerical experiments carried out. Special attention is given to the geometrical features, the soil's constitutive law as well as the caisson-soil interface.

2.2. The Finite Element Model

2.2.1. Geometry

The studied problem is a square plan caisson of width *B* and embedment depth *D* that is subject to combined vertical load *N*, horizontal load *Q* and overturning moment. The problem is analyzed with the use of the advanced Finite Element code ABAQUS. ***Figure 2.1*** shows a half caisson cut through one of the orthogonal planes of symmetry. The size of the finite element mesh is *5Bx5Bx5B* carefully weighing the effect of boundaries on the caisson's response and the computational time. Zero-displacement boundary conditions prevent the out of-plane displacements at the vertical sides of the model, while the base is fixed in all three coordinate directions. We investigate 3 typical embedment ratios: *D/B = 1, 2* and *3* and the respective models are displayed in ***Figure***

2.2. Note that embedment ratios *1* and *3* represent the limits of caisson foundations according to the conventional distinction.

Both caisson and soil are modeled with C3D8 3-D elements, elastic for the former and nonlinear for the latter. The caisson is either rigidly connected to the soil ("bonded" interface), which means that separation and slippage are not allowed to occur, or connected through a special contact surface that allows for realistic simulation of the phenomena described above ("nonlinear" interface). In this latter case, we adopt a Coulomb friction law with a parametrically investigated coefficient of friction. To achieve a reasonable stable time increment without jeopardizing the accuracy of the analysis, we modified the default hard contact pressure-overclosure relationship with a suitable exponential relationship (***Fig. 2.3***) Considering the fact that till now most approaches to the problem of caisson-soil interaction have been limited to bonded interface conditions, this special interface approach gains particular importance. To ensure uniform stress distribution at the head of the caisson, the nodes of the associated elements are properly kinematically constrained.

2.2.2. Soil behaviour

For the total stress analysis under undrained conditions, soil behavior is modeled through a nonlinear constitutive model [*Gerolymos and Gazetas, 2006*] which is a slight modification of a model incorporated in ABAQUS. It uses the Von Mises failure criterion with yield stress *σy* related to the undrained shear strength S_u as:

$$\sigma_y = \sqrt{3} S_u \qquad \textbf{(2.1)}$$

along with a nonlinear kinematic and isotropic hardening law and an associative plastic flow rule. The model parameters are calibrated to fit published G-γ curves of the literature. The soil profile studied herein is of a constant undrained shear strength S_u = *50 kPa* (***Fig. 2.4***). Hence, the equivalent Von Mises yield stress equals $\sigma_y = 50\sqrt{3} = 86.6\, kPa$. The soil has a modulus of elasticity of *E = 50 MPa*, leading to a "stiffness ratio" of E/S_u = *1000*, and a Poisson's ratio of *v = 0.3*. The foundation is considered rigid

concrete and is represented by a modulus of elasticity of E_{beton} = *150000 MPa*. The ratio E_{beton}/E_{soil} along with the relatively small slenderness ratios considered render the rigidity assumption safe.

2.2.3. Theory of the Von Mises Yield Criterion

The von Mises yield criterion suggests that the yielding of materials begins when the second deviatoric stress invariant J_2 reaches a critical value. In engineering, the von Mises yield criterion is usually formulated in terms of the von Mises stress or equivalent tensile stress σ_v, in which case yielding occurs when the equivalent stress reaches a critical value known as the yield strength S_y. The von Mises stress is used to predict yielding of materials under any loading condition from results of simple uniaxial tensile tests. Prior to yield, material response is assumed to be elastic.

Because the von Mises yield criterion is independent of the first stress invariant, it is applicable for the analysis of plastic deformation for ductile materials such as metals, as the onset of yield for these materials does not depend on the hydrostatic component of the stress tensor.

Mathematically the criterion is expressed as:

$$J_2 = k^2 \qquad \textbf{(2.2)}$$

where k is the yield stress of the material in pure shear. The magnitude of the shear yield stress in pure shear is √3 times lower than the tensile yield stress in the case of simple tension. Thus, we have:

$$k = \frac{S_y}{\sqrt{3}} \qquad \textbf{(2.3)}$$

where S_y is the yield strength of the material. If we set the von Mises stress equal to the yield strength and combine the above equations, the von Mises yield criterion and expressed as:

$$\sigma_v = \sqrt{3J_2} \qquad \textbf{(2.4)}$$

or

$$\sigma_v{}^2 = 3J_2 = 3k^2 \qquad \textbf{(2.5)}$$

By definition of the second stress invariant, ***Eq. 2.5*** yields:

$$\sigma_v{}^2 = \frac{1}{2}[(\sigma_{11} - \sigma_{22})^2 + (\sigma_{22} - \sigma_{33})^2 + (\sigma_{33} - \sigma_{11})^2 + 6(\sigma_{12}{}^2 + \sigma_{23}{}^2 + \sigma_{31}{}^2)] \qquad \textbf{(2.6)}$$

This equation defines the yield surface as a circular cylinder (***Fig. 2.5***) whose yield curve, or intersection with the deviatoric plane, is a circle of radius $\sqrt{2}k$. This implies that the yield condition is independent of hydrostatic stresses.

In the case of pure shear stress, the von Mises criterion becomes:

$$\sigma_{12} = k = \frac{S_y}{\sqrt{3}} \qquad \textbf{(2.7)}$$

Figures

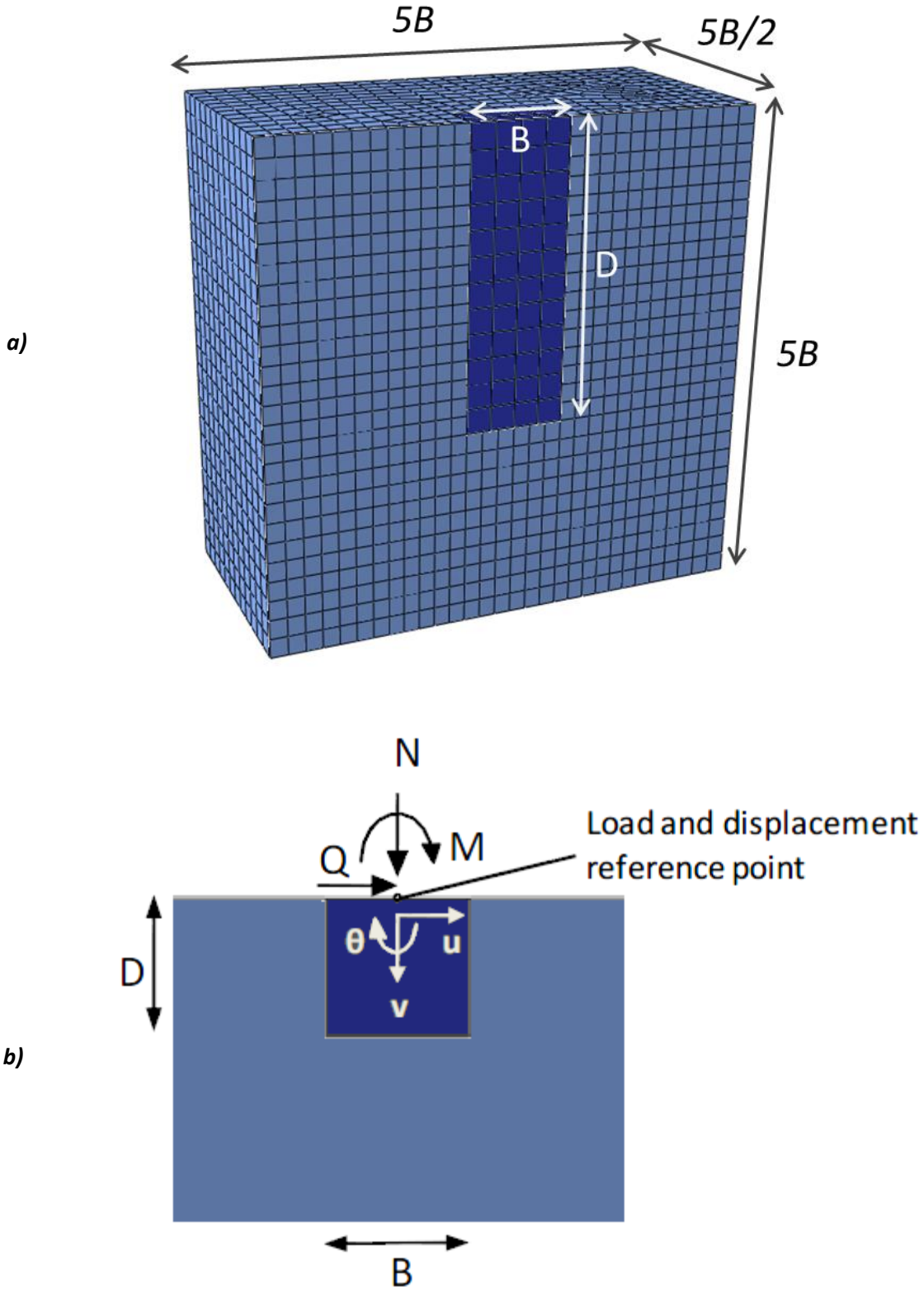

Figure 2.1 *a) Geometry of the 3D Finite Element model used in the numerical analyses. b) Sign convention for loads and displacements.*

a)

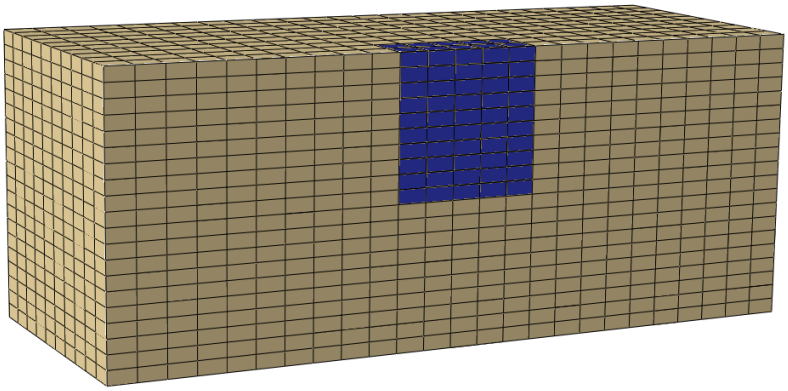

b)

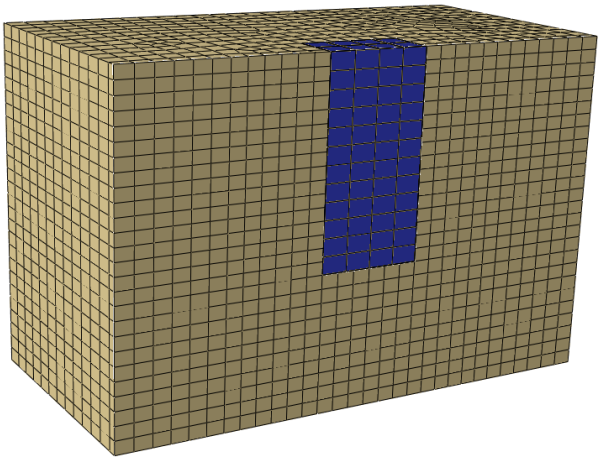

c)

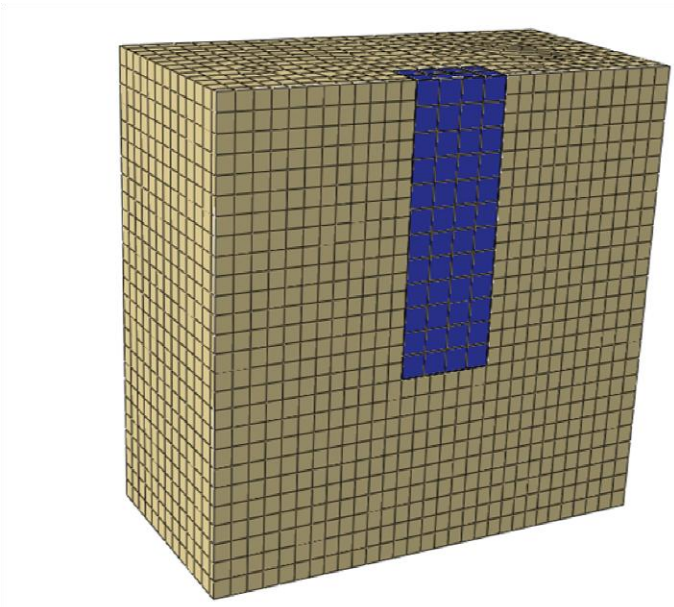

Figure 2.2 *3-D visualization of the FE models for the three embedment ratios considered. a) D/B = 1, b) D/B = 2, c) D/B = 3*

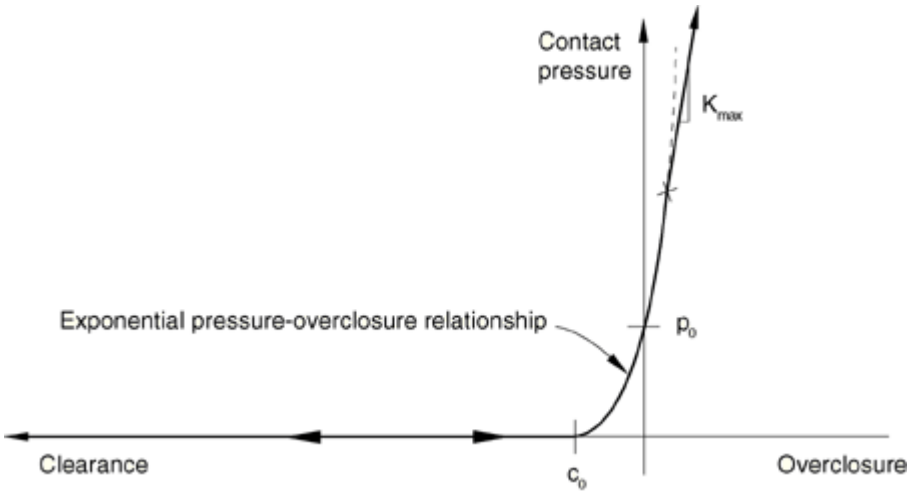

Figure 2.3 *The modified pressure-overclosure relationship for the nonlinear interface adopted in the model.*

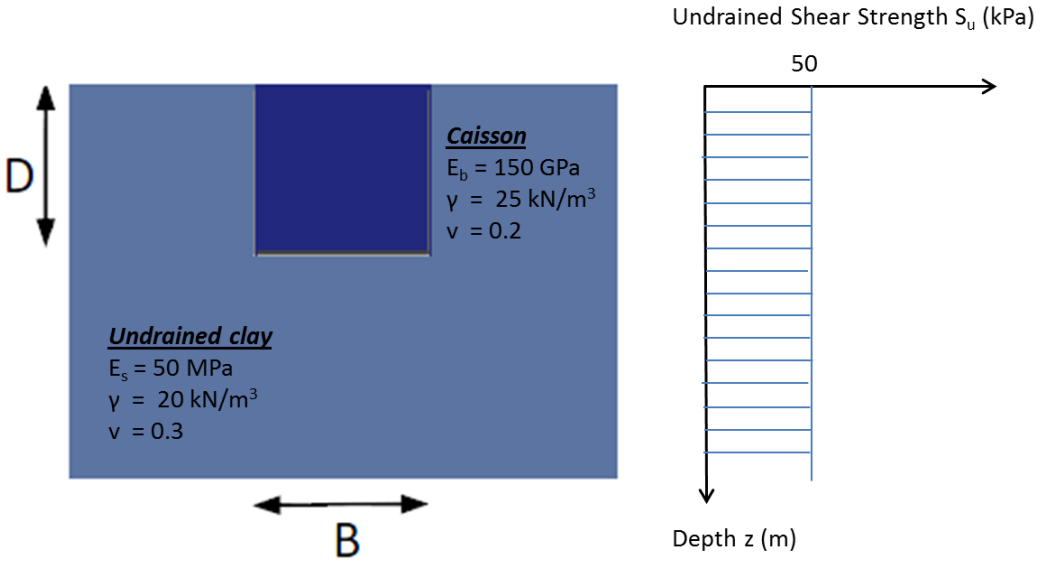

Figure 2.4 *The soil profile considered in the FE analyses. Soil conditions are considered undrained with the clay's undrained shear strength being uniformly distributed with the depth. The enormous stiffness ratio renders the foundation absolutely rigid with respect to the caisson for the embedment ratios considered.*

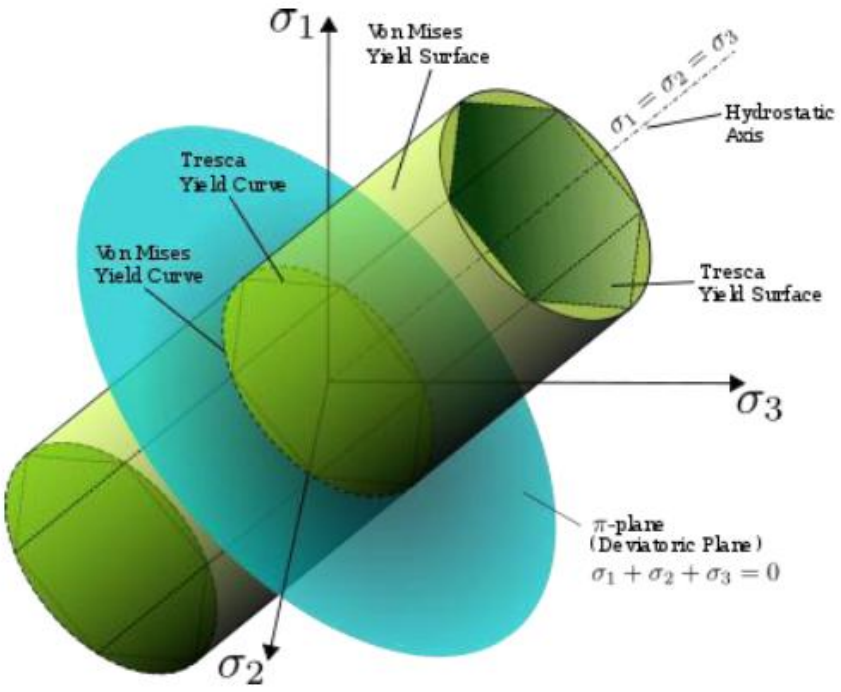

Figure 2.5 *The von Mises criterion is represented by a cylinder of radius* $\sqrt{2}k$ *that runs along the hydrostatic axis in the* σ_1-σ_2-σ_3 *space. The yield surface is compared with that proposed by Tresca.*

CHAPTER 3
Failure envelopes

3.1. Introduction

The term “failure envelope” defines the locus of the points that represent failure of the foundation in *M-Q-N* space. The relationship between two of the above – in other words a cross-section of the failure envelope – is conventionally termed an “interaction curve”. ***Figures 3.1 a)*** and ***b)*** depict typical failure envelopes of surface foundations on sand [*Nova and Montrasio 1991; Gottardi and Butterfield 1995; Chatzigogos, Figini, Pecker, Salençon 2011*] and clay respectively [*Cremer, Pecker, Davenne 2001*]). As part of this thesis, we aim to produce failure envelopes in the case of caisson foundations on undrained clay, where two soil-caisson contact interfaces are considered. The first is a simple interface where the caisson is considered rigidly connected to the soil and is referred hereafter as “bonded interface”. The second is a more realistic simulation of the interface where both slippage and gapping can occur. Slippage is controlled by the Coulomb law, in which the effect of the value of the coefficient of friction is parametrically investigated.

Generally, emphasis is given to the extraction and analytical representation of the failure surfaces for the case of the nonlinear interface rather than that of the bonded interface. Regarding the latter, our results are utilized for the purposes of validating previous work done by Gerolymos, Zafeirakos and Souliotis [*2012*] as well as effectively comparing them with the special interface of interest in order to provide insight to the effect of interface nonlinearities.

3.2. Load reference point

In the case of surface foundations the choice of the load reference point has a negligible impact on the shape of a failure envelope due to their inherent symmetry. However, in the case of embedded foundations, failure envelopes are increasingly asymmetric with respect to the embedment ratio as will be shown below. ***Figures 3.2*** and ***3.3*** illustrate the yield surfaces in *M*-*Q* space for embedded foundations in the case where the load reference point is at the base and the head of the foundation respectively. In the first case, the over-strength section of the curve is manifested in the first quadrant where *M,Q* act in the same direction. In the second case, on the other hand, the over-strength section appears at the second quadrant where *M,Q* act in a counterbalancing way. Note that In the following analysis, we have selected the top of the caisson as a reference point.

3.3. Methods for the extraction of failure envelopes

Various methods have been developed for the extraction of interaction curves referring to embedded foundations, extending the ones already known from previous studies on surface foundations. The two most common methods are *(a)* static pushover tests and *(b)* swipe tests and they are distinguished by different loading paths leading to the failure of the soil-foundation system. In this thesis, static pushover tests are mainly used to extract the failure envelopes, while the use of swipe tests is limited to validation purposes.

3.3.1. Static pushover tests

Considering that the foundation supports a 1-DoF oscillator, one expects that radial loading paths on the *M-Q* plane are applied in the system. Through a series of force-controlled analyses the failure envelope is ultimately determined. Prior to that, the foundation has undergone vertical loading *N* to a fraction $\chi = N/N_u$ of its ultimate capacity. [*Cremer, Pecker, Davenne 2001; Gouvernec 2004; Gajan, Kutter, Phalen, Hutchinson, Martin 2005*].

3.3.2. Description of the method

The steps followed in our numerical experiments represent the actual conditions in the field. The soil undergoes geostatic loading and then a part of the soil is replaced by the foundation, on which a vertical load N is applied increasingly till a specified value of $\chi = N/N_u$ is reached. Afterwards, the vertical load is kept constant and a combination of horizontal force and moment is applied at the head of the caisson till the complete failure of the system. Apparently, this implies the state in which no further lateral loading can be undertaken. The above procedure is repeated for various factors of safety against vertical loading and for various radial loading paths. Our aim is to extract the ultimate capacities under pure moment M_u and pure horizontal force Q_u, and then sweep the *M-Q* plane so that a cross-section of the failure envelope is revealed.

3.4. Ultimate capacity under pure loading

3.4.1. Bonded interface

In general, embedment increases vertical, horizontal and moment capacity as failure mechanisms are forced deeper within the soil mass. The soil mechanisms that are developed in the case of pure horizontal and pure moment loading at the head of the caisson are analyzed in detail in section ***3.6***.

Figures 3.4 and ***3.5*** illustrate the change in ultimate horizontal and moment capacity of caisson foundations - given in dimensionless terms - of three distinct embedment ratios *1, 2* and *3* with respect to the inverse factor of safety χ. The values derived from the numerical analyses are compared with the analytical expression proposed by Gerolymos et al, as shown below:

$$Q_u = BDS_u \left(\frac{D}{B}\right)^{-2.15} (1 + \frac{D}{B})^{2.89}(1 - \chi)^{0.17} \qquad \textbf{(3.1)}$$

$$M_u = 0.46B^2DS_u \left(\frac{D}{B}\right)^{-1.49} (1 + \frac{D}{B})^{3.39}(1 - \chi)^{0.17} \qquad \textbf{(3.2)}$$

As expected, the soil plastification taking place around the caisson prior to the lateral loading increases as the vertical load (χ) increases, thus reducing the system's margins for further plastification till failure. The embedment ratio is shown to have a significant effect on the ultimate capacities and especially the moment capacity M_u. As *D/B* increases the soil resisting mechanisms are forced deeper into the soil mass mobilizing a greater part of it. Note also that the two capacities decline in about the same fashion with respect to FS_V, a fact that justifies the adoption of a common reduction factor in the above expressions. The analytical fit to the numerical data is fairly satisfactory.

Regarding the effect of the undrained shear strength, Souliotis and Gerolymos have shown that the ultimate capacities have a linear dependence on S_u at least in the case where it is uniformly distributed with depth. In fact, S_u is the sole indicator of the system's strength since the interface is considered bonded, and slippage or gapping may not occur. This assumption is carried on to the case of the nonlinear interface where the above phenomena are taken into account.

3.4.2. Nonlinear interface

The same series of numerical analyses were carried out in the case of the more realistic nonlinear interface in order to deduce the respective ultimate capacities. In contrast to the previous case where the vertical load had a monotonic effect on the

ultimate lateral capacity, the latter now changes in a parabolic fashion with respect to χ. ***Figures 3.6*** and ***3.7*** show the dimensionless horizontal and moment capacities for the three characteristic embedment ratios considered and for four distinct values for the coefficient of friction $\mu = 0.1, 0.5, 1, 2$. Note that a coefficient of friction of *0.1* corresponds to a smooth interface where slippage is very likely to occur by the initial stages of loading. On the other hand, a coefficient of friction of *2* amounts to nearly no slippage at all, which means that the nonlinear interface may only experience gapping.

As the vertical load increases, the ultimate lateral capacities increase until they reach a peak at $\chi \approx 0.5$. As the vertical loading becomes more considerable, however, the trend is reversed. Until $\chi \approx 0.8 - 0.9$, depending mainly on the embedment ratio, the capacities have once again reached their $\chi = 0$ values. Finally, as the vertical load approaches the foundation's vertical capacity, the lateral capacities decline sharply until they are nullified for $\chi = 1$.

Two antagonistic mechanisms are observed, the interplay between which leads to the parabolic shape displayed. For $\chi < 0.5$ the interface enjoys an increase in the total normal force applied both on the sidewalls and the base, while the plastification around the caisson is still limited. Taking into account the nature of the Coulomb law, the interface's shear strength and hence the foundation's overall lateral capacity is increased. Above that limit value of χ, however, the plastification taking place in the soil immediately surrounding the caisson becomes considerable and the lateral capacity starts to decline. It takes a $\chi \approx 0.85$ in order for the two mechanisms to be equalized. Apparently, until $\chi = 1$, plastification governs the overall response in the last branch of the curve.

There are various mechanisms that lead to an increase of the total force applied on the soil-caisson interface leading to enhanced shear strength, as stated above. The most significant of these mechanisms are given below:

(a) The soil exhibits dilative behavior due to a Poisson's ratio of 0.3 adopted in the model, which means that vertical loading is partly translated to increased sidewall pressure as a result of embedment.

(b) At the foot of the caisson, where the passive wedge is formed, the shear stress developed due to the applied horizontal load or moment has to overcome the shear stress derived from the applied vertical load. On the other hand, the two types of shear stress induced at the top passive wedge have the same direction. The system derives extra strength from the fact that the foot wedge mechanism is more considerable than the head wedge one due to embedment. Hence, the application of a greater horizontal force or moment is required in order for the foundation to overcome the already applied shear stress and reach failure.

(c) There is an explicit increase in the pressure applied at the base of the caisson, which results in its enhanced shear strength. However, this mechanism is important mainly in lightly embedded foundations, where a significant fraction of the vertical load is undertaken by the base.

Figure 3.6 presents plastic strain magnitude contours at the point of failure in the case of horizontally applied load Q for three characteristic inverse factors of safety χ *= 0, 0.5, 0.95*. It becomes evident that the soil plastification due to vertical loading gradually comes to govern the response.

Following the work of Gerolymos et al in the case of the bonded interface,the following expressions were derived by fitting the numerical results:

$$Q_u = \alpha_Q B D S_u \left(\frac{D}{B}\right)^{\beta_Q} (1+\frac{D}{B})^{\gamma_Q}\left[1+\varepsilon_Q\chi-(\varepsilon_Q+1)\chi^2\right]^{\zeta_Q} \qquad \textbf{(3.5)}$$

where:

$$\alpha_Q = 6.71\mu^{0.02851}(1+\mu)^{-1.551} \qquad \textbf{(3.6)}$$

$$\beta_Q = 0.477\mu^2 - 2.29\mu + 1.013 \qquad \textbf{(3.7)}$$

$$\gamma_Q = -0.564\mu^2 + 2.834\mu - 1.162 \qquad \textbf{(3.8)}$$

$$\varepsilon_Q = 7.48 + 2.89\left(\frac{D}{B}\right)^{-3} \qquad \textbf{(3.9)}$$

$$\zeta_Q = -0.298 + 0.496\left(\frac{D}{B}\right)^{-0.134} \quad \textbf{(3.10)}$$

$$M_u = \alpha_M B^2 D S_u \left(\frac{D}{B}\right)^{\beta_M} (1+\frac{D}{B})^{\gamma_M}[1+\varepsilon_M\chi-(\varepsilon_M+1)\chi^2]^{\zeta_M} \quad \textbf{(3.11)}$$

where:

$$\alpha_M = 0.718\mu^{-0.361}(1+\mu)^{0.285} \quad \textbf{(3.12)}$$

$$\beta_M = -2.97 + 2.17\mu^{-0.235} \quad \textbf{(3.13)}$$

$$\gamma_M = 5.027 - 2.677\mu^{-0.23} \quad \textbf{(3.14)}$$

$$\varepsilon_M = 6.37 - 1.17\left(\frac{D}{B}\right)^{1.04} \quad \textbf{(3.15)}$$

$$\zeta_M = 0.0365 + 0.163\left(\frac{D}{B}\right)^{0.247} \quad \textbf{(3.16)}$$

Apparently the above expressions are much more complex compared to the equivalent bonded interface ones in order for the effect of slippage and gapping to be taken into account. Parameters α, β, γ were found to be functions of μ, while ε, ζ are generally functions of both μ and *D/B*. Note that the equations of α, β, γ could not be formed in such a way that they can account for limit values of variable μ; instead they can be used in the (wide) range examined herein. A clear trend of ε, ζ as far as μ is concerned was not evident in the results of the numerical analyses, a fact which led us to adopt a fit to their mean value. Thus ε, ζ are shown above as expressions of *D/B* solely. In ***Figures 3.7*** and ***3.8*** the numerical data are compared to the analytical expression and the fit is satisfactory especially for greater embedment ratios. Moving to more lightly embedded foundations, the base gradually contributes more to the overall response. Taking into account that the base is most immediately affected by the interplay of FS_V and μ, and some of its aspects are only implicitly taken into account in the analytical expressions, the fit gradually becomes worse; yet, the observed error does not surpass 10-15% in any case.

Due to the complex interplay of slippage and gapping, there can be no simple interpretation of the various parameters in respect to their equivalent ones in the case of a bonded interface. We also observe that χ has a different effect on Q_u and M_u because of the different soil resisting mechanisms deployed and the different effect that gapping has in each case.

3.4.3. Design considerations

In contrary to what may have been originally expected as the effect of slippage and gapping on the horizontal load and overturning moment, the dimensionless $Q_u - \chi$ curve of the Coulomb interface does not necessarily lie within that of the bonded one. While gapping cannot act in favour of the caisson in any case, the adoption of a Coulomb law seems to provide extra strength to the foundation under great values of μ. ***Figure 3.9*** compares the dimensionless Q_u curves of a deeply embedded caisson foundation ($D/B = 3$) under bonded and nonlinear interface conditions. In the latter case, a value of $\mu = 0.5$ has been applied. While for $\chi < 0.5$, the Coulomb interface displays a reduction in the horizontal capacity, in the remaining curve the capacity lies above the "unconservative" bonded interface. A practical approach would be to evaluate the coefficient of friction and adopt the intersection of the curves for design applications.

3.5. Failure envelopes

3.5.1. Introduction

Figure 3.10 illustrates the interaction curve derived from multiple pushover tests in the case of a deeply embedded ($D/B = 3$) lightly loaded ($\chi=0.2$) caisson foundation normalized by the ultimate capacities under pure horizontal force and overturning moment. This kind of normalization was initially introduced by Bransby and Randolph [*1999*], who noticed that the shape of the interaction curve is virtually

unaffected by the vertical factor of safety. This observation has been validated by various researchers including Gerolymos et al [*2012*] who went on to analytically express the effect of the embedment ratio to the shape of the normalized interaction curve. These observations have been very helpful in the analytical representation of the complete failure envelope and its direct implementation in a "macro-element" approach of embedded foundations. By deducing the vertical, horizontal and overturning moment capacity as well as their normalized interaction law, the complete failure envelope can be determined.

3.5.2. The shape of the failure envelope

3.5.2.1. Failure envelopes of embedded foundations

As a first analysis of the shape of the interaction curve, two general regions should be distinguished (***Fig. 3.10***). In the first quadrant, the horizontal force and overturning moment at the head of the caisson act in the same direction and mobilize relevant soil resisting mechanisms. Their relationship is approximately linear since they tend to "draw" resistance from these similar mechanisms. In the second quadrant, however, the overturning moment becomes counterbalancing to the horizontal force and the system exhibits an enhanced capacity derived from its embedment. This is a characteristic that is typical of embedded foundations only.

3.5.2.2. Bonded interface

Figures 3.11 a), b) and ***c)*** illustrate the effect of the factor of safety against vertical loading to the shape of the normalized interaction curves for three distinct embedment ratios in the case of a bonded soil – caisson interface [*Gerolymos and Souliotis, 2012*]. It is evident that this effect is adequately small so that it can be assumed that the shape of the curves remains unchanged with FS_V, especially when it comes to deeply embedded foundations. This has a direct impact on the analytical representation of the yield surface as will be shown further below.

Figure 3.3 compares the normalized interaction curves for the three characteristic embedment ratios *1,2* and *3.* As the embedment ratio increases, the yield surface becomes increasingly eccentric in accordance with observations by Yun and Bransby [*2007*].

3.5.2.3. Nonlinear interface

In the case where interface nonlinearities are considered, the shape of the curve displays a higher variability with FS_V, as ***Fig. 3.12*** suggests. It seems that the adoption of the Coulomb friction law is mainly responsible for this effect rather than the detachment of the caisson from the surrounding soil.

Figure 3.13 compares the interaction diagrams for caisson foundations of $FS_V = 2$ and of the three embedment ratios considered, where the coefficient of friction μ takes up two characteristic values *0.1, 1.* As stated earlier in this chapter, a value of $\mu = 1$ corresponds to a smooth soil - caisson interface, in which slippage is likely to occur at the very early stages of loading, while $\mu = 1$ represents interface conditions where slippage is considerably limited. The shape of the failure envelope seems to be generally unaffected by the value of the coefficient of friction, perhaps with the exception of the *D/B = 1* case. In the latter, where the contribution of the base to the overall response is significantly greater, the value of the coefficient of friction differentiates the interplay of the mechanisms deployed at the over-strength region, leading to an enhanced maximum horizontal capacity.

As part of our approach, the variability of the shape of the failure envelope with respect to either FS_V or μ is considered limited and will thus not be taken into account in the analytical representation of the envelopes, as will be shown in section ***3.5.4.2.***

As with the case of the bonded interface, the shape of the failure envelope is most significantly affected by the embedment ratio. ***Fig. 3.14*** illustrates the aforementioned effect in the failure envelopes of caisson foundations of an $FS_V = 2$ and a Coulomb interface of $\mu = 1$. Apart from expanding, the failure envelope also seems to be rotating in a clockwise fashion as *D/B* increases. This rotational trend is more evident

in ***Fig. 3.15***, which compares the failure envelopes of caisson foundations of the selected embedment ratios for the two different types of interfaces considered and an $FS_V = 2$. For small embedment ratios ($D/B = 1$) the envelope for the sophisticated nonlinear interface is considerably rotated with respect to the envelope for the bonded interface, while the expansion is of about the same magnitude. As the embedment increases, however, the nonlinear interface envelopes appear less rotated with respect to the bonded interface ones. A difference in the expansion of the two types of curves is also evident.

The fact that the observed rotation is greater in low embedment ratios leads us to investigate the effect of soil – caisson detachment on the failure mechanisms for different embedment ratios. This topic is analyzed in detail in section ***3.5.3.2*** of this thesis. Prior to that, it is essential to analyze the soil deformation mechanisms developed along the yield surface, starting from the case of the simple bonded interface.

3.5.3. Soil Deformation Mechanisms

3.5.3.1. Bonded interface

In order to gain insight into the various mechanisms deployed as part of the lateral response of an embedded foundation, it is required that we delve into a thorough investigation of the soil deformation patterns, which will reveal the interplay of the horizontal force and the overturning moment. As many researchers [*Salençon and Pecker 1995; Bransby and Randolph 1998; Ukritchon et al. 1998*] have pointed out in the past, the soil resisting mechanisms developed along an interaction curve varies with the load angle *M/Q*.

Bransby and Yun [2009] carried out a series of upper-bound plasticity analyses in order to distinguish the different types of failure observed under combined M-Q loading of skirted foundations. This type of foundation differs from the solid embedded foundations in that soil deformation may also take place inside the skirts. The

researchers concluded that there are 5 distinct soil mechanisms that can be developed : *(a) " forward scoop" , (b) "scoop-slide", (c) "internal Hansen", (d) " reverse scoop" and (e) "internal double scoop"* (***Fig. 3.16***) Among these mechanisms, *(c)* and *(e)* may only be developed in skirted foundations. In order to find a single point on the failure envelope two load components were selected. Upper-bound work calculations were then carried out numerically in a spreadsheet with each available deformation mechanism to find the lowest value of the unknown load. For each mechanism, the kinematic variables were changed to give the lowest collapse load. The lowest value found represented the best estimate (lowest upper-bound solution) of the combined *V–H–M* failure condition. This process was then repeated for different values of the load components to describe key sections of the failure envelope.

Figures 3.17 a), b) and ***c)*** illustrate the plastic strain magnitude contours at the point of failure for caisson foundations of the three embedment ratios considered herein and for two characteristic factors of safety against vertical loading $FS_V = 2, 5$. The failure points along the yield surface were picked to match either a limit value of a load component *M* or *Q* or a characteristic location of the pivot point in respect to the depth of embedment *D*. These points include:

(a) Pure moment capacity: $Q = 0$, $M = M_u$

(b) Pure horizontal load capacity: $Q = Q_u$, $M = 0$

(c) Inverted pendulum: $Q > 0$, $M < 0$, $z_p = D$

(d) Maximum horizontal capacity: $Q = Q_{max}$, $M < 0$, $z_p = \infty$

(e) Maximum moment capacity: $Q > 0$, $M = M_{max}$, $z_p = 0$

The above points and any other along the yield surface of an embedded foundation may be represented by one of the basic mechanisms illustrated in ***Figure 3.18***. These are *a)* the "*scoop"* mechanism, manifested at pure moment capacity, *b)* the *"scoop-slide"* mechanism, developed in the *a-c* region of the yield surface, *c)* the *"diffusive mechanism",* exhibited at maximum horizontal capacity for deeply embedded foundations and *d)* the *"sliding mechanism",* exhibited at maximum horizontal capacity

for shallow embedded foundations. In the remaining part of the yield surface we observe an oppositely directed *"scoop-slide"* mechanism referred to by many researchers as *"reverse-scoop"* mechanism. The above considerations allow us to map the yield surface according to ***Fig. 3.19***.

The differentiation between the mechanisms that shallow and deep embedded foundations exhibit at maximum horizontal capacity is of particular importance. In the former, the small depth of embedment allows for a localized shear zone to be developed while both the caisson and the soil lying above the failure zone move as a "rigid" body. In the case of a deeply embedded foundation, however, it seems that the critical type of failure is not localized but rather diffusive. This means that plastification is not limited to a small shear band but is diffused to the soil surrounding the caisson. A smaller diffusive mechanism is also deployed at the point where deeply embedded foundations exhibit their maximum moment capacity. Driven by the similar characteristics of the *d)-e)* region of the envelope - lack of a specific pivot point - we make the assumption that deeply embedded foundations actually exhibit the above behavior in the whole *d)–e)* region of their yield surface.

The above mechanisms are manifested for about the same *M/(QD)* ratios regardless of the embedment ratio or the factor of safety against vertical loading. The above is validated by ***Figures 3.20 a), b)*** and ***c)*** that show the depth of the pivot point with respect to the load angle for each of the embedment ratios considered herein. As *M/(QD)* approaches *+/-* ∞, namely for pure moment capacity (point a)), the foundation rotates around a point located approximately at the middle of the caisson's height. Moving along the yield surface in a clockwise fashion, for absolutely smaller load angles, the depth of the pivot point increases, reaching the depth of embedment *D* at point c). At this point, the caisson moves as an inverted pendulum. After that point, the depth of the pivot point increases dramatically approaching infinity at point d) (pure sliding). This is actually the deepest "scoop-slide" mechanism that can be developed. In a very short region in terms of *M/(QD),* the depth of the pivot point is nullified and a pendulum mechanism is revealed. In the final section, the pivot point is lowered again reaching its starting value, this time for negative pure moment capacity. Comparing the three graphs, we conclude that the pivot path is fairly insensitive to the embedment ratio.

3.5.3.2. Nonlinear interface

Figures 3.21 a), b) and ***c)*** illustrate the plastic strain magnitude contours at the point of failure for caisson foundations of the three embedment ratios considered herein and for two characteristic factors of safety against vertical loading $FS_V = 2, 5$ under nonlinear interface conditions. As with the bonded interface, the failure points along the yield surface were picked to match either a limit value of a load component *M* or *Q* or a characteristic location of the pivot point in respect to the depth of embedment *D*, revealing the various mechanisms developed. The latter differ from the ones developed under bonded interface conditions in a different fashion depending on the depth of embedment, while there is generally no active wedge failure observed behind the foundation. ***Fig. 3.22*** displays the gapping effect for different embedment ratios and for each of the basic mechanisms already analyzed in the case of bonded interface conditions. Gapping is shown to occur at a greater extent in the case of the shallow embedded foundation, which becomes completely detached on the back side at the point of maximum horizontal capacity. An interesting observation is that detachment cannot occur only at a specific point in the yield surface, that of the maximum moment capacity (see ***Fig. 3.23***).

Figures 3.24 a), b) and ***c)*** illustrate the depth of the pivot point with respect to the load angle *M/(QD)* in the case of nonlinear interface conditions. In the case of *D/B = 1,* we observe that the distance between the two branches of the curve increases and the transition to the extreme values becomes smoother. In addition, the depth of the pivot point appears to be systematically greater than in the case of the bonded interface. This is because the detachment from the soil, which occurs mainly near the surface, drives the caisson to seek resistance in deeper mechanisms.

After this short investigation of the soil deformation mechanisms that govern the response of embedded foundations, we now attempt to justify the rotational effect observed in ***3.5.2.1. Figure 3.25*** presents the deformed FE mesh for the caisson foundations of the three embedment ratios investigated at a point of the yield surface located between points c) and d), little before exhibiting their maximum horizontal

capacity. In the case of the shallow embedded foundation, detachment leads to complete loss of the resisting passive wedge at the foot which translates into decreased capacity to undertake moment (since it is the moment rather than the horizontal force that relies mostly on the presence of a lever arm for resistance). This, in turn, means that the pure sliding point moves towards smaller load angles and the caisson exhibits its maximum horizontal and moment capacity "sooner" that in the case of a bonded interface. This phenomenal expansion of the yield locus in the scoop-slide region, however, does not come without a price. The failure envelope experiences a contraction in the reverse scoop region, where the decreased moment capacity seizes to act in favor of the caisson. Ultimately, the yield surface exhibits a counter-clockwise rotation with respect to the one where bonded interface conditions are considered. The above phenomenon becomes less evident for the *D/B = 2* caisson, where the passive wedge is weakened rather than deactivated, and almost vanishes for *D/B = 3*. This is because the detachment from the surrounding soil affects mainly the upper part of the foundation as the embedment increases.

3.5.4. Analytical expressions and validation

3.5.4.1. Bonded interface

Relevant studies on embedded foundations have suggested that the shape of the yield surface can be described by an oblique parabola in the *M*-*Q* space. For instance, Bransby and Yun [*2007*] have proposed the following equation representing the yield locus of lightly embedded foundations:

$$\left(\frac{H}{H_{max}}\right)^2 + \left(\frac{M^*}{M_0}\right)^2 = 1 \qquad \textbf{(3.17)}$$

where:

- H, H_{max} are the applied and the maximum horizontal force for the foundation respectively

- M*, M_0 are the applied moment and the pure moment capacity of the foundation

Through an optimization technique, Gerolymos et al have concluded that the following form of equation most accurately represents the failure envelope of an embedded foundation:

$$f = (\frac{Q}{Q_u})^2 + (\frac{M}{M_u})^2 + n_3\left(\frac{Q}{Q_u}\right)\left(\frac{M}{M_u}\right) - 1 = 0 \qquad \textbf{(3.18)}$$

where n_3 is a function of the embedment ratio capturing the expansion of the curve and is given by:

$$n_3 = 1.84 - 0.21(\frac{D}{B})^{-1.98} \qquad \textbf{(3.19)}$$

Figure 3.26 provides a visualization of the expansion that n_3 introduces in the yield surfaces of multiple embedment ratios. This expression effectively captures the large difference in the expansion of the *D/B = 2* surface with respect to the *D/B = 1* one, as compared to the smaller difference observed between greater embedment ratios. In fact, the value of the embedment ratio above which the embedment increases only marginally the foundation's maximum normalized horizontal capacity is shown to equal *1.7* [*Gerolymos et al*]. On this basis, any foundation with embedment ratio above this marginal value is effectively a deeply embedded foundation.

The next set of Figures (***3.27***, ***3.28***) validates the fitness of the expressions ***(3.1)***, ***(3.2)*** and ***(3.17)*** by comparing them with the numerical data derived from the experiments in normalized and dimensionless terms respectively. Multiple embedment ratios and factors of safety against bearing capacity failure are considered. The fit to the numerical data, even in dimensionless terms, is great.

3.5.4.2. Nonlinear interface

As previously stated, the effect of both the factor of safety against vertical loading FS_V and the coefficient of friction μ on the shape of the failure envelope was

considered adequately small so that none of them are taken into account in the analytical expressions to be determined in the case of the nonlinear soil – caisson interface. Instead, the envelopes were fitted to the mean value of the numerical data for various values of the factor of safety and 2 limit values for the coefficient of friction. In other words, we suggest that the shape of the envelope be affected only by the embedment ratio as in the case of the bonded interface. In order to capture both the rotation and the expansion of the yield surface the following expression was given as input in an optimization procedure:

$$f = (\frac{Q}{Q_u})^{n_1} + (\frac{M}{M_u})^{n_2} + n_3 \left(\frac{Q}{Q_u}\right)\left(\frac{M}{M_u}\right) - 1 = 0 \qquad \textbf{(3.20)}$$

where parameters n_1, n_2 control the yield locus's rotation (introduced by the detachment of the caisson from the soil) and n_3 controls the yield locus's expansion, both in respect to the embedment ratio *D/B*.

The following expressions were deduced for the above parameters:

$$n_1 = 2 - 0.25(\frac{D}{B})^{-2.06} \qquad \textbf{(3.21)}$$

$$n_2 = 2 + 0.1(\frac{D}{B})^{-1.135} \qquad \textbf{(3.22)}$$

$$n_3 = 1.891 - 0.386(\frac{D}{B})^{-2.361} \qquad \textbf{(3.23)}$$

Figures 3.29 a) and ***b)*** illustrate plots of the above expressions together with the equivalent bonded interface expressions. As the embedment ratio increases, n_1 increases, while n_2 decreases until they ultimately converge to the value that corresponds to bonded interface conditions for an embedment ratio slightly greater than 3. This is in excellent accordance with the observation made that, as the embedment increases, the detachment of the caisson from the soil is limited to a small upper part and thus has a small effect on the overall response. The above allows us to conclude that surface nonlinearities need not be taken into account for embedment ratios higher than 3. Parameter n_3 also seems to be converging to the value of (***Eq. 3.7***), yet following a slightly different path. Finally, ***Fig. 3.30*** presents the combined effect of

n_1, n_2, n_3 on the shape of the failure envelope for multiple values of the embedment ratio *D/B*.

The final set of figures (***3.31 - 3.33***) validates the capacity of the above proposed approach to capture the failure envelopes of embedded foundations in the more realistic case where slippage and gapping are allowed to occur. The analytical expressions are compared to the data derived from the numerical experiments for multiple values of the embedment ratio, the factor of safety against vertical loading as well as the coefficient of friction in both normalized and dimensionless terms. The fit to the numerical data, even in dimensionless terms, is fairly satisfactory.

Figures

a)

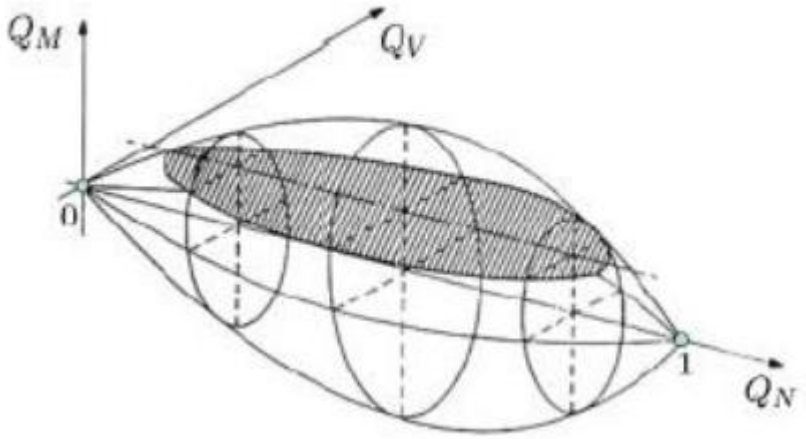

b)

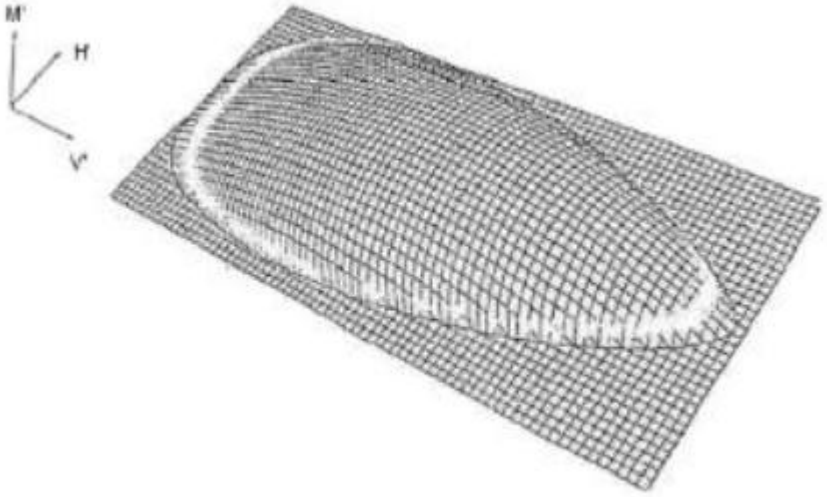

Figure 3.1 *a) Rugby-balls shaped yield surface for surface foundations in cohesionless soil and b) yield surface for surface foundations on cohesive soil.*

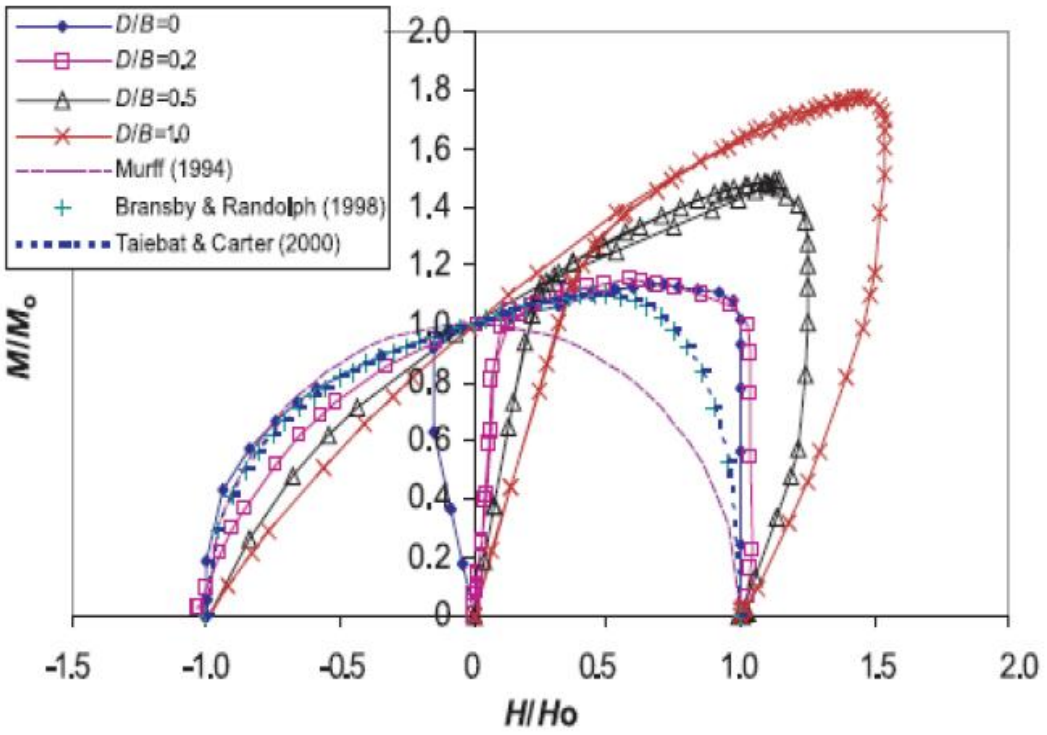

Figure 3.2 *Yield surfaces for lightly embedded foundations in the case where the center of the foundation base has been chosen as a load reference point. The surfaces exhibit an expansion in their first quadrant where M, Q act in the same direction.*

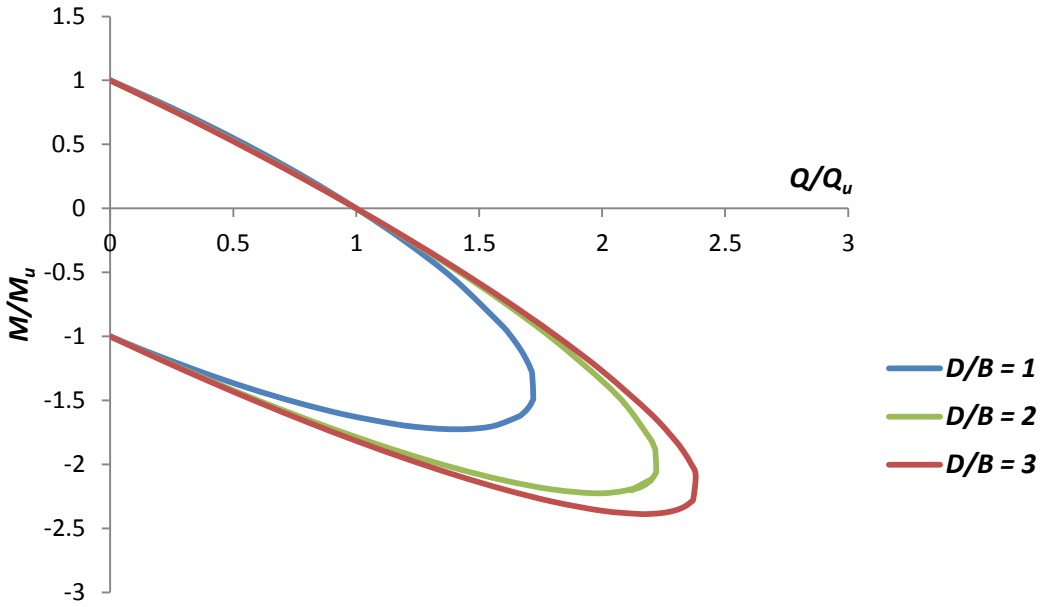

Figure 3.3 *Yield surfaces for embedded foundations in the case where the head of the foundation has been chosen as a load reference point. The surfaces exhibit an expansion in their second quadrant where M, Q act in opposite directions.*

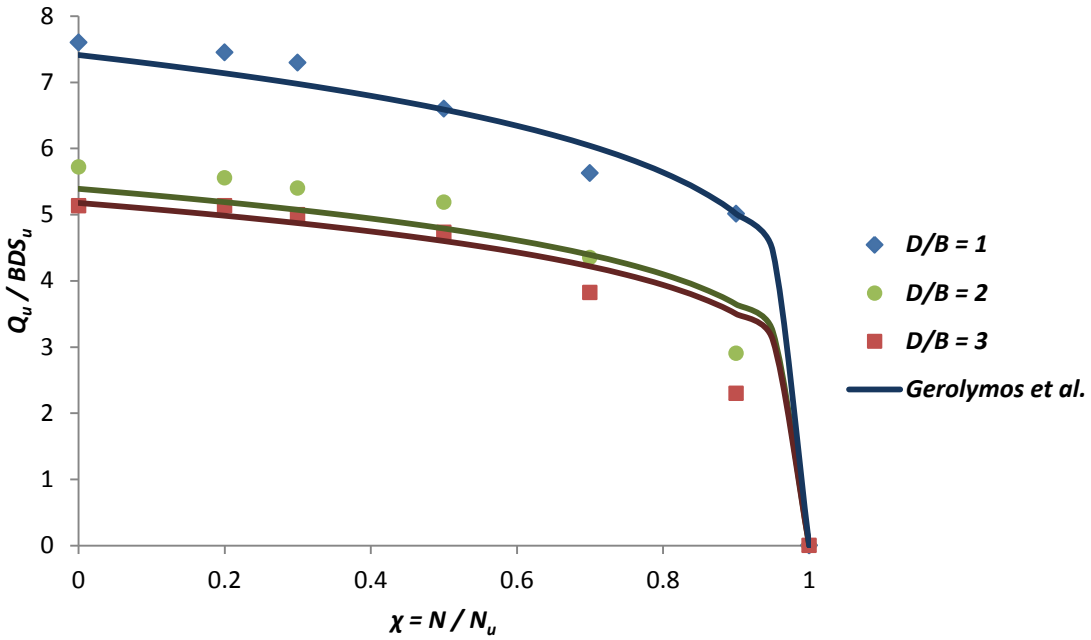

Figure 3.4 *The dimensionless horizontal capacity values derived from the numerical analyses for selected values of χ and D/B (data points) are compared to the analytical expression of Gerolymos et al (lines).*

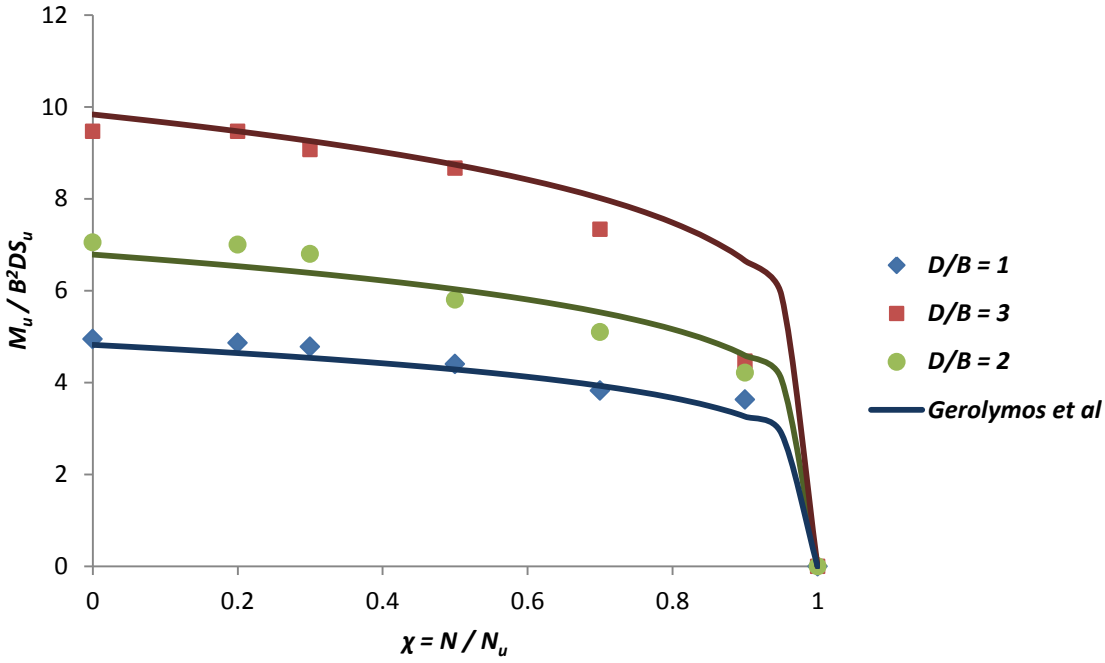

Figure 3.5 *The dimensionless moment capacity values derived from the numerical analyses for selected values of χ and D/B (data points) are compared to the analytical expression of Gerolymos et al (lines).*

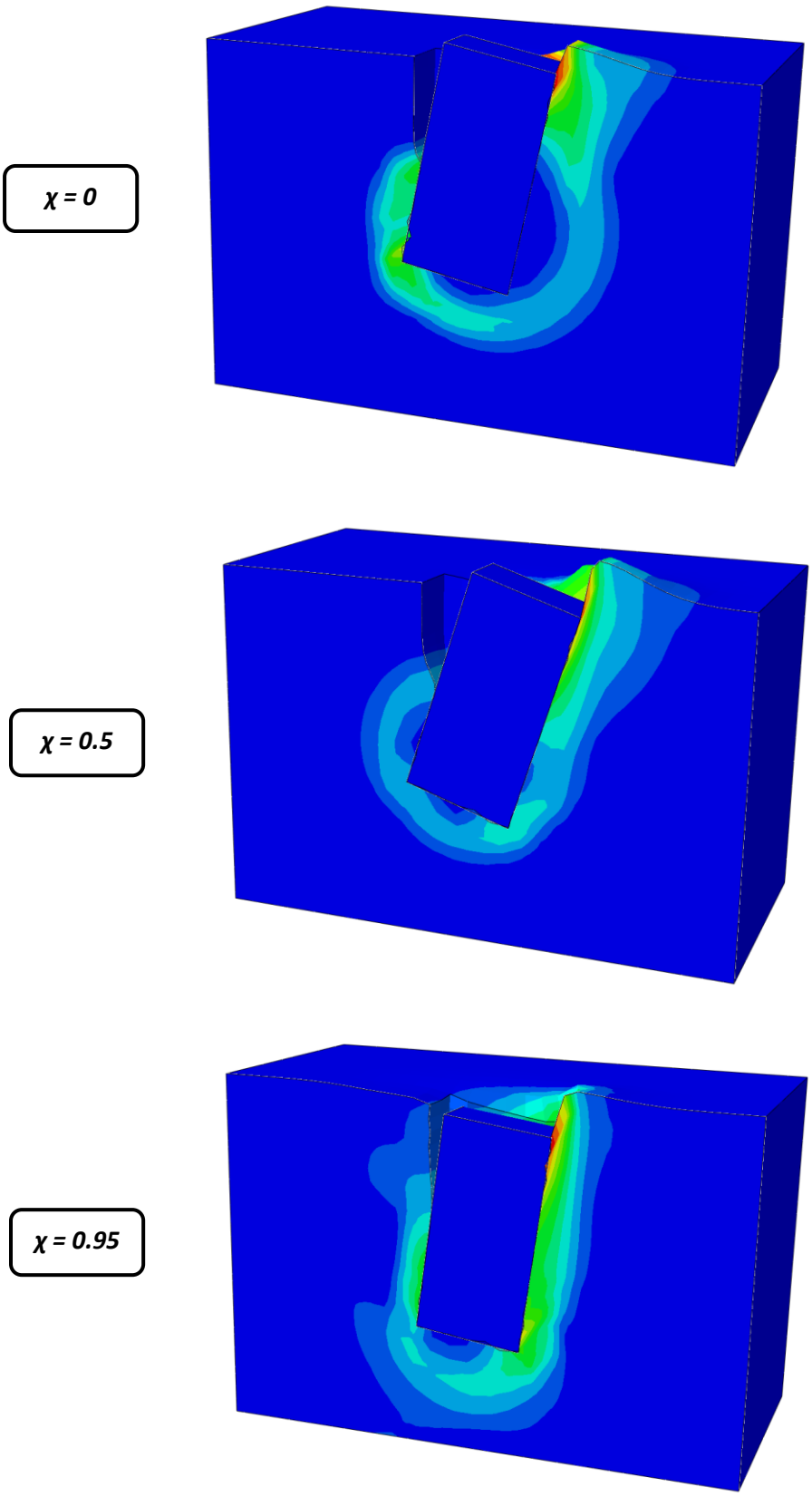

Figure 3.6 *Plastic strain magnitude contours for a deeply embedded (D/B =3) foundation subjected to pure horizontal loading at the top for three values of the inverse factor of safety against vertical bearing a) χ = 0, b) χ = 0.5 and c) χ = 0.95. Interface nonlinearities are taken into account.*

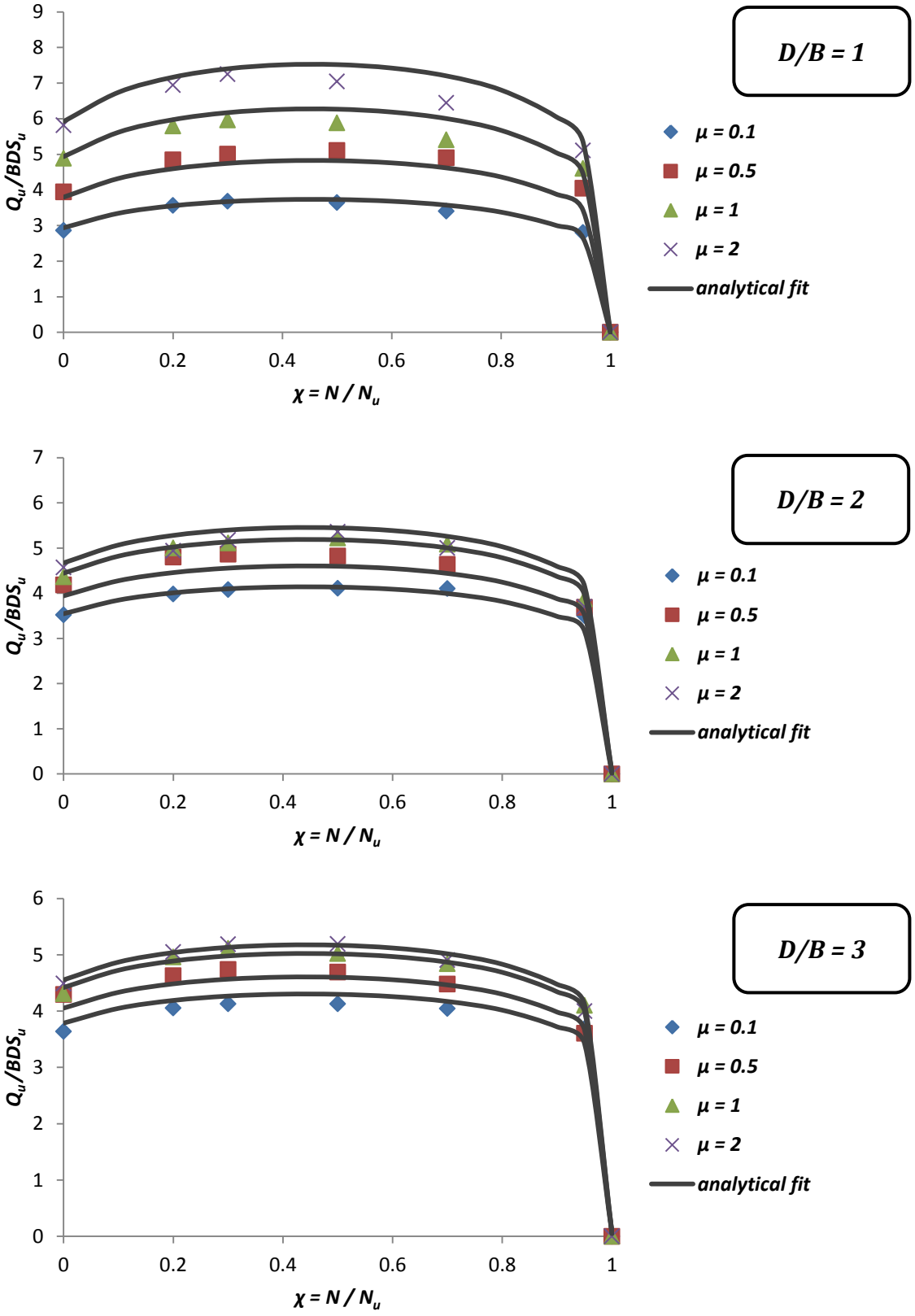

Figure 3.7 *The dimensionless pure horizontal capacities derived from the FE analyses for selected values of D/B and μ (data points) are compared to the proposed analytical expression (lines).*

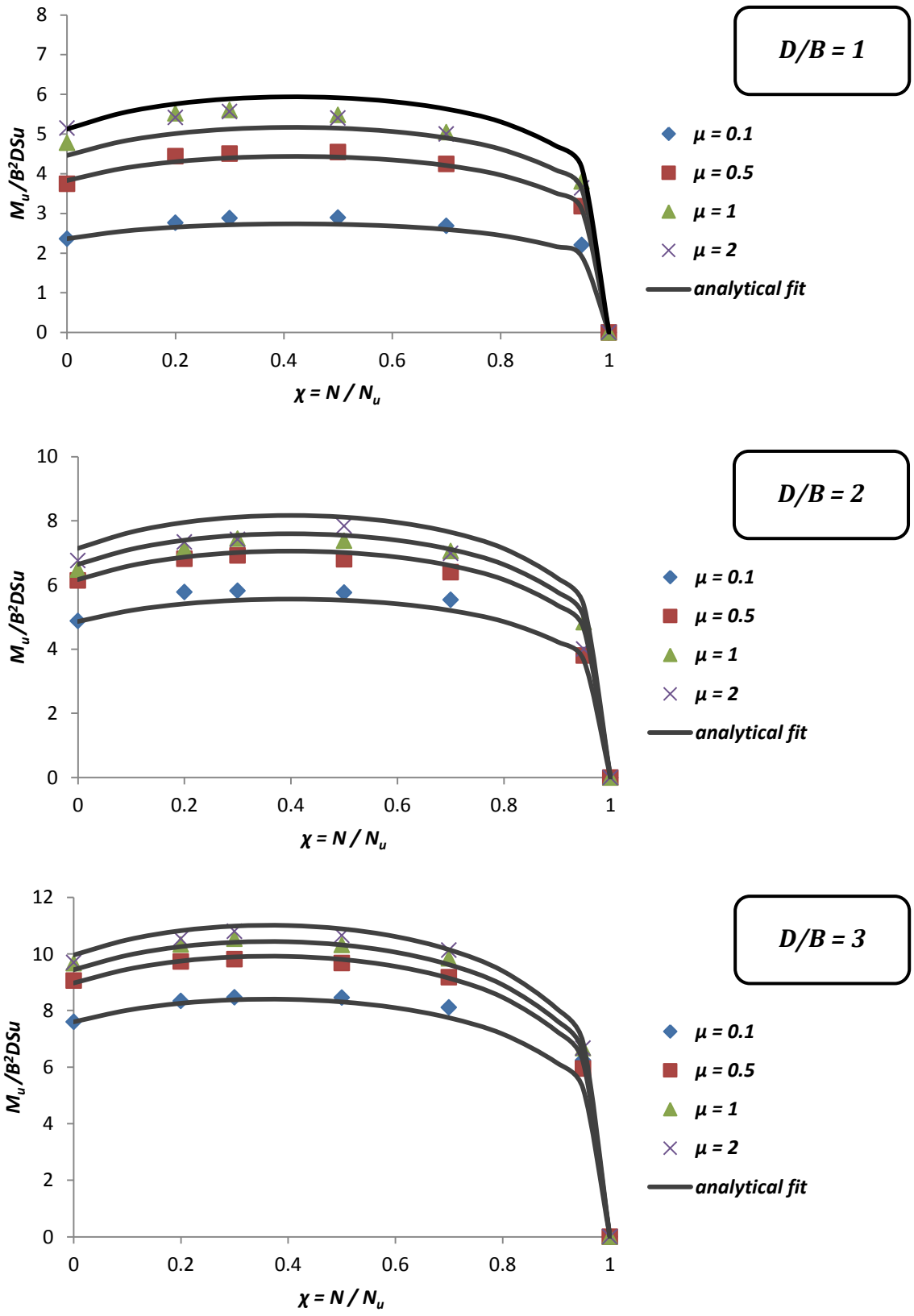

Figure 3.8 *The dimensionless pure moment capacities derived from the FE analyses for selected values of D/B and μ (data points) are compared to the proposed analytical expression (lines).*

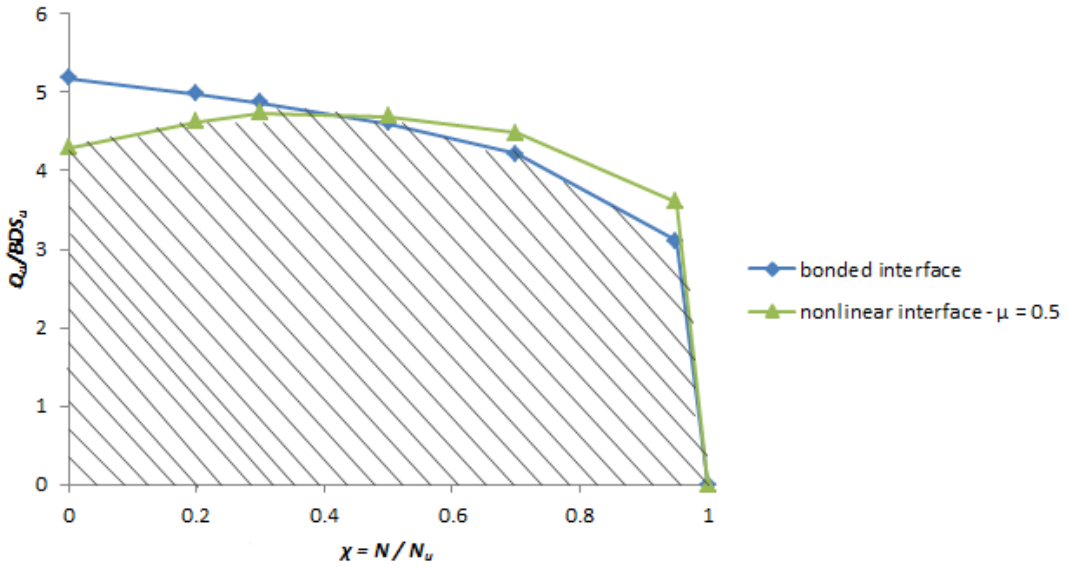

Figure 3.9 *A conservative design consideration for the horizontal capacity of caisson foundations with respect to the inverse factor of safety against vertical bearing capacity failure.*

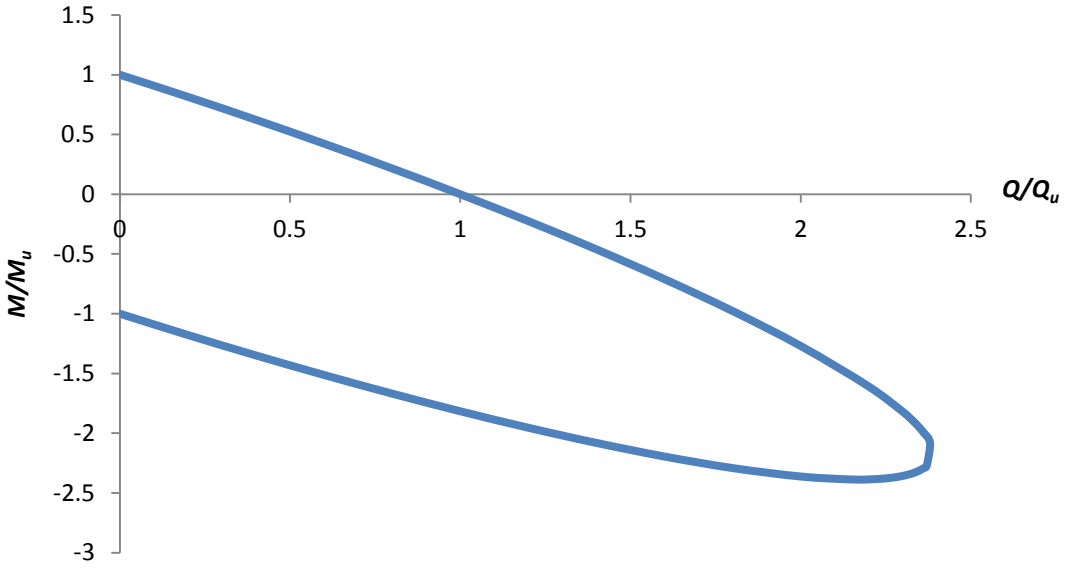

Figure 3.10 *Yield Surface of a lightly loaded (χ = 0.2) deeply embedded (D/B = 3) caisson foundation in the M-Q space deduced by multiple pushover tests and normalized with the ultimate capacities under pure loading.*

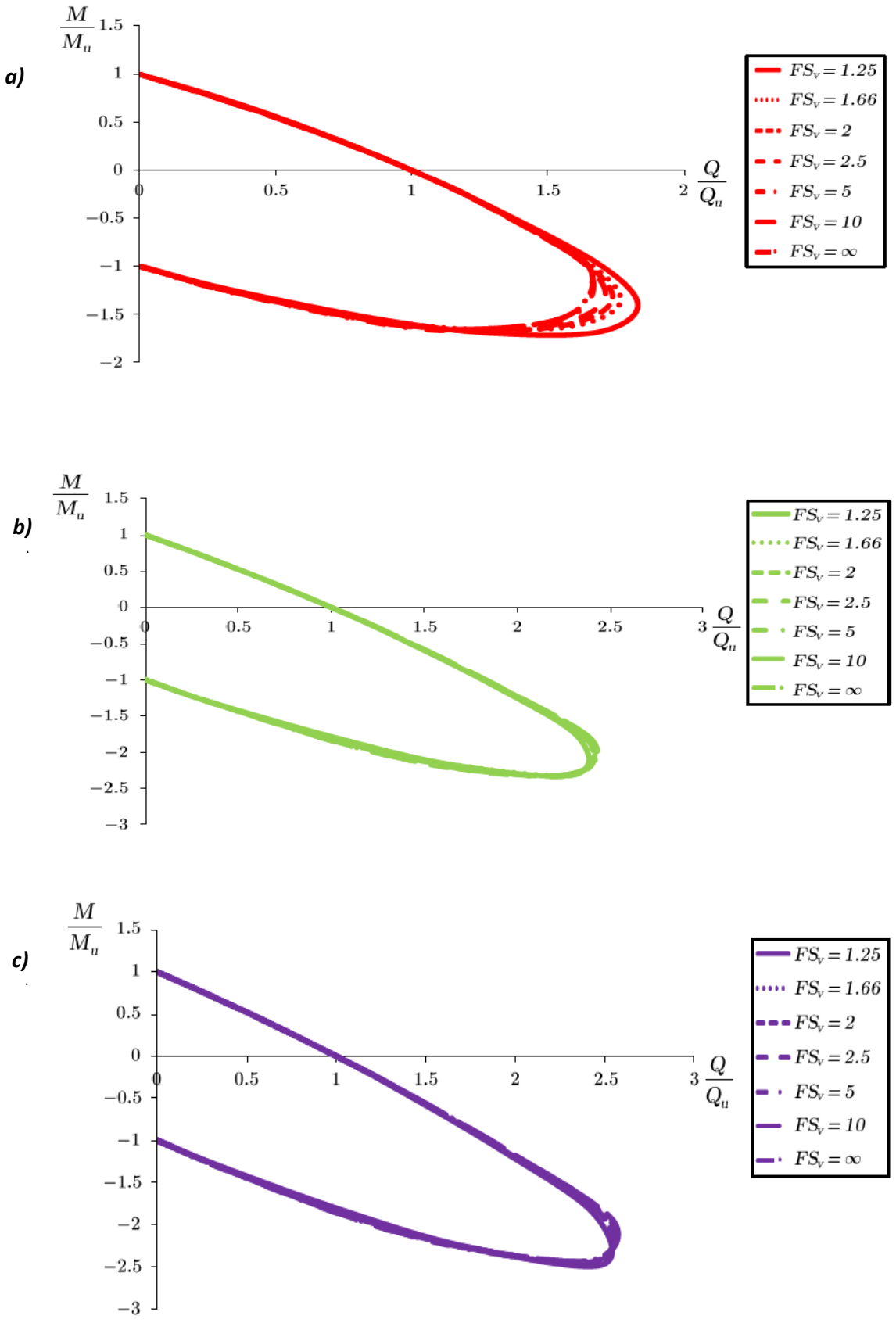

Figure 3.11 *Illustration of the effect of the factor of safety against vertical bearing capacity failure to the shape of the normalized interaction curves for three distinct embedment ratios a) D/B = 1, b) D/B = 2 and c) D/B =3. Interface is considered bonded. (Gerolymos and Souliotis, 2012)*

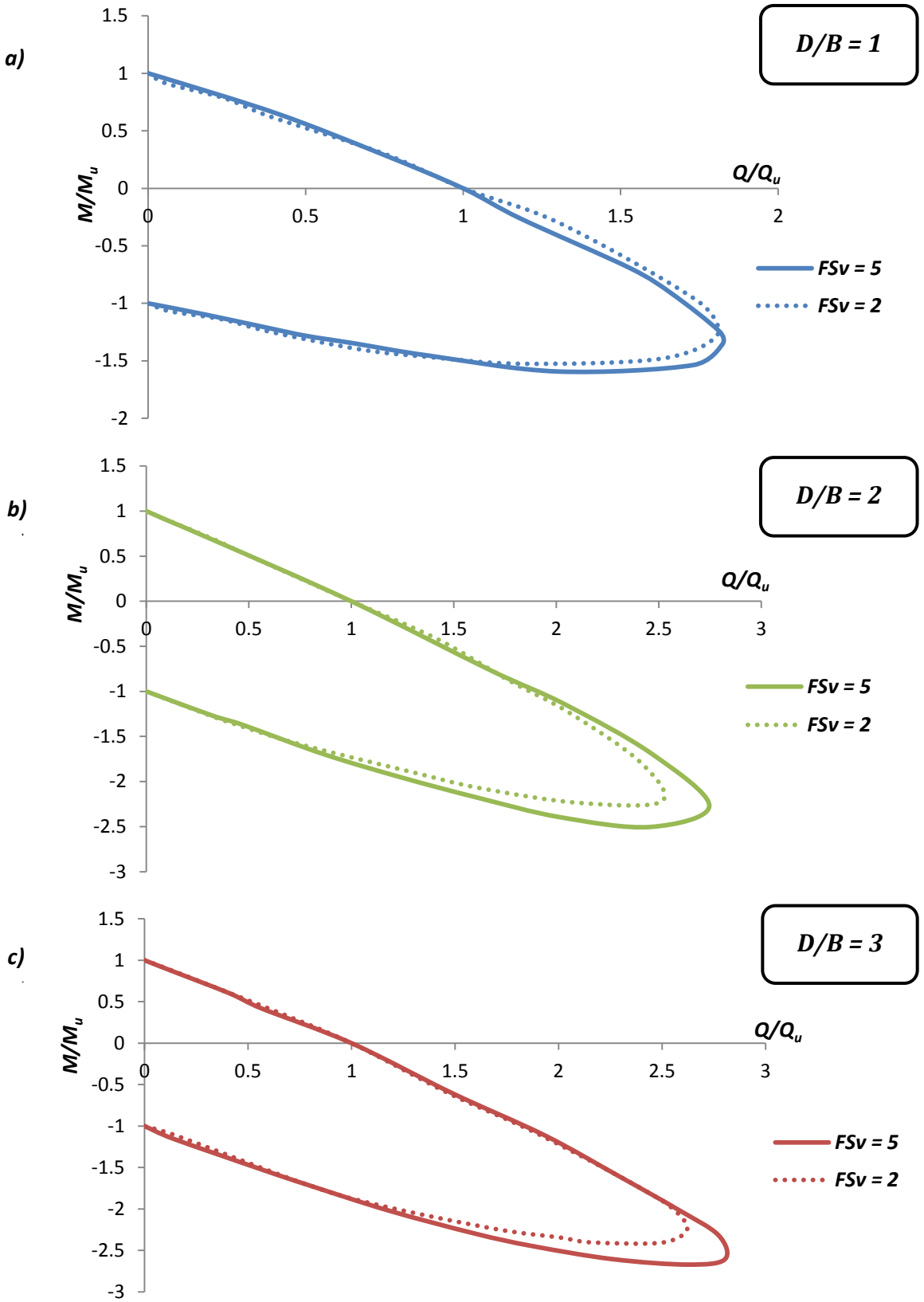

Figure 3.12 *Illustration of the effect of the factor of safety against vertical bearing capacity failure to the shape of the normalized interaction curves for three distinct embedment ratios a) D/B = 1, b) D/B = 2 and c) D/B =3. In this case of Coulomb interface considered, a value of coefficient of friction of μ = 1 has been applied.*

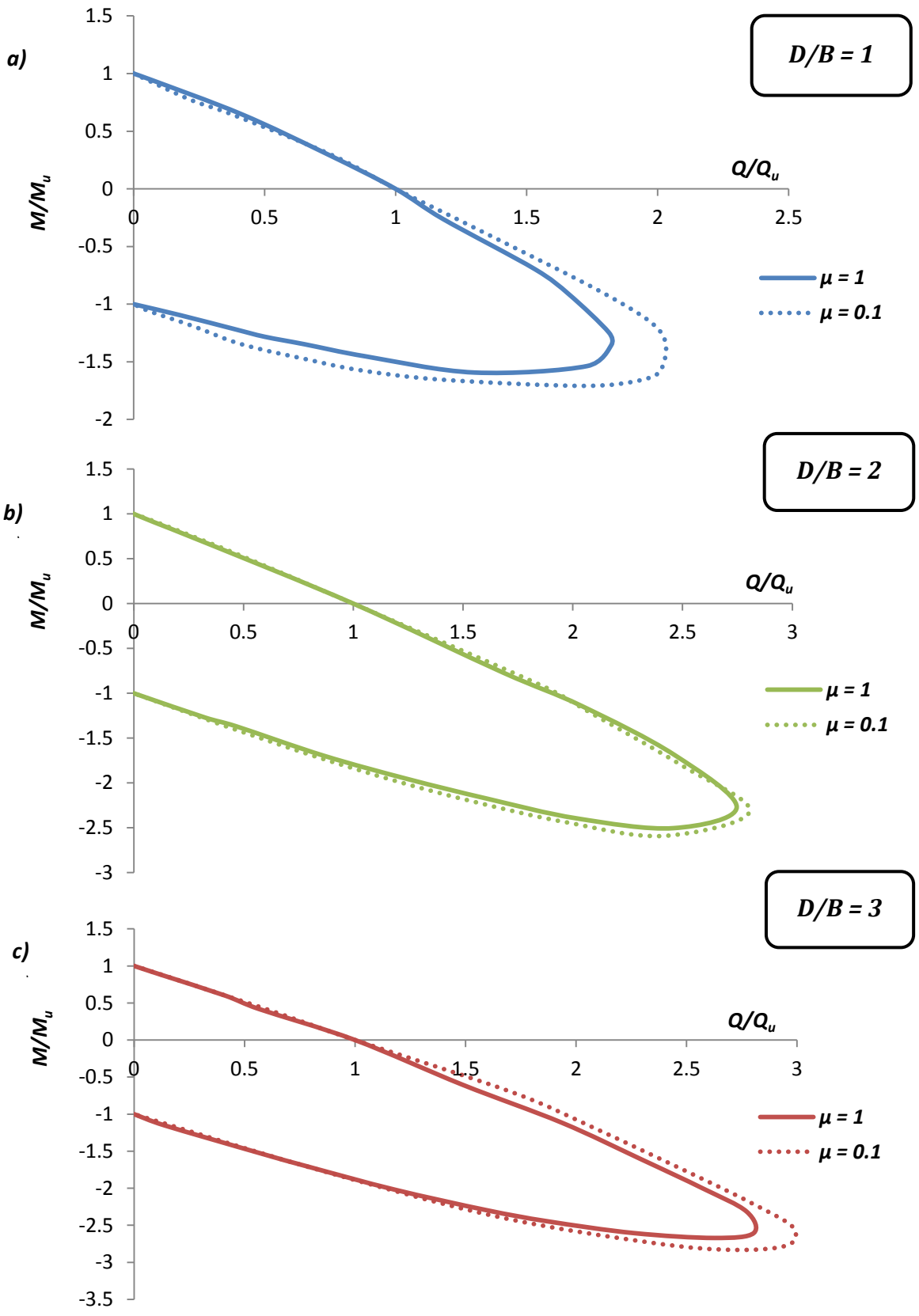

Figure 3.13 *Illustration of the effect of the value of the coefficient of friction μ to the shape of the normalized interaction curves for $FS_V = 5$ and for three distinct embedment ratios a) D/B = 1, b) D/B = 2 and c) D/B =3.*

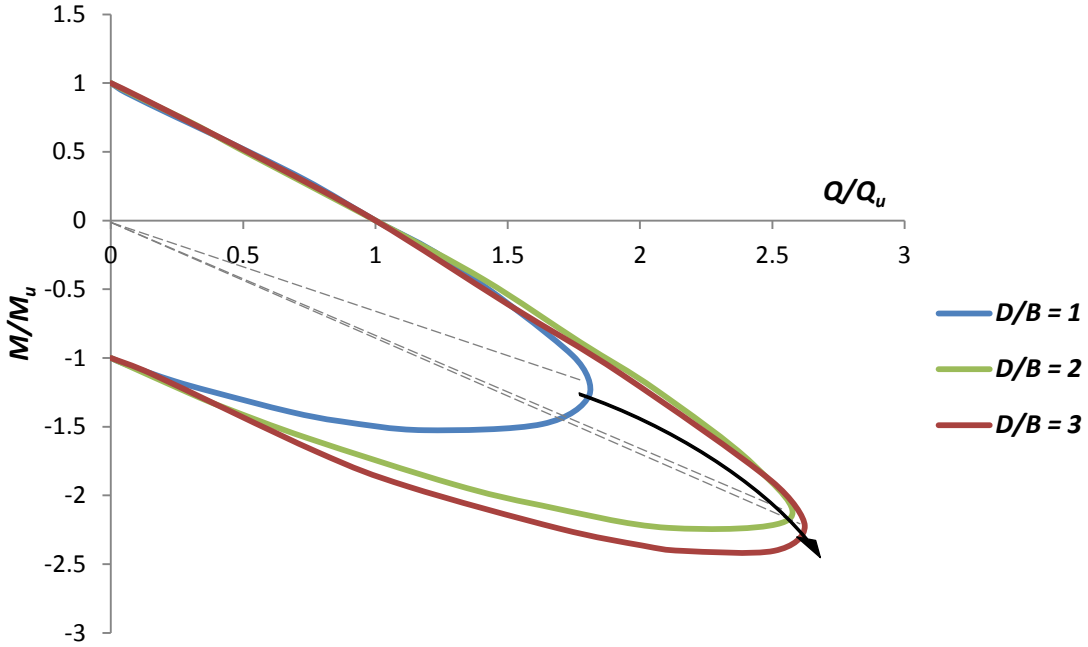

Figure 3.14 *Expansion and rotation of the failure envelopes of caisson foundation (FS_V = 2, μ = 1) as an effect of the embedment ratio D/B in the case where interface nonlinearities are taken into account.*

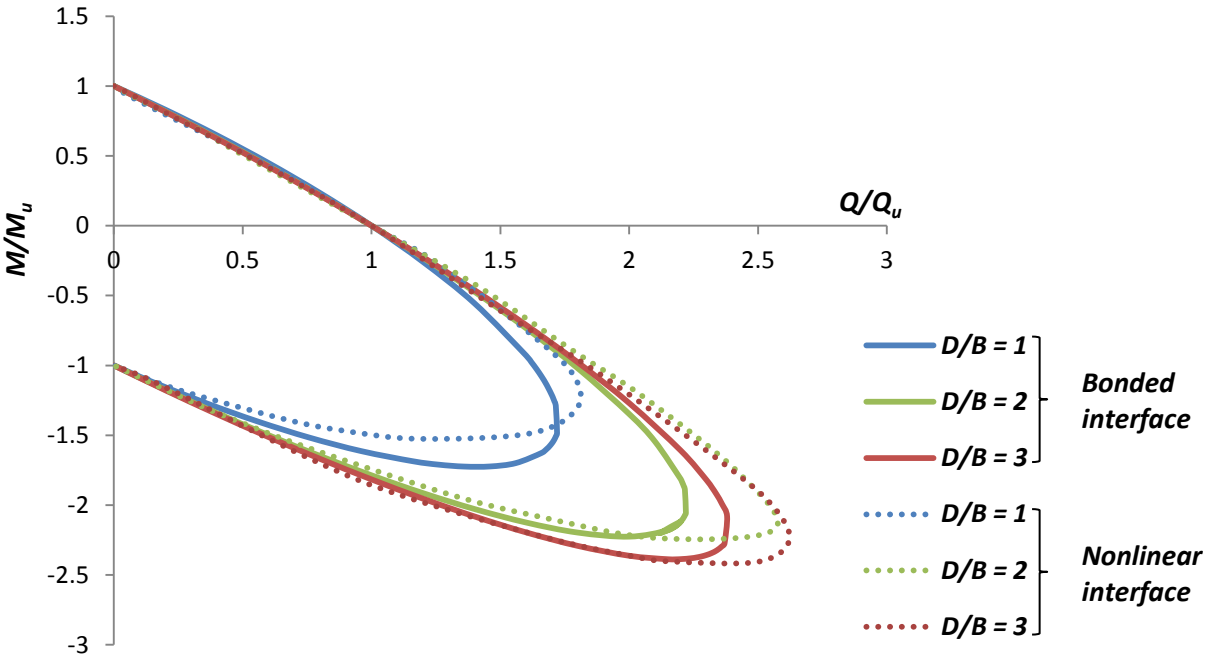

Figure 3.15 *Comparison of the shape of the failure envelopes for multiple embedment ratios and the two types of interfaces considered. In the case of the simple bonded interface, we observe a sole expansion of the envelope with increasing D/B, whereas in the sophisticated gapping Coulomb interface, D/B affects the shape of the curve in a dual fashion: through both an expansion and a rotation.*

A)

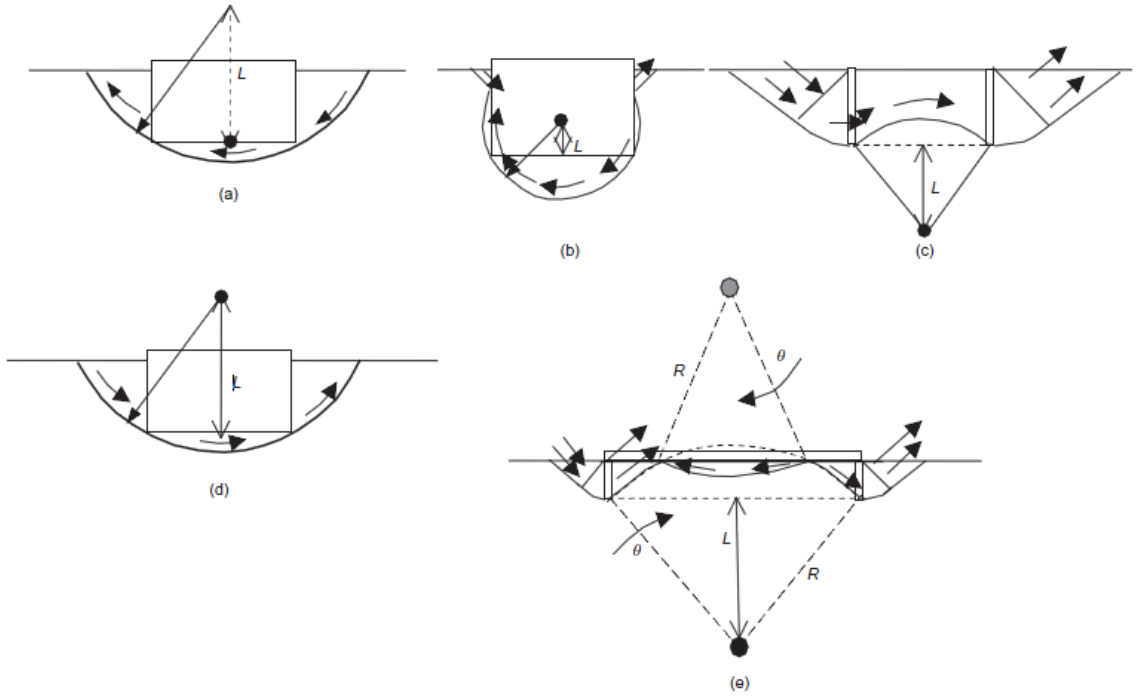

B)

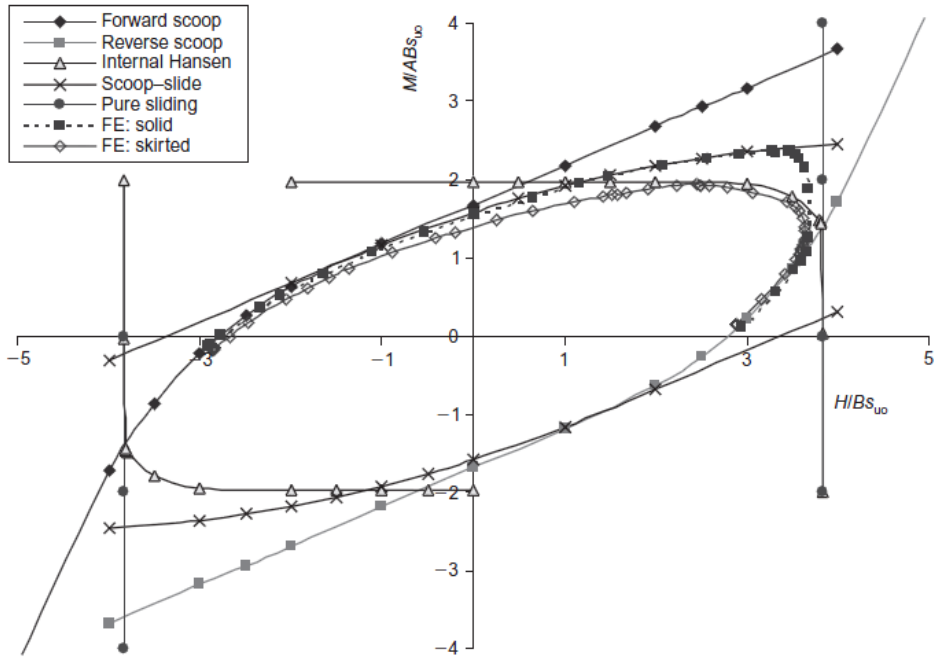

Figure 3.16 *A) The 5 distinct soil mechanisms that can be developed by skirted foundations as recognized by Bransby and Yun [2009]: (a) "forward scoop", (b) "scoop-slide", (c) "internal Hansen", (d) "reverse scoop" and (e) "internal double scoop". Of these, (c) and (e) cannot be deployed by embedded foundations, where there is no internal soil to be mobilized. B) Effective sweep of the failure envelope through upper bound plasticity analyses based on the above soil deformation patterns. [Bransby and Yun, 2009]*

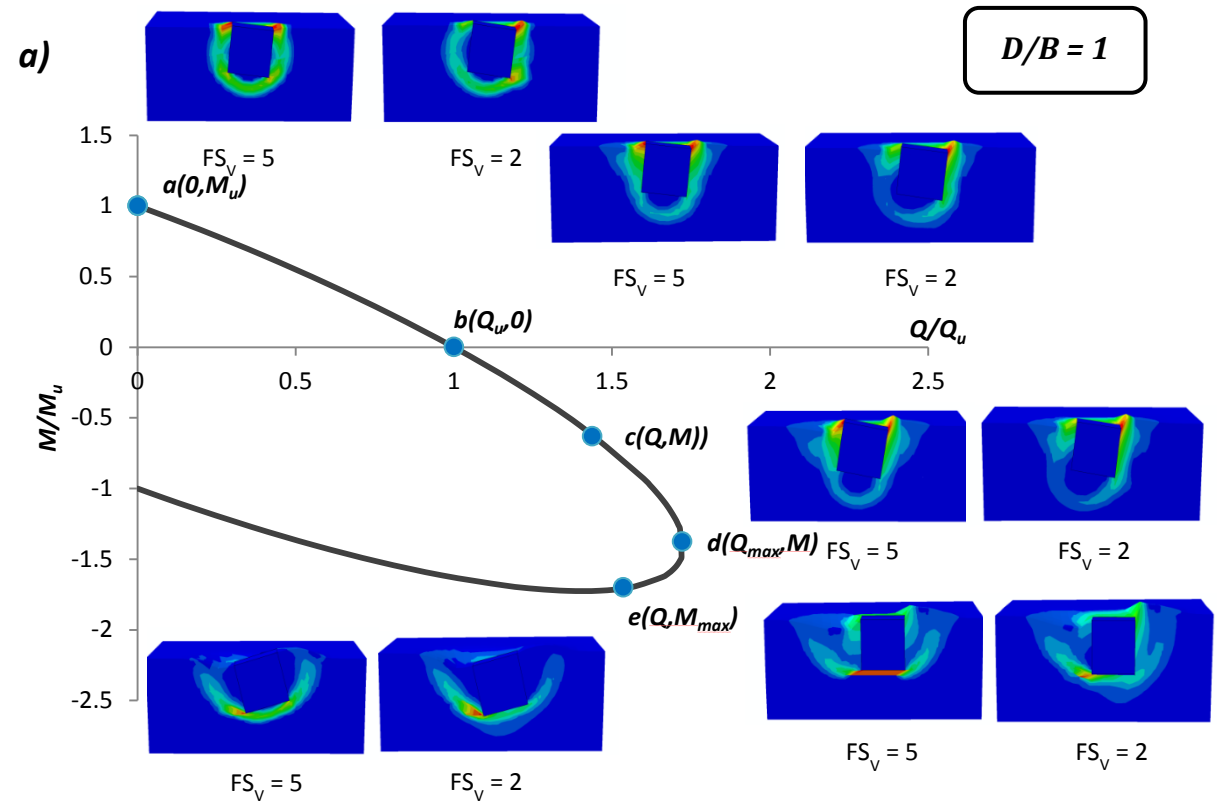
a)
D/B = 1
FS$_V$ = 5
FS$_V$ = 2
a(0,M$_u$)
b(Q$_u$,0)
c(Q,M))
d(Q$_{max}$,M)
e(Q,M$_{max}$)
M/M$_u$
Q/Q$_u$
1.5
1
0.5
0
-0.5
-1
-1.5
-2
-2.5
0
0.5
1
1.5
2
2.5

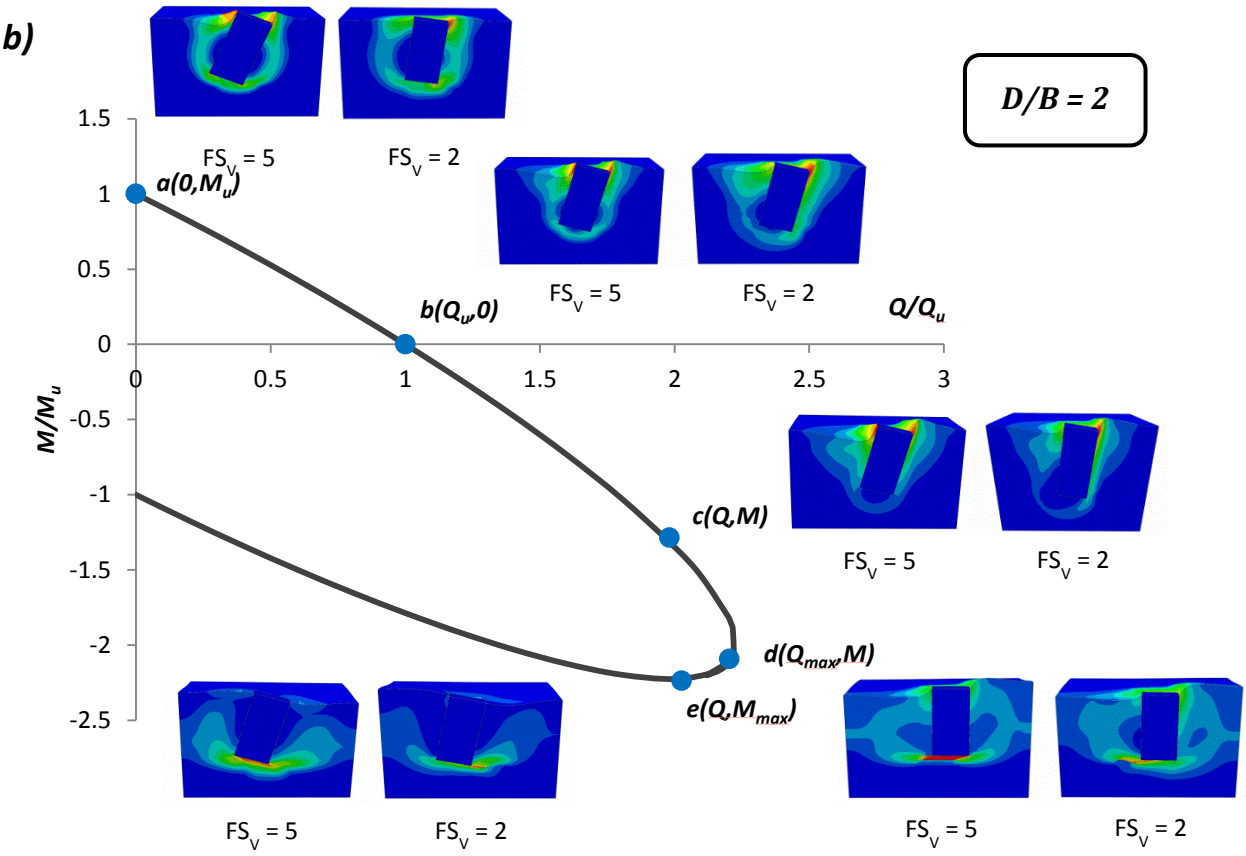
b)
D/B = 2
FS$_V$ = 5
FS$_V$ = 2
a(0,M$_u$)
b(Q$_u$,0)
c(Q,M)
d(Q$_{max}$,M)
e(Q,M$_{max}$)
M/M$_u$
Q/Q$_u$
1.5
1
0.5
0
-0.5
-1
-1.5
-2
-2.5
0
0.5
1
1.5
2
2.5
3

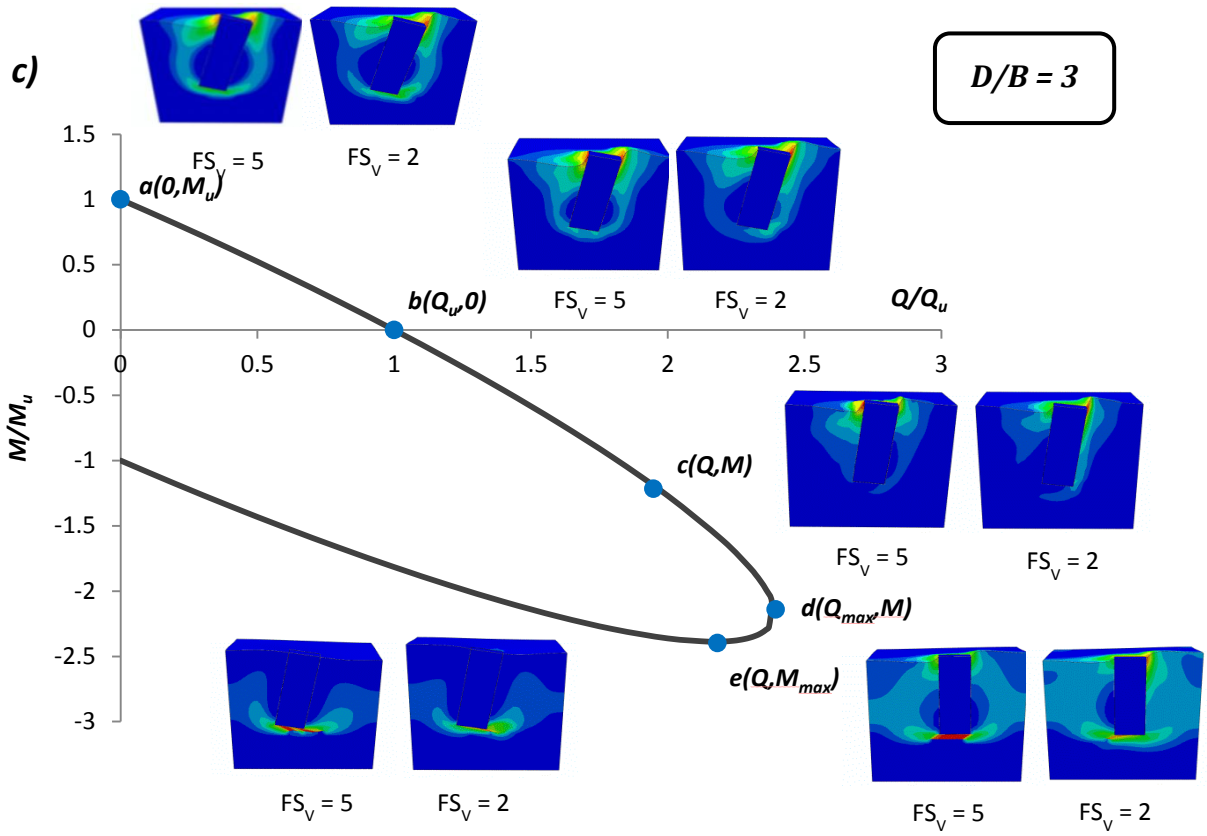

Figure 3.17 *Illustration of the plastic strain magnitude contours developed at characteristic points along the yield surface for 2 distinct factors of safety against vertical loading and embedment ratio a) D/B = 1, b) D/B = 2 and c) D/B = 3. Bonded interface conditions are considered.*

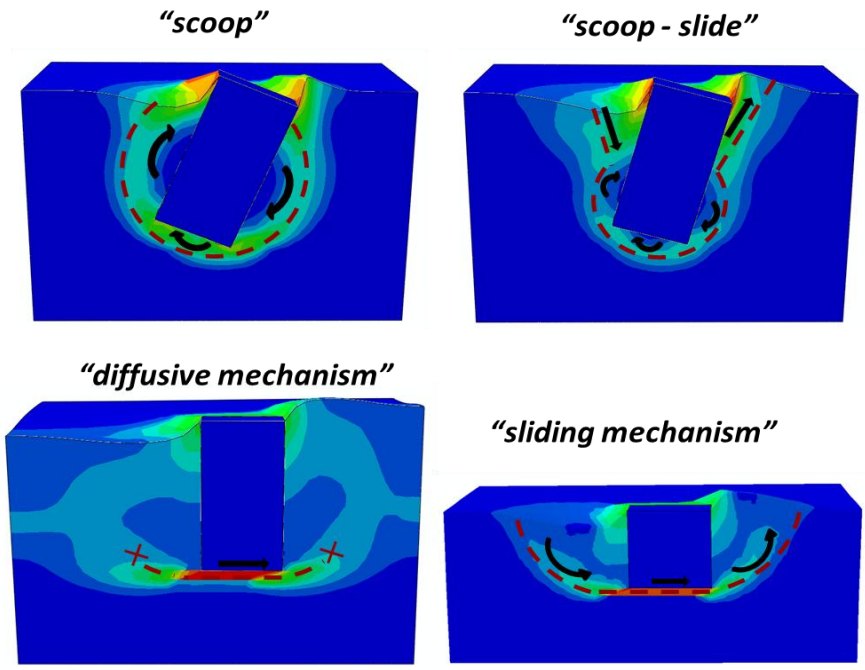

Figure 3.18 *The four distinct types of soil resisting mechanisms that are deployed by embedded foundations subject to combined M-Q loading. The "diffusive mechanism" may only be developed by deeply embedded foundations exhibiting their maximum horizontal capacity, while the "sliding mechanism" may only be developed by shallow embedded foundations exhibiting their maximum horizontal capacity as well.*

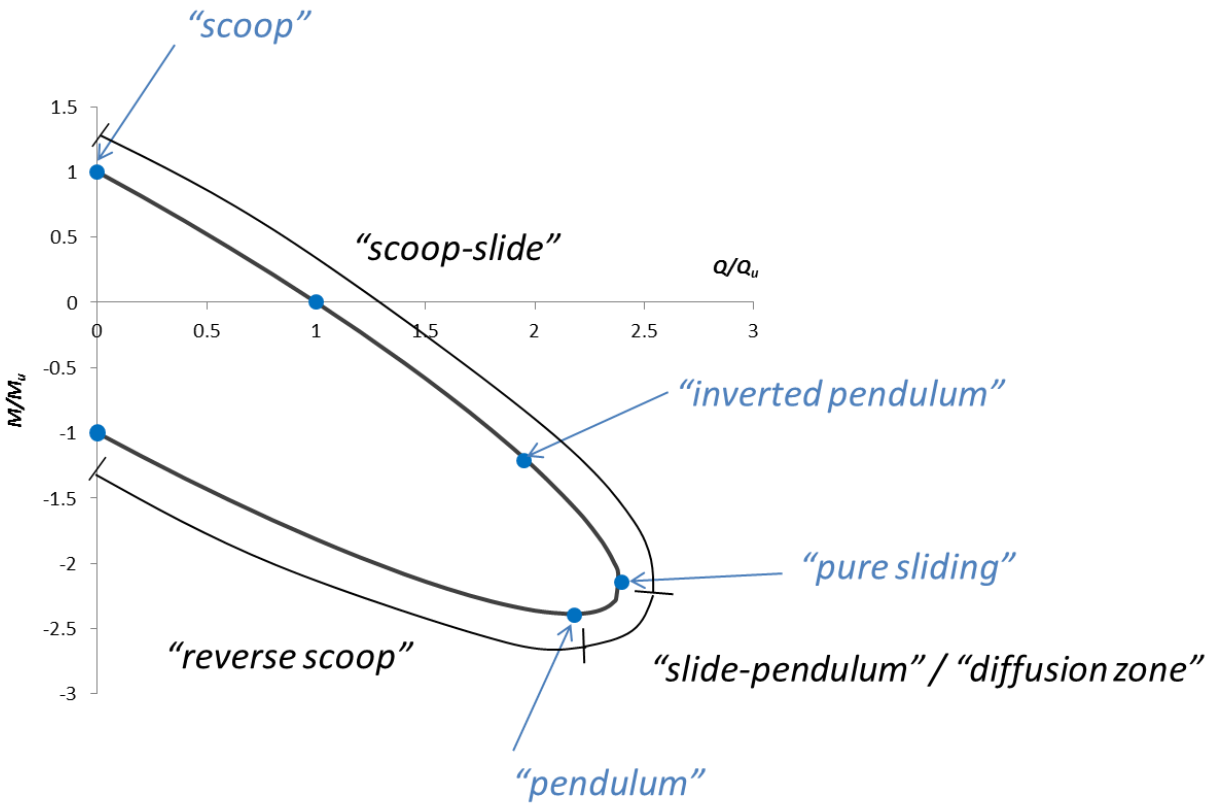

Figure 3.19 *Map of the yield surface of embedded foundations accounting for mechanism types and individual mechanisms observed.*

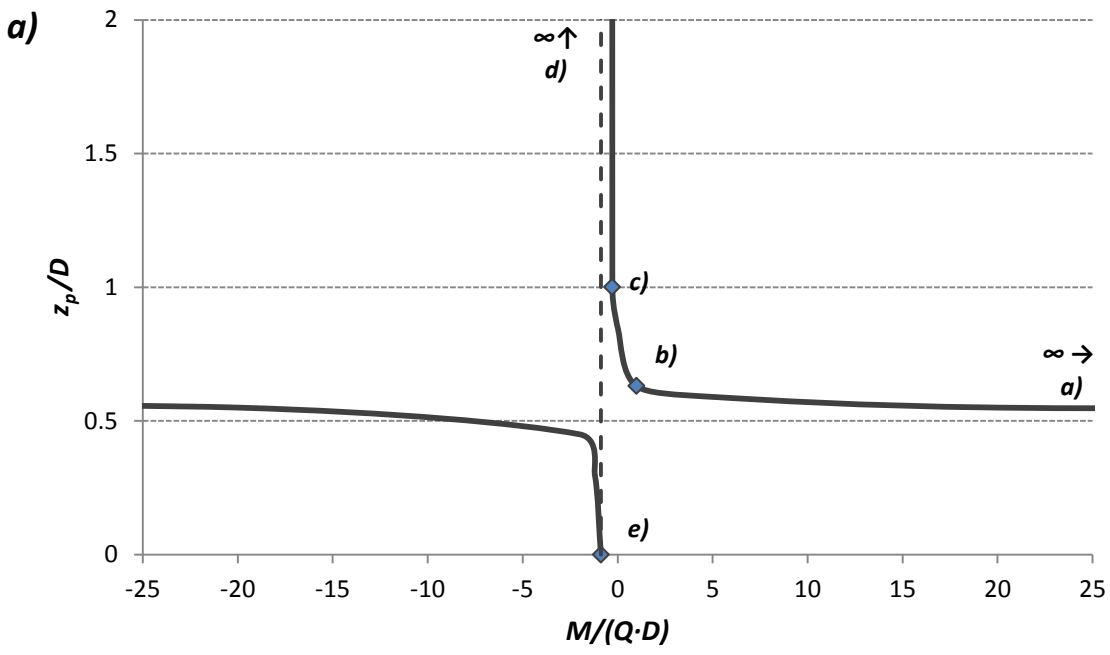

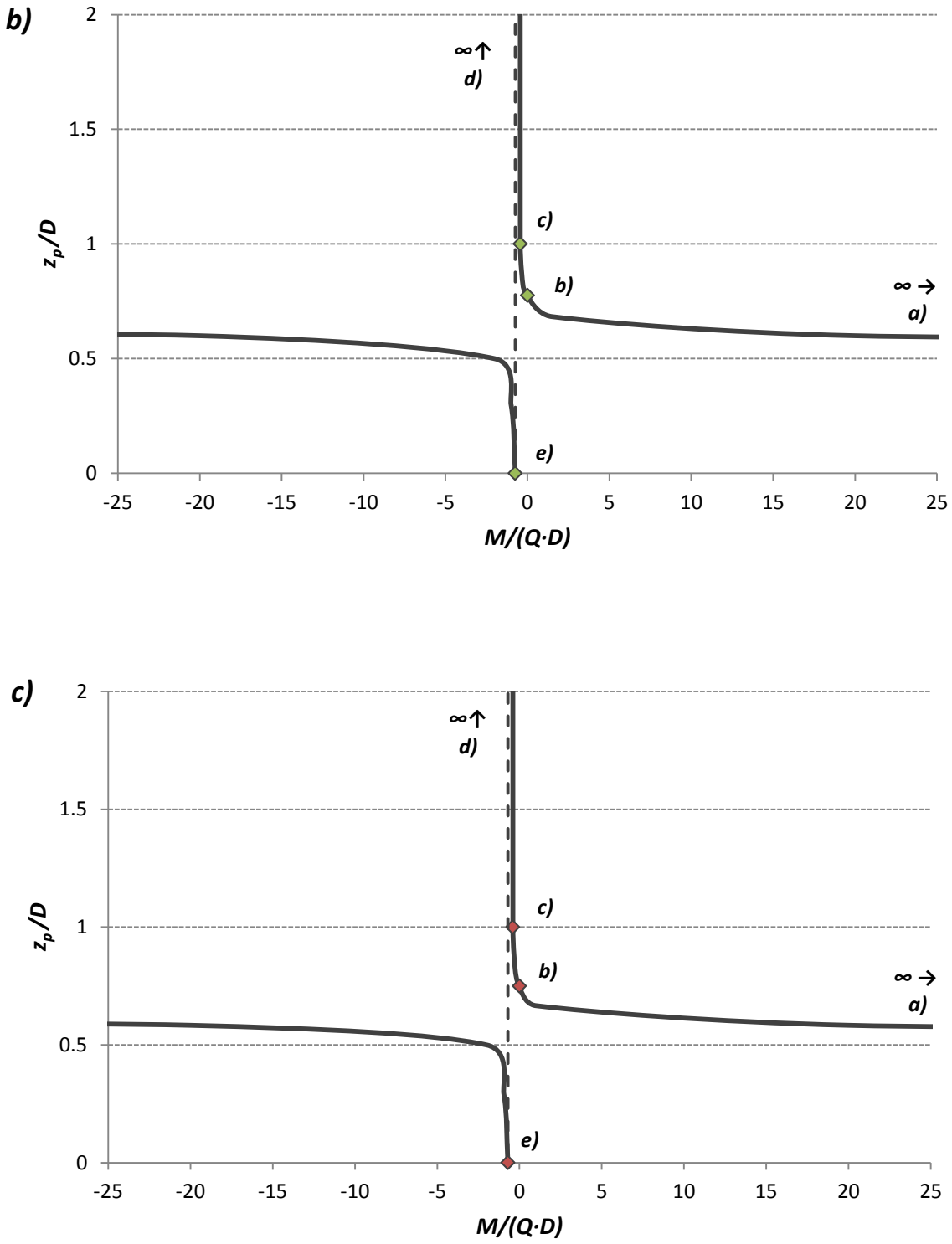

Figure 3.20 *Dimensionless depth of pivot point versus loading angle M/(Q·D) for embedment ratios a) D/B =1, b) D/B =2 and c) D/B =3 under bonded interface conditions. The pivot point path is almost identical regardless of the embedment ratio.*

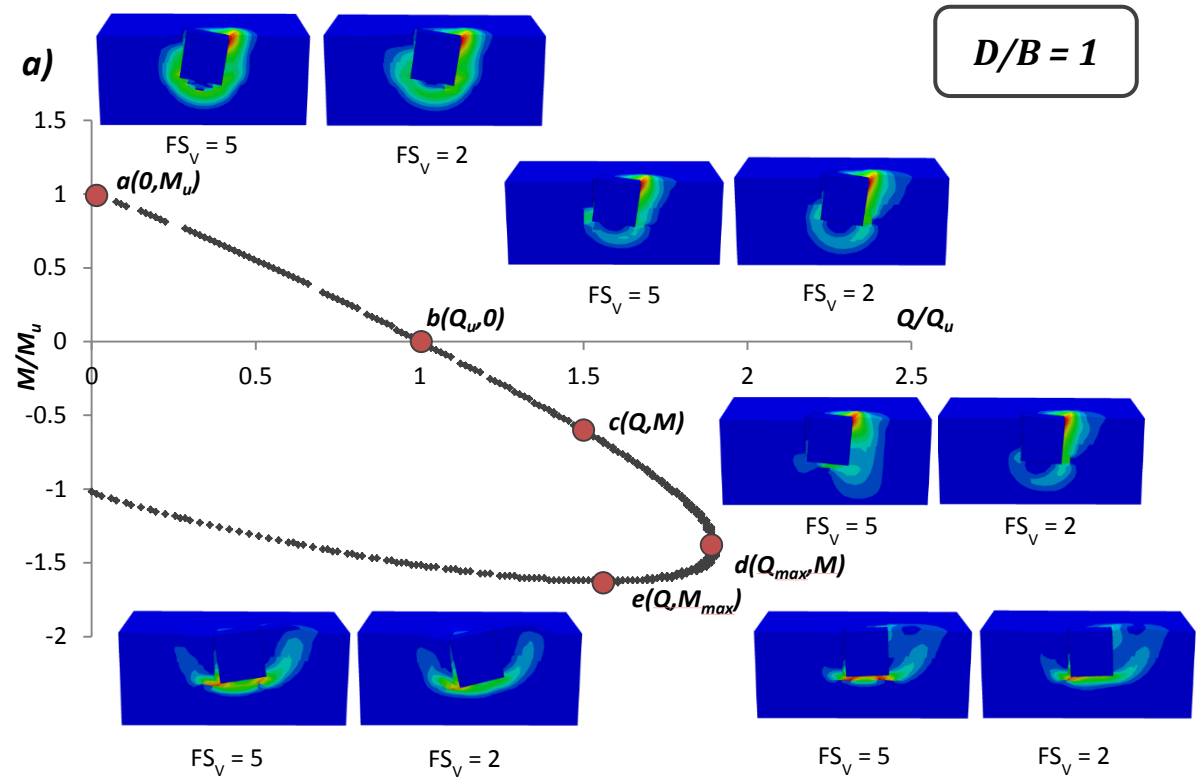
a)
D/B = 1
1.5
1
0.5
0
-0.5
-1
-1.5
-2
M/M_u
0
0.5
1
1.5
2
2.5
Q/Q_u
a(0,M_u)
b(Q_u,0)
c(Q,M)
d(Q_max,M)
e(Q,M_max)
FS_V = 5
FS_V = 2

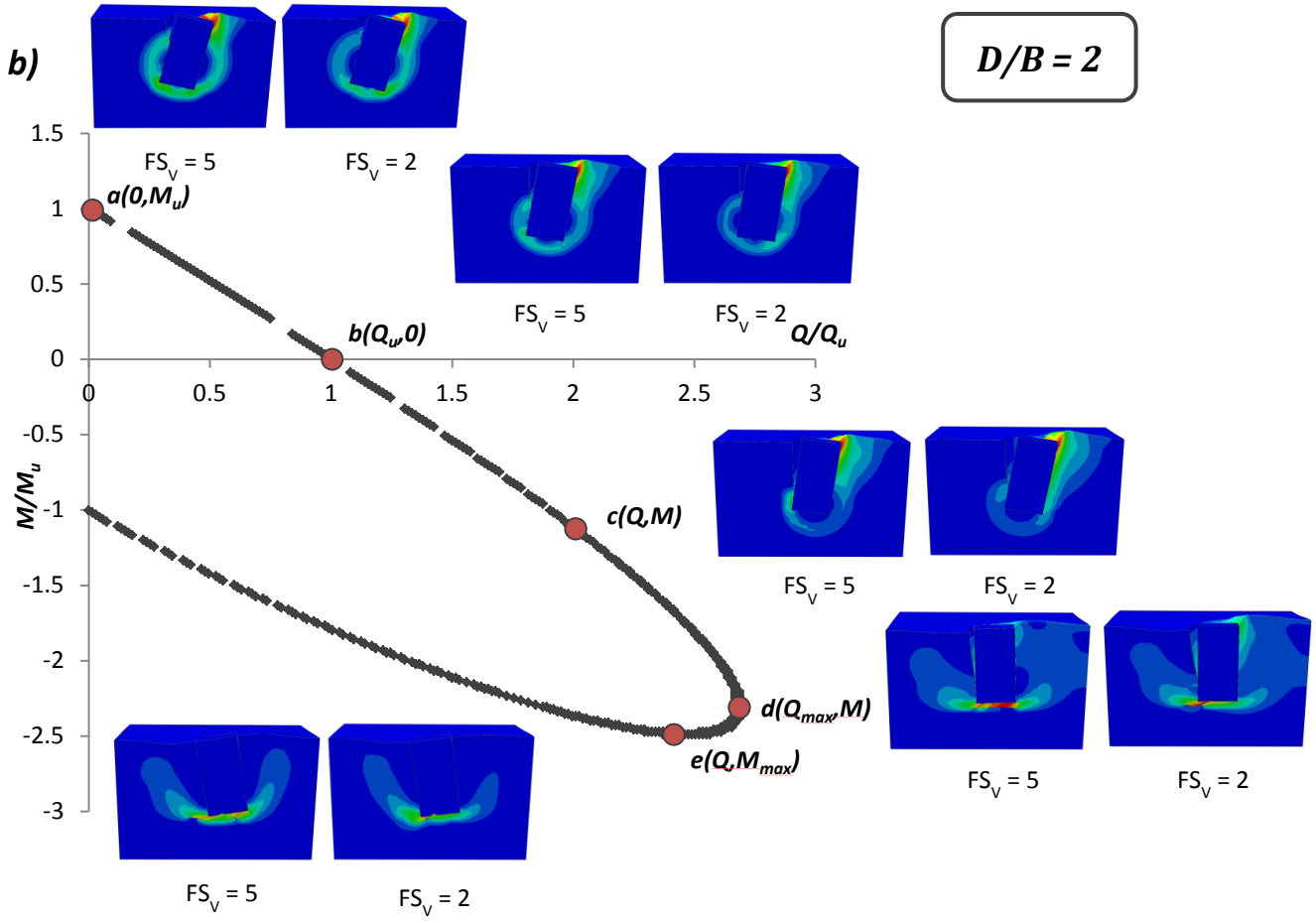
b)
D/B = 2
1.5
1
0.5
0
-0.5
-1
-1.5
-2
-2.5
-3
M/M_u
0
0.5
1
1.5
2
2.5
3
Q/Q_u
a(0,M_u)
b(Q_u,0)
c(Q,M)
d(Q_max,M)
e(Q,M_max)
FS_V = 5
FS_V = 2

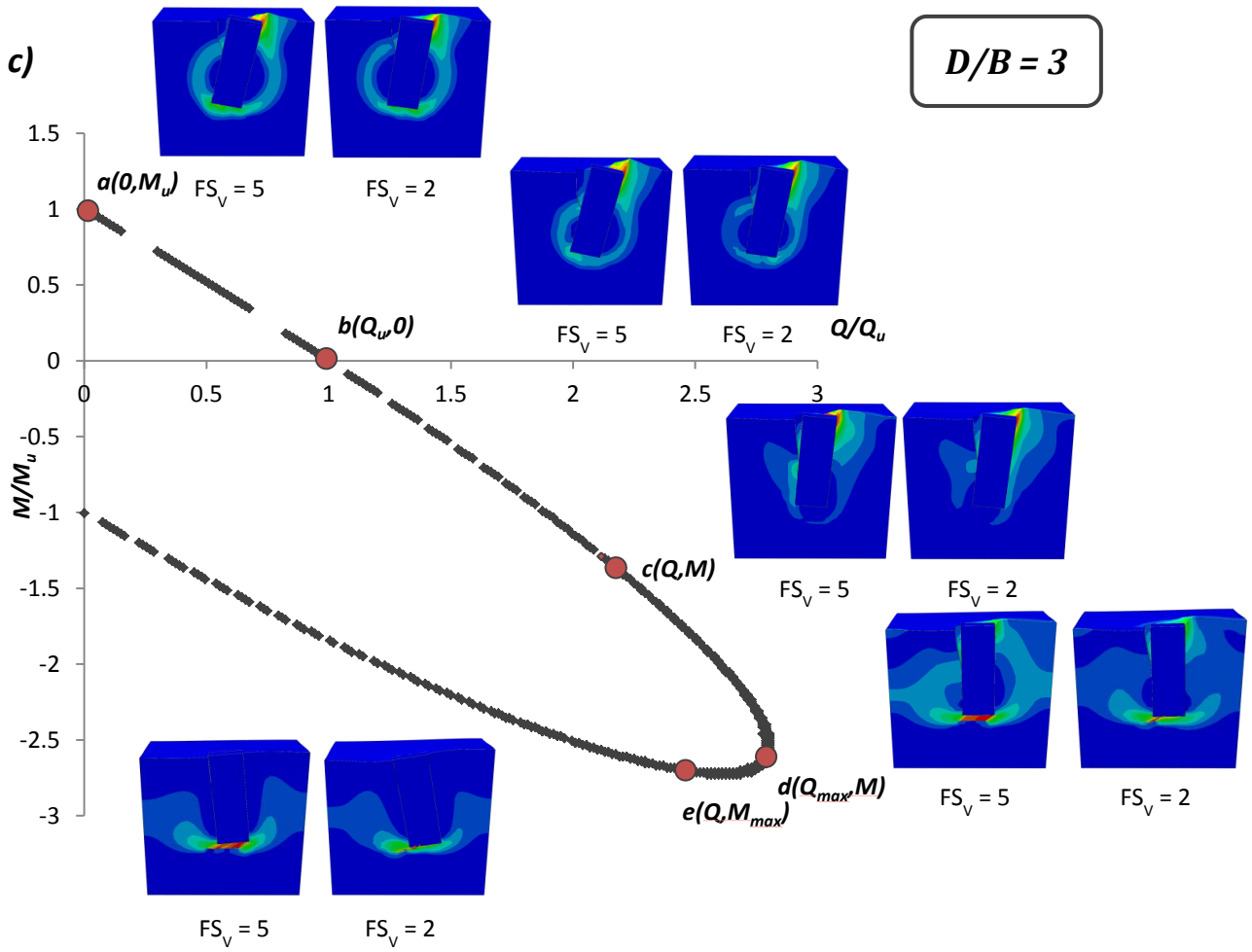

Figure 3.21 *Illustration of the plastic strain magnitude contours developed at characteristic points along the yield surface for 2 selected factors of safety against vertical loading and embedment ratio a) D/B = 1, b) D/B = 2 and c) D/B = 3. Nonlinear interface conditions are considered.*

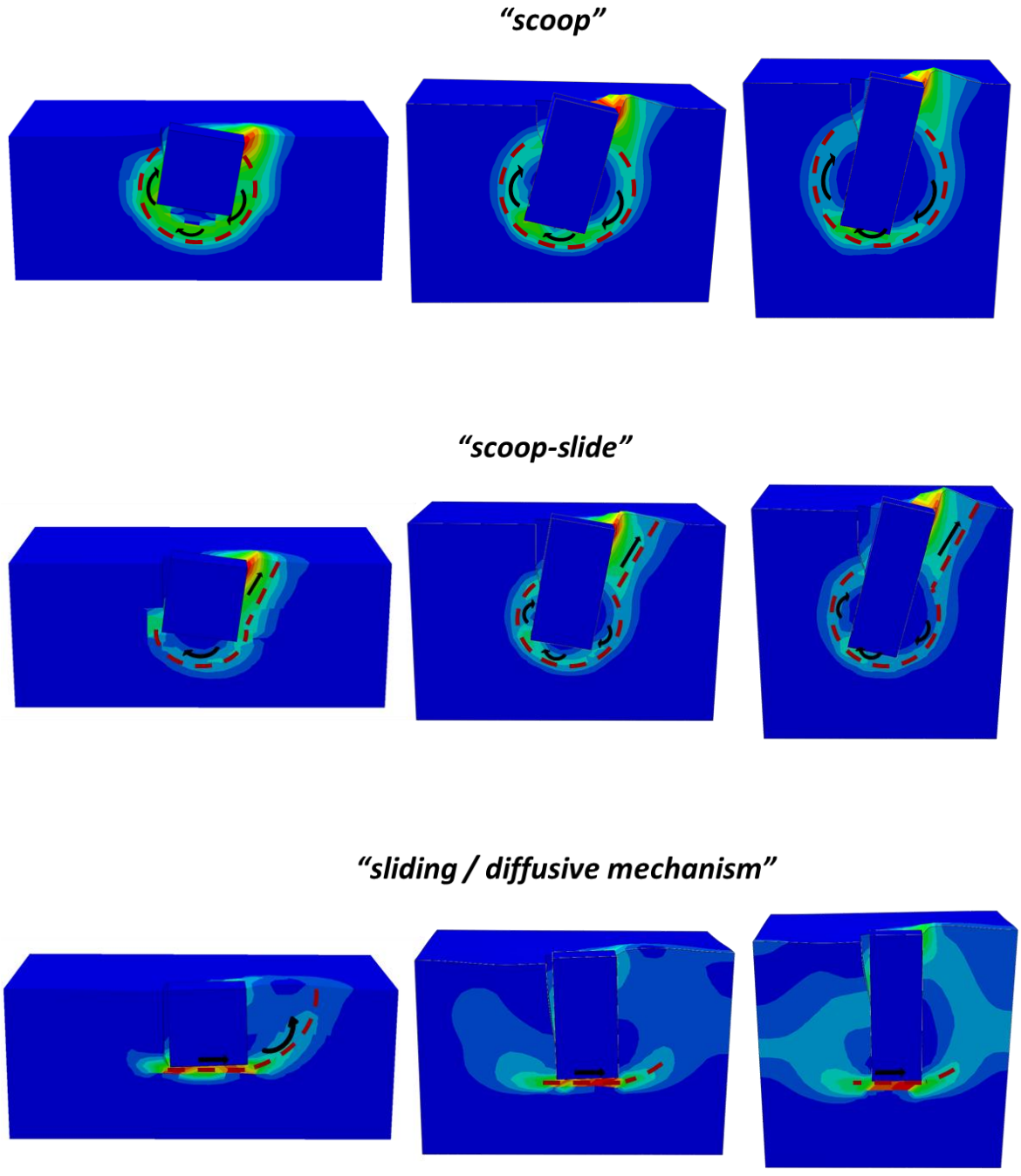

Figure 3.22 *Effect of interface nonlinearities on the four basic types of soil resisting mechanisms deployed by embedded foundations subject to combined M-Q loading. The "diffusive mechanism" may only be developed by deeply embedded foundations exhibiting their maximum horizontal capacity, while the "sliding mechanism" may only be developed by shallow embedded foundations exhibiting their maximum horizontal capacity as well.*

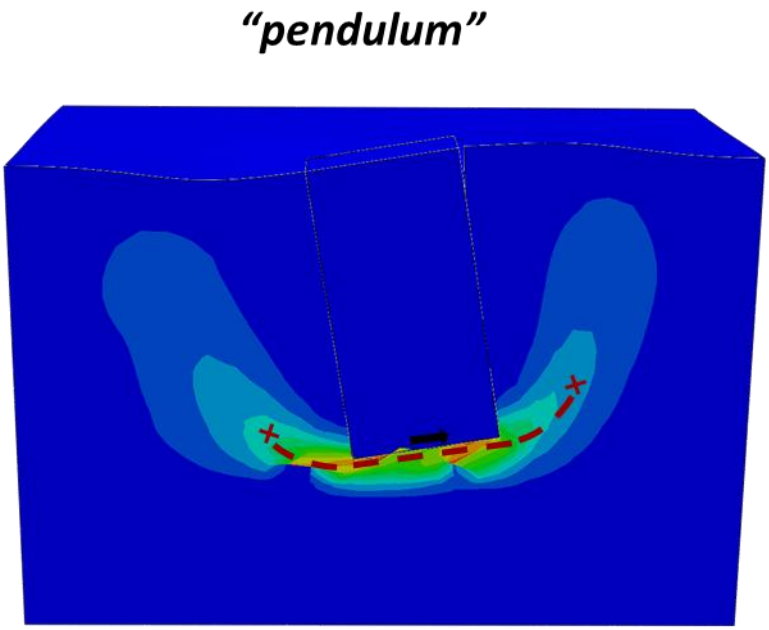

Figure 3.23 *Detachment is impossible to occur under maximum moment capacity loading conditions.*

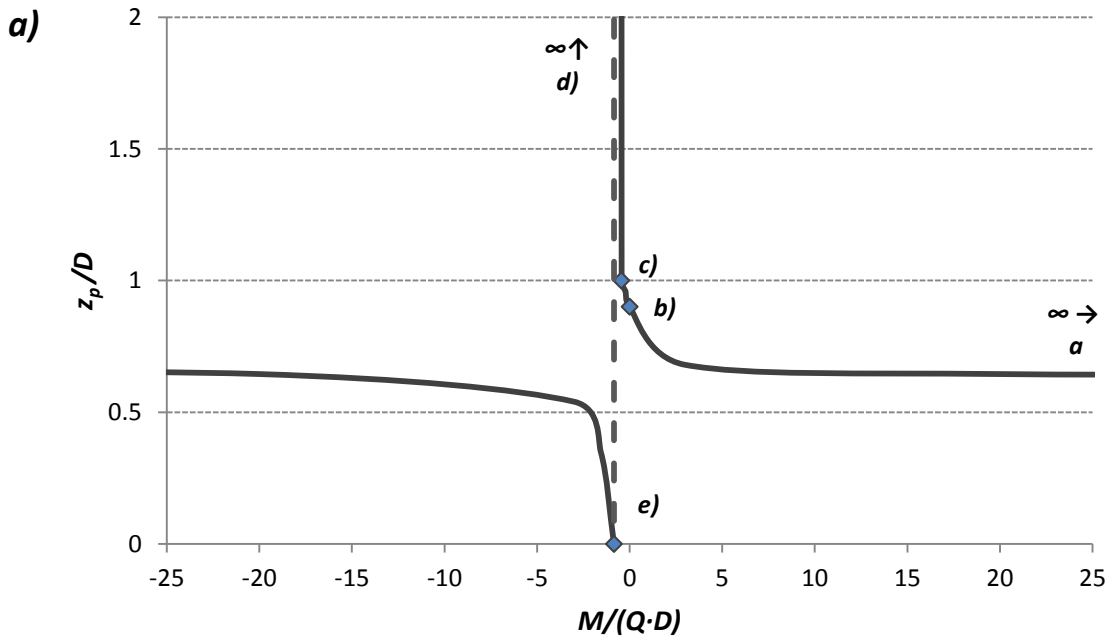

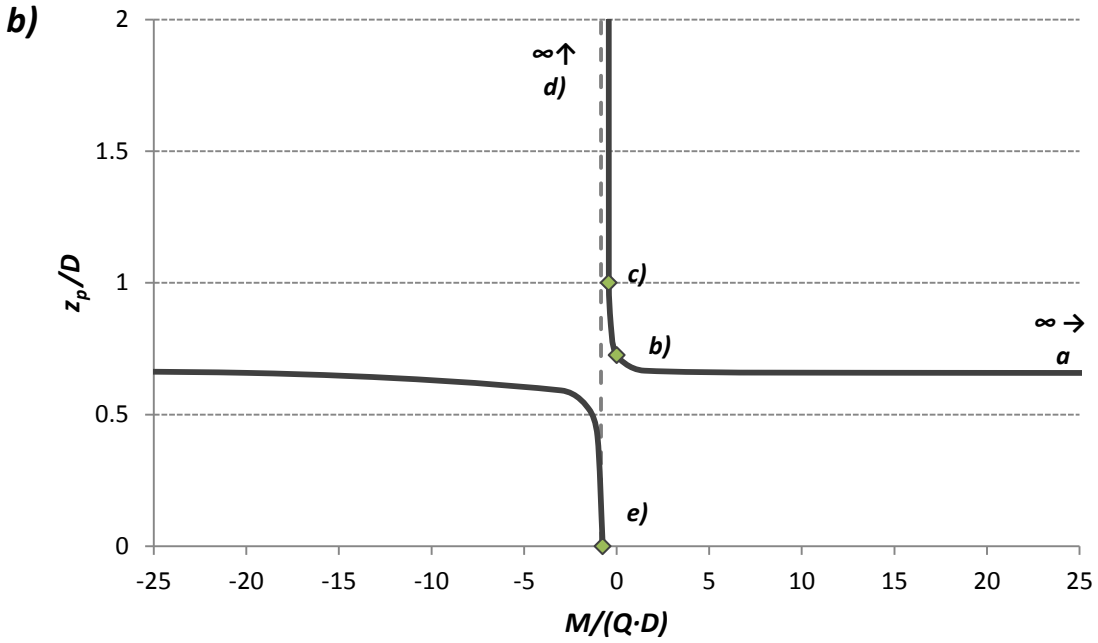

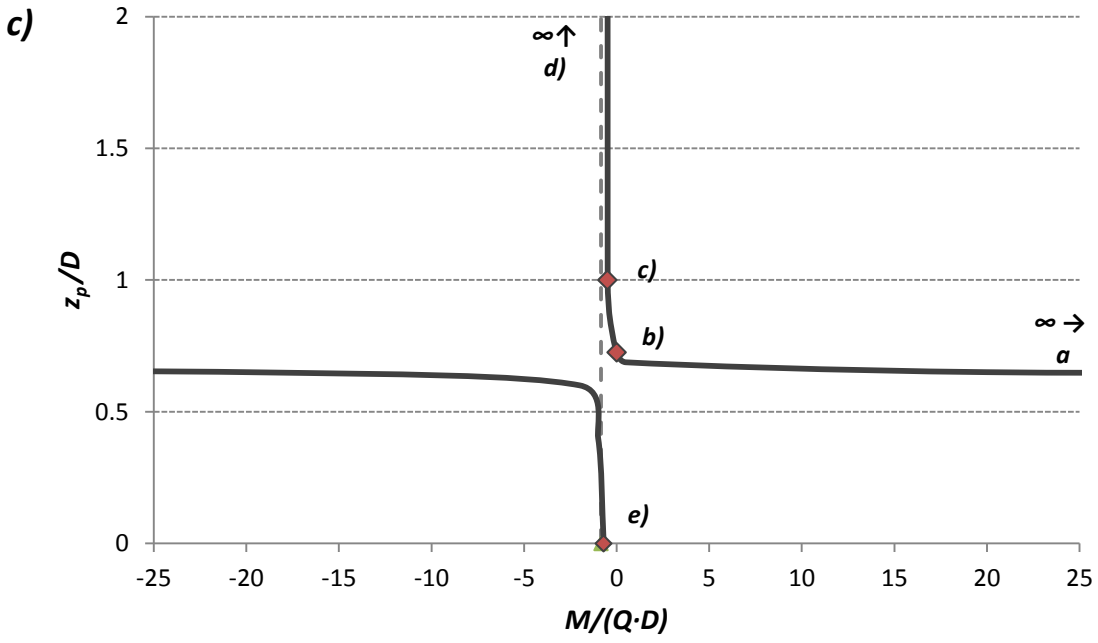

Figure 3.24 *Dimensionless depth of pivot point versus loading angle M/(Q·D) for embedment ratios a) D/B =1, b) D/B =2 and c) D/B =3 under nonlinear interface conditions. The pivot point path displays some variability with the embedment ratio and generally lies above that of the bonded interface.*

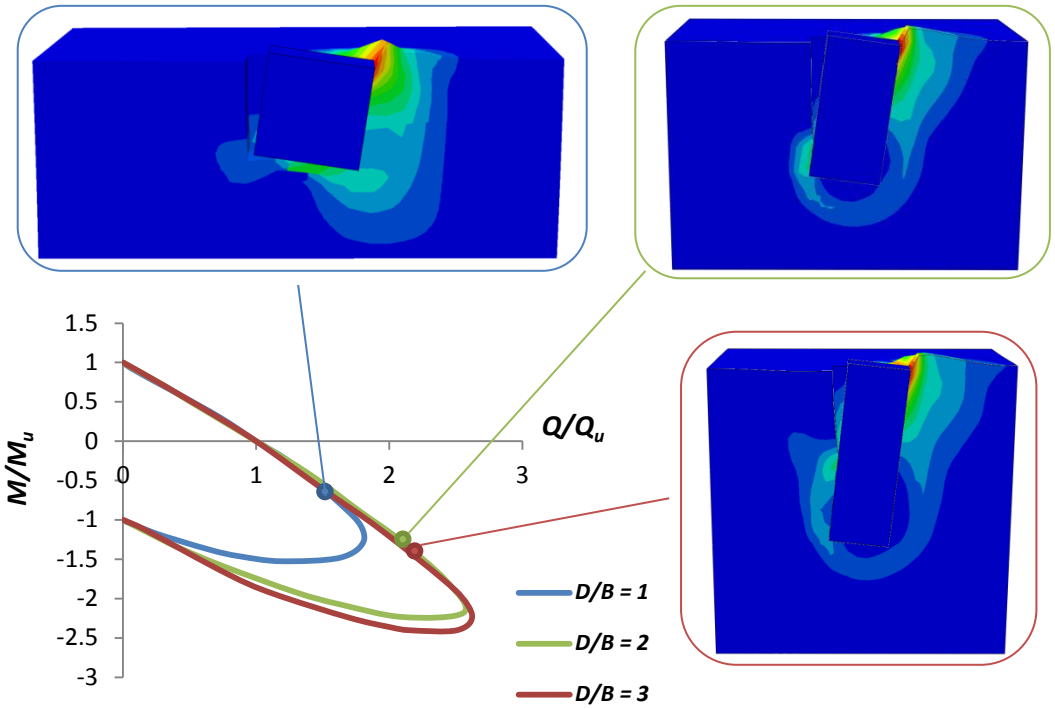

Figure 3.25 *Visualization of the rotational effect that caisson - soil detachment introduces to the yield surface of caisson foundations of distinct embedment ratios. For the shallow embedded foundation, gap formation leads to complete loss of the resisting passive wedge at the foot which translates into decreased capacity to undertake moment. This effect becomes less important for moderately embedded foundations, where the passive wedge is weakened, and almost vanishes for deeply embedded foundations.*

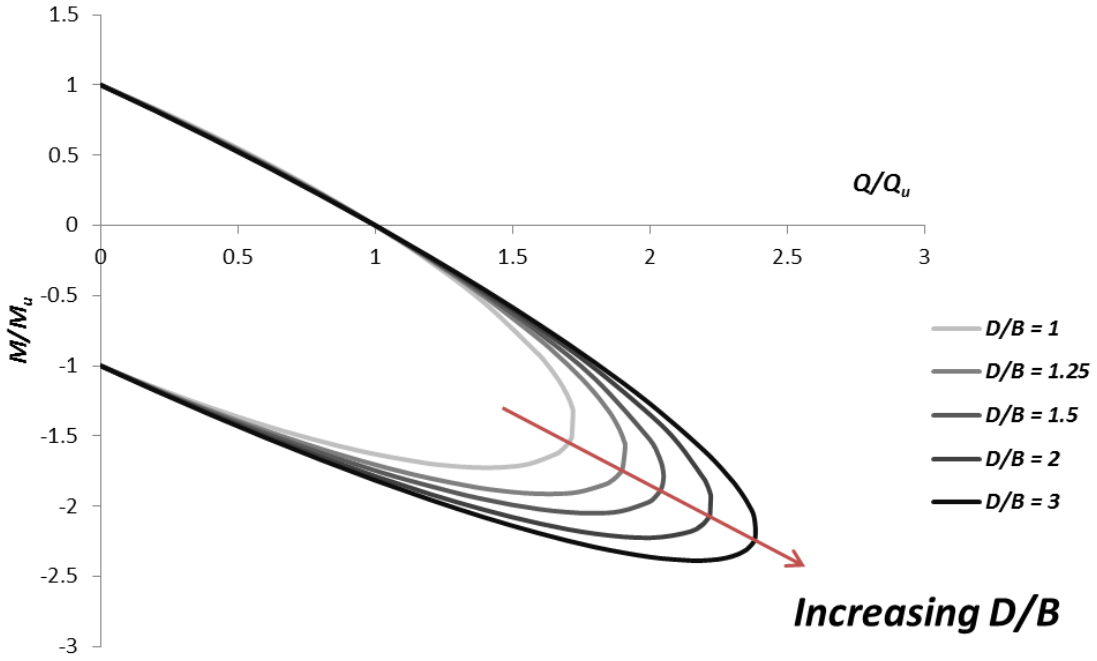

Figure 3.26 *The effect of n_3 on the shape of the yield surface under bonded interface conditions [Gerolymos et al, 2012].*

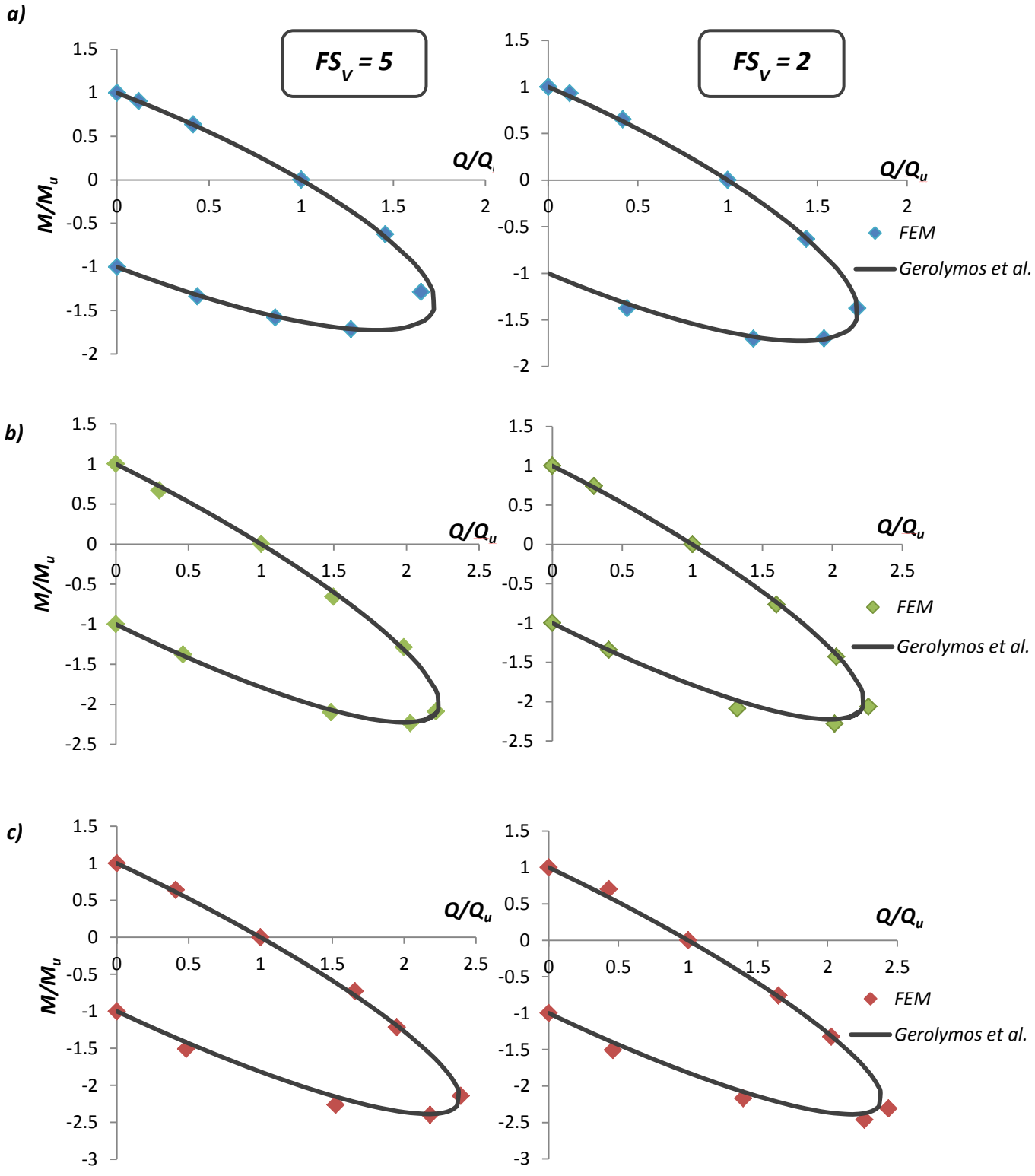

Figure 3.27 *Comparison between the data derived from the numerical experiments (points) and the analytical expression proposed by Gerolymos et al for the yield surfaces of caisson foundations of two different factors of safety and embedment ratio a) D/B = 1, b) D/B = 2 and c) D/B = 3, given in normalized values. The foundation is considered rigidly connected to the soil (bonded interface conditions).*

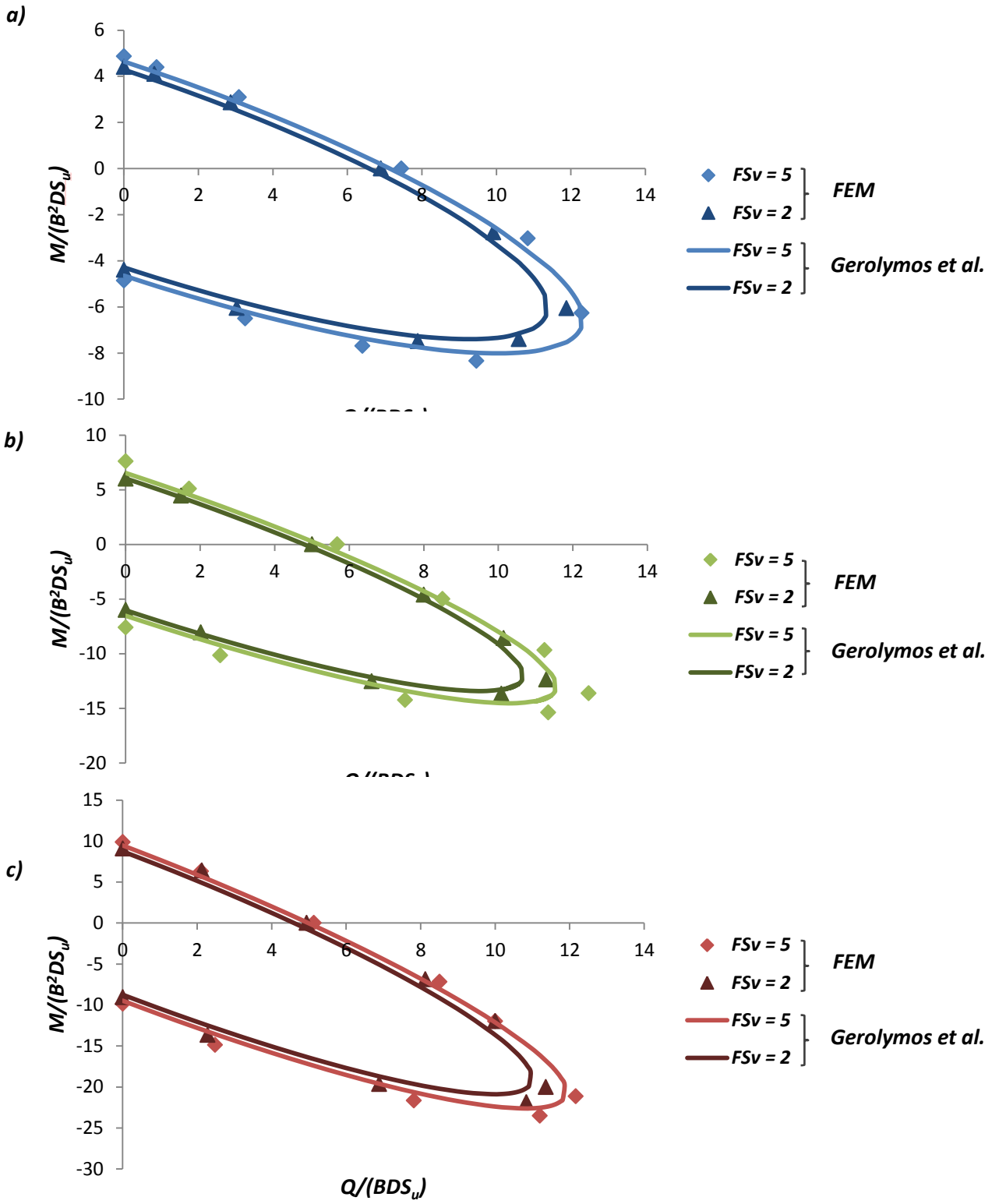

Figure 3.28 *Comparison between the data derived from the numerical experiments (points) and the analytical expression proposed by Gerolymos et al for the yield surfaces of caisson foundations of two different factors of safety and embedment ratio a) D/B = 1, b) D/B = 2 and c) D/B = 3, given in dimensionless terms. The foundations is considered rigidly connected to the soil (bonded interface conditions).*

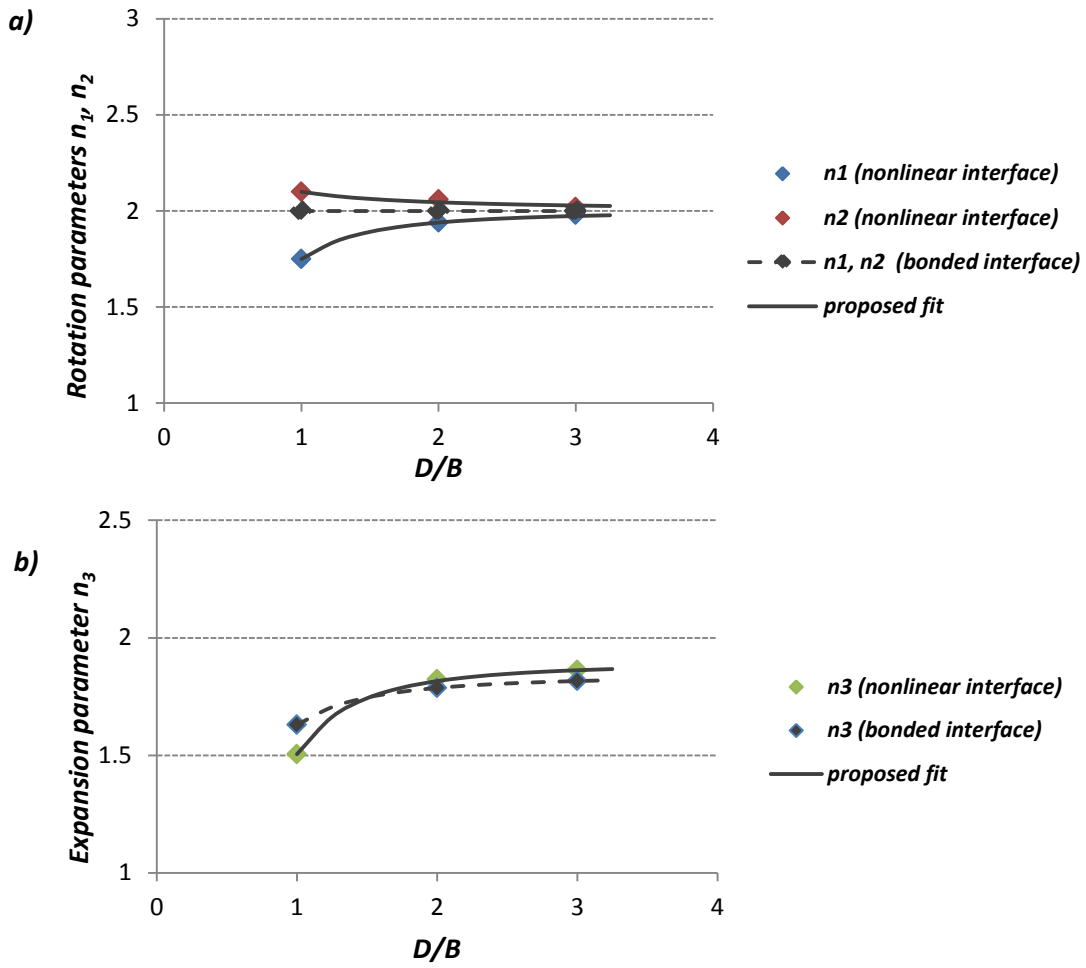

Figure 3.29 *Plots of a) the rotation and b) the expansion parameters that control the shape of the yield locus under bonded (Gerolymos et al) and nonlinear (proposed) interface conditions.*

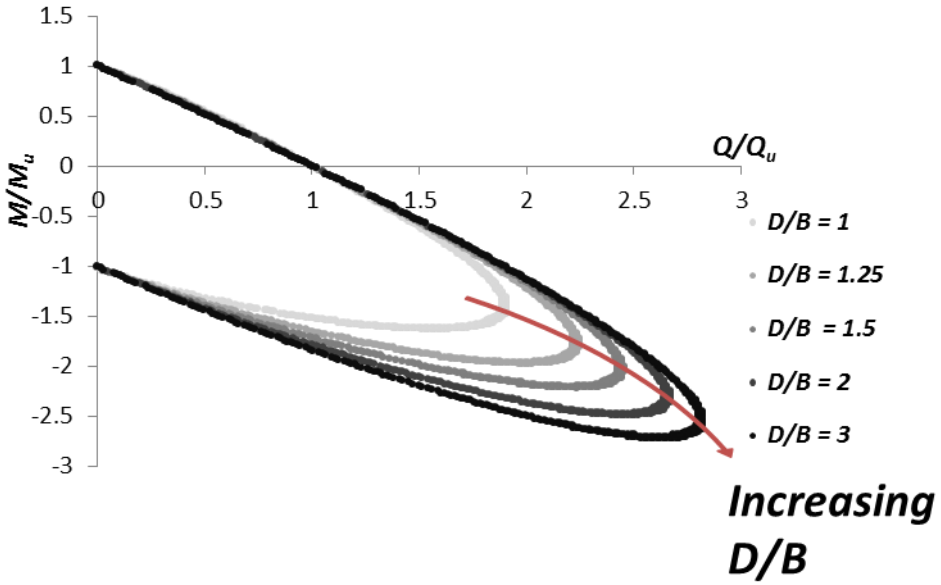

Figure 3.30 *The effect of $n_1 n_2, n_3$ on the shape of the yield surface under nonlinear interface conditions.*

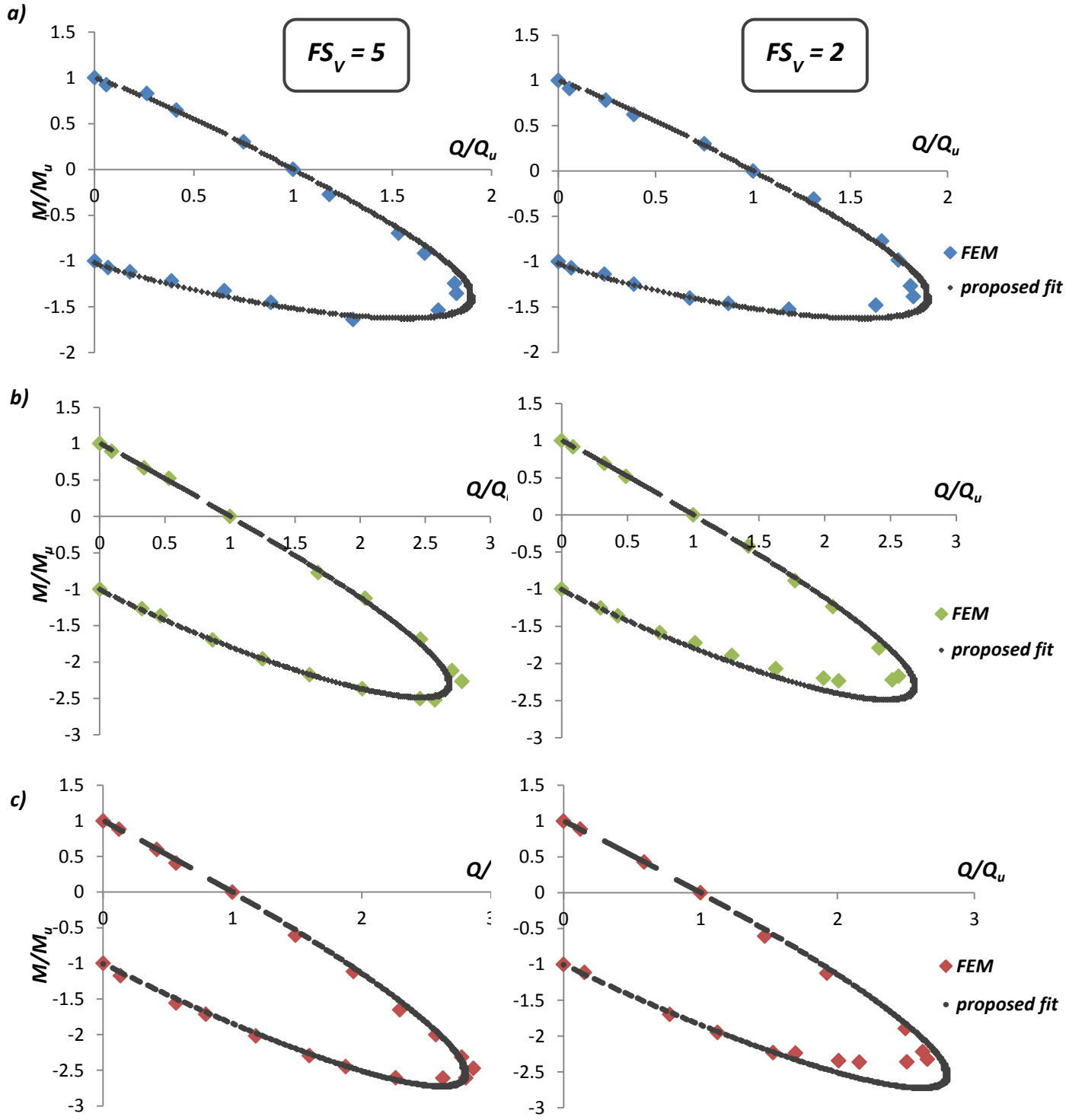

Figure 3.31 *Comparison between the data derived from the numerical experiments (points) and the analytical expression proposed for the yield surfaces of caisson foundations of two different factors of safety and embedment ratio a) D/B = 1, b) D/B = 2 and c) D/B = 3, given in normalized values. The foundation may experience gapping and slippage according to a Coulomb friction law with a coefficient of μ = 1.*

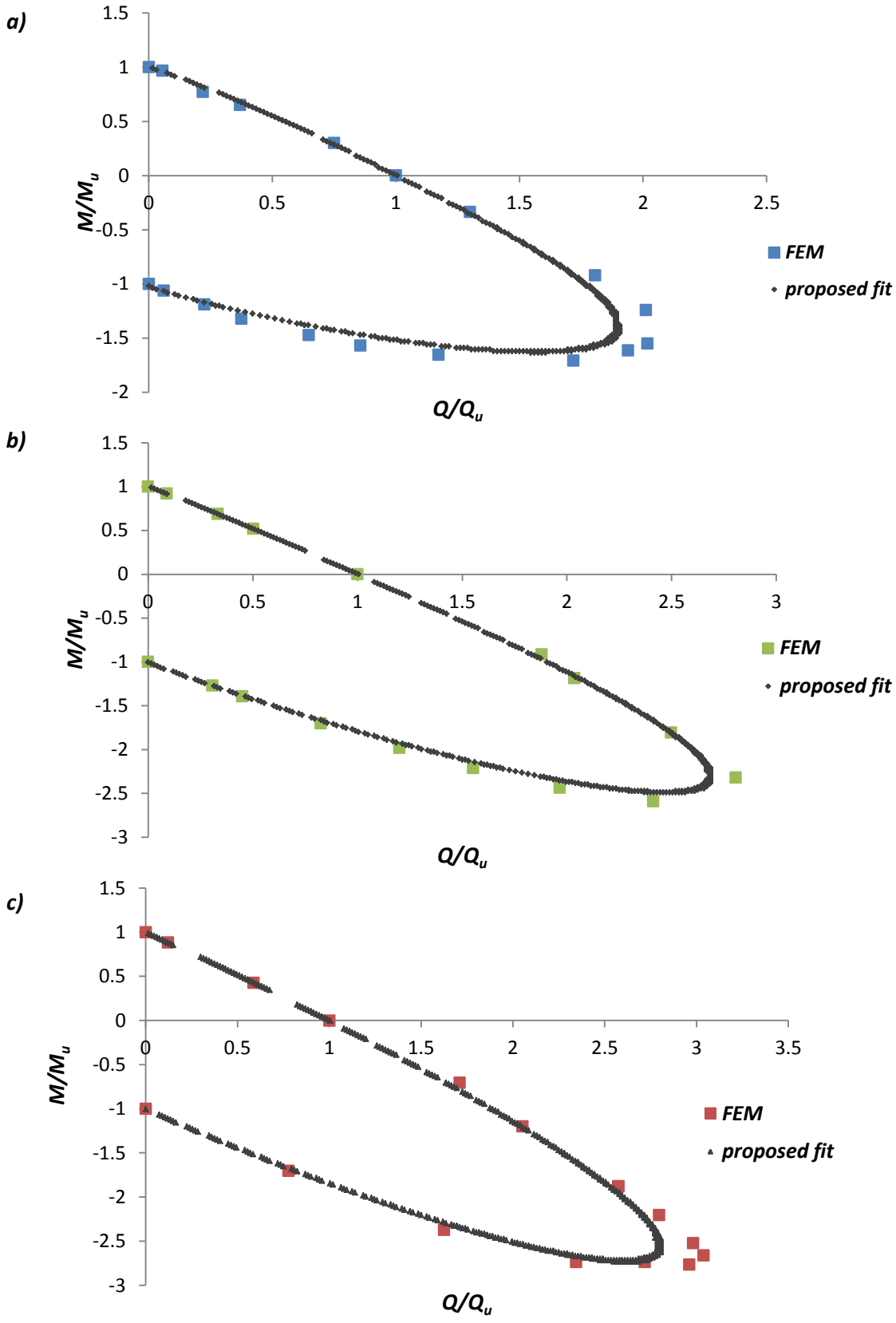

Figure 3.32 *Comparison between the data derived from the numerical experiments (points) and the analytical expression proposed for the yield surfaces of caisson foundations of a factor of safety $FS_V = 5$ and embedment ratio a) D/B = 1, b) D/B = 2 and c) D/B = 3, given in normalized values. The foundation may experience gapping and slippage according to a Coulomb friction law with a coefficient of $\mu = 0.1$.*

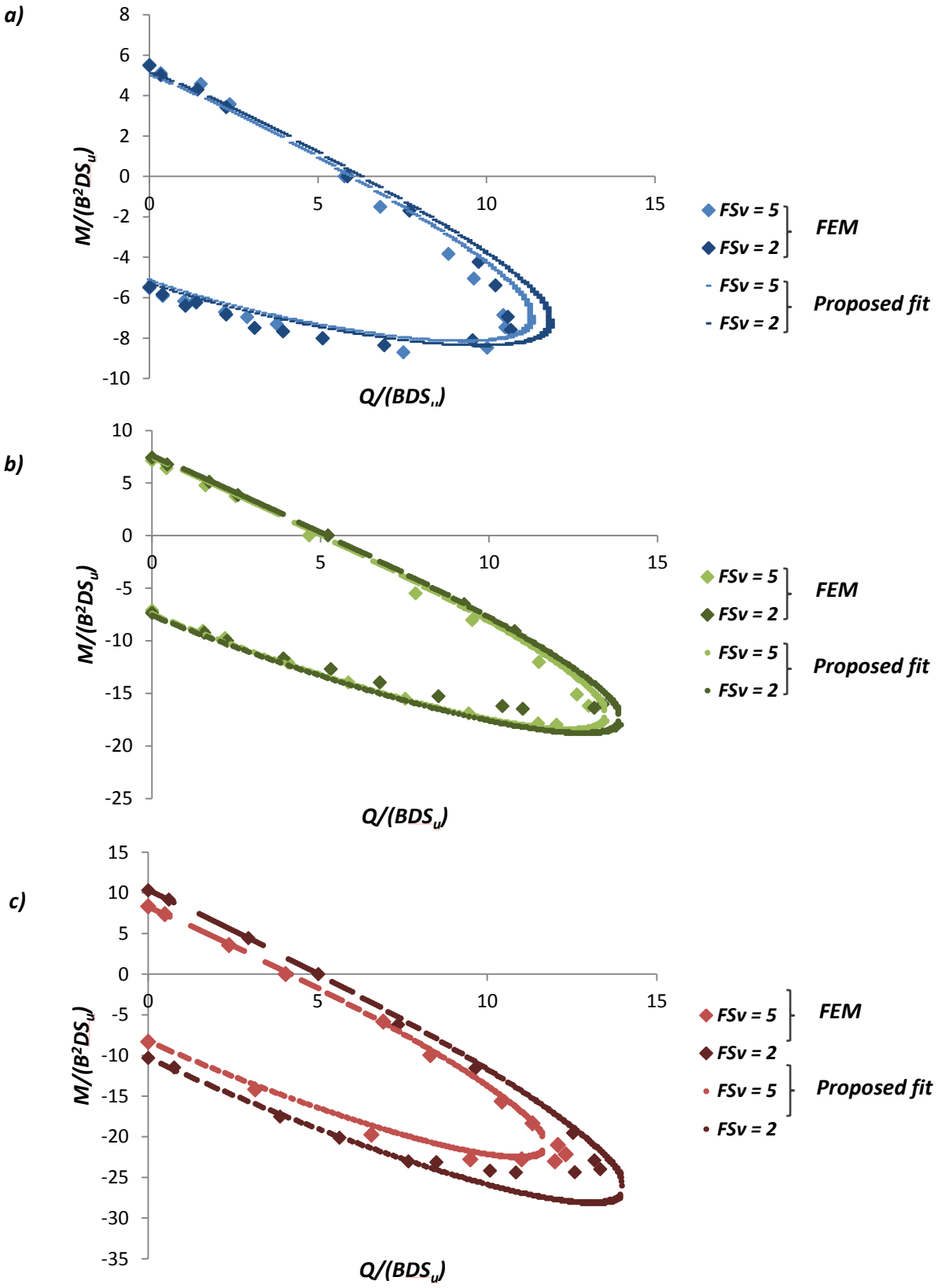

Figure 3.33 *Comparison between the data derived from the numerical experiments (points) and the analytical expression proposed for the yield surfaces of caisson foundations of a factor of safety $FS_V = 5$ and embedment ratio a) D/B = 1, b) D/B = 2 and c) D/B = 3, given in dimensionless terms. The foundation may experience gapping and slippage according to a Coulomb friction law with a coefficient of $\mu = 1$.*

CHAPTER 4

Constitutive Modeling

4.1. Introduction

In this chapter, we analyze the sophisticated BWGG Winkler model developed by Gerolymos and Gazetas [*2006*] by presenting its characteristics and key parameters, while also referring to basic calibration procedures. Then, we provide a short outline of a recently developed "macro–element" model [*Gerolymos and Souliotis, 2012*] and proceed to a comparison of the two models.

4.2. The BWGG Winkler Model

4.2.1. Model description

This model deals with rigid caisson foundations, i.e. those displaying a depth to width ratio (slenderness ratio) ranging from 1 to 3, depending on soil deformability. They differ substantially from pile foundations, in which the lateral soil reaction is the sole resisting mechanism. In contrast, caisson foundations also rely on the shear tractions at the circumference of the shaft due to their increased plan dimensions. The contribution of the base of the caisson may also be important depending on the slenderness ratio of the caisson, but it is usually limited to a 10-40% of the response. On the contrary, in

embedded foundations (with slenderness ratios below 0.5) the base provides most of the resistance.

In this model, the vertical component of loading is assumed to be far from vertical bearing failure and so it is the foundation capacity to combinations of moment and horizontal loading that is critical. Considering the relatively high design factors of safety under vertical loading in such structures, the above assumption is well founded.

The mechanisms that govern the response of a caisson include:

- The passive and active pressures developed on the two sides transverse to the loading plane (lateral soil reaction)
- The shear tractions on the periphery of the caisson
- The normal and shear stresses acting on the caisson base-soil interface

Figure 4.1 illustrates the stress pattern for a caisson with circular and rectangular cross-section.

This nonlinear four-spring model incorporates distributed translational (lateral) and rotational (rocking) springs and dashpots, as well as concentrated translational (shear) and rotational (moment) springs and dashpots at the base of the caisson. These four types of springs and dashpots are related to the resisting forces acting on the caisson shaft and base, as follows:

- The distributed lateral springs k_x and dashpots c_x are associated with the horizontal soil reaction on the circumference (shaft) of the caisson.
- The distributed rotational springs k_ϑ and dashpots c_ϑ are associated with the moment produced by the vertical shear tractions on the circumference (shaft) of the caisson.
- The resultant base shear translational spring K_h and dashpot C_h associated with the horizontal shearing force on the base of the caisson.
- The resultant base rotational spring K_r and dashpot C_r associated with the moment produced by normal pressures on the base of the caisson.

The model is presented in ***Figure 4.2***

4.2.2. Elastic model

4.2.2.1. Formulation

The problem studied in this first section is that of a circular, square or rectangular in plan caisson embedded in homogeneous elastic soil over deformable bedrock. The foundation is subjected to a combination of dynamic shear and moment excitation $Q_0(t)$ and $M_0(t)$ respectively. The positive rotation and overturning moment is clockwise. The foundation is a rigid block of mass *m* and mass moment of inertia about the center of gravity J_c. The depth of embedment is D while the height of the sidewall that is in contact with the surrounding soil is d.

Dynamic shear equilibrium in respect to the base of the caisson gives:

$$Q_0 - m \cdot \ddot{u}_c - P_x - Q_b = 0 \qquad \textbf{(4.1)}$$

where u_c is the displacement of the caisson at its center of gravity, given by:

$$u_c = u_b + \theta_c \cdot \frac{D}{2} \qquad \textbf{(4.2)}$$

where u_b is the displacement of the caisson base and ϑ_c the rotation angle of the caisson.

$$P_x = \int_0^d p_x(z,t)dz = \int_0^d [k_x(z)u(z,t) + c_x(z)\dot{u}(z,t)]dz \qquad \textbf{(4.3)}$$

where *z* represents the depth coordinate starting from the base of the caisson and *u* is the displacement of the caisson at the location z as determined by:

$$u = u_b + \theta_c \cdot z \qquad \textbf{(4.4)}$$

Q_b is the shear resistance at the base of the caisson given by the expression:

$$Q_b = K_h u_b + C_h \dot{u}_b \qquad \textbf{(4.5)}$$

Dynamic moment equilibrium in respect to the base of the caisson gives:

$$M_0 + Q_0 D - J_c \cdot \ddot{\theta}_c - m\frac{D}{2}\ddot{u}_c - M_x - M_\theta - M_b = 0 \qquad \textbf{(4.6)}$$

where M_x and M_ϑ are the resisting moments arising from the horizontal soil reaction and the vertical shear stresses on the caisson shaft and are expressed as:

$$M_x = \int_0^d p_x(z,t) z dz = \int_0^d [k_x(z)u(z,t) + c_x(z)\dot{u}(z,t)] z dz \qquad \textbf{(4.7)}$$

$$M_\theta = \int_0^d m_\theta(z,t) dz = \int_0^d \left[k_\theta(z)\theta_c(t) + c_\theta(z)\dot{\theta}_c(t)\right] dz \qquad \textbf{(4.8)}$$

and M_b is the resultant resisting moment at the base of the caisson.

$$M_b = K_r\theta_c + C_r\dot{\theta}_c \qquad \textbf{(4.9)}$$

Equations (4.1) and (4.6) can be rewritten in the form of a matrix as:

$$\boldsymbol{M_b} \cdot \begin{Bmatrix} \ddot{u}_b \\ \ddot{\theta}_b \end{Bmatrix} + \boldsymbol{C_b} \cdot \begin{Bmatrix} \dot{u}_b \\ \dot{\theta}_b \end{Bmatrix} + \boldsymbol{K_b} \cdot \begin{Bmatrix} u_b \\ \theta_b \end{Bmatrix} = \boldsymbol{P_b} \qquad \textbf{(4.10)}$$

In the above expression we can distinguish:

- the mass matrix

$$\boldsymbol{M_b} = \begin{bmatrix} m & m\frac{D}{2} \\ m\frac{D}{2} & J_c + m\frac{D^2}{4} \end{bmatrix} \qquad \textbf{(4.11)}$$

- the stiffness matrix

$$\boldsymbol{K_b} = \begin{bmatrix} K_{hh} & K_{hr} \\ K_{hr} & K_{rr} \end{bmatrix} = \begin{bmatrix} K_h + \int_0^d k_x(z)dz & \int_0^d k_x(z) z dz \\ \int_0^d k_x(z) z dz & K_r + \int_0^d k_x(z) z^2 dz + \int_0^d k_\theta(z) dz \end{bmatrix} \qquad \textbf{(4.12)}$$

- the damping matrix

$$\boldsymbol{C_b} = \begin{bmatrix} C_{hh} & C_{hr} \\ C_{hr} & C_{rr} \end{bmatrix} = \begin{bmatrix} C_h + \int_0^d c_x(z)dz & \int_0^d c_x(z) z dz \\ \int_0^d c_x(z) z dz & C_r + \int_0^d c_x(z) z^2 dz + \int_0^d c_\theta(z) dz \end{bmatrix} \qquad \textbf{(4.13)}$$

- as well as the external force vector

$$\boldsymbol{P_b} = \begin{Bmatrix} Q_0 \\ M_0 + Q_0 D \end{Bmatrix} \quad \textbf{(4.14)}$$

In the frequency domain the complex stiffness matrix of the caisson is calculated as:

$$\widetilde{\boldsymbol{K}}_{\boldsymbol{b}} = \boldsymbol{K_b} + i\omega \boldsymbol{C_b} \quad \textbf{(4.15)}$$

Using (***Eq. 4.12***) and (***Eq. 4.13***) the above expression yields:

$$\widetilde{\boldsymbol{K}}_{\boldsymbol{b}} = \begin{bmatrix} \widetilde{K}_h + \tilde{k}_x D & \tilde{k}_x \dfrac{D^2}{2} \\ \tilde{k}_x \dfrac{D^2}{2} & \widetilde{K}_r + \tilde{k}_\theta D + \dfrac{1}{3}\tilde{k}_x D^3 \end{bmatrix} \quad \textbf{(4.16)}$$

The dynamic impedance matrix can be easily transformed in order to refer to the top of the caisson as follows:

$$\tilde{\boldsymbol{S}} = \begin{bmatrix} \tilde{S}_{hh} & \tilde{S}_{hr} \\ \tilde{S}_{hr} & \tilde{S}_{rr} \end{bmatrix} = \begin{bmatrix} \widetilde{K}_{hh} & \widetilde{K}_{hr} - D\widetilde{K}_{hh} \\ \widetilde{K}_{hr} - D\widetilde{K}_{hh} & \widetilde{K}_{rr} - 2D\widetilde{K}_{hr} + D^2\widetilde{K}_{hh} \end{bmatrix} \quad \textbf{(4.17)}$$

The force and moment equilibrium on the caisson as considered above as well as the meaning of the impedances S_{ij} are sketched in ***Fig. 4.3***.

4.2.2.2. Calibration of the elastic parameters

Calibration of the elastic spring and dashpot coefficients is based on published complex dynamic impedances of embedded foundations. Gazetas et al. have developed closed form expressions for the impedances of arbitrarily shaped foundations in plan view and are expressed in the following form:

$$\widetilde{K}_{emb} = K_{emb}\chi_{emb}(\omega) + i\omega C(\omega) \quad \textbf{(4.18)}$$

where

$$\widetilde{\boldsymbol{K}}_{\boldsymbol{emb}} = \begin{bmatrix} \widetilde{K}_{HH} & \widetilde{K}_{HM} \\ \widetilde{K}_{HM} & \widetilde{K}_{MM} \end{bmatrix} \quad \textbf{(4.19)}$$

In respect to the lateral stiffness of a caisson, Gazetas et al. have extracted the following expression:

$$K_{HH}(\omega) = K_H(1 + 0.15\sqrt{\frac{2D}{B}})\left[1 + 0.52\left(\frac{8hA_w}{BL^2}\right)^{0.4}\right]\chi_{emb}(\omega) \qquad \textbf{(4.20)}$$

where K_H is the static horizontal stiffness of the caisson base and $\chi_{emb}(\omega)$ an appropriate stiffness coefficient.

The parameters involved in the computation of the stiffness and damping in (***Eq.4.18***) are:

- the shear modulus G_s, the elasticity modulus E_s, the shear wave velocity V_s, the apparent analog velocity V_a, and Poisson's ratio v.
- the width B, the length L, the depth of embedment D and the height d of the caisson sidewall that is in contact with the surrounding soil.
- the area A_b and moment of inertia I_b of the caisson base as well as the distance h of the centroid of the effective sidewall from the ground surface.
- the total area A_w of the actual sidewall-soil contact surface.
- the projected areas $A_{w,s}$ and $A_{w,ce}$ of all the sidewall areas in direction parallel and perpendicular to loading subjected to shear and compression-extension type of soil reaction respectively.
- the sum of the polar moments of inertia J_{ws} about the off-plane axis of rotation of all surfaces actually shearing the soil, and the sum of moments of inertia J_{wce} of all surfaces actually compressing the soil about their base axes parallel to the axis rotation.
- the distance Δ_i of surface $A_{wce,i}$ from the x-axis.

The horizontal dashpot coefficient is given by:

$$C_{HH}(\omega) = C_H(\omega) + \rho V_s A_{ws} + \rho V_a A_{wce} \qquad \textbf{(4.21)}$$

where $C_H(\omega)$ is the damping coefficient of the caisson base.

The coupled swaying-rocking impedance is approximated by:

$$\widetilde{K}_{HM} = \frac{1}{3} d\widetilde{K}_{HH} \qquad \textbf{(4.22)}$$

In respect to the dynamic rocking stiffness of a caisson, Gazetas et al. have extracted the following expression:

$$K_{MM}(\omega) = K_M(1 + 0.92\left(\frac{2d}{L}\right)^{0.6})\left[1.5 + \left(\frac{2d}{L}\right)^{1.9}\left(\frac{d}{D}\right)^{-0.6}\right](1 - 0.3a_0) \qquad \textbf{(4.23)}$$

where K_M is the static rocking stiffness of the caisson base.

The rocking dashpot coefficient is given by:

$$C_{MM}(\omega) = C_M(\omega) + \rho V_{La} I_{wce} c_1(\omega) + \rho V_s \left[J_{ws} + \sum_i A_{wcei} \Delta_i^2\right] c_1(\omega) \qquad \textbf{(4.24)}$$

where $C_M(\omega)$ is the damping rocking coefficient of the caisson base.

By equating the diagonal terms of (***Eq. 4.16***) and (***Eq. 4.19***), Gerolymos et al. have extracted approximated expressions for the distributed springs and dashpots. Especially in the case of the square caisson the following expressions can be used in the formulation of the model:

$$k_x = 2.18\left(\frac{D}{B}\right)^{-0.13} E_s \qquad \textbf{(4.25)}$$

$$k_\theta = 1.20\left(\frac{D}{B}\right)^{-1.71} E_s D^2 \qquad \textbf{(4.26)}$$

Despite its simplicity, the elastic Winkler model captures the important characteristics of the caisson's response and compares well to the results of 3-D FEM analyses e.g. when subjected to kinematic loading due to vertical shear wave propagation [*Gerolymos and Gazetas*, *2006*].

4.2.3. Extension to the non-linear BWGG model

4.2.3.1. Introduction

In order to realistically capture the response of the caisson foundation under large amplitude static or dynamic loading (up to failure), Gerolymos and Gazetas replaced the linear Winkler springs with sophisticated non-linear springs. With this new formulation of the model, effects of separation and slippage at the caisson–soil interface, uplift of the caisson base, stiffness and strength degradation with large number of cycles are now taken into account. Additionally, the dashpots are modified in order to account for the effects of gap formation and non-linear soil response on the radiation damping.

4.2.3.2. Ultimate soil reactions

The lateral soil reaction p_x includes two stress components:

- the compressive and tensile normal stresses at the front and back of the caisson, at the direction of loading and
- the shear stresses developed at the sides of the caisson, perpendicular to the direction of loading

At the sides of the caisson vertical shear stresses also develop and they contribute significantly to the overall response due to the rigidity and large dimensions of typical caisson foundations. These stresses produce a resisting moment m_θ per depth about the horizontal axis perpendicular to the direction of loading and passing through the center of the caisson cross-section.

Similarly, at the base of the caisson, shear stresses at the direction of loading contribute to the resultant resisting force Q_b and normal stresses produce the resisting moment M_b.

4.2.3.3. Constitutive equations

The lateral soil reaction p_x is expressed as the sum of two components, the hysteretic p_s and the viscoplastic p_d.

$$p_x = p_s + p_d \tag{4.27}$$

The hysteretic component p_s is expressed in the Bouc-Wen fashion as:

$$p_s = a_x k_x u + (1 - a_x) p_y \zeta_x \tag{4.28}$$

in which:

p_s is the resultant in the direction of loading of the normal and shear tractions along the shaft of the caisson,

u is the horizontal displacement of the caisson at the location of the spring,

k_x is the initial stiffness of the translational spring,

a_x is a parameter that controls the post yield stiffness,

p_y is the ultimate soil reaction

and ζ_x is a hysteretic dimensionless quantity that controls the nonlinear behavior of the lateral soil reaction.

The latter is governed by the following differential equation with respect to time, *t*:

$$\frac{d\zeta_x}{dt} = \lambda_x \frac{h_x}{u_y}\left[\frac{du}{dt} - (1 + r_x)\left(b_x \frac{du}{dt}|\zeta_x|^{n_x} + g_x \left|\frac{du}{dt}\right| |\zeta_x|^{n_x - 1}\zeta_x\right]\right. \tag{4.29}$$

where

$$h_x = h_x(\zeta_x) = 1 - \zeta_0 \exp\left[-\left(\frac{u_y \zeta_x}{\delta \Delta}\right)^2\right] \tag{4.30}$$

is the pinching factor used to model the gap formation.

Parameters b_x, g_x, n_x, λ_x, r_x, ζ_0, Δ are dimensionless quantities that control the shape of the monotonic curve as well as that of the hysteresis loop; u_y is defined as $u_y = \frac{p_y}{k_x}$. The exact role of each of the above parameters is illustrated in the next section.

The original form of the equations is attributed to Bouc & Wen and the specific form of (***Eq. 4.29***) and (***Eq. 4.30***) was developed by Gerolymos & Gazetas for the case of the caisson problem studied herein.

Eq. 4.29 can be rewritten in an incremental form by eliminating *t*:

$$d\zeta_x = \lambda_x \frac{h_x}{u_y}\{1 - (1 + r_x)|\zeta_x|^{n_x}[b_x + g_x sign(du\zeta_x)]\}du \qquad \textbf{(4.31)}$$

The solution is not frequently dependent, which confirms its hysteretic nature.

The viscoplastic component of the lateral soil reaction is given by:

$$p_d = c_x \frac{\partial u}{\partial t}\left[a_x + (1 - a_x)\frac{\partial \zeta_x}{\partial u}\right]^{c_{xd}} \qquad \textbf{(4.32)}$$

where c_x is the dashpot coefficient at small amplitude motions and c_{xd} is a viscoplastic parameter which controls the coupling of soil and soil-caisson interface nonlinearity with radiation damping.

Similarly, the resisting moment per unit depth is expressed as the resultant of the hysteretic m_s and the viscoplastic m_d component

$$m_\theta = m_s + m_d \qquad \textbf{(4.33)}$$

where

$$m_s = m_y \zeta_\theta \qquad \textbf{(4.34)}$$

in which m_y is the ultimate resisting moment at initiation of slippage at the soil-caisson interface at a specific depth. m_y generally depends on the lateral soil reaction p_s although this kind of coupling may be not significant as will be displayed afterwards. As with ζ_x, ζ_θ is a hysteretic dimensionless quantity that controls the nonlinear response of the resisting moment per unit depth and is governed by the equivalent differential equation:

$$\frac{d\zeta_\theta}{dt} = \lambda_\theta \frac{1}{\theta_y}\left[\frac{d\theta}{dt} - (1 + r_\theta)(b_\theta \frac{d\theta}{dt}|\zeta_\theta|^{n_\theta} + g_\theta \left|\frac{d\theta}{dt}\right| |\zeta_\theta|^{n_\theta - 1}\zeta_\theta\right] \qquad \textbf{(4.35)}$$

Parameters b_θ, g_θ, n_θ, λ_θ and r_θ are dimensionless quantities that control the shape of the monotonic curve as well as that of the resisting moment – rotation hysteresis loop; θ_y is defined as $\theta_y = \frac{m_y}{k_\theta}$.

Note that ***Eq. 4.35*** is similar to ***Eq. 4.29*** except for the fact that there is no term for h_ϑ.

The viscoplastic component of the resisting moment per unit depth is given by:

$$m_d = c_\theta \frac{\partial\theta}{\partial t}\left[a_\theta + (1 - a_\theta)\frac{\partial\zeta_\theta}{\partial\theta}\right]^{c_{\theta d}} \qquad \textbf{(4.36)}$$

where c_ϑ is the dashpot coefficient at small amplitude motions and $c_{\vartheta d}$ is a viscoplastic parameter which controls the coupling of soil inelasticity and slippage at the soil-caisson interface. With the occurrence of sliding at the interface, the term inside the brackets vanishes and so does therefore m_d. This means that the system generates no radiation damping from rotational oscillation when slippage takes place at the interface.

In a similar manner, the shear force Q_b and resisting moment M_b at the base of the caisson are expressed with their hysteretic and viscoplastic components:

$$Q_b = Q_{bs} + Q_{bd} \qquad \textbf{(4.37)}$$

$$M_b = M_{bs} + M_{bd} \qquad \textbf{(4.38)}$$

whose equations are analogous to the ones presented above for the case of the lateral soil reaction and the resisting moment per unit depth.

Note that the use of concentrated springs and dashpots at the base of the caisson allows only for an implicit consideration of coupled uplifting and soil inelasticity phenomena through appropriate calibration of the model parameters.

4.2.3.4. Explanation of model key parameters

Parameters associated with the shape of the monotonic curve:

Parameter *n* (n_x for the lateral soil reaction and n_θ for the resisting moment) controls the rate of transition from the elastic to the yield state, namely the elastic-plastic coupling. A large value of *n* (greater than 10) models approximately a bilinear hysteretic curve, whereas decreasing values of n lead to a smoother transition, where plastic deformation occurs even at low loading levels. On the other hand, parameter *a* (a_x for the lateral soil reaction and a_ϑ for the resisting moment) is the ratio of post-yield to initial elastic stiffness. The combined effect of *n, a* on the monotonic curve is aptly illustrated in ***Figures 4.4*** and ***4.5.***

Based on the choice of proper *n, a* values the model can account for different types of soils.

Parameters associated with the shape of the hysteresis loop:

Parameters *b* and *g* control the shape of the unloading-reloading curve. One can recognize four basic hysteretic shapes (***Figure 4.5***) of which two are the most characteristic:

- In the case where *b = g = 0.5* the stiffness upon reversal equals the initial stiffness (Masing criterion) and remains constant until reversal of *ζ.*
- In the case where *b = 1, g = 0*, the hysteretic loop collapses to the monotonic loading curve (nonlinear elastic behavior).

Parameters associated with stiffness and strength degradation:

Both stiffness and strength degradation with cyclic behavior can be accounted for independently in the BWGG model. The parameter λ expressed as a function of dissipated hysteretic energy or cumulative displacement controls the reduction of stiffness through cyclic response, whereas the parameter *r* simulates strength degradation. Increasing *r* reduces the soil strength in proportion to *(1+r)*. Gerolymos and Gazetas propose that *r* be prescribed as an increasing function of the dissipated energy according to:

$$r_x(t) = \beta \left[(1 - \alpha_x) p_y \int_0^t \zeta_x(u,t) u(\dot{t}) dt \right]^{\gamma} \quad \textbf{(4.39)}$$

where β,γ are experimentally determined parameters.

Parameters associated with gap formation and slippage at the soil-caisson interface

Gap opening up around the caisson (particularly significant with stiff clays), and slippage at the soil–caisson interface (significant for both sands and clays), are treated as coupled phenomena. Gapping is implemented through the pinching function h_x presented above. The calibration methods and the conditions under which separation and slipping occurs are presented in [*Gerolymos and Gazetas, 2006b*].

Parameters associated with the uplifting of the caisson's base:

Base uplifting may significantly contribute to the dynamic response of the caisson foundation for low values of slenderness ratio D/B mainly in terms of stiffness. For very shallow foundations uplifting may even dominate the response. Depending on the factor of safety against vertical loading, Gerolymos and Gazetas provide calibration guidelines for parameters n_r and b_r.

Finally, the researchers present a thorough methodology for the calculation of ultimate resistance and radiation damping parameters for a circular caisson. The reader is referred to [*Gerolymos and Gazetas, 2006b*] for the details on the above approach.

4.3. A Macro-element model for the lateral response of embedded foundations

4.3.1. Introduction

Recently, research in foundation engineering has focused on the development of unified mathematical tools able to fully represent the foundation's behaviour in terms of generalized force – displacement with respect to a reference point [*Chatzigogos, Figini, Pecker and Salençon 2011*]. This type of tool is conventionally termed a "macro-element". The first "macro-element" was developed by Nova and Montrasio [*1991*] and referred to the modeling of a surface foundation into an elasto-plastic constitutive model governed by an isotropic hardening law. Various researchers modified and extended this approach to account for cyclic and dynamic loading. A milestone in the field of "macro-element" research is the study of Cremer [*2001*] and Cremer et al. [*2001*], who developed a complex macro-element for surface foundations that can account for the detachment of the foundation from the supporting soil under extreme moment.

In the case of embedded foundations, however, there has been no substantial work by researchers into developing such a unified mathematical tool. In this sense, the recent work of Gerolymos and Souliotis [*2012*] has been one of the first macro-element approaches regarding this type of foundations. They developed a 2-degree of freedom model by incorporating the following four aspects of an embedded foundation's response, as displayed in ***Fig. 4.6***:

- Elastic response
- Failure envelope
- Plastic flow rule
- Hardening law

In the next section, we provide a brief analysis for each of these aspects as well as their incorporation to a complete mathematical formulation.

4.3.2. Elasticity

The researchers incorporated closed-form analytical expressions for the dynamic stiffness of rigid deeply embedded foundations on a linear elastic homogeneous half-space published by Gazetas et al, as analyzed previously on chapter ***4.2.1.2.*** The top of the caisson was chosen as a reference point, by appropriately modifying the elasticity matrix, in order to comport with the failure envelopes that were deduced.

4.3.3. Failure envelopes

Considering bonded interface conditions along the shaft of the caisson, Gerolymos et al. fully determined the failure envelopes of embedded foundations as presented in Chapter 2 of this thesis. The final expression for the yield surface is given below:

$$f(M,Q,N) = (1-\frac{N}{N_u})^{-0.34} \cdot \left[\left(\frac{Q}{{Q_u}^*}\right)^2 + \left(\frac{M}{{M_u}^*}\right)^2 + n_3 \frac{Q}{{Q_u}^*}\frac{M}{{M_u}^*}\right] - 1 = 0 \qquad \textbf{(4.40)}$$

4.3.4. Plastic flow rule

The researchers assessed the applicability of a macroscopic associative flow rule by checking the normality of the displacement vectors to the yield locus. They concluded that normality is satisfied all along the yield locus (***Fig. 4.7***) regardless of the embedment ratio or the factor of safety against vertical loading. Mathematically, the associative flow rule is expressed as:

$$\begin{Bmatrix}\partial u^{pl} \\ \partial \theta^{pl}\end{Bmatrix} = \begin{Bmatrix}\dot{u^{pl}} \\ \dot{\theta^{pl}}\end{Bmatrix} = \lambda \begin{Bmatrix}\dfrac{\partial f}{\partial Q} \\ \dfrac{\partial f}{\partial M}\end{Bmatrix} \qquad \textbf{(4.41)}$$

relating the increment of the yield function *f* to that of the plastic generalized displacement *u,* where λ is a non-negative multiplying factor that defines the magnitude of the plastic generalized displacement with respect to the load angle *M/Q*.

4.3.5. Hardening law

The hardening law adopted in this model is based on the work-hardening plasticity theory. Using a tangential approximation and 3 hardening parameters *n, a, b-g*, the model calculates the incremental displacements by updating the stiffness matrix K_t at every loading step.

4.3.6. Formulation

The incremental load is related to the incremental displacement via the tangential stiffness matrix K_t :

$$\Delta \boldsymbol{F} = \boldsymbol{K}_t \cdot \Delta \boldsymbol{\delta} \qquad \textbf{(4.42)}$$

while the incremental work is expressed as:

$$\Delta \boldsymbol{W} = \Delta \boldsymbol{F} \cdot \Delta \boldsymbol{\delta} \qquad \textbf{(4.43)}$$

The stiffness matrix ultimately acquires the following form:

$$\boldsymbol{K}_t = \begin{bmatrix} 1-a & 0 \\ 0 & 1-a \end{bmatrix} \cdot \boldsymbol{K}_{top} \cdot 2 \cdot (\boldsymbol{I} - \boldsymbol{B} \cdot \boldsymbol{H_1} \cdot \boldsymbol{H_2}) + \begin{bmatrix} a & 0 \\ 0 & a \end{bmatrix} \cdot \boldsymbol{K}_{top} \qquad \textbf{(4.44)}$$

where:

- $I = \begin{bmatrix} \mathbf{1} & \mathbf{0} \\ \mathbf{0} & \mathbf{1} \end{bmatrix}$

- $\boldsymbol{B} = \boldsymbol{\Phi} \cdot E \cdot \boldsymbol{\Phi}^T \cdot \boldsymbol{K}_{top}$

- $E = (\boldsymbol{\Phi}^T \cdot \boldsymbol{K}_{top} \cdot \boldsymbol{\Phi})^{-1}$

- $\boldsymbol{\Phi} = \begin{Bmatrix} \frac{\partial f}{\partial Q} \\ \frac{\partial f}{\partial M} \end{Bmatrix} = \frac{1}{\lambda} \cdot \frac{\partial u}{\partial \theta}$

- $\boldsymbol{H}_1 = \begin{bmatrix} f(M,Q,N) + 1^n & 0 \\ 0 & f(M,Q,N) + 1^n \end{bmatrix}$

- $\boldsymbol{H}_1 = \begin{bmatrix} b + g \cdot sign(\Delta W) & 0 \\ 0 & b + g \cdot sign(\Delta W) \end{bmatrix}$

4.4. Comparison of the two models

Both models may be considered as “macro-elements” since they effectively substitute the soil-foundation system with an appropriate nonlinear stiffness matrix able to account for its total behaviour. Their difference lies in the so-called “macro-scale”, which represents the macroscopic level of “replacement” of the actual resisting mechanisms that is accomplished by the model. In the Winkler BWGG model, plasticity lies in the soil-reaction level (nonlinear distributed springs), while in the second model it derives from the failure envelopes themselves. Possibly, a more suitable term for the Winkler model would be a “meso-element”.

Regarding elasticity, the Winkler model appears to be, at first sight, less able to capture the response of embedded foundations due to the lack of translational-rotational coupled springs. The coupled diagonal terms in the elasticity matrix may only be determined in an approximate fashion as explained before. On the contrary, the “macro-element” model incorporates the complete elasticity matrix, where the coupled diagonal terms may be determined separately. However, this is true only for uniform soil profiles

where the elasticity matrix of embedded foundations can be directly determined. The majority of soil profiles is practically non-uniform or layered, which calls for a replacement of the soil with Winkler springs in order to determine the elasticity matrix. In this case, the two models are absolutely equivalent.

Similarly, the ultimate capacity of embedded foundations can be captured in a more realistic fashion by the “macro-element” in the case of a uniform soil profile. The extension, however, to the - more realistic - layered soil profile is very difficult since it requires numerous FE experiments to serve as the basis for its calibration. On the other hand, the Winkler model can readily account for multi-layered and non-uniform soil profiles by modifying the parameters of the distributed translational and rotational springs. It is certainly a more versatile model and a more physical approach to the response of laterally loaded caisson foundations.

The transition from the elastic to the plastic aspect of the response derives from the nonlinear behavior of the springs in the Winkler model, while in the “macro-element” it is a purely mathematic invention (mapping rule). In addition, the post-yield behaviour of the foundation is determined by the physics of the Winkler model, whereas the “macro-element” requires the incorporation of an appropriate flow rule as described above.

Ultimately, the two models can save considerable computational time compared to the conduction of time-consuming 3D Finite Element analyses. Yet, the difference in the computational time of the two models is relatively insignificant.

Figures

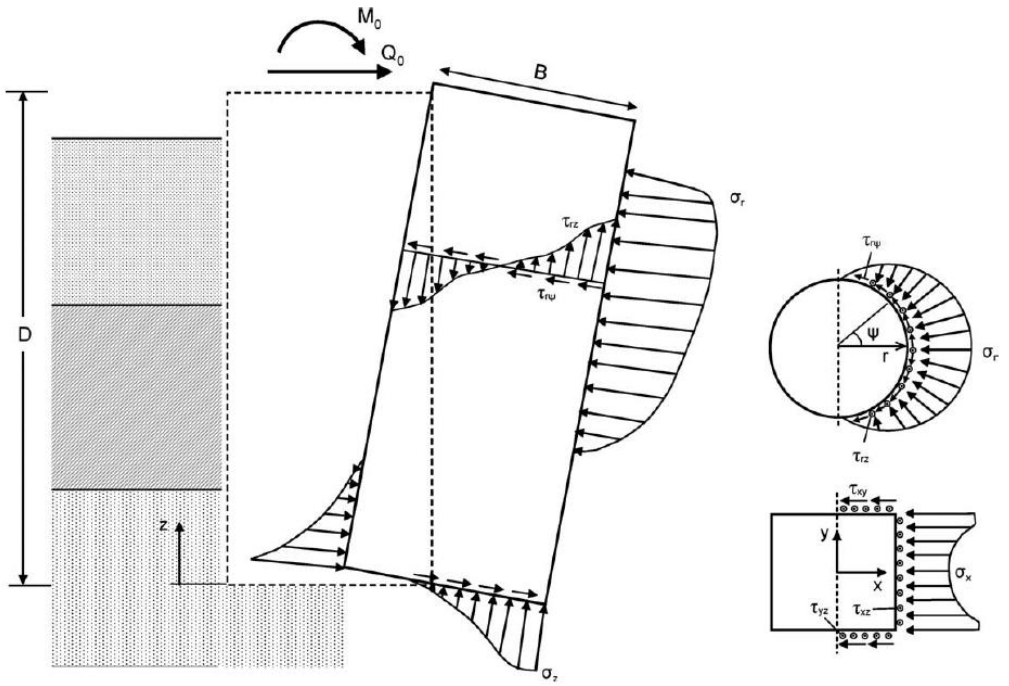

Figure 4.1 *The normal and shear stress patterns at the caisson-soil interface, with circular or square plan shape.*

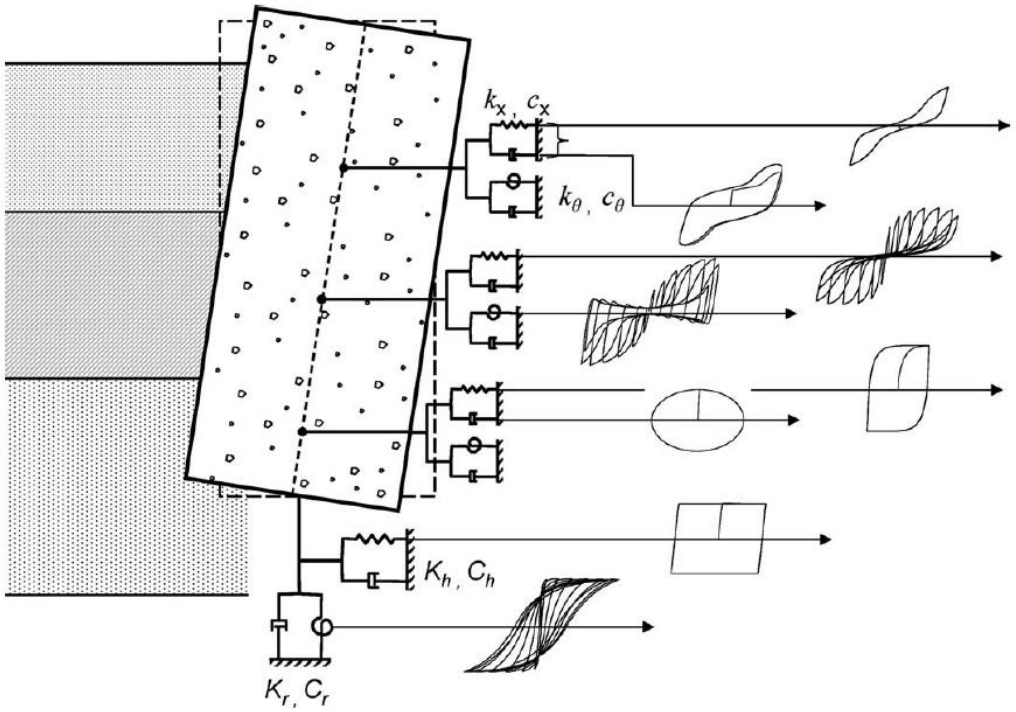

Figure 4.2 *Nonlinear Winkler model for the analysis of laterally loaded caisson foundations.*

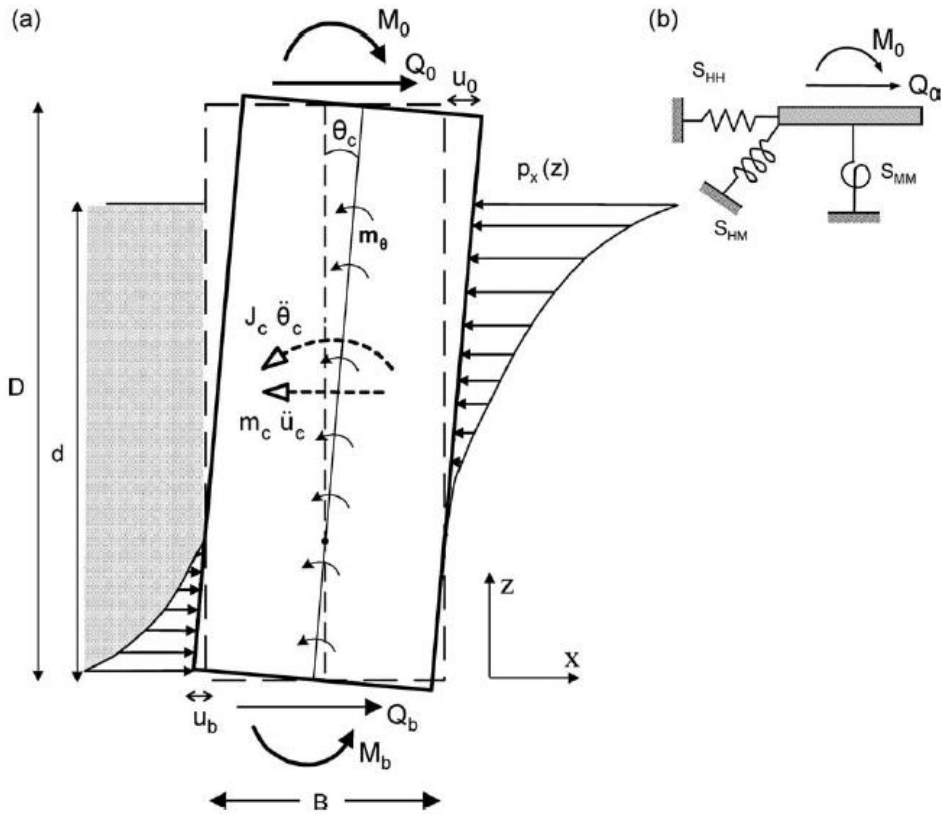

Figure 4.3 *Elastic response of a caisson subjected to lateral dynamic loading M_0, Q_0 at its top. Schematic definition of the global stiffnesses in lateral translation (S_{HH}), rotation (S_{MM}) and cross-coupling of the translation and the rotation (S_{HM}).*

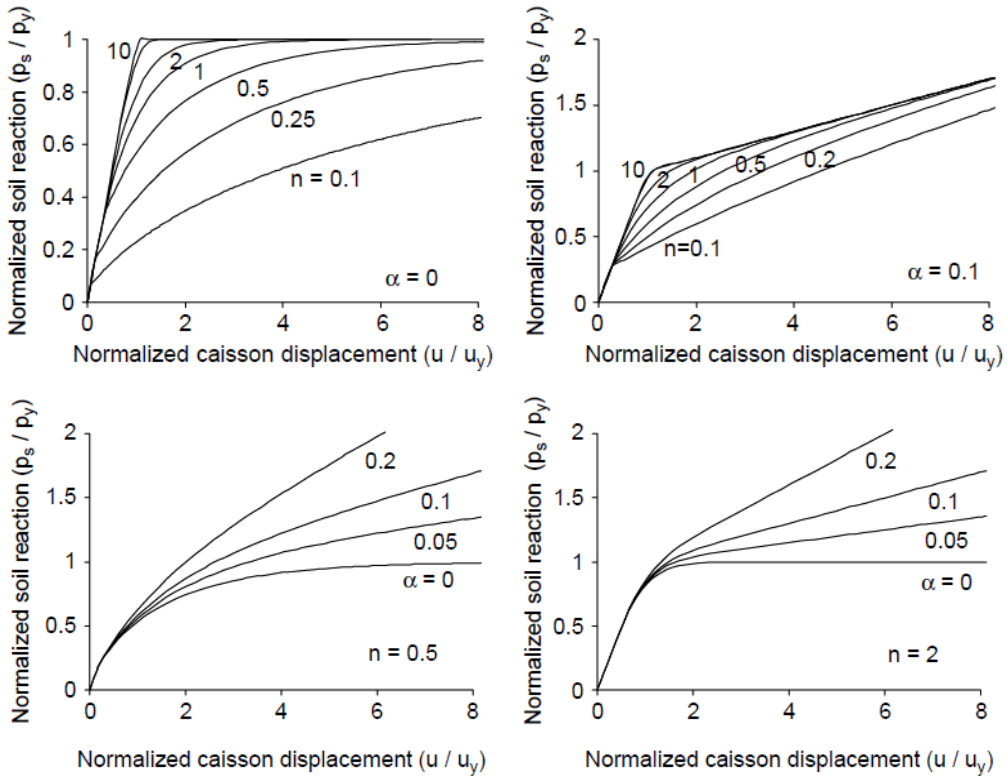

Figure 4.4 *Normalized soil reaction-caisson displacement to monotonic loading for selected values of the hardening and post-yielding parameters n, a respectively.*

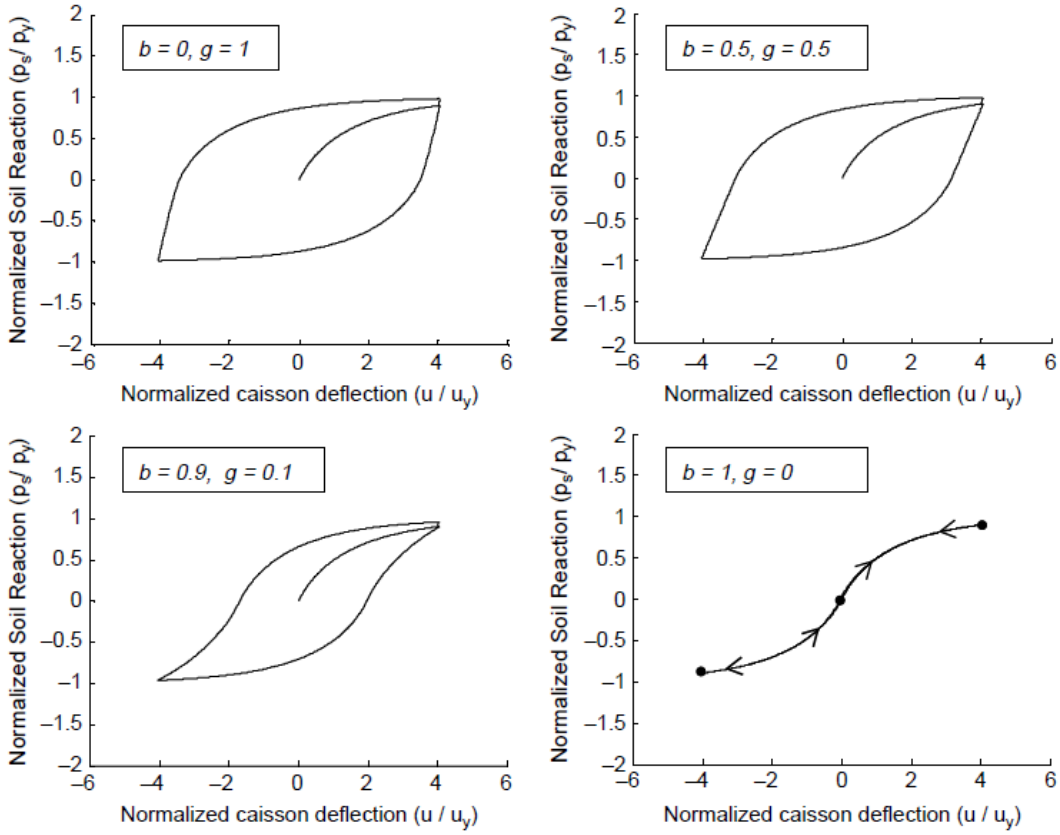

Figure 4.5 *Hysteresis loops for normalized soil reaction-caisson displacement for distinct values of b, g and n = 1. The Masing criterion is obtained for b = g = 0.5.*

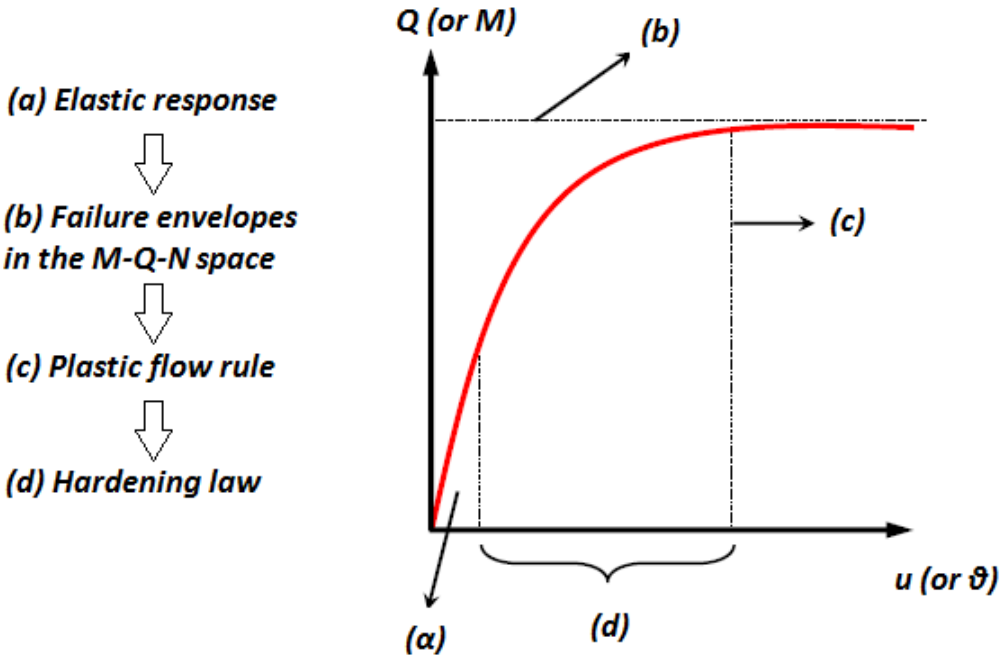

Figure 4.6 *The four aspects of the macro-element developed by Gerolymos and Souliotis [2012], and their effect on the force-displacement response of an embedded foundation.*

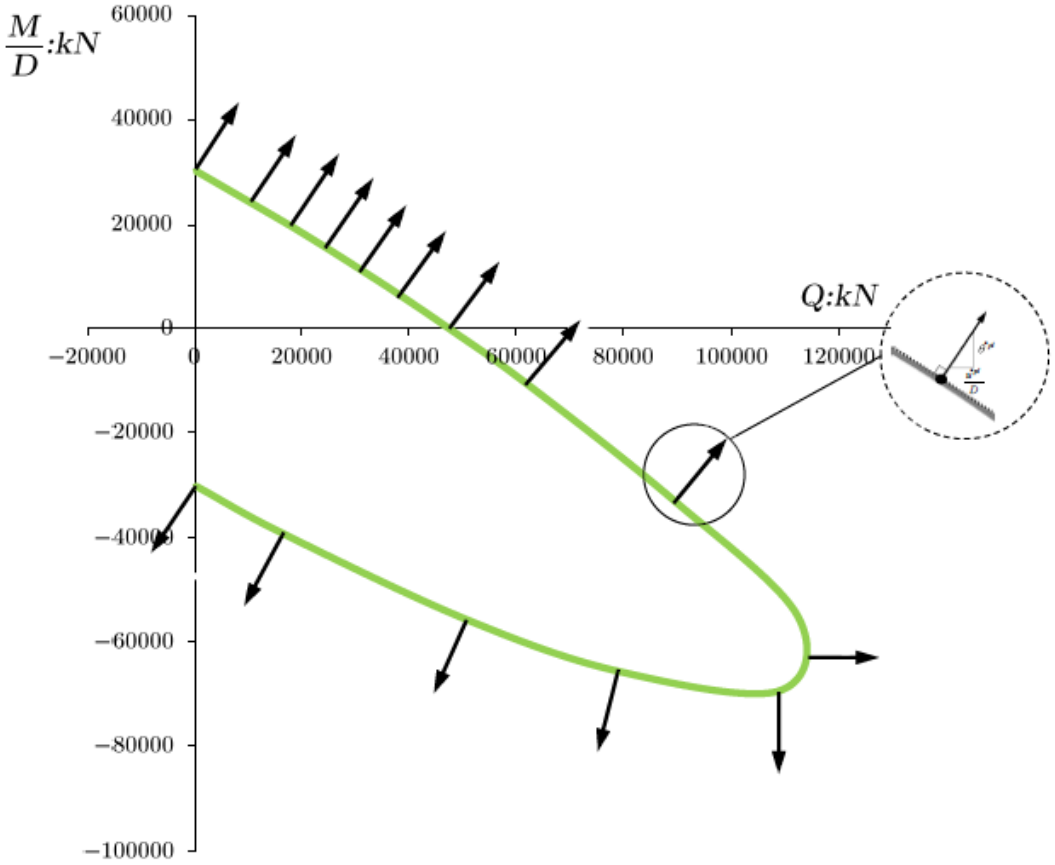

Figure 4.7 *The incremental plastic displacement vectors at the point of failure appear to be normal to the yield locus confirming the validity of the associative flow rule.*

CHAPTER 5
Calibration of the BWGG Model

5.1. Introduction

A series of numerical experiments of lateral monotonic and cyclic static loading of caisson foundations are carried out, which serve as the basis for the calibration of the BWGG Winkler model. We are especially interested in the calibration of ultimate resistance, hardening and strength degradation parameters as described in the previous chapter. As in the macroscopic approach preceded in *Chapter 3*, we study the problem of rigid square foundations of multiple embedment ratios in a homogenous undrained clay layer of S_u *= 50 kPa* and E_s *= 50 MPa,* in which the caisson is considered rigidly connected to the surrounding soil. The BWGG Winkler model is formulated in Matlab and a robust calibration methodology is developed.

The work of Gerolymos and Gazetas [*2006b*] is adopted as far as the elastic response is concerned. In our initial approach to the problem in terms of strength, we soon discover an incapability of the model that leads us to diverge from the original definition of constant (with respect to the load angle) ultimate resistance parameters. We establish a "hybrid" calibration method based on surface stress integration from the numerical analysis and a dual force-displacement curve fit with the help of sophisticated optimization techniques. Analytical expressions are determined for the resistance parameters and neural networks are trained for the hardening parameters.

Finally the model's capability of capturing the lateral response of caisson foundations is validated in multiple aspects (force-displacement curves, failure envelopes, swipe tests, soil reactions, etc.) and we provide relevant design considerations. The model's major deficiencies our outlined and recommendations are given for further calibration.

5.2. Elasticity

5.2.1. Initial Elastic Stiffness

The stiffness of the distributed lateral and the rotational springs is derived through an approximate calibration method described by Gerolymos et al. as stated in *Chapter 4*. The complex dynamic stiffness of arbitrarily shaped embedded foundations determined by Gazetas et al. (***Eq. 4.19***) is modified to account for square plan caisson foundations and its diagonal terms are equated with those of the model's stiffness matrix (***Eq. 4.16***), checking that the resulting cross-coupling term of the latter is similar to its respective term. The static horizontal and rocking stiffness of the base in (***Eq. 4.16***) is similarly derived from the analytical expressions of Gazetas et al. where the embedment effect is not taken into account. The above methodology yields the following stiffnesses for the distributed springs:

$$k_x = 2.18\left(\frac{D}{B}\right)^{-0.13} E_s \qquad \textbf{(5.1)}$$

$$k_\theta = 1.20\left(\frac{D}{B}\right)^{-1.71} E_s D^2 \qquad \textbf{(5.2)}$$

As will be displayed later on in this chapter, this approach may lead to discrepancies in the elastic response of a foundation in the case where the rocking-translational coupling is considerable. The load path to maximum horizontal capacity is an illustrative example of such a case. This problem may only be solved by adding a third type of spring accounting for this cross-coupling effect, depriving, however, the model of its direct physical interpretation.

5.2.2. Effect of plastification due to vertical loading

A series of numerical analyses were carried out in order to determine the effect of the initial plastification due to vertical loading to the lateral elastic response of caisson foundations. This effect is taken into account in a simplified way through an equivalent reduction of the soil's modulus of elasticity *Es*. As ***Figure 5.1*** suggests, a mean curve was fitted to the numerical results derived from various embedment ratios and load angles, ultimately yielding:

$$E_s/E_s^* = (1-\chi^3)^{1.5} \qquad \textbf{(5.3)}$$

5.3. Ultimate resistance and hardening parameters

5.3.1. Model assumptions

Given that we consider a soil profile of uniformly distributed undrained shear strength, it is fairly reasonable to assume both a lateral soil resistance p_y and a resisting moment per unit depth m_ϑ that are uniformly distributed as well. Despite the fact that, even in this case, the embedment has been shown to introduce an increasing soil resistance profile, this effect was not taken into consideration herein. In other words, this model adopts the mean soil reaction as the local one. Using simple dimensional analysis we conclude that the ultimate resistance parameters can be expressed as:

$$p_y = \alpha S_u B \qquad \textbf{(5.4)}$$

$$m_y = \beta S_u B^2 \qquad \textbf{(5.5)}$$

$$Q_{by} = \gamma S_u B^2 \qquad \textbf{(5.6)}$$

$$M_{by} = \delta S_u B^3 \qquad \textbf{(5.7)}$$

Figure 5.2 provides an outline of the model where the above consideration for the ultimate resistance parameters is taken into account. In the sake of clarity, only the hysteretic component (major in static loading) of the reactions is illustrated.

A time-consuming yet rigorous methodology is provided, however, for the purpose of defining the actual distribution of p_y with depth and is illustrated in ***Figure 5.3.***

The applicability of the assumption made in the first paragraph is validated in ***Figures 5.4 a)*** and ***b)*** showing the distribution of the lateral soil reaction and the resisting moment along the depth of the caisson for each of the mechanisms involved as well as their total values, as derived from surface stress integration in the case of a laterally loaded deeply embedded caisson foundation (*D/B = 3*). The displayed distribution is compared with the uniform distribution adopted in the model. Except for the exhibited peaks due to stress concentration at the head and foot of the caisson, the lateral soil reaction and the resisting moment per unit depth may be safely represented by an equivalent uniform distribution.

Our ultimate goal is to determine the effect of various parameters to the values of *α, β, γ* and *δ*. We initially expect that these parameters are only affected by the factor of safety against vertical loading FS_V. Specifically, the ultimate resistance parameters are expected to decrease along with the FS_V accounting for the effect of the initial plastification due to vertical loading on the lateral response of the foundation. Note that *γ* and *δ* are generally a function of the FS_V of the caisson's base rather than the overall FS_V; yet in this simplified approach, these parameters will be determined with respect to the overall FS_V. Insight into the problem will later reveal that the major 3D effects governing the response of caisson foundations render the ultimate resistance parameters functions of the embedment ratio and even the loading path -in the case of p_y.

Similarly, we aim to determine the effects of the above parameters to the value of the hardening parameters n_x, n_r. As part of this approach, the post-yielding stiffness parameters have been set $a_x = a_r = 0$, since the system itself seems to be introducing post-yielding stiffness.

5.3.2. Outline of the calibration method

Initially, a series of swipe tests were carried out in order to determine the model's capability of capturing the shape of the yield locus, using the values of the ultimate resistance parameters proposed by Gerolymos et al. for the case cylindrical caisson foundations:

$$p_y = 8S_u B \quad \textbf{(5.8)}$$

$$m_y = S_u B^2 \quad \textbf{(5.9)}$$

$$Q_{by} = \frac{\pi}{4} S_u B^2 \quad \textbf{(5.10)}$$

$$M_{by} = \frac{2\pi}{5} S_u B^3 \quad \textbf{(5.11)}$$

Despite the fact that we deal with square plan caisson foundations, this initial consideration allows us to properly evaluate the model's capabilities in the above aspect. ***Figure 5.5*** compares the yield locus determined in the case of a deeply embedded (*D/B = 3*) foundation, using our model and the above constant values, to the actual yield surface of the same foundation as derived from FE analyses. In the latter, an $FS_V = \infty$ is considered. It is evident that constant values of the resistance parameters cannot effectively capture the expansion of the yield surface.

This observation leads us to establish a robust calibration method in which all 6 parameters are evaluated against various embedment ratios, factors of safety against vertical bearing capacity failure as well as load angles. Evaluating the weight of the above effects on each parameter, we aim to produce simple yet effective analytical expressions able to be incorporated in the model.

For each of three characteristic embedment ratios (*D/B = 1, 2, 3*) and 6 inverse factors of safety against vertical loading $\chi = 0, 0.2, 0.3, 0.5, 0.7, 0.9$, force-controlled FE analyses are carried out using the models described in *Chapter 2* of this thesis sweeping the yield surface at characteristic points (***Fig. 5.6***). The horizontal force – head displacement and moment – rotation curves are deduced and the equivalent Winkler model curves are fitted to them through an optimization procedure established in

Matlab (***Fig. 5.7***). The initial approach was a 6-parameter optimization (4 strength and 2 hardening parameters), but was soon modified on the basis of two major observations:

- This is a highly nonlinear optimization problem that requires to be appropriately constrained by setting upper and lower boundaries at least for the ultimate resistance parameters.
- The contribution of the base does not exceed *10 %* of the overall response, in the case of deeply embedded foundations, which leads to unsatisfying results regarding Q_{by} and M_{by}. In other words, the *γ* and *δ* terms of the solution display high variability.

In order to address these two problems, we modify our approach to a 4-parameter optimization (*α, β, n_x, n_r*), while the ultimate base shear and moment resistance is derived from surface stress integration, which is described further below. The latter is also used to provide the upper and lower boundaries for the lateral soil reaction as well as the resisting moment per unit depth. This method adequately simplifies the problem so that Matlab converges to the optimum solution fairly easily all along the yield surface. The fit is then verified in terms of head displacement – rotation response.

Ultimately, the proposed method is considered a hybrid method for it effectively combines direct physical interpretation of the soil reaction (stress integration) with a purely mathematical approach (dual curve fit) to the problem.

5.3.3. Stress integration

For the purposes of determining *a)* the base ultimate shear and moment reaction and *b)* the boundaries of the lateral soil reaction and the resisting moment per unit depth, normal and shear stresses derived from the numerical analyses are rigorously integrated. After identifying the components of each type of soil reaction, the integration technique is presented and evaluated.

5.3.3.1. Lateral soil reaction

The lateral soil reaction p_x involves two distinct mechanisms:

- The passive and active pressures developed on the two sides transverse to the loading plane and
- The horizontal shear tractions on the sides longitudinal to the loading plane.

Both mechanisms are presented in Figures ***5.8 a), b)*** and ***5.9 a)***, ***b)***, which illustrate the distribution time histories of the passive and active pressures on the sides transverse to the loading plane, as well as those of the horizontal shear tractions on the sides longitudinal to the loading plane for two distinct radial load paths (on the 1st and 2nd quadrant of the yield surface). The passive and active soil pressures represent the primary resisting mechanism accounting for approximately 90% of the lateral soil reaction, while the sidewall horizontal shear accounts for the remaining 10%. Even in the case of the extensive passive soil pressure, a uniform plateau is evident, justifying once again the assumptions of our model. This is even more evident in the horizontal shear tractions.

The stress components of the lateral soil reaction are vectorially summed and their absolute values are calculated. The latter are then subjected to rigorous surface integration, from which the mean lateral soil reaction is deduced. ***Fig. 5.10*** presents the mean lateral soil reaction vs the horizontal displacement at the caisson head in dimensionless terms, where the formation of a plateau is evident. The value at the plateau corresponds to the dimensionless ultimate mean lateral soil reaction, namely α.

Note that the ultimate lateral soil reaction as defined above deviates from its conventional definition as the passive soil reaction. Active pressures and possible soil failure are taken into account in this approach.

5.3.3.2. Resisting moment per unit depth

Similarly, the resisting moment m_θ involves three distinct mechanisms:

- The moment generated by the vertical shear tractions developed on the two sides transverse to the loading plane, with a lever arm of length *B*
- The moment generated by the vertical shear tractions developed on the sides longitudinal to the loading plane and, with a lever arm varying in length (approximately *0.5B*)
- The moment generated by the horizontal shear tractions on the sides longitudinal to the loading plane (contributing to the lateral soil reaction as well).

Figures ***5.11 a), b)*** and ***5.12 a), b)*** illustrate the distribution time histories for the vertical shear tractions developed on the sides transverse and longitudinal to the loading plane respectively, for the two distinct radial load paths mentioned above. As part of our simplified stress integration approach, the horizontal shear tractions on the sides longitudinal to the loading plane are accounted only for their contribution to the lateral soil reaction.

They shear tractions are similarly subject to surface integration and the mean vertical shear resistance per unit depth τ_y is determined. For the total shear stress (derived from the two mechanisms described), we assume a "mean" lever arm *l = 0.8·B,* ultimately yielding a resisting moment per unit depth:

$$m_y = \tau_y \cdot 0.8\, B = \beta S_u B^2 \qquad \textbf{(5.12)}$$

Fig. 5.13 presents the mean resisting moment per unit depth vs the rotation of the caisson in dimensionless terms. In contrast to the mean lateral soil reaction, the mean resisting moment exhibits softening behavior. The normalized ultimate mean resisting moment per unit depth *β* is identified as the peak of the curve.

The low density of the FE mesh along with several simplifying assumptions made in the process requires that the accuracy of the integration in terms of lateral response is verified. ***Figure 5.14*** illustrates the remarkable fit of the soil reaction curve to the externally applied horizontal moment and force for a caisson foundation subject to a

radial loading path on the 1st quadrant of the *M-Q* plane. The accuracy of the integration scheme is validated.

This process is repeated for every considered embedment ratio, factor of safety against vertical bearing capacity failure as well as load path, in order to supply the optimization procedure with appropriate upper and lower boundaries. In fact, α,β serve as the mean values on which a 20% deviation is applied to yield the above boundaries for each case.

5.3.3.3. Base resistance

A similar methodology is applied in order to determine the ultimate shear and moment resistance of the base. Figures ***5.15 a), b)*** illustrate the distribution time history of the shear tractions developed at the base of the caisson for the two radial load paths considered herein. In the next figure (***5.16***), the normalized mean base shear resistance is given with respect to the displacement of the base in dimensionless terms. The ultimate base shear resistance is deduced at the point where the curve exhibits its peak. As with the shear tractions at the sidewall, we observe a softening behavior.

In the same fashion, Figures ***5.17 a), b)*** present the distribution time history of the normal pressures developed at the base of the caisson for the two radial load paths and the mean base shear resistance as a function of the base displacement respectively. In the next figure (***5.18***), the normalized base moment resistance is given with respect to the rotation of the base in dimensionless terms. The ultimate base moment resistance is deduced at the point where the curve exhibits its peak.

In the sections ***5.3.5*** and ***5.3.6*** the results are analyzed in detail and analytical expressions are deduced.

5.3.4. Optimization

This nonlinear optimization problem was addressed with the use of a hybrid algorithm, incorporating a genetic algorithm and a constrained minimizing function of Matlab. In fact, the former is utilized in order to locate the global minimum and in a second step, the latter captures the optimum solution, as visualized in ***Figure 5.19*** for an equivalent 3-dimensional problem. Choosing the most efficient goal function and the right parameters of the genetic algorithm's structure (initial population, generations, mutation, migration and crossover) is of great importance in order to efficiently solve the problem. As stated previously, the minimizing function refers to the distance between the FE curve and the equivalent Winkler model one. The square root of the summed squares of the differences in the ordinate (horizontal force or moment) corresponding to an appropriately gridded abscissa (head displacement or rotation) was found to be fairly effective. In the case of pure horizontal force or pure moment application, the dual curve fit involved the equivalent displacement – rotation curves except for the horizontal force–head displacement or moment rotation curve respectively.

Various structure characteristics were utilized, before concluding to a 120-individual initial population, 80-generation-limited, adaptive-mutation, back-and-forth-migration, heuristic-crossover approach that could effectively solve the problem. In addition, a pareto-front multi-objective optimization was carried out in order to ensure that the group of solutions was adequately narrow - so that no significantly different combination of the values of the 4 parameters could lead to an equally well-fitted curve. We ensured the good fit by accepting a solution to the optimization problem that provides a goal function value below an acceptable limit. For five characteristic force-controlled load paths along the yield surface (***Fig. 5.20***) of a deeply embedded caisson foundation ($D/B = 3$) under a factor of safety of $FS_V = 5$, ***Figures 5.21 a) – e)*** illustrate the dual curve fit accomplished with the above methodology. The result is satisfactory in every case with the exception of some minor discrepancies in cases *c)* and *d)*. Specifically, in the former case the model fails to capture the marginally negative trend for the head displacement, while in the latter it underestimates the initial elastic

stiffness. This is due to the increased translational-rotational coupling at this delicate point.

5.3.5. Results

In this section, we analyze the general trends that were derived through our hybrid optimization approach for the strength as well as the hardening parameters in respect to the embedment ratio, the factor of safety against vertical loading and the load angle.

5.3.5.1. Lateral Soil Reaction

Figure 5.22 illustrates the normalized ultimate lateral soil reaction α in respect to the load angle, expressed as M/QD, for the case of a $D/B = 2$ caisson foundation characterized by an inverse factor of safety against vertical loading of $\chi = 0.2$. Parameter α does not remain constant with respect to the load angle, but rather forms a "bell" curve exhibiting its peak at the load angle corresponding to maximum horizontal capacity. This exhibited variability suggests that the ultimate lateral soil reaction should no longer be considered an invariant in the case of caisson foundations, as opposed to pile foundations, due to the enhanced 3-D effects.

In order to validate the above assumption, it is required that we check any simplifications in our model that could have led to the displayed variability of α, the most significant being the adoption of a uniform soil resistance profile. Since α seems to increase in order to effectively capture the expansion of the yield surface, we equivalently seek such a lateral soil reaction and resisting moment profile that could yield the entire failure locus with their ultimate values being constant.

An extensive series of swipe tests are carried out in order to deduce the normalized failure envelopes of deeply embedded caisson foundations ($D/B = 3$) under a parametrically investigated lateral soil reaction and resisting moment profile expressed as:

$$p_y = \left[a_1 + \alpha_2 (\frac{z}{D})^{a_3}\right] S_u B \qquad \textbf{(5.13)}$$

and

$$m_y = \beta \cdot \left[a_1 + \alpha_2 (\frac{z}{D})^{a_3}\right] S_u B^2 \qquad \textbf{(5.14)}$$

We make the reasonable simplifying assumption that the shape of the profile is the same for p_y and m_y, thus limiting the number of parameters under investigation to four. ***Figures 5.23 a) – c)*** illustrate the effect of the above parameters on the shape of the yield surface as compared with the latter being derived from FE tests. Figures *a)* and *b)* illustrate the effect of the magnitude of the increase and the shape of the soil resistance profile respectively on the shape of the yield locus. Both figures imply that an increasing ultimate soil reaction profile does not necessarily capture the expansion of the yield surface better than a uniform one, while the differences observed are not significant. Figure *c)*, on the other hand, serves to provide the magnitude for the resisting moment in respect to the lateral soil reaction.

Based on the above, we conclude that the "uniform soil profile" simplification of our model cannot account for the increasing lateral soil reaction observed as we approach the over-strength region. In fact, it seems that in this region the translational-rotational cross-coupling is of considerable magnitude and that a two-spring model is not able to realistically simulate the response unless provided with a suitable coupling law. We assume that this problem is solved by adding a third type of spring – a translational-rotational coupling one – that can account for this effect. This would deprive, however, the model of its direct physical interpretation. Thus, we are led to implicitly provide such a coupling by considering the major soil reaction p_y as a function of the load angle. The major 3-D effects that govern the response of caisson foundations render the ultimate lateral soil reaction no longer an invariant in a two-spring model.

In the following graphs that involve the load angle *M/QD*, its values are restricted to the range *(-20, 20)* as this captures about *98%* of the yield locus, which of course is symmetric about *(M, Q) = (0, 0)*. This way we can focus on the interesting areas of the scoop-slide, the pure sliding, as well as the reverse scoop mechanism. Theoretically, *M/QD* reaches *+/-* ∞ (pure moment), but the value of the ultimate lateral soil reaction at pure moment application are evident early from *M/Q·D = +/- 20*.

Figure 5.24 illustrates the effect of the factor of safety against vertical bearing capacity on the ultimate lateral soil reaction. As expected, p_y decreases with increasing χ (decreasing FS_V) accounting for the plastification taking place in the soil surrounding the caisson, which serves to limit its margin for resistance. As χ reaches 1, p_y is nullified, whereas for values of χ less than *0.3,* α appears to be stabilizing. A more thorough investigation of the effect of the vertical factor of safety on the ultimate lateral soil resistance is provided in the section of the analytical representation of the results (**5.3.6**).

The 3-D effects that have led p_y to diverge from its conventional definition as an invariant vary with the embedment ratio, which makes it evident that the former may also be a function of *D/B*. ***Figure 5.25*** illustrates the effect of the embedment ratio on the ultimate lateral soil reaction. As the embedment ratio decreases, the ultimate lateral soil reaction decreases at the plateau (pure moment) and displays an enhanced variability with the load angle. In addition, it suffers a loss of symmetry with respect to the pure sliding point. The above are evidence of enhanced 3-D effects as the embedment ratio decreases. As will be shown in the analysis of the resisting moment per unit depth further below, the latter exhibits the opposite trend; m_y increases with *decreasing D/B* ultimately acquiring approximately the same value with p_y in the case of a cubic caisson, implying that the two mechanisms are of equal importance in that case!

In the magnified region of the same figure, note also the effect of *D/B* on the position of the pure sliding point in terms of *M/QD*. The latter tends to move to absolutely greater load angles as D/B increases. Finally, the last effect that *D/B* introduces to the ultimate lateral soil resistance is a widening of the bell curve, a fact that will be investigated further below (**5.3.6**).

5.3.5.2. Resisting moment per unit depth

Figure 5.26 illustrates the normalized ultimate resisting moment per unit depth β in respect to the load angle *M/QD*, for the case of a *D/B = 2* caisson foundation and three characteristic values of the factor of safety against vertical loading. As with the

ultimate lateral soil reaction, the ultimate resisting moment per unit depth does not remain constant with respect to the load angle; yet forms an inverse "bell" curve similarly exhibiting its lowest point at the load angle corresponding to maximum horizontal capacity. Note, however, that θ exhibits a significantly smaller variability with respect to the load angle, a fact that will be exploited later on in the analytical representation of the ultimate resistance parameters.

As expected, m_y decreases with increasing χ (decreasing FS_V) accounting for the plastification taking place in the soil surrounding the caisson, which serves to limit its margin for resistance. As χ reaches 1, m_y is nullified, whereas for values of χ less than *0.3,* θ appears to be stabilizing.

Figure 5.27 illustrates the effect of the embedment ratio on the ultimate resisting moment per unit depth. In accordance with the lateral soil reaction, as the embedment ratio decreases, the ultimate resisting moment decreases at the plateau (pure moment) and displays an enhanced variability with the load angle. In addition, it suffers a loss of symmetry with respect to the pure sliding point. The above are evidence of enhanced 3-D effects as the embedment ratio decreases. However, m_y exhibits the opposite trend regarding the embedment ratio; it increases with decreasing *D/B* accounting for the enhanced contribution of the shear tractions at the sides transverse to the loading plane in the overall response.

5.3.5.3. Base resistance

Figures 5.28 and ***5.29*** present the normalized ultimate horizontal and moment resistance of the caisson's base versus the load angle *M/QD* for multiple values of the factor of safety against vertical loading. These are derived from direct stress integration in Abaqus in the case of a deeply embedded (*D/B = 3*) caisson foundation. Apparently, the two base ultimate capacities exhibit opposite trends with respect to the system's load angle *M/QD.* The horizontal capacity displays its minimum value (essentially nullified) at the load angle where the inverted pendulum mechanism is deployed. At the same point, the moment capacity takes its maximum value, considering the quadratic yield function of an equivalent surface foundation in *M-Q* terms. Similarly, at the point

where the pure sliding (or diffusive mechanism) is unveiled, the horizontal capacity is maximized while moment capacity is minimized (essentially nullified). The dotted lines (mean values) represent possible design values of the above in the case where they are considered uncoupled.

Figure 5.30 qualitatively correlates the previous figures with the *M-Q* failure envelope of the base for the equivalent factors of safety against vertical loading referring to the caisson's base. As the figure suggests, the overall and the base factor of safety against vertical loading are correlated through the embedment ratio *D/B*. The next section (***5.3.6***) provides such a correlating law. The dotted lines represent the simplified uncoupled horizontal and moment capacities that could be adopted, as a simplified approach.

Considering the fact that the base contributes to small percentage to the overall response (approximately 10% for *D/B = 3* and up to 40% for *D/B =1*), the horizontal and moment base capacities may indeed be considered uncoupled with no considerable loss of accuracy especially for caisson foundations with embedment ratios greater than 1.2. A different approach would require the incorporation of a shallow foundation "macro-element" in the model, and would be suitable for shallow embedment foundations (*D/B < 1.2*).

5.3.5.4. Hardening parameters

Figures 5.31 and ***5.32*** present the hardening parameters n_x and n_r of the translational and rotational springs respectively versus the load angle *M/QD* for multiple values of the factor of safety against vertical loading and three embedment ratios considered herein. The two hardening parameters exhibit approximately the same complex behavior with respect to the three variables.

For the lightly loaded systems, the values of the hardening parameters decline as the loading approaches maximum horizontal capacity either way. While being considerable for deeply embedded foundations, this decline appears to be negligible in the case of the *D/B = 1* foundation. The correlation to the developed soil resisting

mechanism is evident. In the diffusive mechanism (deep embedment), the response of the caisson is unable to reach a plateau due to the participation of an ever increasing part of the surrounding soil to the resisting mechanism, hence the sharp increase in p_y and the sharp decline in n_x -n_r. In fact, at that point, the system exhibits great post-yielding stiffness, but since the post-yielding parameters are considered constant, the hardening parameters are burdened instead. On the other hand, In the case of the sliding mechanism (shallow embedment) the response suggests a considerably less coupled elasto-plastic behaviour, due to the formation of a shear band.

As the vertical aspect of loading increases, the value of the hardening parameters appears to decrease. Beyond a characteristic value of $\chi \approx 0.4\text{-}0.5$, they respond differently with regard to the load angle as a result of enhanced soil plastification. Regarding the effect of the embedment ratio, no clear trend is visible except for the decline in the values of the hardening parameters in lightly loaded shallow embedded systems.

5.3.6. Analytical expressions

The observed trends in the above parameters allow us to assume suitable forms of functions able to capture their basic trends, and then subject them to multivariate regression analysis. This, however, was possible only in the case of the ultimate resistance parameters, whereas the highly nonlinear nature of the hardening parameters with respect to *M/QD*, FS_V and *D/B* left no option but to train appropriate neural networks, as will be displayed in the next section.

5.3.6.1. Lateral Soil Reaction

The normalized lateral soil reaction $\alpha = \frac{p_y}{S_u B}$ has been shown to approximately follow a modified Gaussian distribution with respect to the load angle *M/QD* as shown below:

$$\alpha = \alpha_1 + \alpha_2 \cdot e^{-\frac{\left|\frac{M}{QD}-\alpha_3\right|^{0.7}}{{\alpha_4}^{0.7}}} \quad \textbf{(5.15)}$$

where parameters a_1, a_2, a_3, a_4 control the variability of the lateral soil reaction in respect to the load angle, the vertical factor of safety and the caisson's embedment ratio.

In fact, correlating α to the load angle indirectly accounts for the translational-rotational coupling, which is shown to increase as the loading approaches maximum horizontal capacity. Each of the parameters of (***Eq. 5.15***) has a physical interpretation and a direct correspondence to the *M- Q* failure envelope.

In particular:

- a_1 accounts for the normalized ultimate lateral soil reaction as the load angle approaches pure moment
- a_2 controls the variability of the lateral soil reaction in respect to the load angle in order to account for the developing over-strength
- a_3 captures the change in the load angle where maximum horizontal capacity is exhibited (peak value of α)
- a_4 controls the width of the Gaussian curve and hence the width of the over-strength region

The adoption of (***Eq. 5.15***) for α means that each of the above parameters may be calibrated independently as will be explained below.

Parameter a_1

Regardless of the embedment ratio or the vertical factor of safety, the ultimate lateral soil reaction is shown to acquire its minimum value α_1 as the load angle approaches pure moment. Regression analysis has yielded the following complex function of *D/B* and χ given below:

$$\alpha_1 = (3.49 ln\frac{D}{B} + 2.77)(1 - x^{-0.45\left(\frac{D}{B}\right)+4.33}) \quad \textbf{(5.16)}$$

Fig. 5.33 a) illustrates how the above analytical expression effectively captures the values of α_1 derived from the hybrid optimization. This strength parameter

decreases with decreasing embedment ratio in a logarithmic fashion and, for $\chi > 0.3$, starts to decline in a power fashion. Note that the embedment ratio seems to slightly affect the degradation of α_1 with χ. Ultimate resistance parameter α_1 may be identified somewhat as the microscopic analog of M_u (***Eq. 3.2***), since the lateral soil reaction is the major resistance mechanism (at least in deeply embedded foundations).

Parameter α_2

Parameter α_2 controls the magnitude of the increase in the ultimate mean lateral soil reaction at the point of maximum horizontal capacity. Regression analysis has rendered it to be a function of the embedment ratio and the vertical factor of safety:

$$\alpha_2 = 3.723\left(\frac{D}{B}\right)^{-0.916}\left(1+\frac{D}{B}\right)^{1.026}(1-x^{3.2}) \qquad \textbf{(5.17)}$$

Fig. 5.33 b) illustrates how the above analytical expression effectively captures the values of α_2 derived from the hybrid optimization. In contrast with α_1, this strength parameter increases with decreasing embedment ratio and declines more sharply with respect to χ. The increased variability of α in the case of the *D/B = 1* caisson are attributed to the enhanced 3-D effects governing the response. Ultimate resistance parameter α_2 may be seen as the microscopic equivalent of n_3 (***Eq. 3.17***) controlling the expansion of the yield locus.

Parameter α_3

Through our numerical experiments it has been found that the load angle that represents maximum horizontal capacity varies with the embedment ratio while remaining fairly constant with respect to the factor of safety against vertical loading. The analytical expression that governs the alternating position of the Gaussian peak is given by:

$$\alpha_3 = -0.07\ln\left(\frac{D}{B}\right) - 0.5 \qquad \textbf{(5.18)}$$

Fig. 5.33 c) illustrates this change in the load angle and compares it to the analytical expression proposed. Even though this change may seem negligible, the high variability of α in that region requires that it is incorporated in the model. This parameter has no obvious correlation to the macroscopic behavior of caisson

foundations. Note that this change in the position where the maximum horizontal capacity is exhibited does not imply a rotation of the curve when given in normalized ($M/M_u - Q/Q_u$) but rather in modified $M/D - Q$ terms.

Parameter α_4

Parameter α_4 captures the exhibited increase of the Gaussian curve's width as the vertical aspect of loading increases and as the embedment decreases. In fact, α_4 was determined in order to achieve the overall fit of the numerical data to the Gaussian curve. The following expression was deduced:

$$a_4 = 3\left(\frac{D}{B}\right)^{-0.394}\left(1+\frac{D}{B}\right)^{-0.481}(-0.66\chi^3 + 0.965\chi^2 - 0.068\chi + 0.268) \qquad \textbf{(5.19)}$$

and is plotted in ***Fig. 5.33 d)***. Examining it in macroscopic terms, this parameter captures the change in the shape of the yield surface in "cooperation" with α_2.

Finally, the overall fit to the values of the normalized mean lateral soil reaction is validated in ***Fig. 5.34*** for two limit values of the embedment ratio and two characteristic values of the inverse factor of safety against vertical loading considered. Except for the small asymmetry of the negative branch of the curve, the analytical expression appears to have captured the optimization data satisfactorily.

5.3.6.2. Resisting moment per unit depth

As previously discussed, the normalized ultimate resisting moment per unit depth $\beta = \frac{m_y}{S_u B^2}$ exhibits a limited variability with the load angle $\frac{M}{QD}$ as compared to the great variability of α. Especially, in the case of deeply embedded caisson foundations, this variability is limited to a mere *25%* in a fairly narrow load path region. It is only in the case of *D/B = 1* that this variability increases due to enhanced 3D effects. This observation led us to adopt the asymptotic values (corresponding to pure moment) as constant throughout the yield locus in favor of the simplicity of the model. Regression analysis, with respect to the remaining two variables, FS_V and *D/B*, that affect the ultimate resisting moment yielded the complex expression:

$$\beta = 1.031\left(\frac{D}{B}\right)^{-1.368}\left(1+\frac{D}{B}\right)^{1.792}(1-\chi^{1.96+0.64\frac{D^{-1.4}}{B}}) \qquad \textbf{(5.20)}$$

Fig. 5.35 presents the ultimate resisting moment per unit depth for the three embedment ratios as derived from the hybrid optimization method and validates the expression's capacity of capturing β. As expected, the difference between *D/B = 1* and *2* is considerably greater than between *D/B = 2* and *3*, as a result of the enhanced 3D response of shallow embedded foundations. The decline of β with respect to χ is similar to the decline of α_1.

Fig. 5.36 compares the normalized ultimate lateral soil reaction at its plateau (α_1) and the ultimate resisting moment per unit depth both under zero vertical loading component with respect to the embedment ratio. The intersection at *D/B = 1.2* reminds us of the categorization given in *Chapter 3* on the basis of the yield surface expansion behavior. Here, we introduce a different kind of categorization of the embedded foundations based on the contribution of the lateral soil reaction and the resisting moment per unit depth. We assume that in deeply embedded foundations the response is governed by the lateral soil reaction rather than the resisting moment (derived from the shear tractions at the sidewall). In shallow foundations the contribution of the two resistance components is reversed, whereas in pile foundations shear tractions are negligible and the ultimate lateral soil reaction reaches a plateau.

5.3.6.3. Base Resistance

As explained before, this model adopts uncoupled horizontal and moment capacities for the caisson base with no significant loss of accuracy overall, for embedded foundations of *D/B > 1.2*. These are given as functions of the overall factor of safety against vertical bearing capacity failure and the embedment ratio as follows:

$$Q_{by} = 0.822\left(\frac{D}{B}\right)^{-0.331}\left(1+\frac{D}{B}\right)^{0.312}(1-\chi^2) \qquad \textbf{(5.21)}$$

$$M_{by} = 0.836\left(\frac{D}{B}\right)^{-0.892}\left(1+\frac{D}{B}\right)^{-0.255}(1-\chi^{1.9})^{1.2} \qquad \textbf{(5.22)}$$

The expressions are plotted in ***Figures 5.37*** and ***5.38***. While the two capacities follow a similar law with respect to χ, the embedment ratio affects the ultimate moment capacity to a far greater extent. In these expressions, the embedment ratio serves to correlate the overall factor of safety of the caisson with the factor of safety of the caisson's base, while also accounting for the confinement introduced. This a simplified approach, that is viable only in cases where the contribution of the base is small enough to minimize the error.

5.3.7. Neural networks

5.3.7.1. Theoretical basis

A neural network is a mathematical model inspired by biological neural networks and is generally used to recognize patterns in data. Such a network consists of at least three layers: *(a)* the *input layer* that receives input data in the form of a matrix and passes the information to the network for processing, *(b)* the *hidden layer* which is a layer of neurons that receives information from the input layer and processes it in a hidden way to the posterior hidden layer or to the out layer, and *(c)* the *output layer* that receives processed information and produces the response of the system.

Each layer has a weight matrix, *w*, a bias vector, *b,* and an output vector, *y.* Each element of the input vector, *x,* is connected to each neuron input through the weight matrix, *w.* The neuron output, *o*, is a scalar number; it is a nonlinear function (known as the *transfer* or "*activation*" function) of the sum of the outputs of all neurons in the most anterior layer (the neuron input net):

$$o_j(net_j) = f\left(\sum_i w_{ij}x_i + b_j\right) \qquad \textbf{(5.23)}$$

The effectiveness of a neural network to simulate highly non−linear problems is partially attributed to the transfer function used for processing the output of a neuron.

There are several types of transfer functions, the appropriate choice of which depends strongly on the nature of the problem and the type of employed neural network. In our case, the powerful hyperbolic tangent was utilized as a transfer function together with a back-propagation learning rule.

Supplying the neural network with sufficient input data, the former is trained by repeatedly applying as much as 75% of the input data and calculating errors with respect to the difference between the target and the output vectors. The weight and bias of each neuron in the network is then updated with the learning rule after each training cycle / "epoch". This procedure is repeated until the network error falls beneath an error goal, or a maximum number of epochs have occurred.

After the training, the neural network is validated and tested for the remaining 25% of the data. In this step, the network's ability to capture the existing patterns and generalize for new input data is confirmed. Besides the above validation, the efficiency of the network is about to be tested as part of the whole model.

5.3.7.2. Representation of the hardening parameters

The highly nonlinear nature of the hardening parameters n_x and n_r, as displayed in ***Fig. 5.31*** and ***5.32***, renders it extremely difficult to deduce analytical expressions that can accurately fit the numerical data. Hence, we are led to train two separate neural networks for each of the hardening parameters, which are then called into the Winkler model code. Using Matlab's neural networking tool, we supply a sufficiently large number of hardening parameter data derived from the optimization approach and test the network's ability to capture the basic hardening trends as well as generalize. The basic architecture of the multilayer neural network developed is shown in ***Fig 5.39***. The input data involve the load angle, the factor of safety against vertical loading and the embedment ratio, while the output is of course one of the hardening parameters for each network. The results of the tests revealed a correlation coefficient $R = 0.98$ for n_x and $R = 0.91$ for n_r, which implies that the network managed to recognize the majority of the patterns lying behind the values of the hardening parameters.

5.3.8. Validation

After determining the ultimate resistance and hardening parameters as explained throughout the previous sections of this chapter, the final calibrated Winkler model for the monotonic lateral loading of caisson foundations is formulated. In the following sections, the model's capability of capturing the macroscopic response of deeply embedded foundations is validated in terms of:

- "Force-displacement" curves and
- Interaction diagrams (swipe tests)

After the validation in macroscopic terms, some indicative soil reaction profiles derived from the calibrated model are presented and compared to those derived from the FE analyses.

5.3.8.1. "Force-displacement" curves

Figures 5.40 – 5.48 compare the horizontal force – head displacement and moment – rotation curves derived from 3D FE analyses with those produced by the Winkler model. Three embedment ratios (*D/B = 1/2/3*) and three factors of safety against vertical bearing capacity failure (FS_V *= 1.4, 2, 5*) are considered herein. The macroscopic behavior of the foundation is examined and compared at 4 distinct points in the yield surface:

a) a point in the 1st quadrant of the scoop slide region
b) a point in the 2nd quadrant of the scoop-slide region
c) the point corresponding to maximum horizontal capacity
d) the point corresponding to maximum moment capacity

The model appears to be able to effectively capture all aspects of the macroscopic response of caisson foundations. Regarding the elastic section of the

generalized force-displacement curves, the model compares remarkably well to the FE analyses thus validating the accuracy of Gazetas's analytical expressions and that of the approximate solution utilized herein. The only exception is perhaps the maximum horizontal capacity curve, where the enhanced translational-rotational coupling renders the approximate solution ineffective.

In regards to the ultimate horizontal and moment capacities, the model curves match equally well those derived from the FE analyses. The fit, however, gradually deteriorates as we move to more shallow embedded foundations, due to the increased contribution of the base, whose ultimate capacities are considered uncoupled. In addition, the model appears to be slightly underestimating the response in the case of small factors of safety against vertical bearing capacity, a fact that can be used as the basis for a potential recalibration of the model. Despite these discrepancies, in any of the cases considered, the ultimate capacity error did not exceed 15% lending reliability to the model.

Finally, the effectiveness of the trained neural networks is validated as to their ability to provide the right hardening aspect to the response. In the majority of the load paths considered, the model's transition to the plastic response matches well that of the FEM.

5.3.8.2. Swipe tests

A series of swipe tests are carried out in order to validate the model's capability of reproducing displacement – controlled load paths and determining the failure surface in that fashion. The fact that the major ultimate resistance parameter is expressed as a function of the load angle *M/QD* does not deprive the model of its ability to reproduce such load paths. Through a repetitive process, the model calculates the load angle at every step, which is then used to deduce the values of ultimate resistance parameters from the analytical expressions, and the values of the hardening parameters by calling the two neural networks.

Figures ***5.49 a) – c)*** illustrate the results of swipe tests for caisson foundations of three embedment ratios (*D/B = 1/2/3*) and a relatively large factor of safety against vertical bearing capacity failure FS_V = 5. The results are compared with the equivalent yield surfaces derived from FE analyses. In all cases the model exhibits remarkable ability to capture the displacement controlled response and satisfactorily outlines the yield locus.

5.3.8.3. Soil reactions

Figures ***5.50 a)*** and ***b)*** presents the lateral soil reaction and resisting moment per unit depth time-histories for a deeply embedded foundations (*D/B = 3*) subject to combined *M-Q* loading corresponding to the scoop-slide region of the yield surface. Comparing those derived from stress integration (FE analysis) and those determined by Winkler model, we conclude that the calibrated model has the potential to simulate the response of caisson foundation in a microscopic level too.

5.3.9. Cyclic loading

5.3.9.1. Investigation based on FE analyses

In this section, we shortly investigate the response of caisson foundations under static cyclic loading based on FE analyses. As before, we analyze foundations with three embedment ratios *D/B = 1,2* and *3* and two characteristic factors of safety against vertical loading FS_V *= 2, 5*, corresponding to heavily and lightly loaded systems respectively. ***Figure 5.51*** illustrates the cyclic force-controlled loading pattern applied to the head of the foundations. Specifically, a combination of horizontal force and moment corresponding to the 1st quadrant of the scoop-slide region is applied. Prior to that, as with the monotonic loading tests, the foundations are subjected to appropriate vertical load (in order to achieve the intended FS_V).

Figures 5.52 - 5.54 illustrate the horizontal force–head displacement and moment-rotation loops derived from the FE analyses for the cases explained above. Both the lightly and the heavily loaded systems exhibit hardening behavior with

decreasing rate. However, the lightly loaded systems ($FS_V = 5$) exhibit a far more symmetric response with the hardening aspect being limited to the first loading cycle. On the other, the heavily loaded systems display a considerably asymmetric response experiencing plastic shakedown involving hardening with decreasing rate.

This type of asymmetry introduced in heavily loaded systems is also evident in the case of slender sDoF systems supported by surface foundations as examined by Panagiotidou, Gazetas and Gerolymos [*2010*]. In that case, the asymmetry is attributed to the *P-δ* effect: In lightly loaded systems, the moment introduced by the weight of the superstructure is constantly in phase with the applied moment, while the foundation experiences uplift. On the contrary, in heavily loaded systems, the two moments are out of face, with the moment due to self-weight counter-balancing the applied moment, thus providing a hardening aspect to the response.

Besides the P-δ effect, there is an additional mechanism that leads to an asymmetric response in the case of caisson foundations and is related to the effect of the vertical load in the foundation system's behavior when lateral loading is reversed. ***Figures 5.55*** and ***5.56*** present time histories of the plastic strain magnitude contours in the case of a lightly loaded ($FS_V = 5$) and a heavily loaded ($FS_V = 2$) caisson foundation subject to the previous cyclic load pattern respectively. In fact the snapshots correspond to absolutely maximum applied load (peaks of loading pattern). In the case of the lightly loaded system, the first loading section leads to a rather symmetric distribution of the plastic strains in the soil surrounding the caisson. As expected, the system retains this symmetry (in fact slight asymmetry) in the next loading sections. On the contrary, in the case of the heavily loaded system, the initial plastification due to vertical loading leads to an unequal distribution of the plastic strain in the soil surrounding the caisson. In fact, plastification appears to be concentrated at the side of the direction of loading. When the loading is reversed, the system responds under totally different initial conditions. Now, the applied horizontal load has to overcome the enhanced resistance of the system since the vertical load appears to be slowing down the rate at which unloading takes place. Ultimately, the load is enough only to counterbalance this asymmetry effectively nullifying the horizontal displacement. This hardening behavior continues at

a declining rate until the surrounding soil is fully plastified, a point at which no asymmetry in the distribution of plastic strains can be observed.

5.3.9.2. Capturing the response with the Winkler model

In this section, the capability of the Winker model to capture the cyclic response of caisson foundations is investigated. In order to capture the shape of the hysteresis loops as derived from the FE analyses, it is required that we appropriately modify the Bouc-Wen equations of the lateral and translational springs.

So far, for the monotonic loading, the equations have taken the form:

$$d\zeta_x = \frac{1}{u_y}\{1 - |\zeta_x|^{n_x}[b_x + g_x sign(du\zeta_x)]\}du \qquad \textbf{(5.24)}$$

$$d\zeta_\theta = \frac{1}{\theta_y}\{1 - |\zeta_\theta|^{n_\theta}[b_x + g_x sign(du\zeta_x)]\}du \qquad \textbf{(5.25)}$$

where it was required that *b + g = 1* (the actual values of *b, g* were of no concern).

In the case of cyclic loading, these equations are generalized into:

$$d\zeta_x = \lambda_x \frac{h_x}{u_y}\left\{1 - \frac{1}{1 + r_x}|\zeta_x|^{n_x}[b_x + g_x sign(du\zeta_x)]\right\}du \qquad \textbf{(5.26)}$$

$$d\zeta_\theta = \lambda_\theta \frac{1}{\theta_y}\left\{1 - \frac{1}{1 + r_\theta}|\zeta_\theta|^{n_\theta}[b_x + g_x sign(du\zeta_x)]\right\}du \qquad \textbf{(5.27)}$$

where:

- *b, g* control the shape of the hysteresis loop
- *r* controls the strength degradation or hardening in this case
- *λ* controls the degradation of stiffness
- *h* captures the pinching effect (gapping interface)

as explained in *Chapter 4*.

Since no considerable stiffness degradation is evident from the FE analyses and no gapping is allowed to occur, the additions to the Bouc-Wen equations are limited to the unloading-reloading parameters and the cyclic hardening parameters. A value of *0.5* is chosen for the parameters *b, g*, practically adopting the Masing criterion, since this was found to better match the numerical results. As for the cyclic hardening parameters r_x and r_θ, we adopt a cumulative displacement and rotation controlled function governed by a suitable power law:

$$r_x = \varepsilon_x \int_0^u \frac{|du|}{D}^{\xi_x} \quad \textbf{(5.28)}$$

$$r_\theta = \varepsilon_\theta \int_0^\theta |d\theta|^{\xi_\theta} \quad \textbf{(5.29)}$$

Our aim is not to fully calibrate the above parameters r_x and r_θ but rather check their capacity to capture the results of FE analyses and especially the different hardening trends with respect to the factor of safety against vertical loading. Based on the results, we provide a calibration outline.

Figures 5.57 and ***5.58*** compare the results of FE analyses and those of the modified Winkler model for lightly and heavily loaded caisson foundations of two embedment ratios *D/B = 1, 3* subjected to the cyclic loading pattern presented before. Note that the loading pattern of the model was modified as a sinusoid rather than a piecewise linear for reasons of viscosity, since the problem is solved dynamically. The piecewise linear pattern led to an enhanced caisson inertia and an expansion of the loops thus demanding unreasonably large viscosity constants. After a rough parametric investigation, appropriate values were given to parameters ε_x, ε_θ, ξ_x and ξ_θ. Ultimately, the model is able to capture the basic trends and in some cases the match is even quantitatively sound.

Figure 5.59 plots the values of cyclic hardening parameter r_x with respect to the normalized cumulative displacement and displays the effect of the factor of safety against vertical loading on them. The parametric investigation has shown that the response of lightly loaded systems can be effectively captured by a limited yet rapidly increasing r_x (and similarly r_θ), whereas the response of heavily loaded systems requires

a greater yet slowly increasing r_x (and similarly r_θ). By carrying out a series of analyses for a wide range of FS_V's an analytical expression may be determined. Since the cumulative displacement is normalized with the depth of embedment *D*, parameters ε, ξ will probably prove unaffected by the embedment ratio.

With the same repetitive process used for the swipe tests that were carried out before, the model should be able to capture the cyclic response in the case of displacement/rotation application too, thus validating the completeness of this model.

5.3.9.3. Effect of nonlinear soil-caisson interface

Figure 5.60 illustrates the force-displacement and moment-rotation curves that were derived from FE analyses for the combined *M-Q* loading of a deeply embedded (*D/B = 3*) lightly and heavily loaded (FS_V *= 5, 2*) caisson foundation. In this case, sliding and gapping are allowed to occur through the adoption of the nonlinear Coulomb interface of *Chapter 3*. In contrast to the bonded interface examined previously, the lightly loaded system exhibits a rather asymmetric response that involves softening behaviour as a result of the growing gap being formed around the caisson. It is evident that detachment takes place at the point where the stiffness declines sharply after the reversal of loading. From that point till the point of maximum (or minimum) applied force, the loops lose their smoothness as a result of the detachment – reentachment with the soil. On the other hand, the heavily loaded system exhibits a more asymmetric response, as expected, which involves a slightly hardening behaviour at decreasing rate. This differentiation between the responses of lightly and heavily loaded systems was expected, considering the fact that lightly loaded foundation systems generally have more potential to "express" the effects of geometric nonlinearities at their interface. The difference between the two responses is further analyzed below.

Figures 5.61 and ***5.62*** present time histories of the plastic strain magnitude contours on the deformed mesh in the case of a lightly loaded (FS_V *= 5*) and a heavily loaded (FS_V *= 2*) in the case of the nonlinear Coulomb interface. The snapshots correspond to absolutely maximum applied load (peaks of loading pattern). In the case of the lightly loaded system, the response is more asymmetric than in the bonded

interface case, since the detachment at the interface induces a greater asymmetry on the resisting mechanism on the first cycle of loading. The gap around the caisson and the plastification of the surrounding soil grow continuously until they somewhat stabilize at the 4^{th} cycle of loading. There is no significant restoration of the gap after the reversal of loading. On the other hand, the response of heavily loaded system is less asymmetric than in the bonded interface case, as the detachment appears to be alleviating the vertical load mechanism described in the previous section (bonded interface). The detachment of the caisson from the soil is not so evident due to the initially plastified nature of the surrounding soil, and some degree of gap restoration can be observed.

This effect can be readily included in the Winkler model through the calibration of the pinching factor h_x as examined previously in *Chapter 4*; yet this work is beyond the purposes of this thesis.

Figures

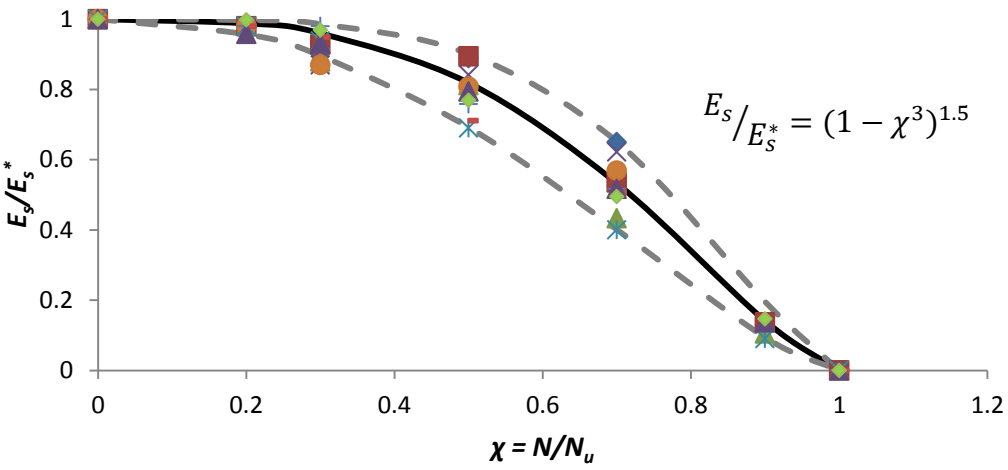

Figure 5.1 *The effect of the initial plastification due to vertical loading to the elastic lateral response of a caisson foundation expressed as an equivalent reduction of the elasticity modulus of the soil.*

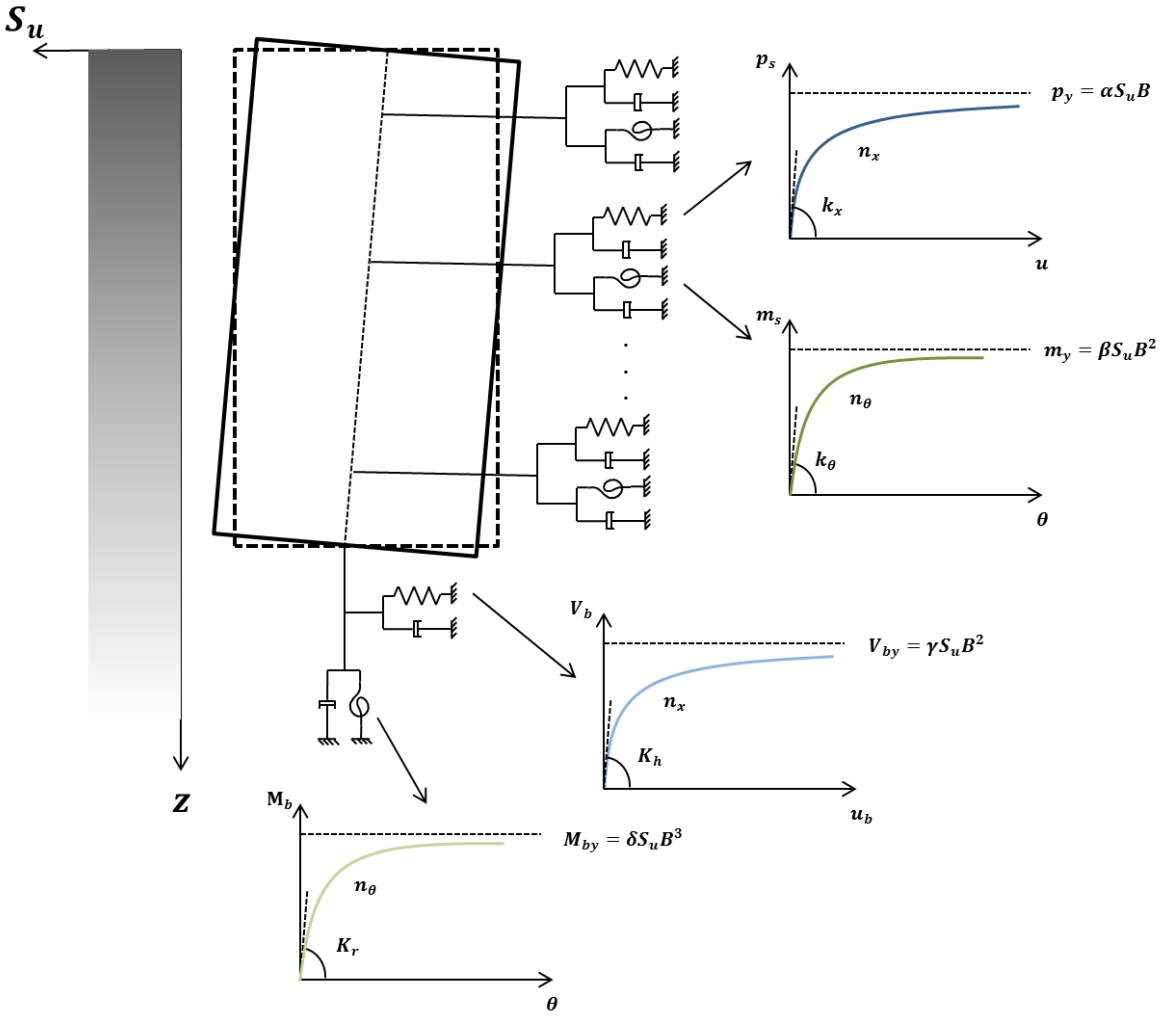

Figure 5.2 *An outline of the Winkler model for lateral static monotonic loading. There are 4 types of uncoupled springs along with their associated dashpots. The elastic stiffness of the springs has been determined through an approximation of Gazetas's closed analytical expressions. Hardening parameters n_x, n_ϑ are common for the distributed and the concentrated springs at the side and at the base of the caisson respectively. The form of the ultimate soil reactions has been determined through simple dimensional analysis.*

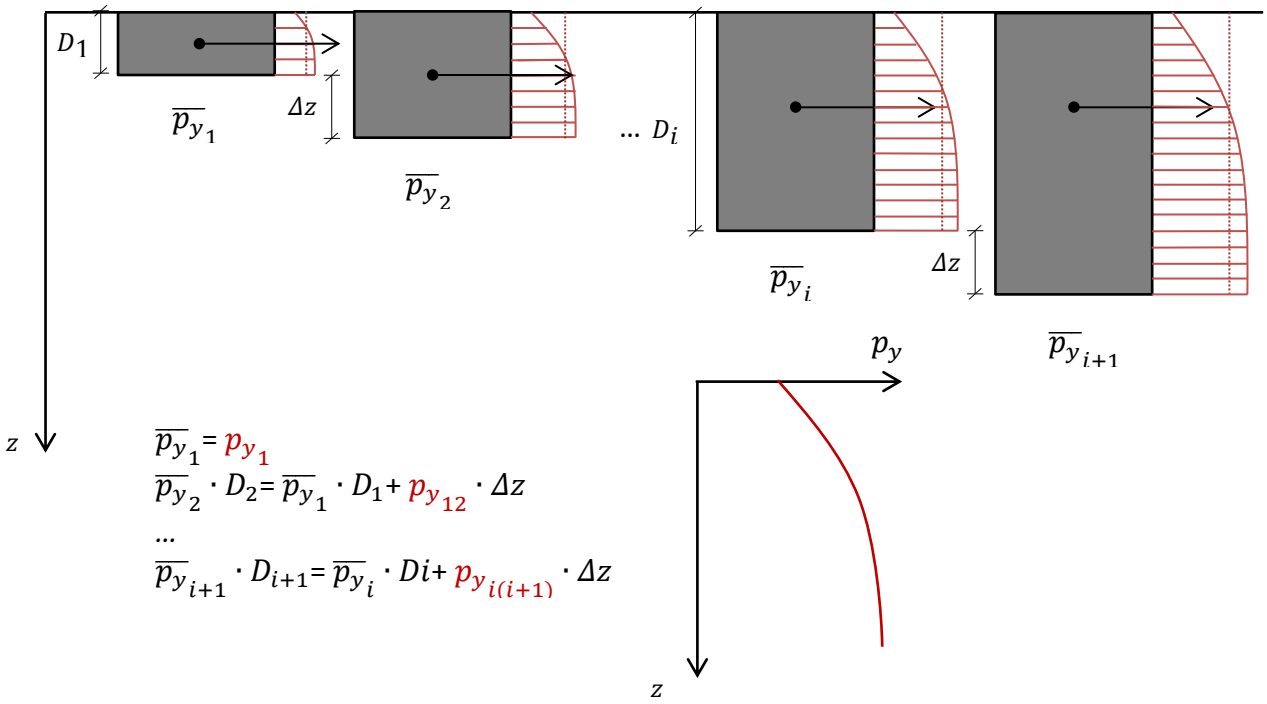

Figure 5.3 *A rigorous methodology for determining the distribution of the ultimate lateral soil reaction with respect to depth.*

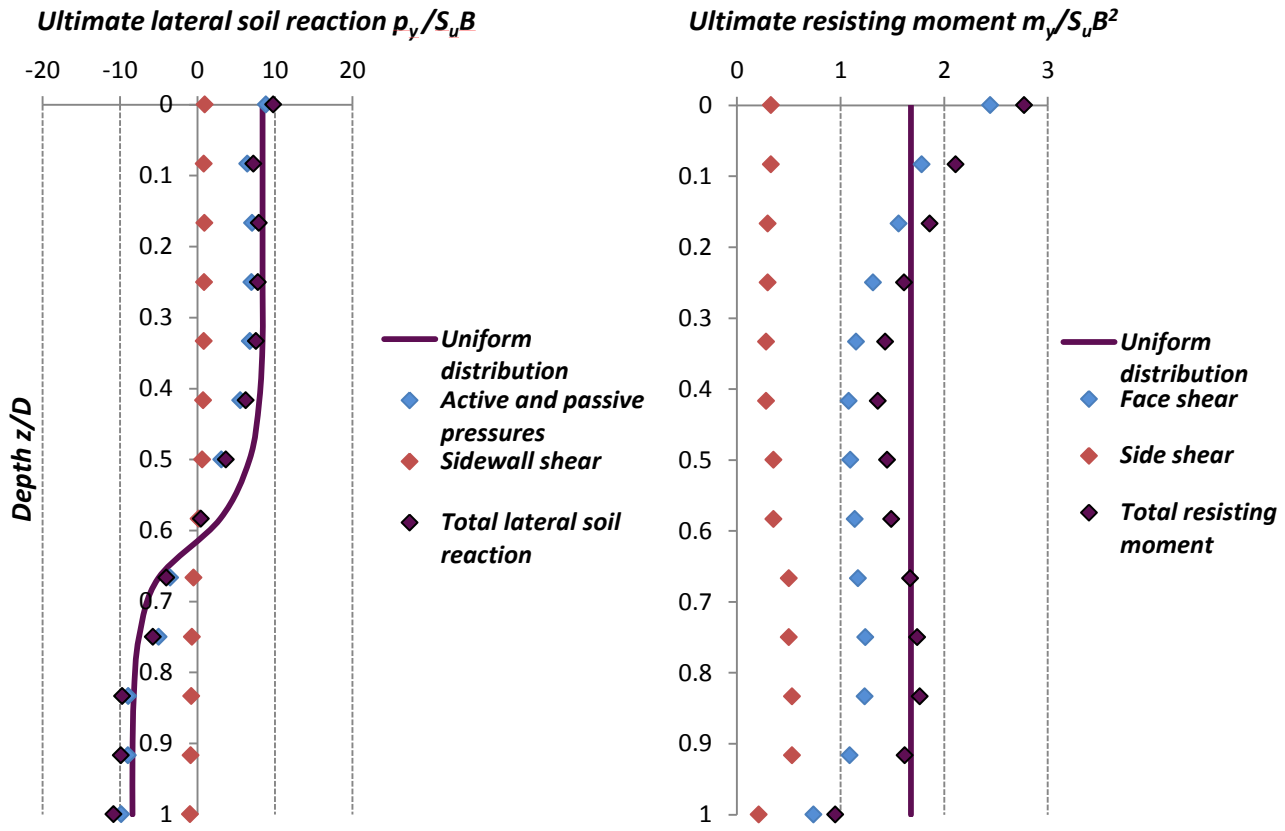

Figure 5.4 *Comparison between the actual distribution of the lateral soil reaction and resisting moment per unit depth with the uniform distribution adopted in the model. The components of lateral soil reaction and the resisting moment per unit depth are thoroughly analyzed in section* ***5.3.2.2.***

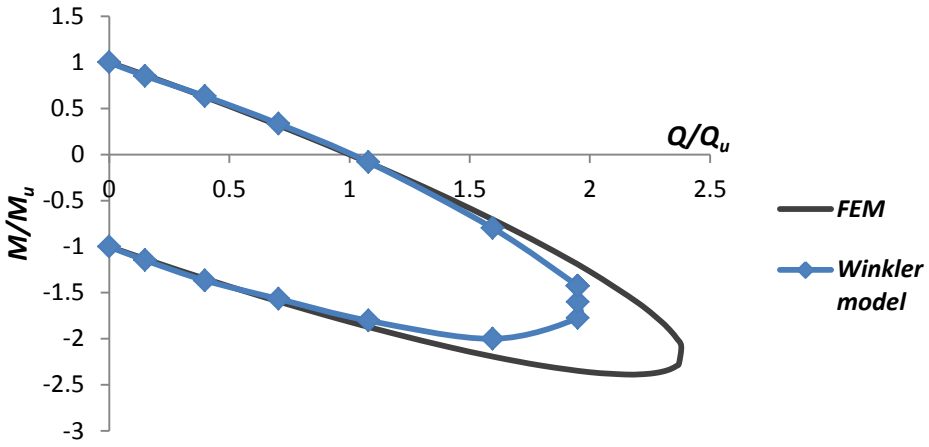

Figure 5.5 *The failure envelope for a caisson foundation of embedment ratio D/B = 3 as captured by a series of swipe tests using the BWGG Winkler model is compared to the envelope derived from the FE analyses. The Winkler model seems to be underestimating the expansion of the yield surface under constant (with the load angle) strength parameters.*

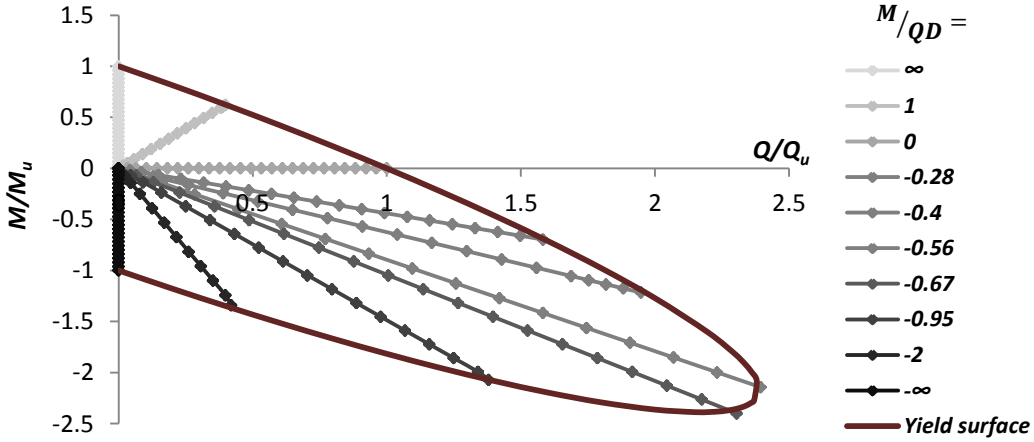

Figure 5.6 *Force controlled analyses utilized in the calibration procedure for various values of the embedment ratio and the factor of safety against vertical bearing capacity failure.*

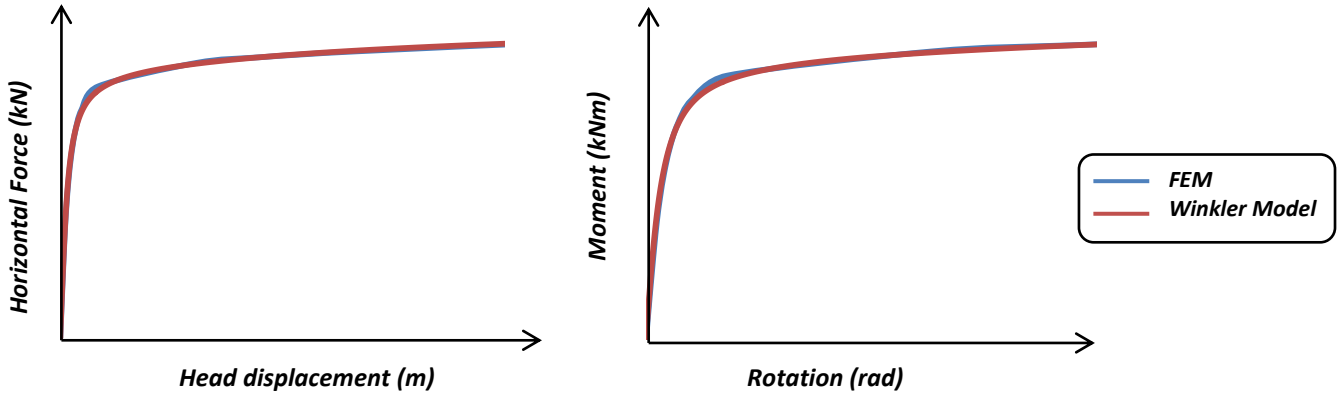

Figure 5.7 *The dual curve fit as part of the optimization technique developed. The force-displacement and moment rotation curves determined by the model are matched to the equivalent FEM curves, by finding the optimum values of α, β, n_x and n_r. The values of γ, δ are directly deduced through surface stress integration in Abaqus.*

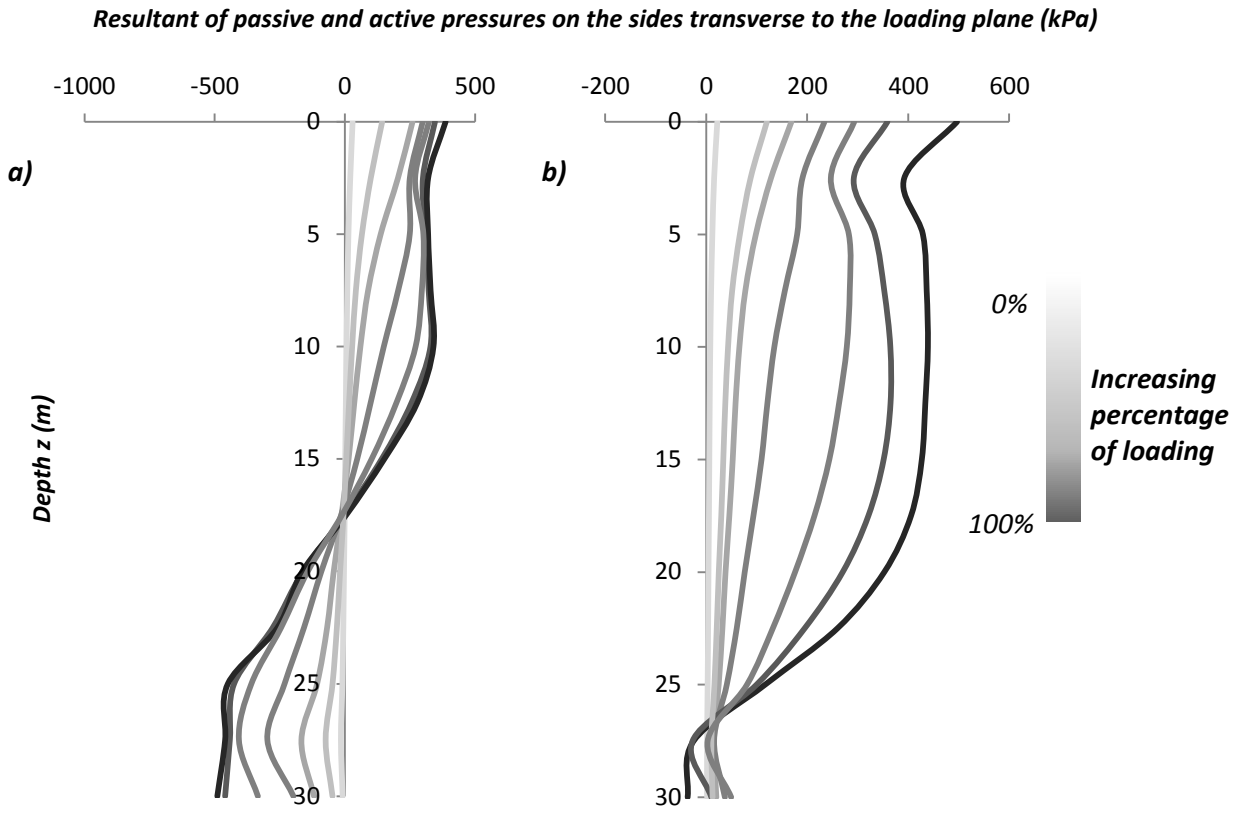

Figure 5.8 *Distribution time histories of the resultant of the passive and active pressures on the face and back of the caisson for a radial load path a) on the 1st quadrant and b) on the 2nd quadrant of the M-Q plane. The formation of a plateau is evident.*

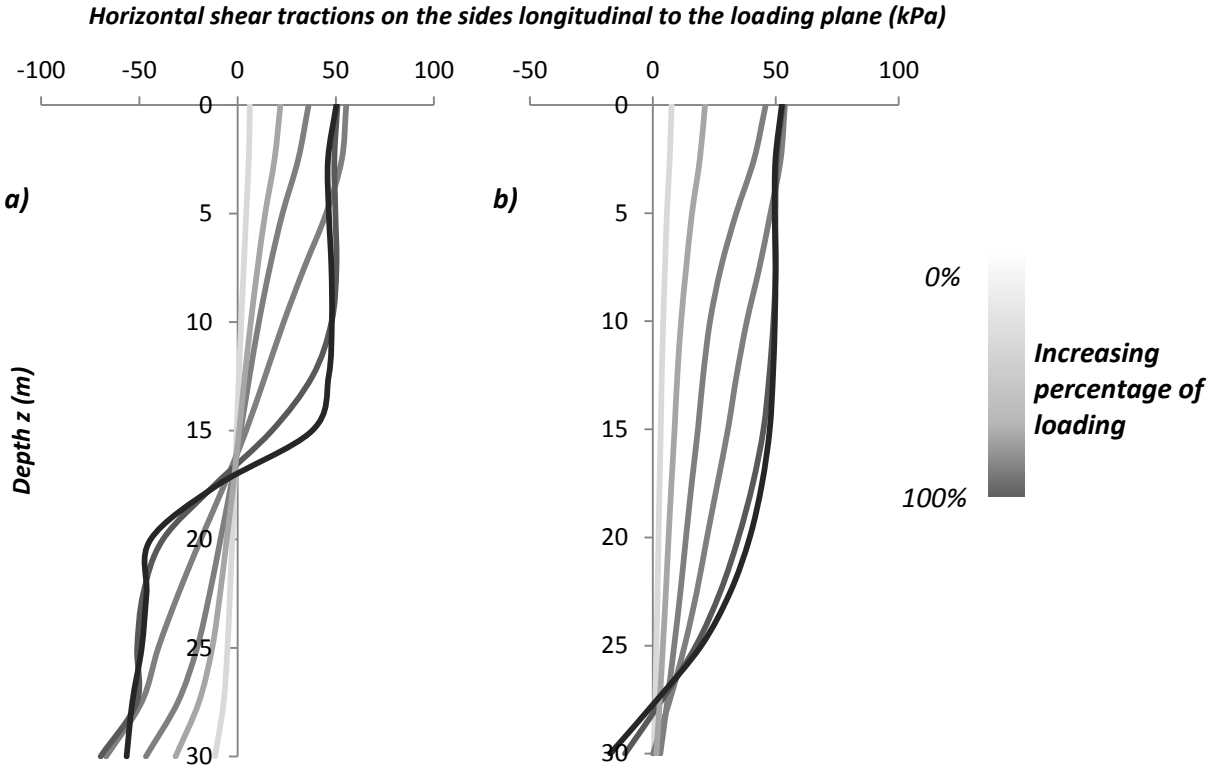

Figure 5.9 *Distribution time histories of the horizontal shear tractions on the sides of the caisson for a radial load path a) on the 1st quadrant and b) on the 2nd quadrant of the M-Q plane. The formation of a plateau is evident.*

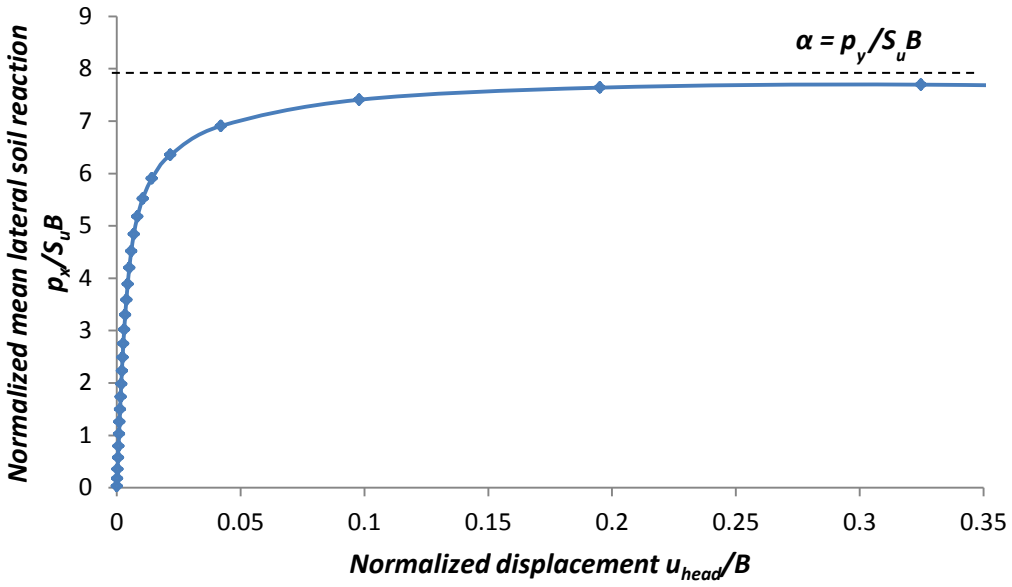

Figure 5.10 *The surface integration of the stress components of the lateral soil reaction yields the ultimate mean lateral soil reaction α, identified at the plateau.*

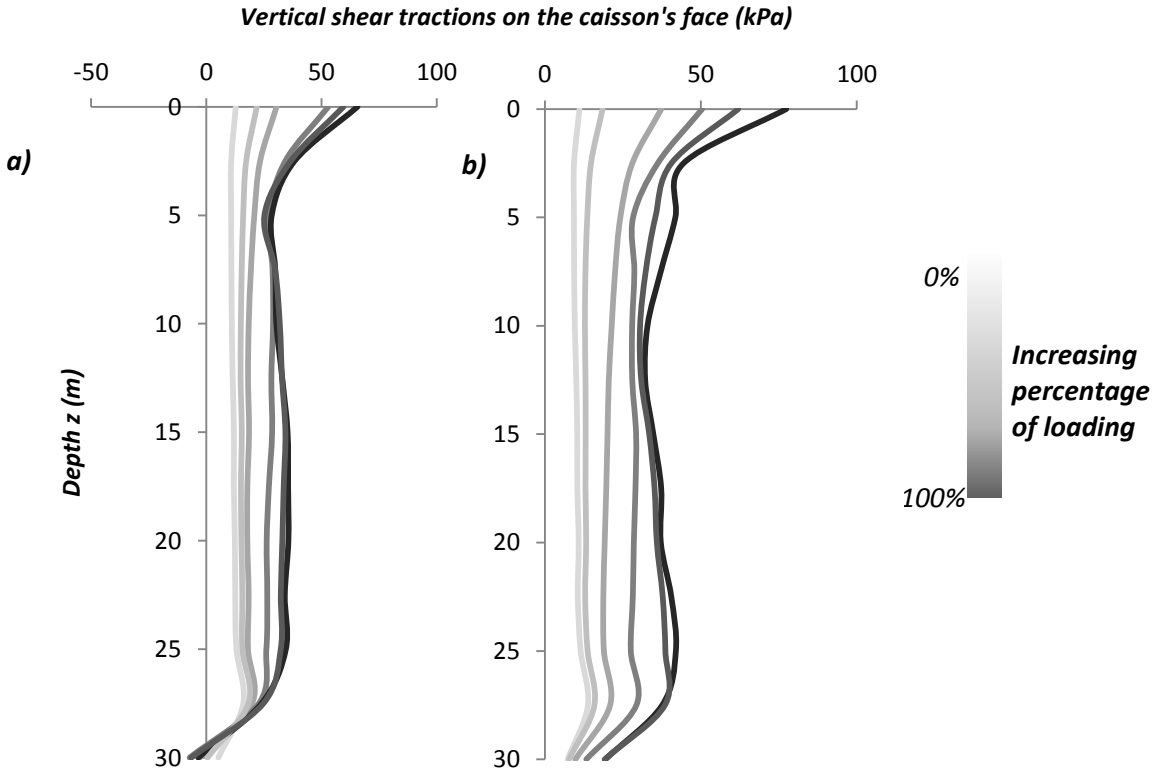

Figure 5.11 *Distribution time histories of the vertical shear tractions developed on the caisson's face for a radial load path on the 1st quadrant and b) on the 2nd quadrant of the M-Q plane. The formation of a plateau is evident.*

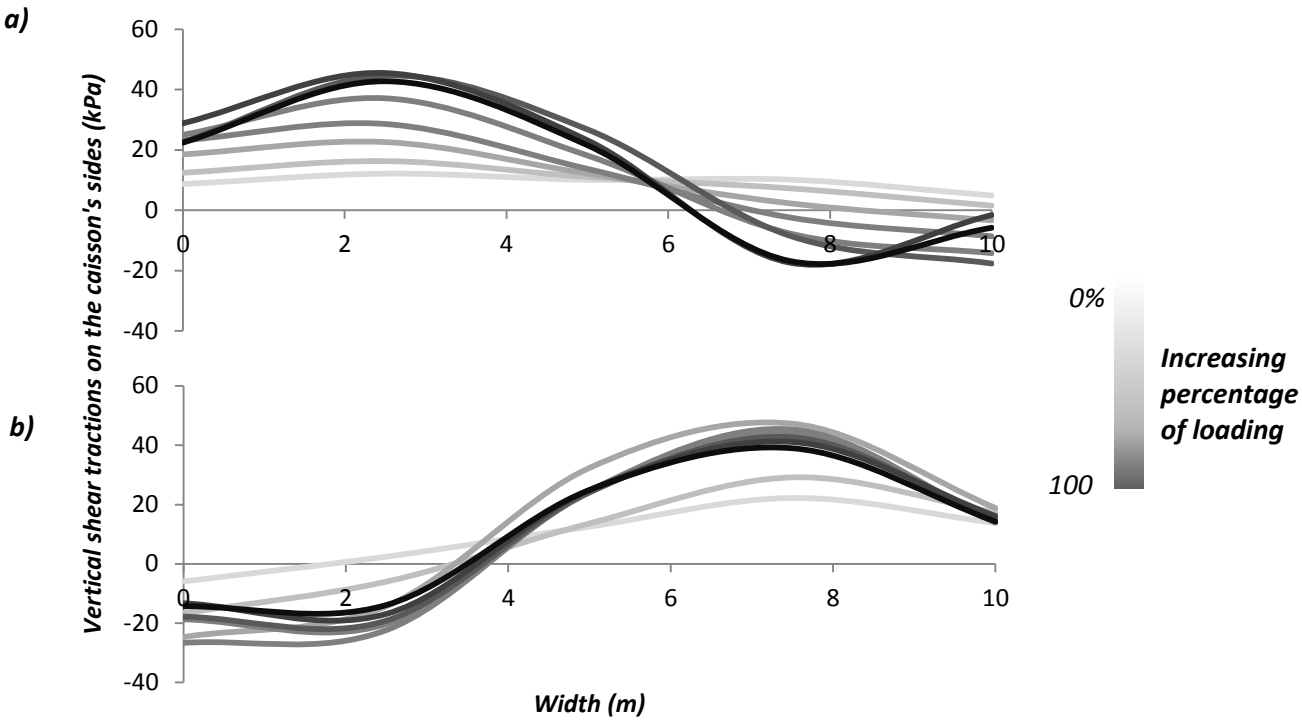

Figure 5.12 *Distribution time histories of the vertical shear tractions developed on the sides of the caisson longitudinal to the loading plane for a radial load path a) on the 1st quadrant and b) on the 2nd quadrant of the M-Q plane.*

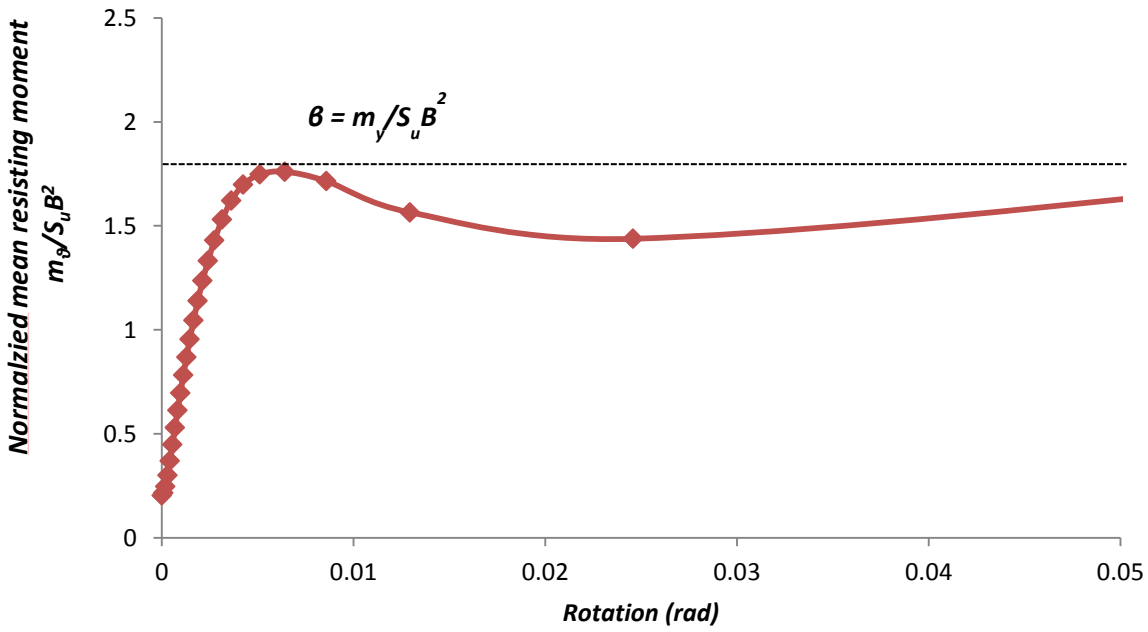

Figure 5.13 *The surface integration of the shear stress components of the resisting moment per unit depth yields the ultimate mean resisting moment per unit depth β. In contrast to the lateral soil reaction, m_ϑ exhibits softening behavior.*

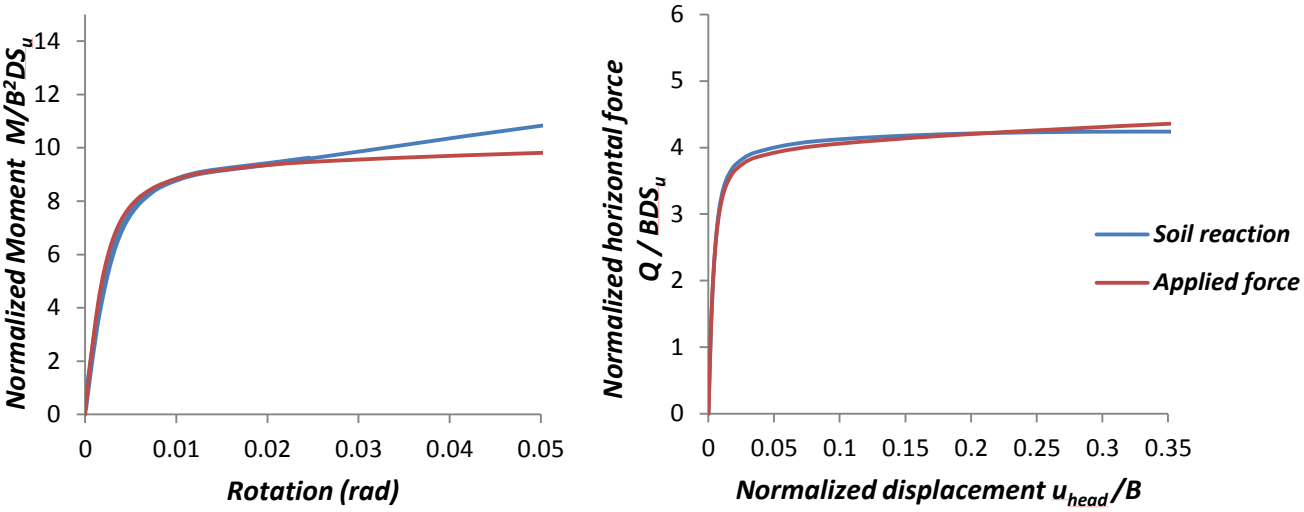

Figure 5.14 *Soil reaction vs externally applied moment/force for a deeply embedded caisson foundation subject to combined horizontal force and moment. The remarkable fit validates the accuracy of the integration scheme in terms of lateral response.*

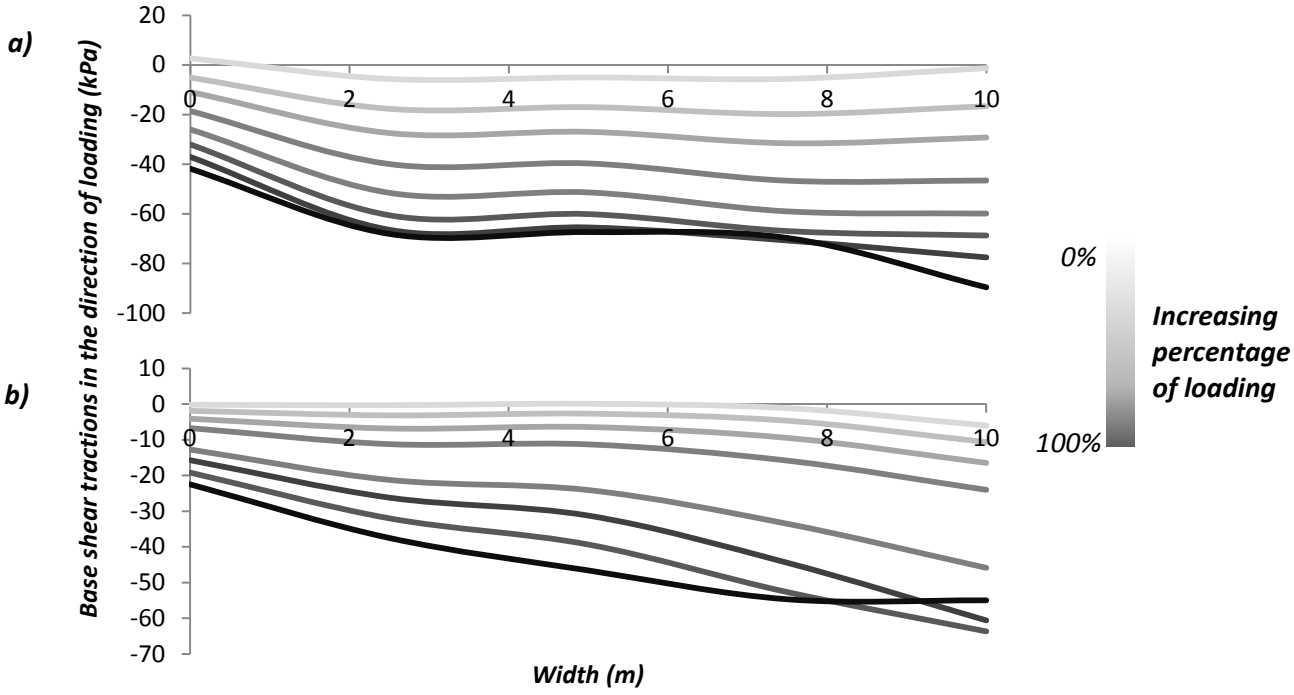

Figure 5.15 *Distribution time histories of the shear tractions developed on the caisson's base for a radial load path a) on the 1st quadrant and b) on the 2nd quadrant of the M-Q plane.*

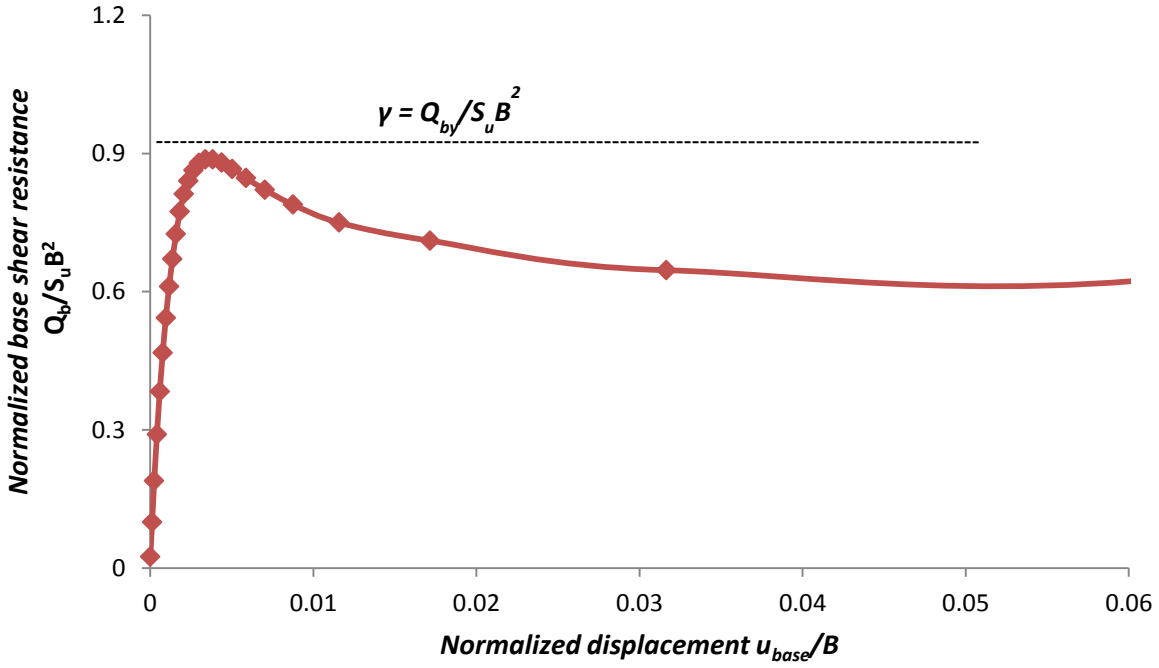

Figure 5.16 *Normalized base shear resistance vs normalized base displacement, yielding the ultimate base shear resistance for a given load path, embedment ratio and overall factor of safety against vertical loading.*

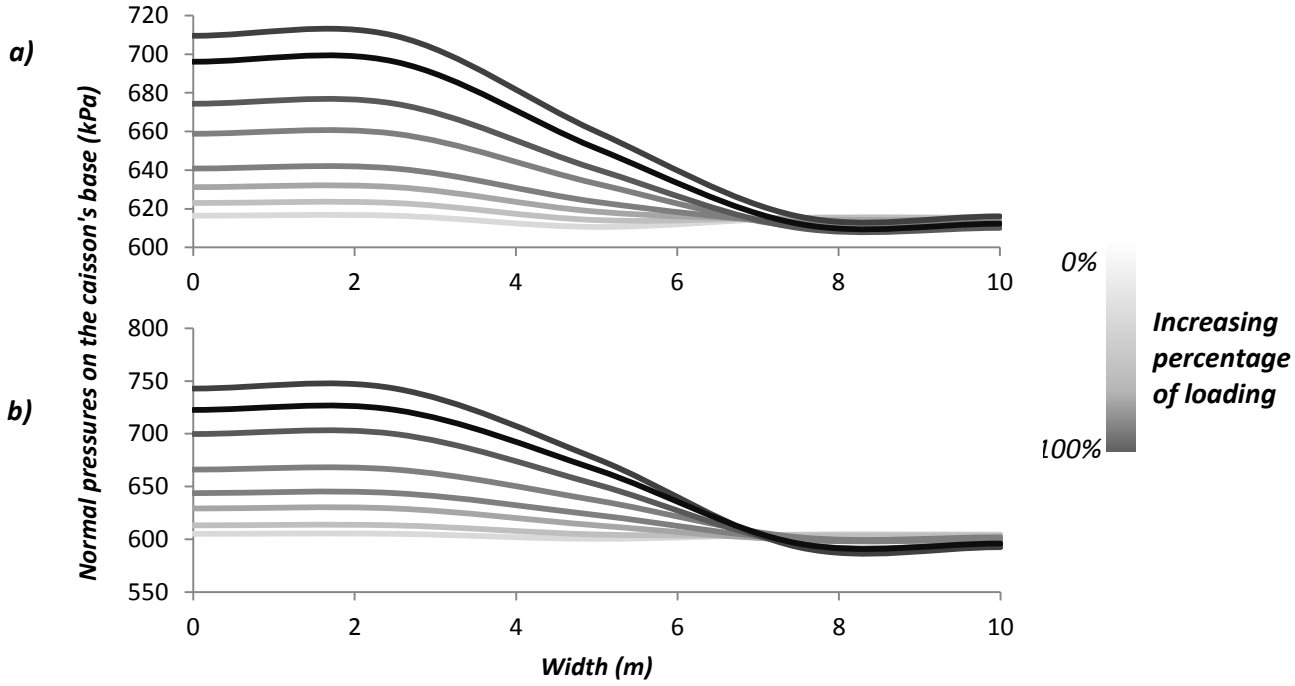

Figure 5.17 *Distribution time histories of the pressures developed on the caisson's base for a radial load path a) on the 1st quadrant and b) on the 2nd quadrant of the M-Q plane.*

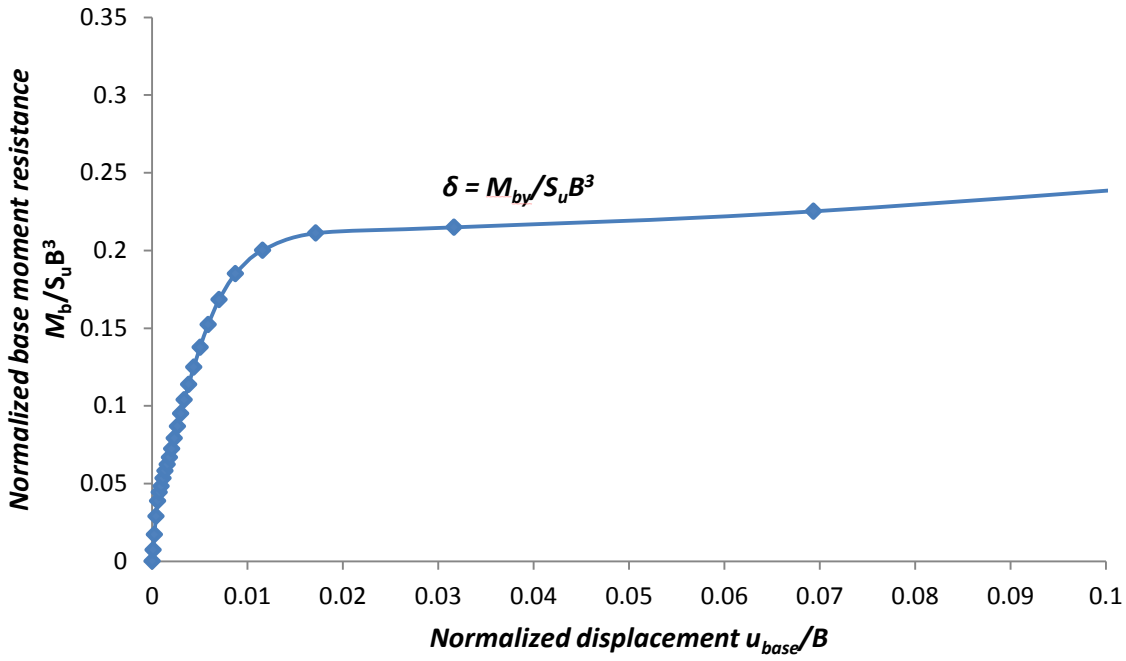

Figure 5.18 *Normalized base moment resistance vs normalized base displacement, yielding the ultimate base moment resistance for a given load path, embedment ratio and overall factor of safety against vertical loading.*

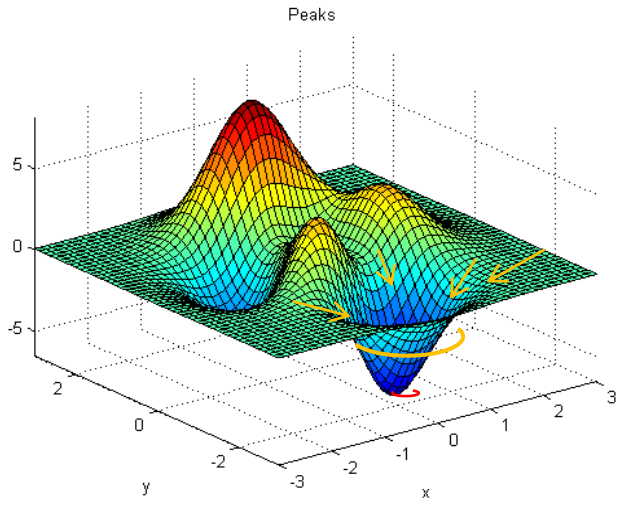

1st step: ***g.a*** *locates the global minimum*

2nd step: ***fmincon*** *finds the optimum solution*

Figure 5.19 *Visualization of the optimization procedure in an equivalent 3-dimensional problem. The actual problem studied herein cannot be visualized, since it is a 4-dimensional one.*

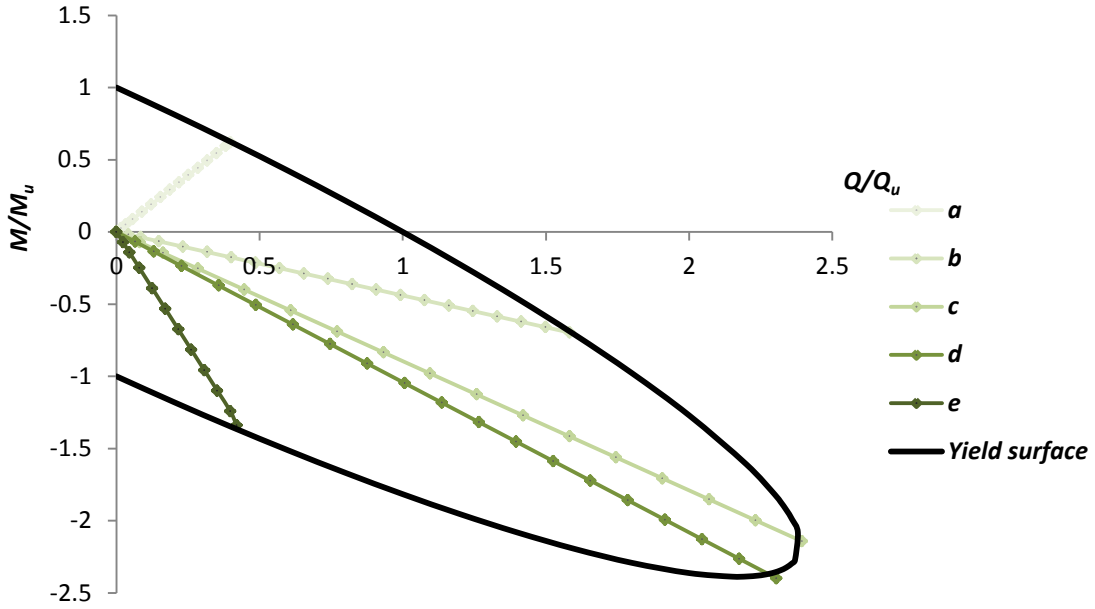

Figure 5.20 *In the following figures, the calibration step is validated in terms of dual curve fit for the 5 characteristic force-controlled load paths presented. A deeply embedded (D/B =3) foundation exhibiting an $FS_V = 5$ is considered.*

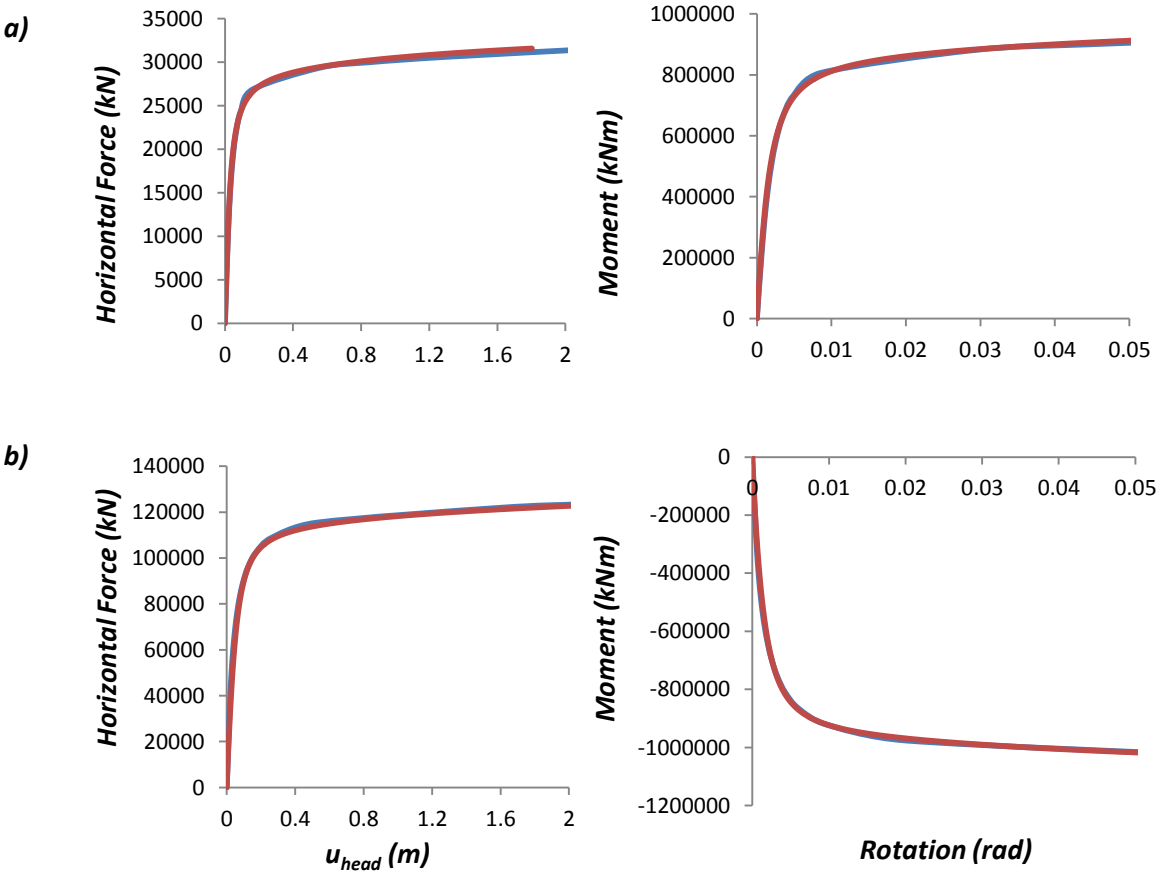

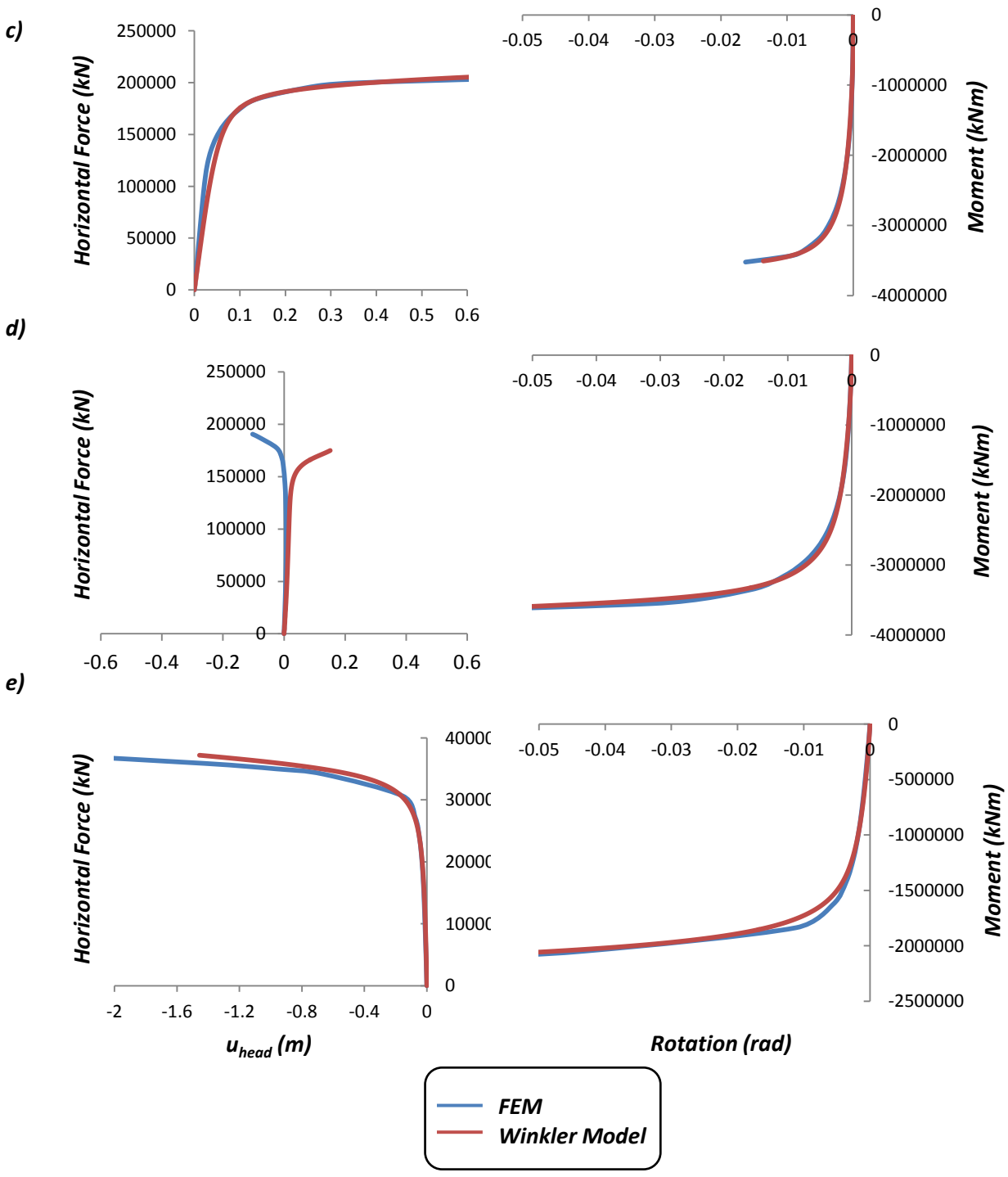

Figure 5.21 *Validation of the curve fit for the 5 radial load paths displayed in Figure 5.18. Curves a), b) and e) refer to random M-Q loading paths in the 1st and 2nd quadrant of the M-Q space, while c) and d) correspond to maximum horizontal and moment capacity respectively.*

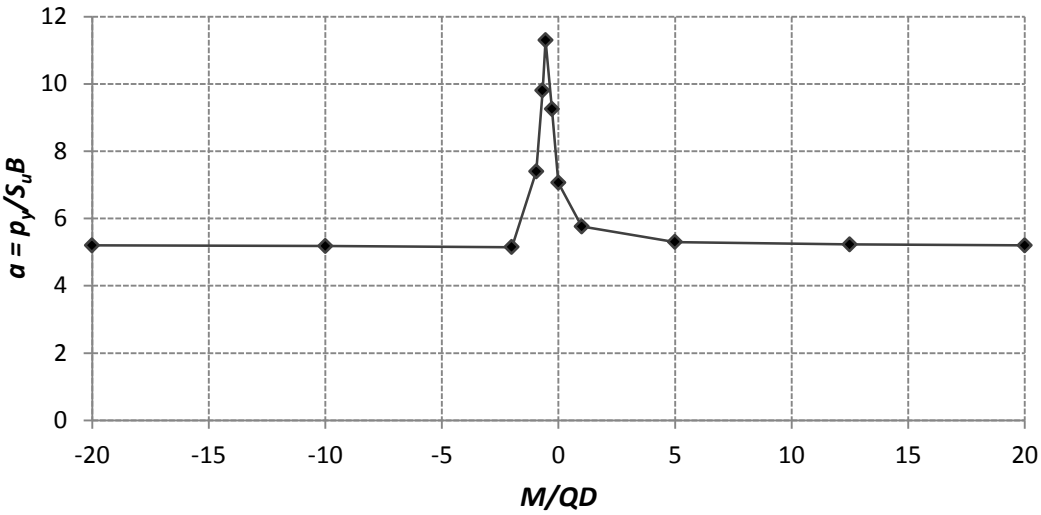

Figure 5.22 *The normalized mean ultimate lateral soil reaction vs the load angle M/QD. P_y seems to be diverging from the conventional definition of the invariable ultimate reaction, as considered in pile foundations.*

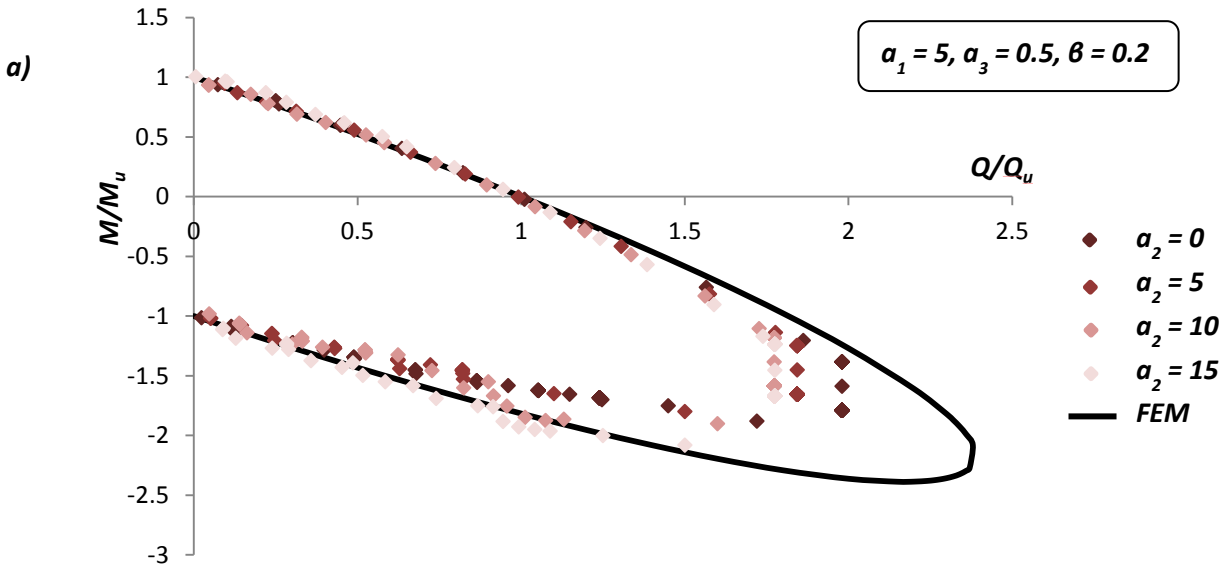

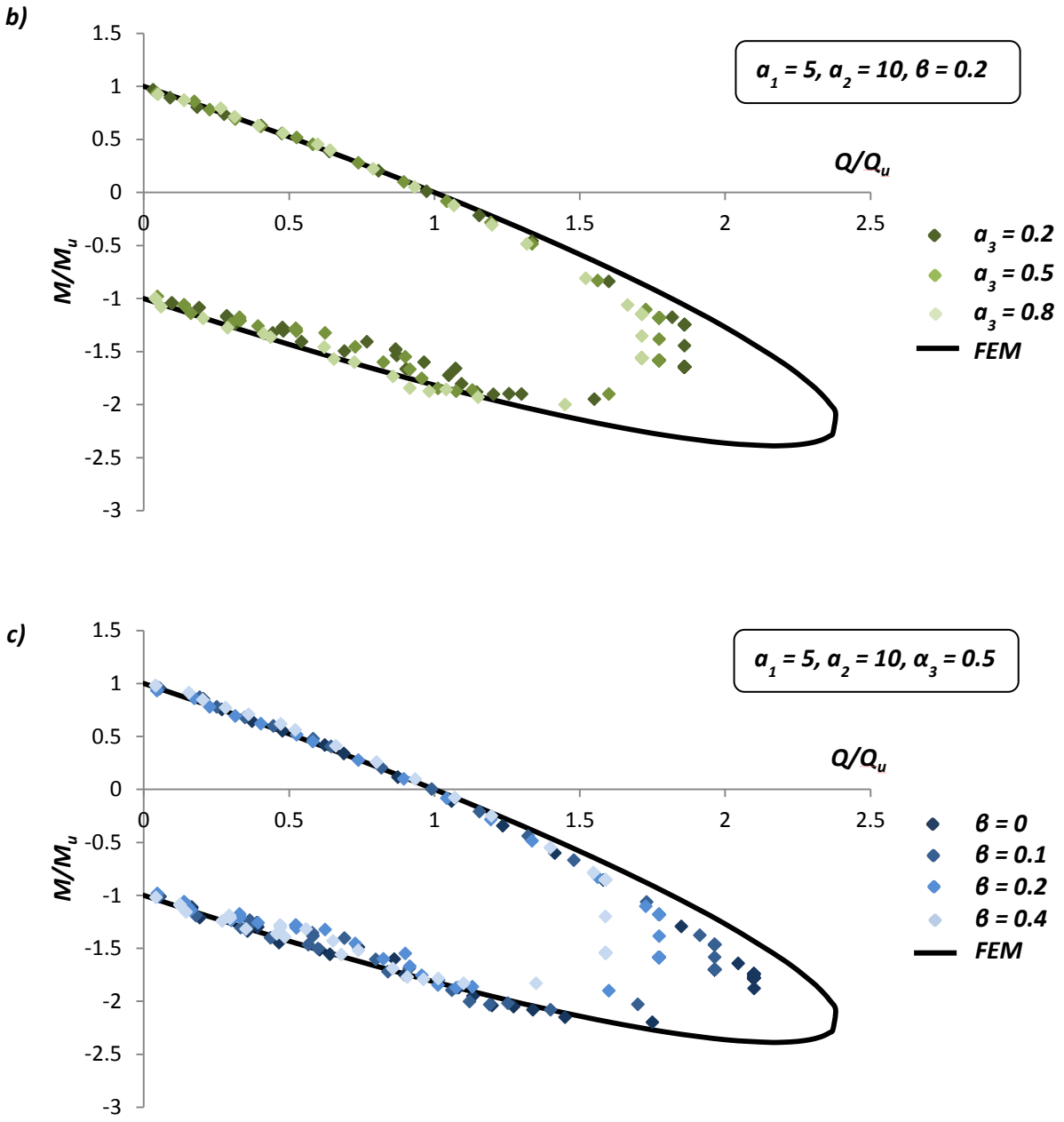

Figure 5.23 *Investigation of the shape of the deduced failure envelope through swipe tests for a versatile 4-parameter soil resistance profile given by (Eq. 5.13 – 5.14). Figure a) shows the effect of the magnitude of the increase in the soil resistance; figure b) shows the effect of the shape of the soil resistance profile; and figure c) illustrates the effect of the resisting moment-lateral soil reaction ratio.*

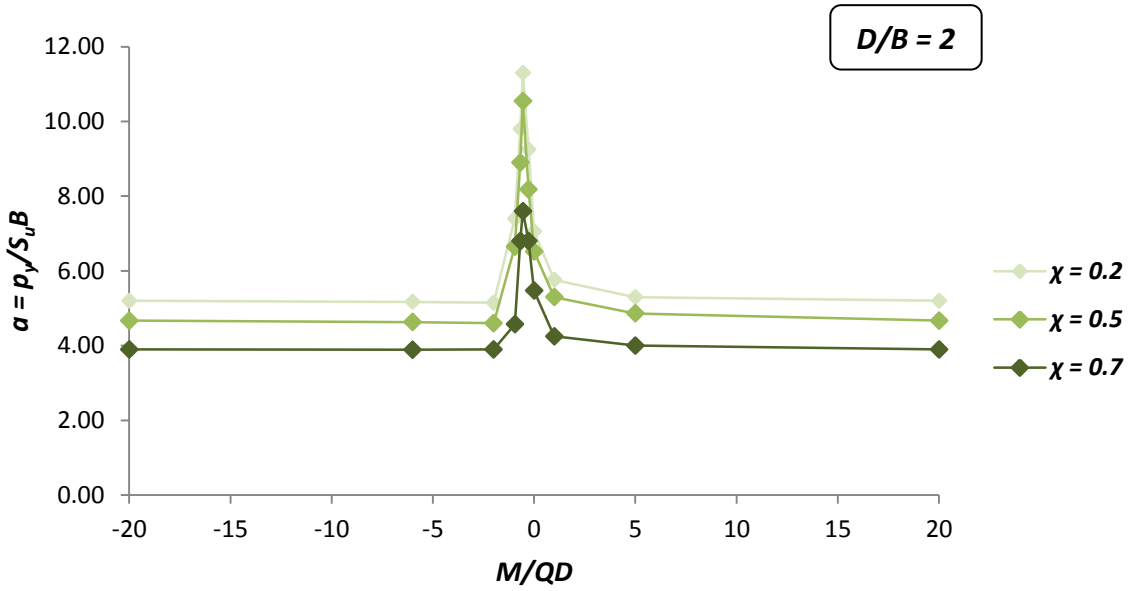

Figure 5.24 *The effect of the factor of safety against vertical loading on the normalized ultimate lateral soil reaction as derived from the hybrid optimization technique.*

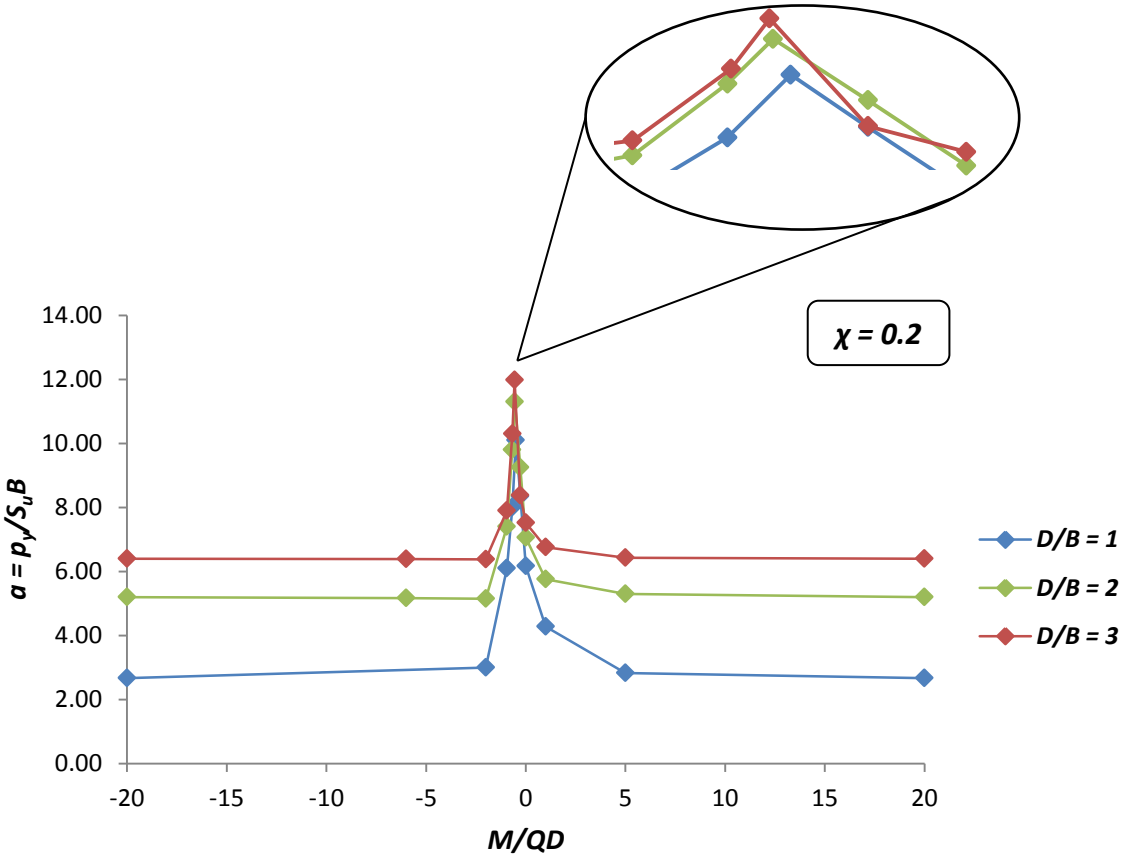

Figure 5.25 *The effect of the embedment ratio on the normalized ultimate lateral soil reaction as derived from the hybrid optimization technique.*

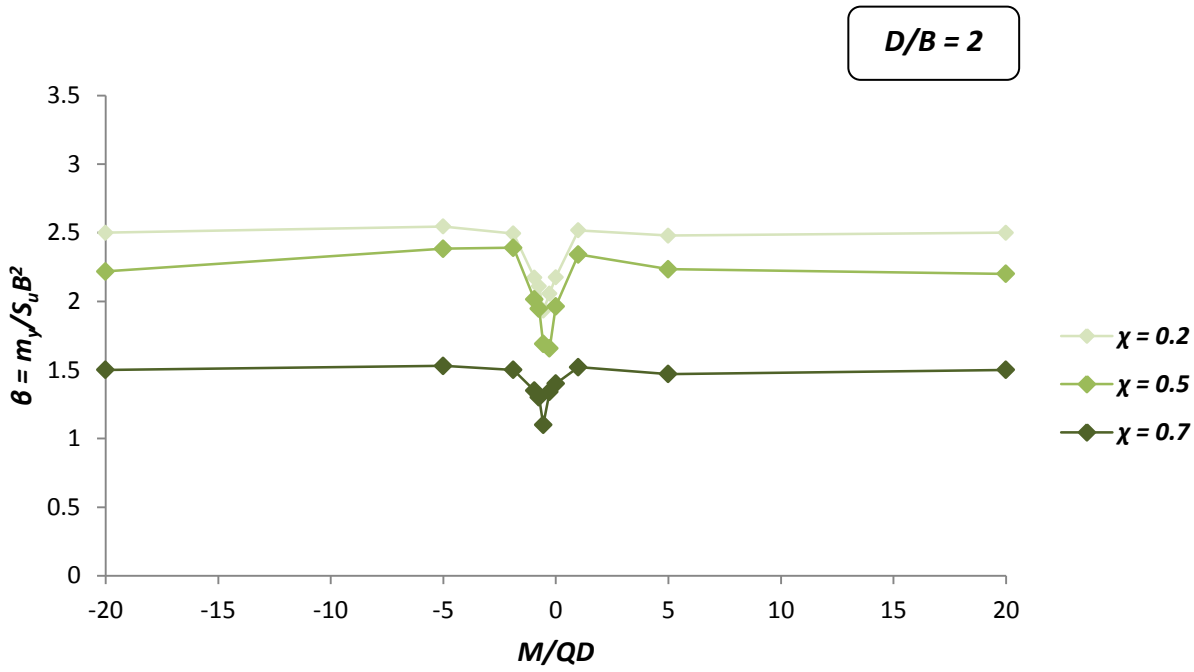

Figure 5.26 *The effect of the factor of safety against vertical loading on the normalized ultimate resisting moment per unit depth as derived from the hybrid optimization technique.*

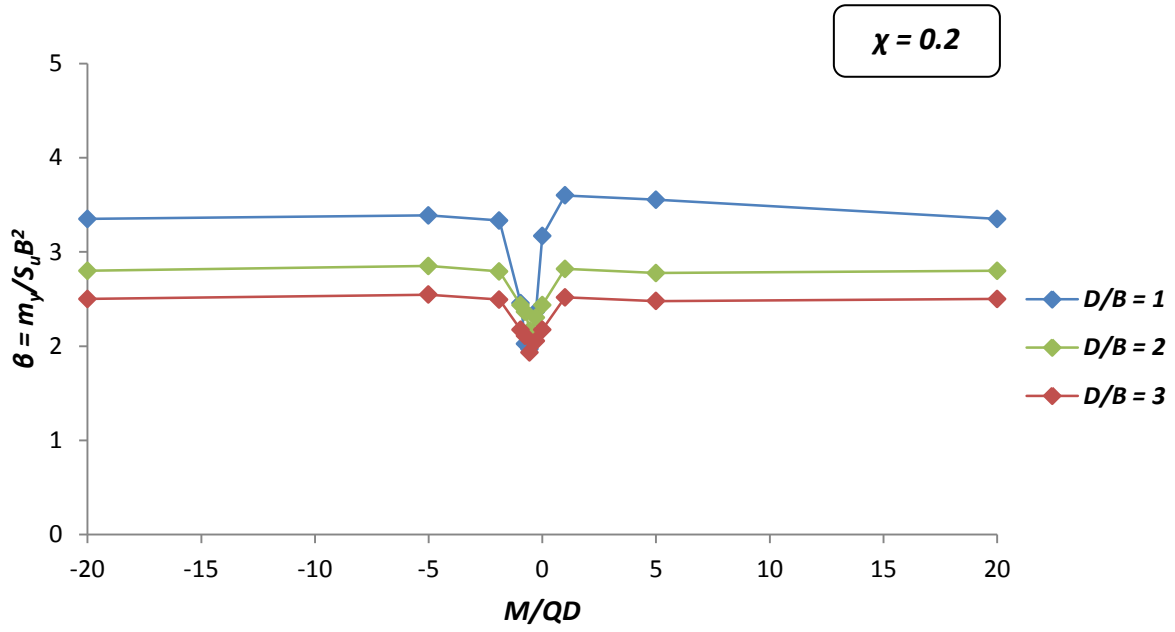

Figure 5.27 *The effect of the embedment ratio on the normalized ultimate resisting moment per unit depth as derived from the hybrid optimization technique.*

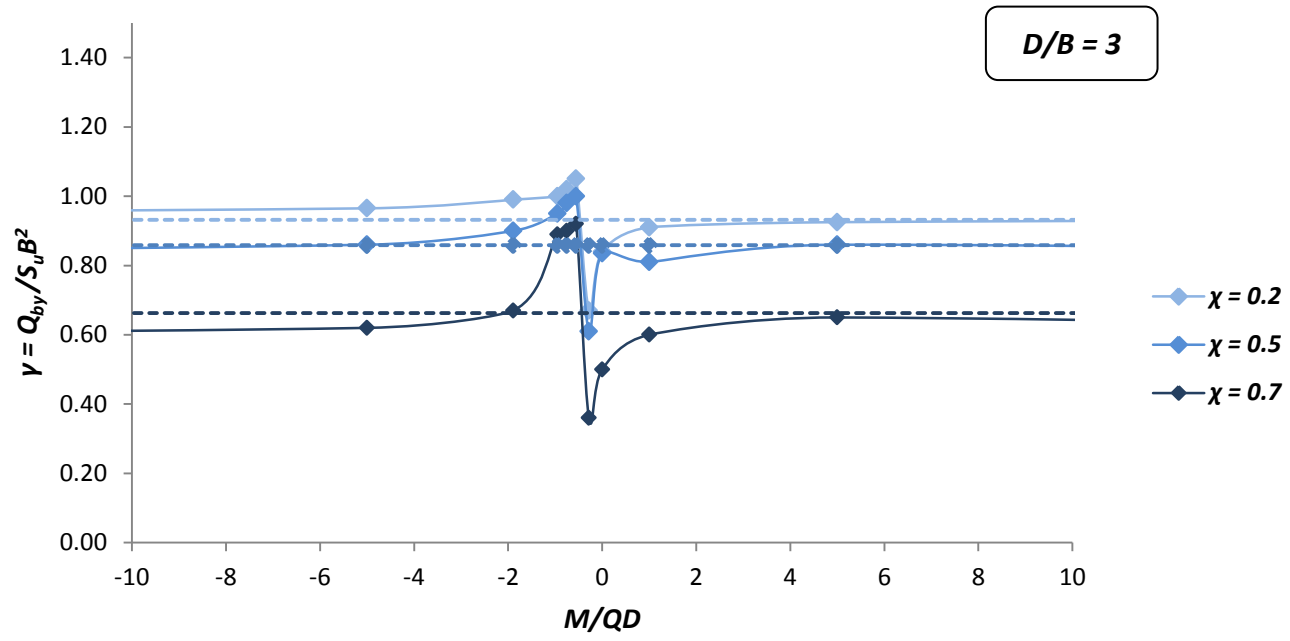

Figure 5.28 *The effect of the vertical factor of safety on the normalized ultimate base horizontal resistance as derived from direct stress integration for a deeply embedded caisson foundation (solid lines). The dotted lines represent possible design values in the case where the ultimate base horizontal and moment resistance are considered uncoupled.*

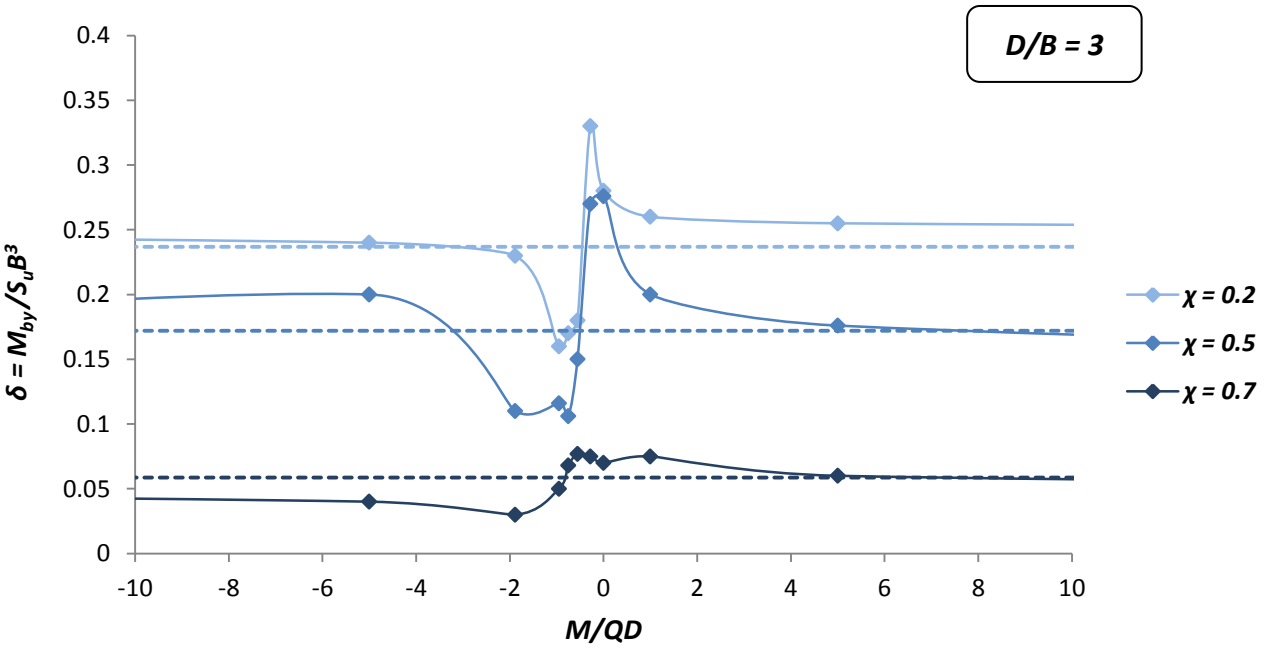

Figure 5.29 *The effect of the vertical factor of safety on the normalized ultimate base moment resistance as derived from direct stress integration for a deeply embedded caisson foundation (D/B = 3). The dotted lines represent possible design values in the case where the ultimate base horizontal and moment resistance are considered uncoupled.*

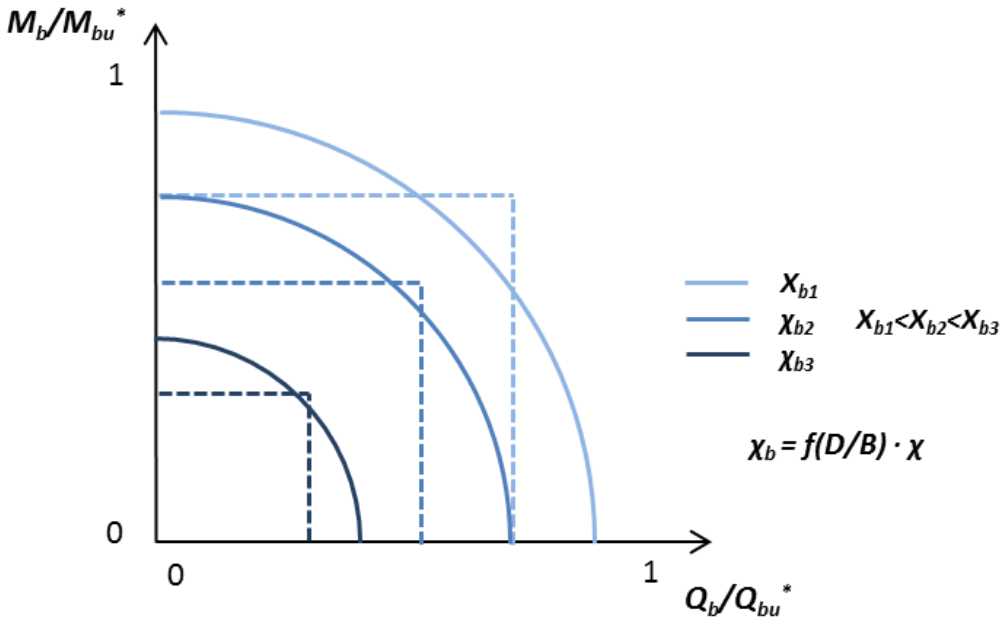

Figure 5.30 *Qualitative illustration of the M-Q interaction surface of the caisson's base for decreasing values of the factor of safety against vertical loading. The solid lines correspond to the solid lines of the previous two figures correlating the M-Q load ratio of the system with that of the base itself. Similarly, the dotted lines represent the dotted lines of the previous two figures, in which the ultimate horizontal and moment capacities are considered uncoupled.*

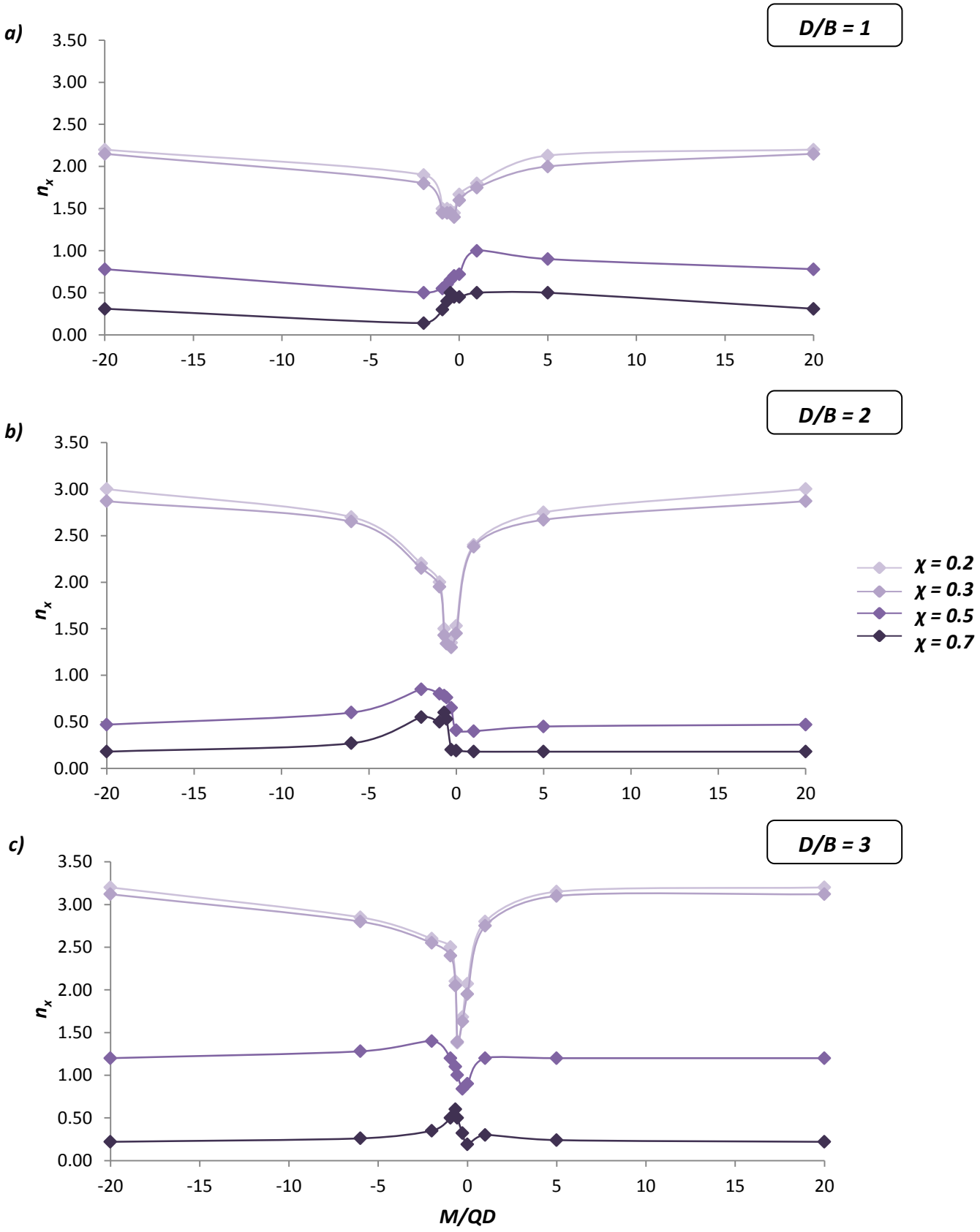

Figure 5.31 *The hardening parameter n_x (referring to the translational springs of the model) vs the load angle M/QD for four characteristic factors of safety against vertical loading and embedment ratio a) D/B =1, b) D/B = 2and c) D/B = 3, as derived from the hybrid optimization approach.*

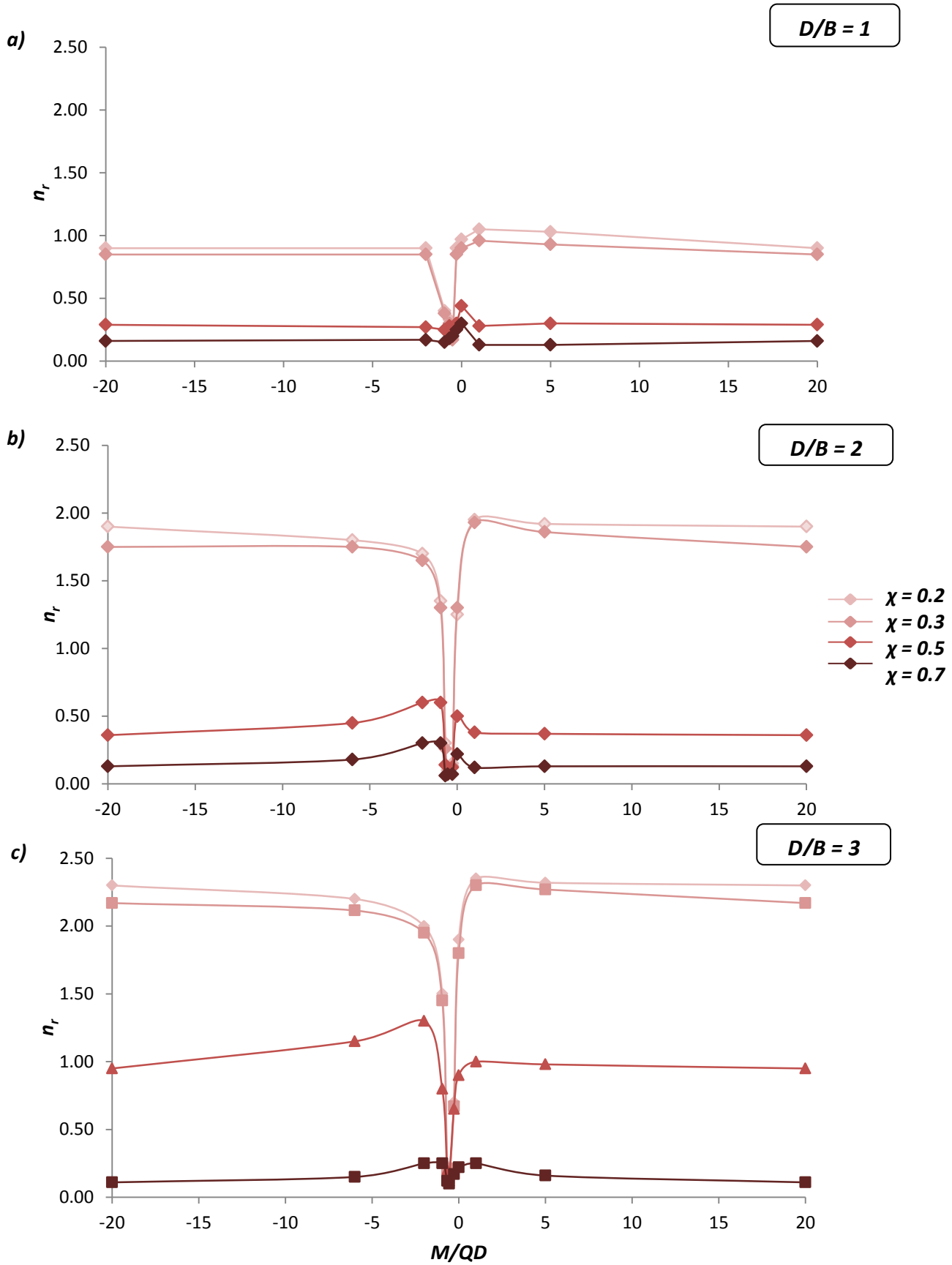

Figure 5.32 *The hardening parameter n_r (referring to the rotational springs of the model) vs the load angle M/QD for four characteristic factors of safety against vertical loading and embedment ratio a) D/B =1, b) D/B = 2and c) D/B = 3, as derived from the hybrid optimization approach.*

a)

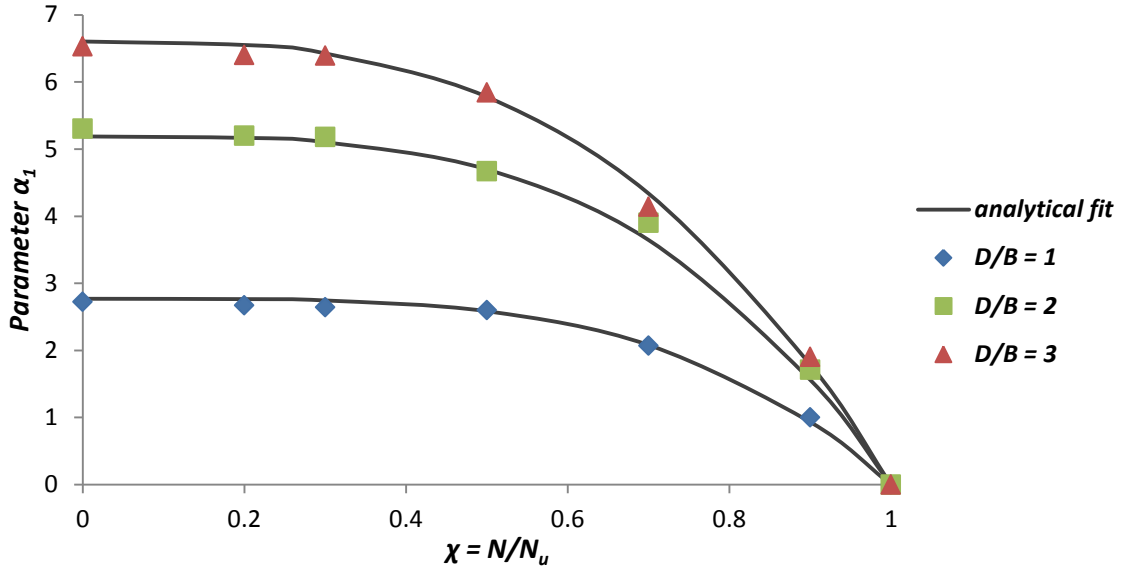
Parameter α_1
$\chi = N/N_u$
analytical fit
D/B = 1
D/B = 2
D/B = 3

b)

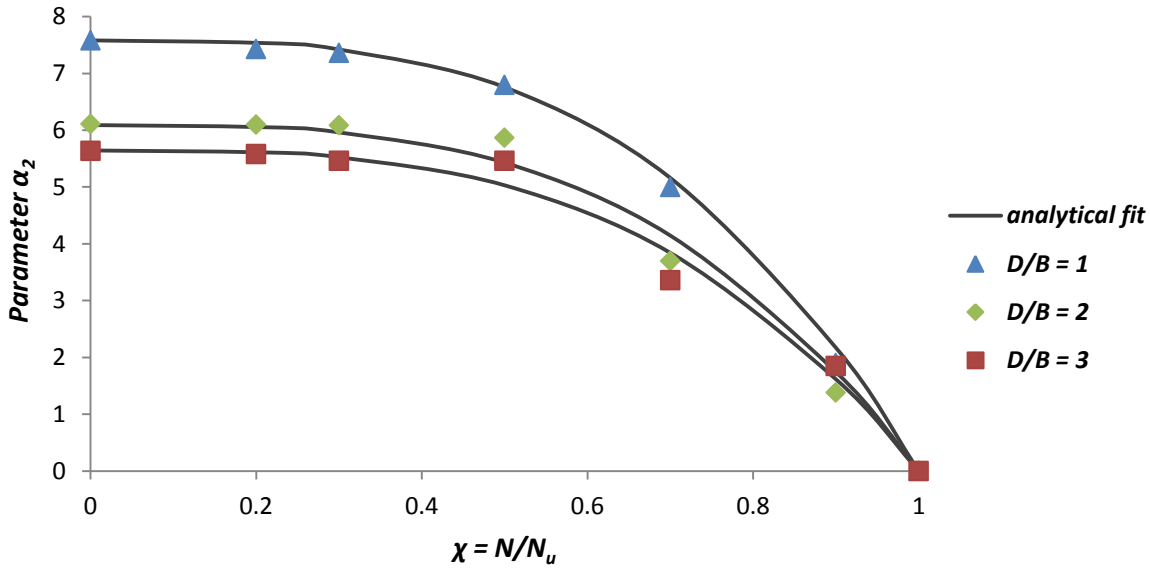
Parameter α_2
$\chi = N/N_u$
analytical fit
D/B = 1
D/B = 2
D/B = 3

c)

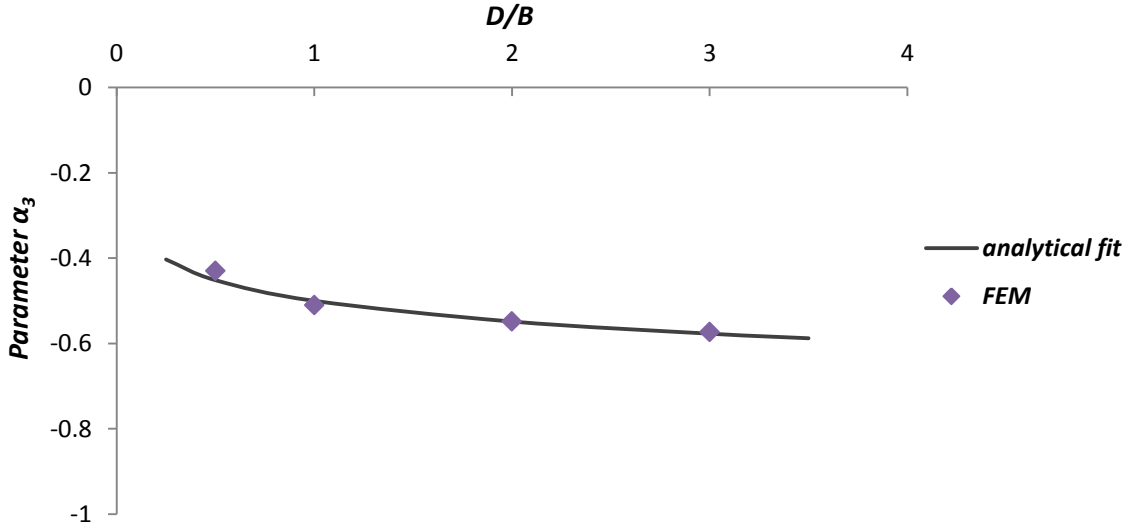
D/B
Parameter α_3
analytical fit
FEM

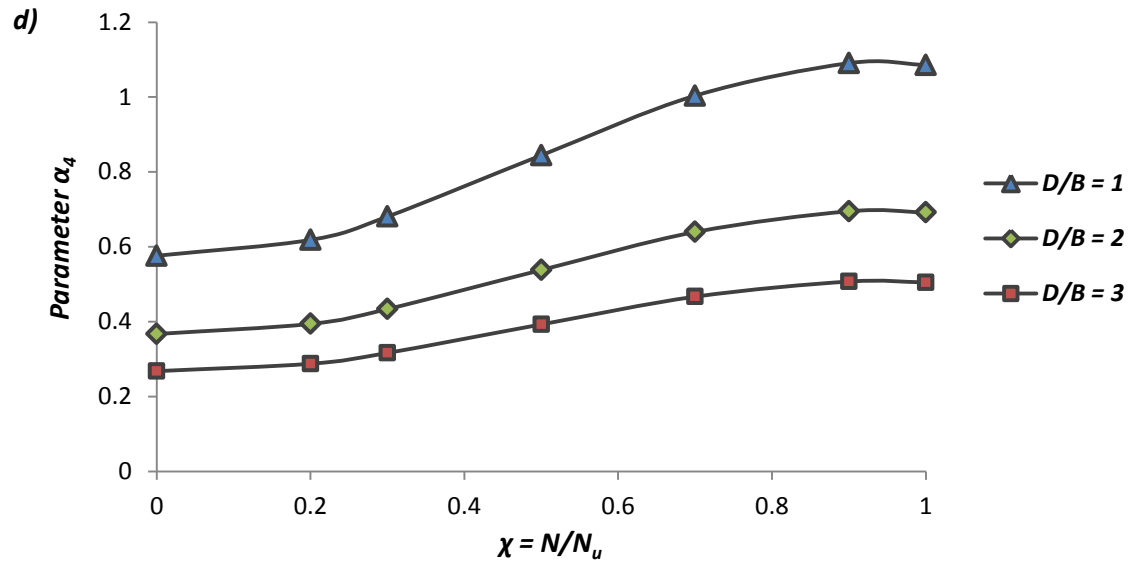

Figure 5.33 *Validation of the effectiveness of the analytical expressions to capture the basic trends of each of the parameters a_1, a_2, a_3 and a_4 that are incorporated in the proposed modified Gaussian distribution of the ultimate lateral soil reaction (Eq. 5.15).*

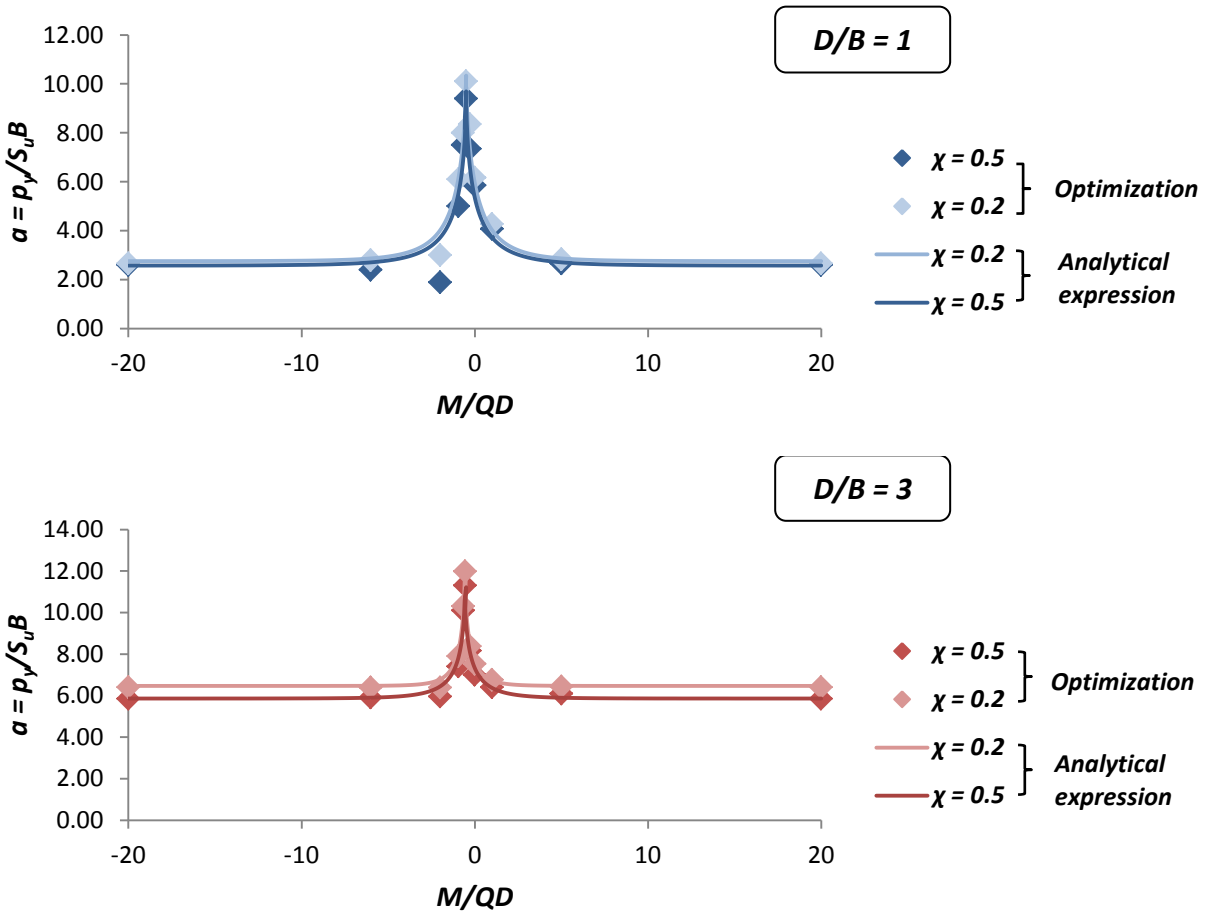

Figure 5.34 *Validation of the complete analytical expression's capacity to capture the ultimate mean lateral soil reaction in the case of two limit values of the embedment ratio and two characteristic values of the inverse factor of safety against vertical loading.*

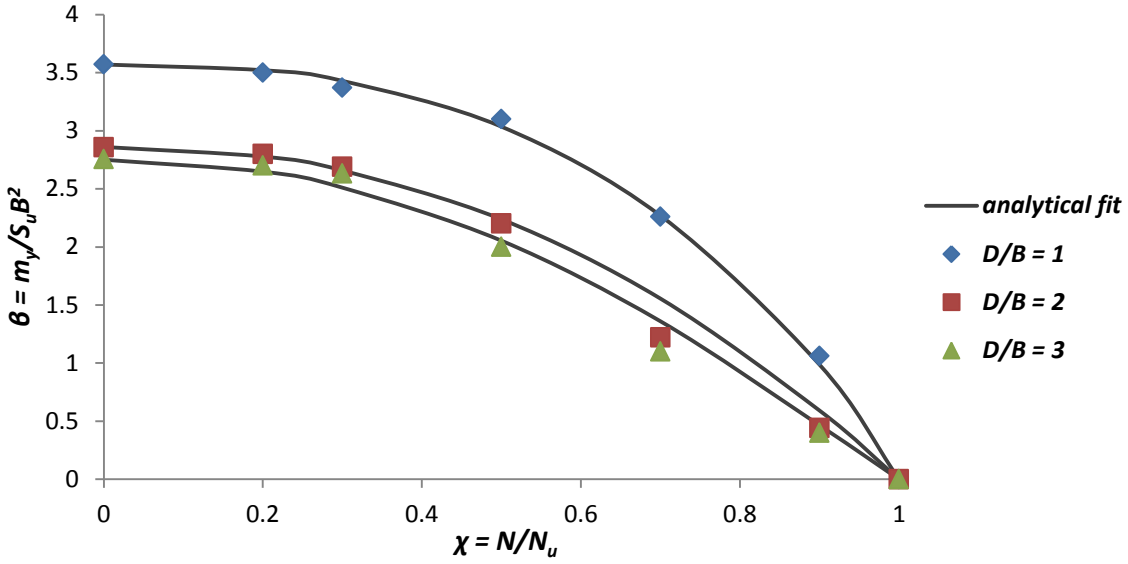

Figure 5.35 *Normalized ultimate resisting moment per unit depth vs Factor of safety against vertical loading for each of the embedment ratios considered herein. The data derived from the hybrid optimization approach are compared to the equivalent analytical expression deduced.*

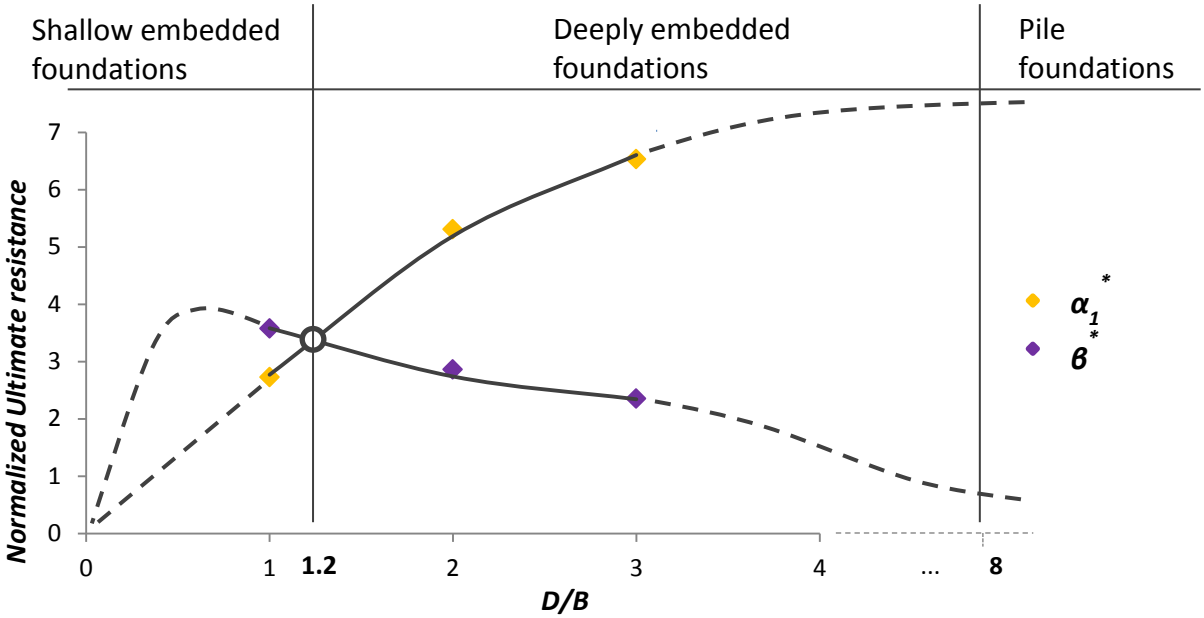

Figure 5.36 *Comparison between the normalized ultimate lateral soil reaction at its plateau and the ultimate resisting moment per unit depth under zero vertical loading component with respect to the embedment ratio. The intersection at D/B = 1.2 reminds us of the categorization given in Chapter 3 on the basis of the yield surface expansion behavior. Here, we introduce a different kind of categorization of the embedded foundations based on the contribution of the lateral soil reaction and the resisting moment per unit depth.*

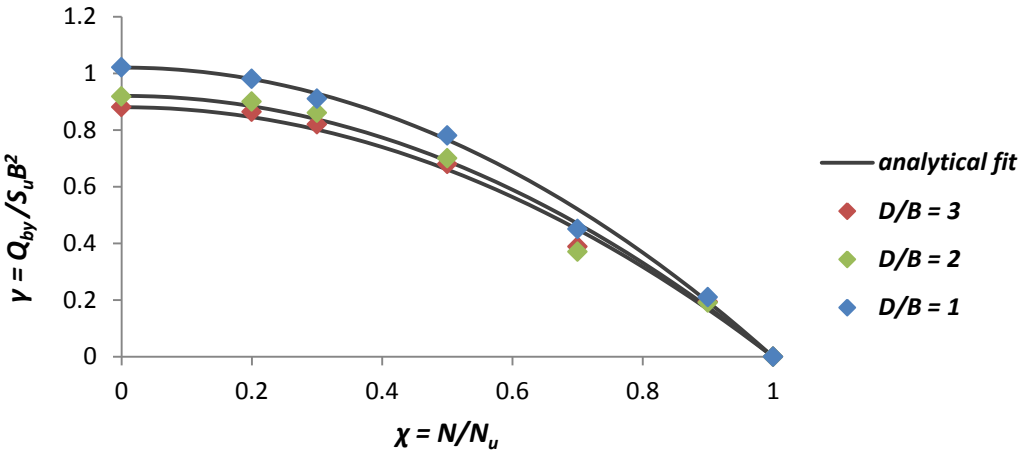

Figure 5.37 *Normalized ultimate base horizontal capacity vs Overall factor of safety against vertical loading for various embedment ratios: A simplified approach in which the uncoupled capacity is indirectly correlated to the factor of safety against vertical bearing capacity of the base via the embedment ratio D/B.*

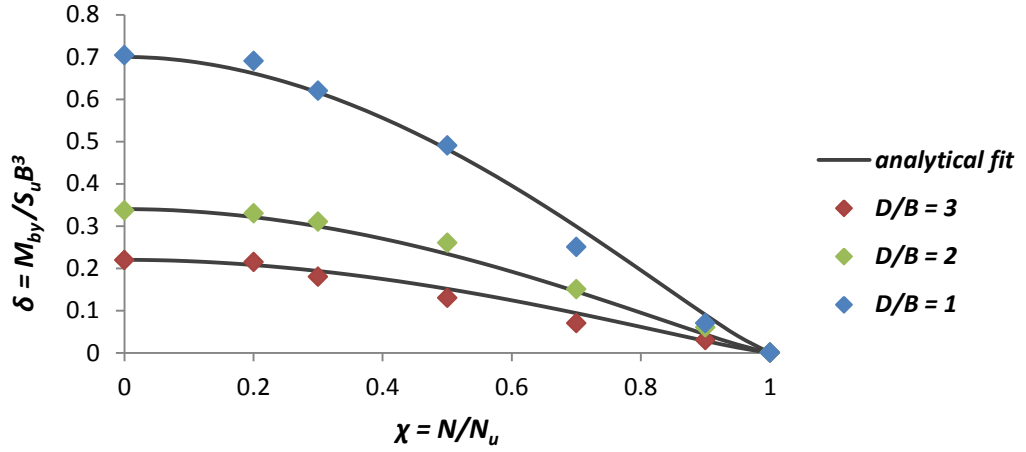

Figure 5.38 *Normalized ultimate base moment capacity vs Overall factor of safety against vertical loading for various embedment ratios: A simplified approach in which the uncoupled capacity is indirectly correlated to the factor of safety against vertical bearing capacity of the base via the embedment ratio D/B.*

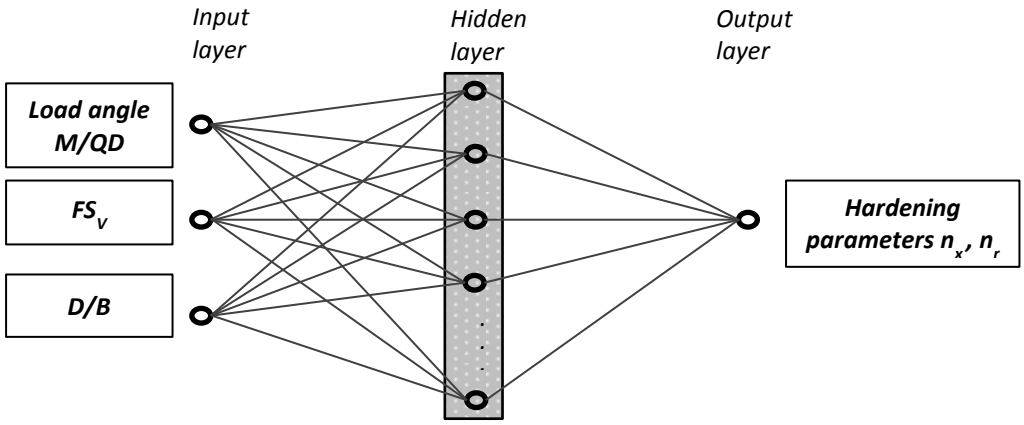

Figure 5.39 *Schematic representation of the neural network incorporated in the model.*

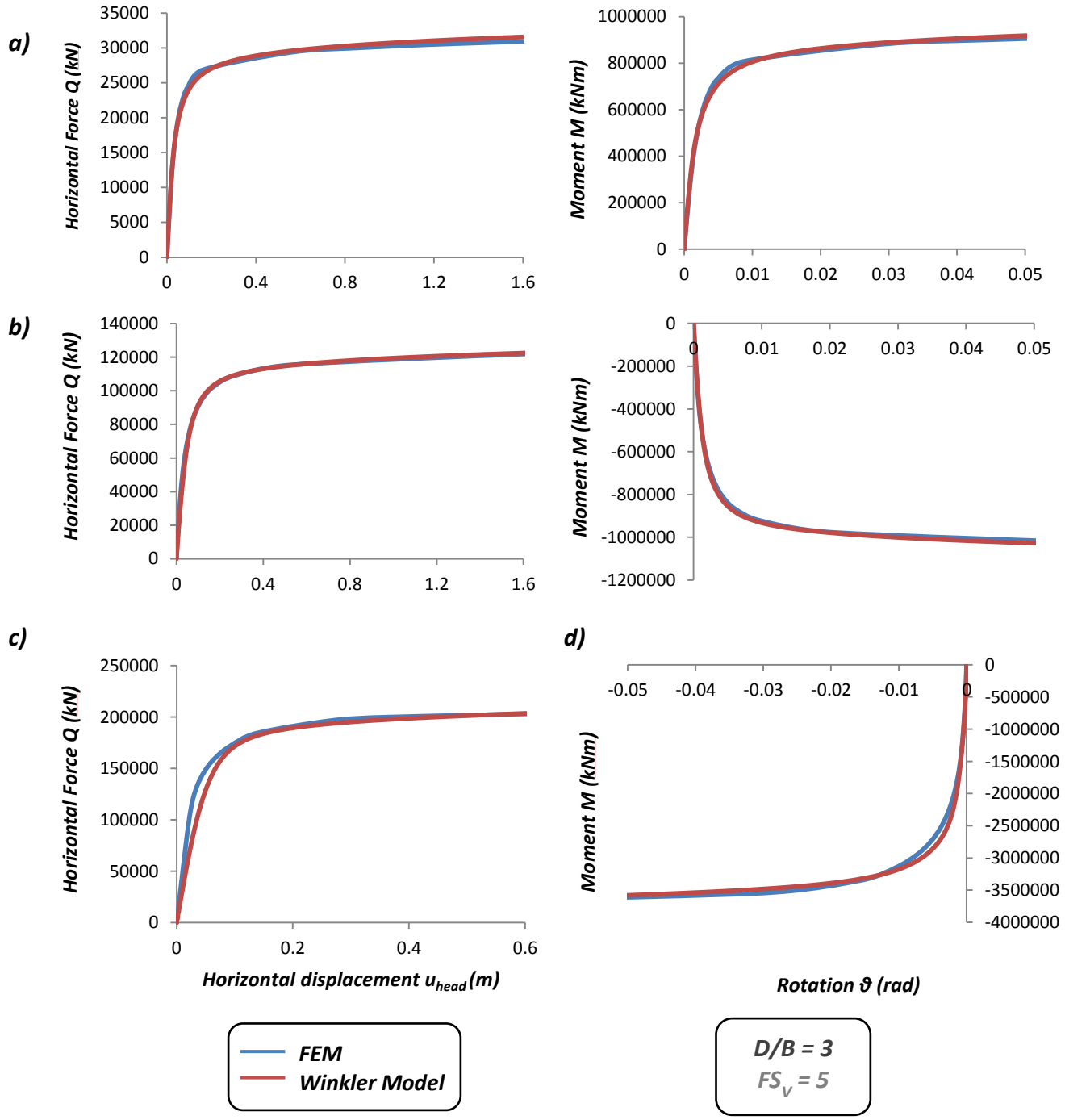

Figure 5.40 *Horizontal force vs horizontal displacement at the head and Moment vs rotation diagrams in the case of a deeply embedded (D/B = 3) caisson foundation characterized by a factors of safety against vertical bearing capacity failure FS_V = 5. The curves derived from 3D FE analyses are represented by the blue lines, whereas the curves produced by the Winkler model are represented by the red lines. Figures a) and b) correspond to points in the scoop-slide region of the yield surface (in the first and second quadrant respectively), while figures c) and d) correspond to the points of maximum horizontal and moment capacity.*

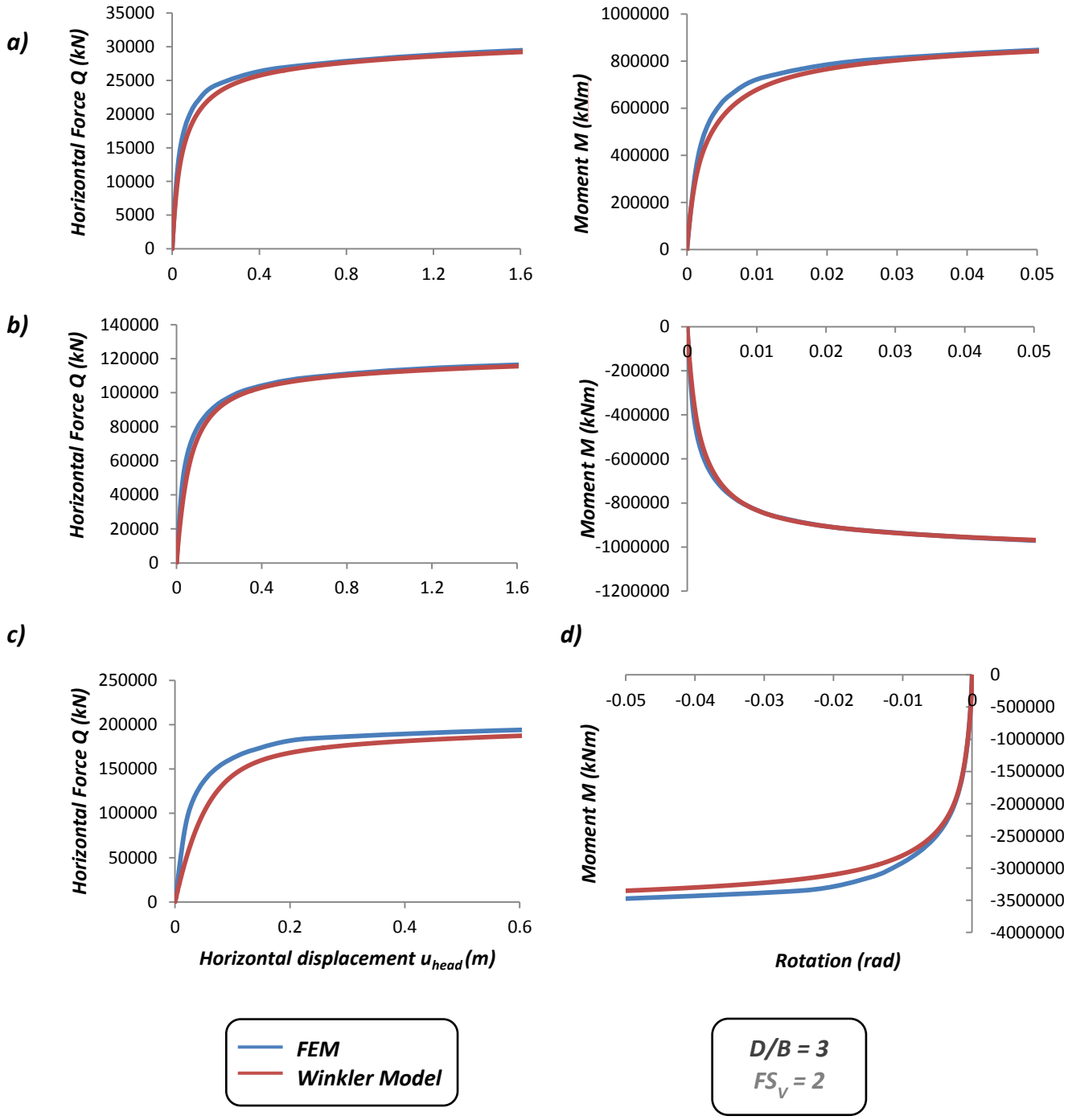

Figure 5.41 *Horizontal force vs horizontal displacement at the head and Moment vs rotation diagrams in the case of a deeply embedded (D/B = 3) caisson foundation characterized by a factors of safety against vertical bearing capacity failure FS_V = 2. The curves derived from 3D FE analyses are represented by the blue lines, whereas the curves produced by the Winkler model are represented by the red lines. Figures a) and b) correspond to points in the scoop-slide region of the yield surface (in the first and second quadrant respectively), while figures c) and d) correspond to the points of maximum horizontal and moment capacity.*

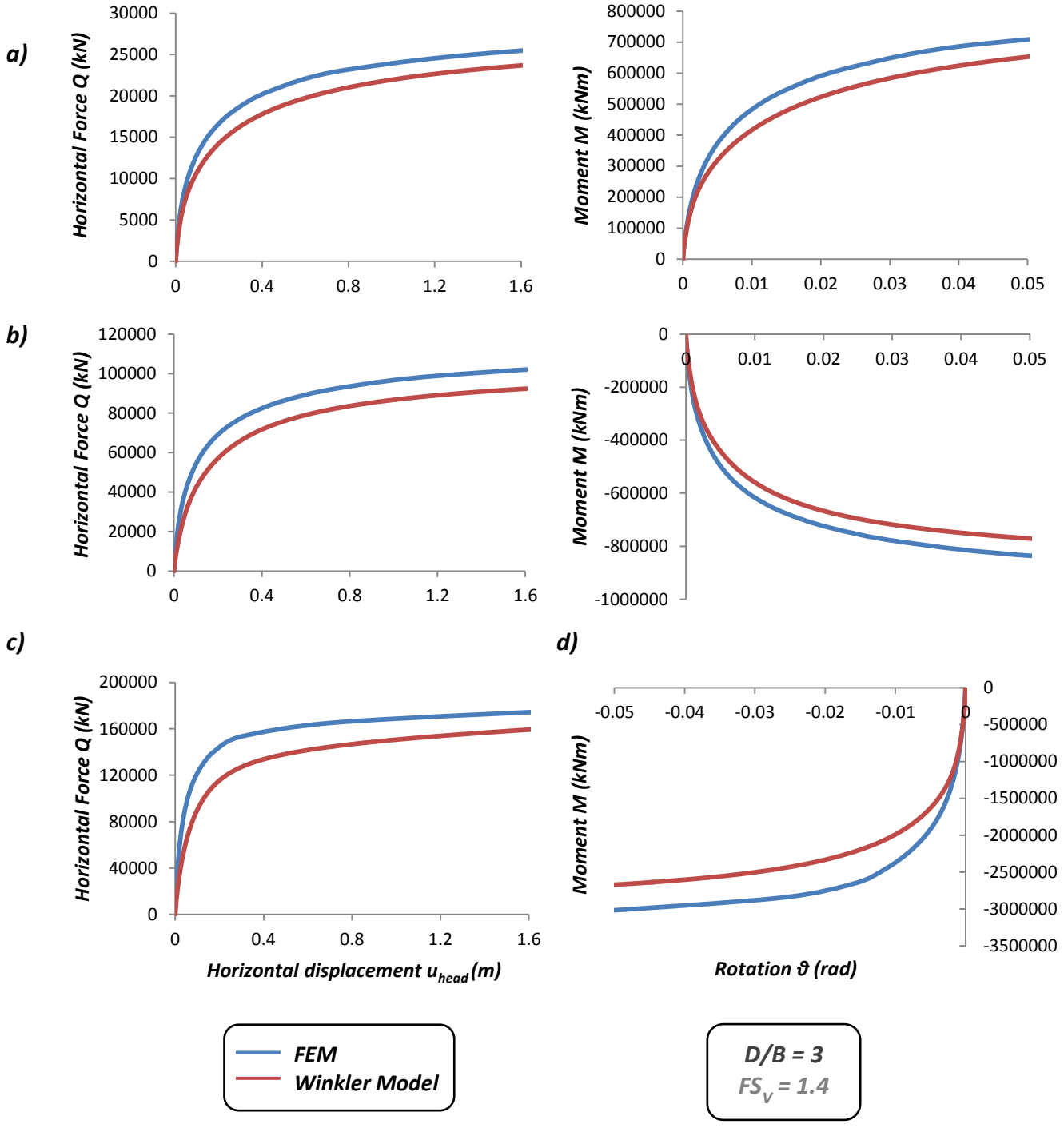

Figure 5.42 *Horizontal force vs horizontal displacement at the head and Moment vs rotation diagrams in the case of a deeply embedded (D/B = 3) caisson foundation characterized by a factors of safety against vertical bearing capacity failure FS_V = 1.4. The curves derived from 3D FE analyses are represented by the blue lines, whereas the curves produced by the Winkler model are represented by the red lines. Figures a) and b) correspond to points in the scoop-slide region of the yield surface (in the first and second quadrant respectively), while figures c) and d) correspond to the points of maximum horizontal and moment capacity.*

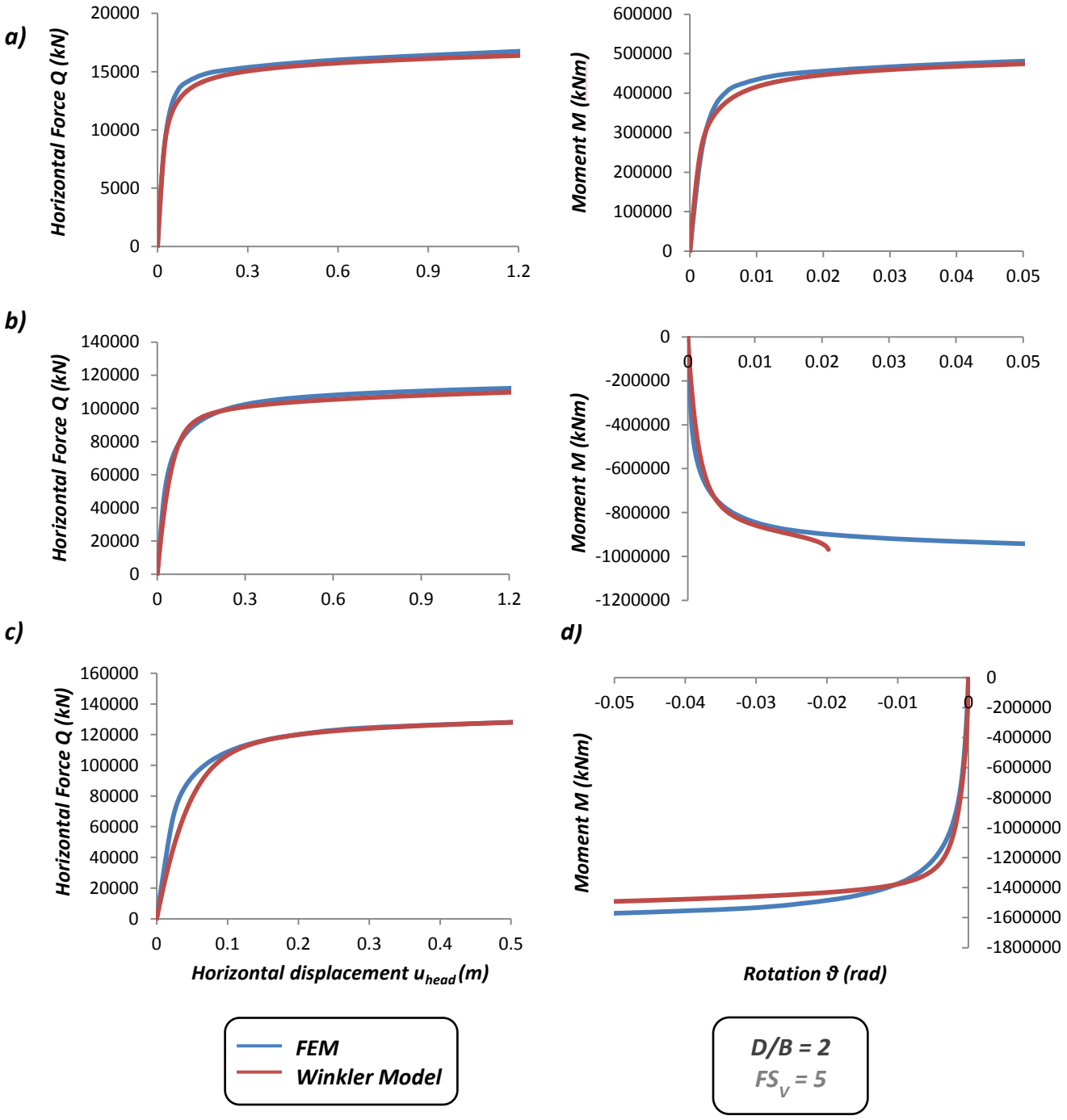

Figure 5.43 *Horizontal force vs horizontal displacement at the head and Moment vs rotation diagrams in the case of a deeply embedded (D/B = 2) caisson foundation characterized by a factor of safety against vertical bearing capacity failure FS_V = 5. The curves derived from 3D FE analyses are represented by the blue lines, whereas the curves produced by the Winkler model are represented by the red lines. Figures a) and b) correspond to points in the scoop-slide region of the yield surface (in the first and second quadrant respectively), while figures c) and d) correspond to the points of maximum horizontal and moment capacity.*

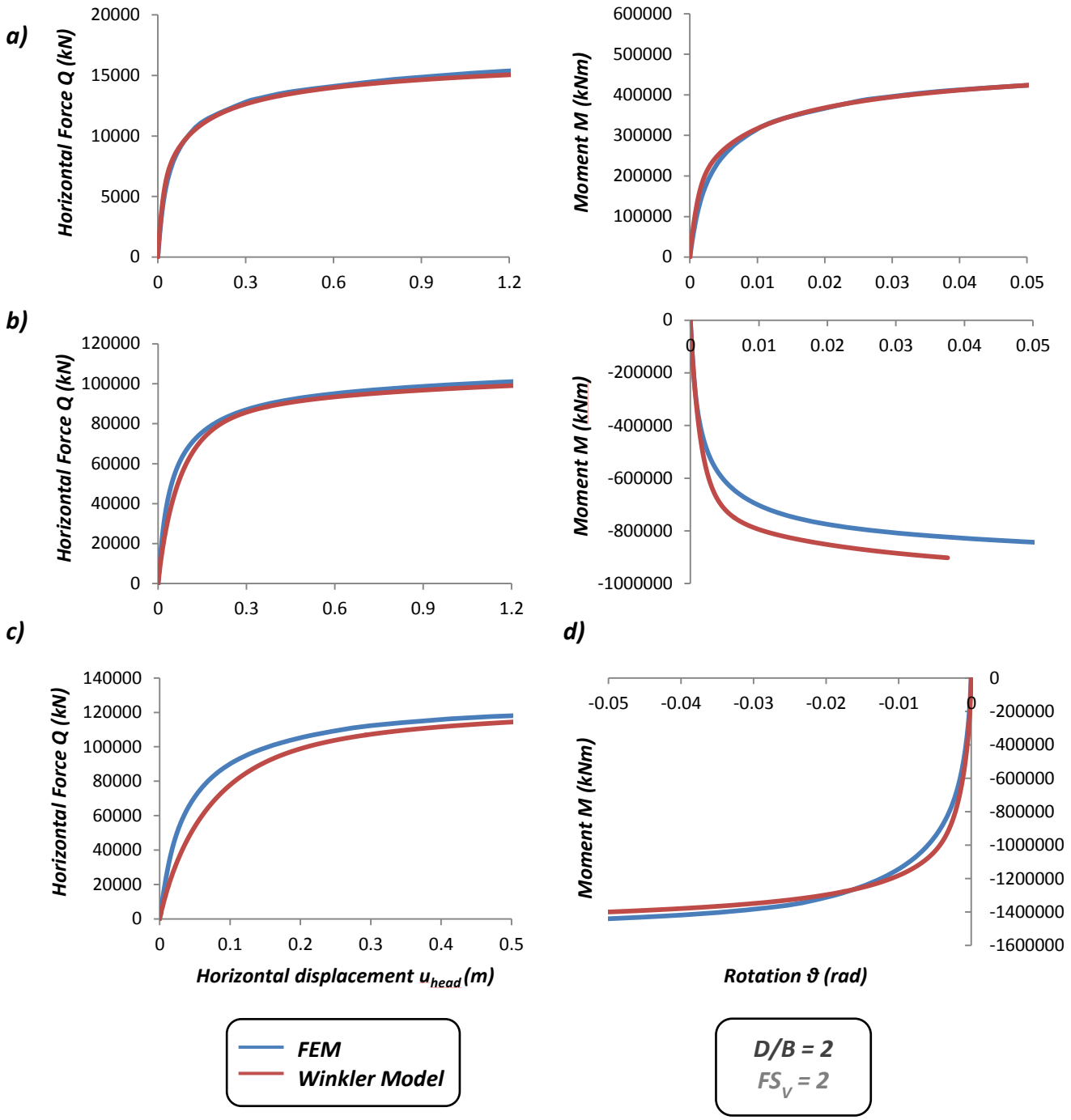

Figure 5.44 *Horizontal force vs horizontal displacement at the head and Moment vs rotation diagrams in the case of a deeply embedded (D/B = 2) caisson foundation characterized by a factor of safety against vertical bearing capacity failure FS_V = 2. The curves derived from 3D FE analyses are represented by the blue lines, whereas the curves produced by the Winkler model are represented by the red lines. Figures a) and b) correspond to points in the scoop-slide region of the yield surface (in the first and second quadrant respectively), while figures c) and d) correspond to the points of maximum horizontal and moment capacity.*

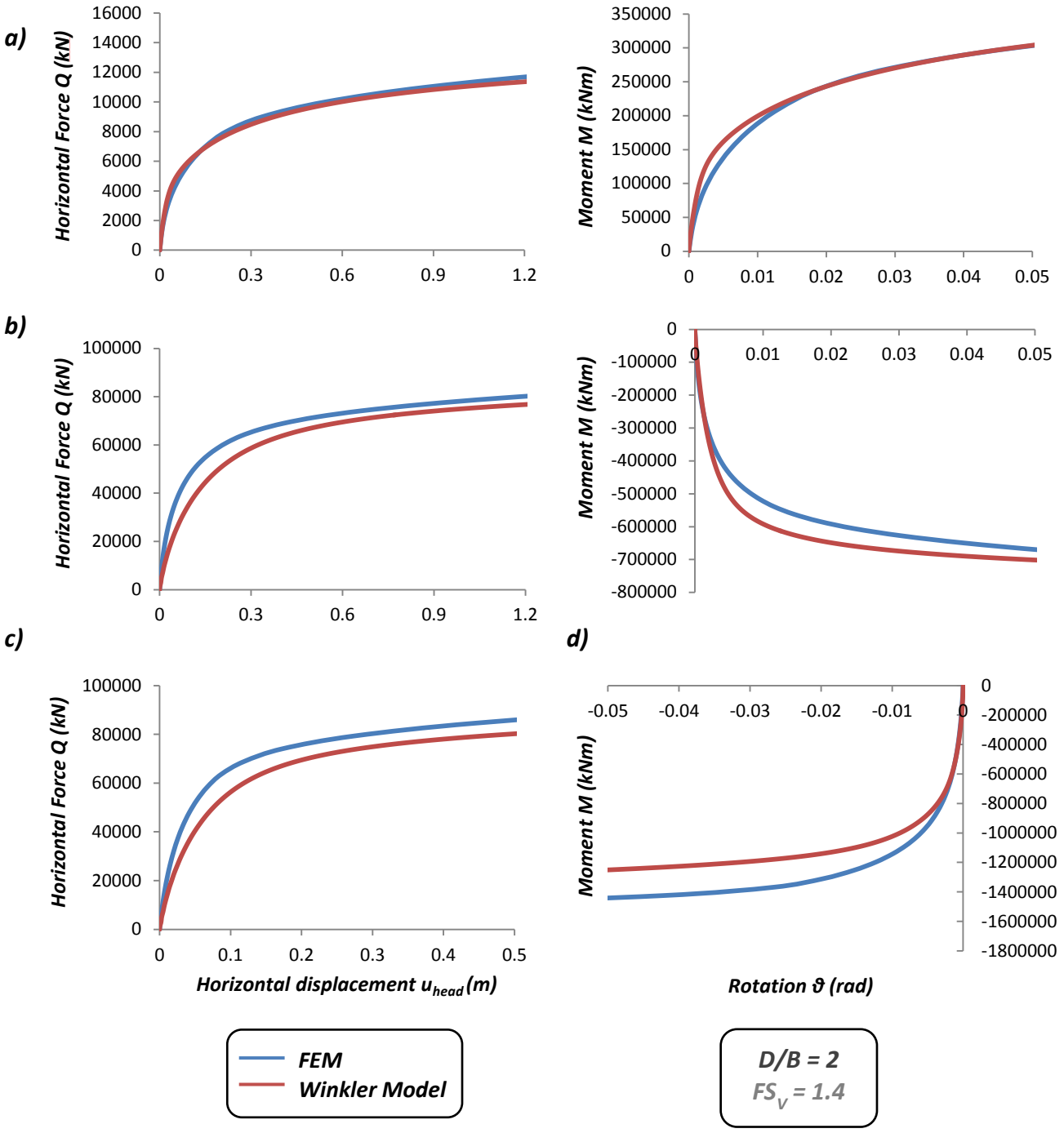

Figure 5.45 *Horizontal force vs horizontal displacement at the head and Moment vs rotation diagrams in the case of a deeply embedded (D/B = 2) caisson foundation characterized by a factor of safety against vertical bearing capacity failure FS_V = 1.4. The curves derived from 3D FE analyses are represented by the blue lines, whereas the curves produced by the Winkler model are represented by the red lines. Figures a) and b) correspond to points in the scoop-slide region of the yield surface (in the first and second quadrant respectively), while figures c) and d) correspond to the points of maximum horizontal and moment capacity.*

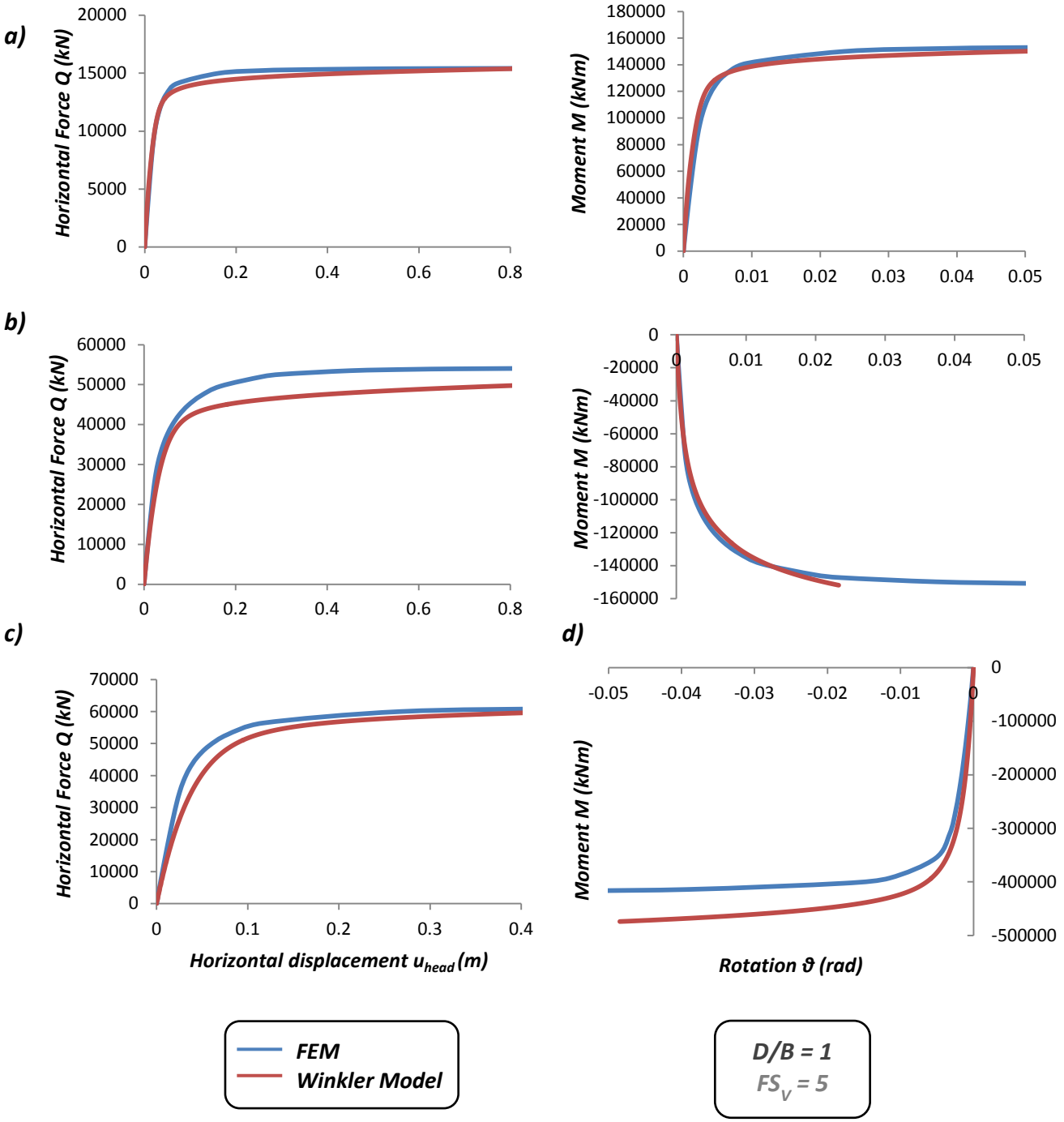

Figure 5.46 *Horizontal force vs horizontal displacement at the head and Moment vs rotation diagrams in the case of a shallow embedded (D/B = 1) caisson foundation characterized by a factor of safety against vertical bearing capacity failure FS_V = 5. The curves derived from 3D FE analyses are represented by the blue lines, whereas the curves produced by the Winkler model are represented by the red lines. Figures a) and b) correspond to points in the scoop-slide region of the yield surface (in the first and second quadrant respectively), while figures c) and d) correspond to the points of maximum horizontal and moment capacity.*

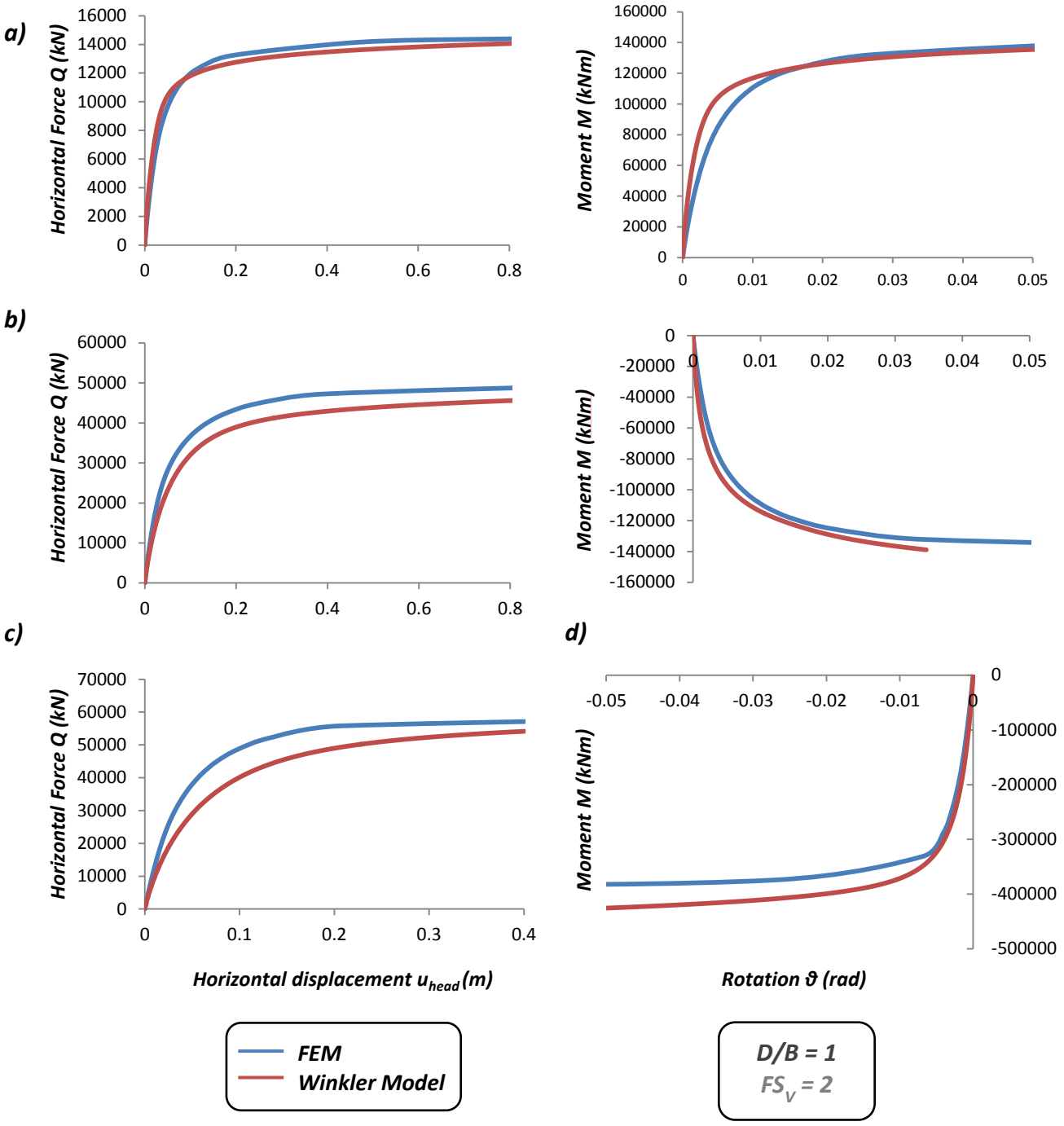

Figure 5.47 *Horizontal force vs horizontal displacement at the head and Moment vs rotation diagrams in the case of a shallow embedded (D/B = 1) caisson foundation characterized by a factor of safety against vertical bearing capacity failure FS_V = 2. The curves derived from 3D FE analyses are represented by the blue lines, whereas the curves produced by the Winkler model are represented by the red lines. Figures a) and b) correspond to points in the scoop-slide region of the yield surface (in the first and second quadrant respectively), while figures c) and d) correspond to the points of maximum horizontal and moment capacity.*

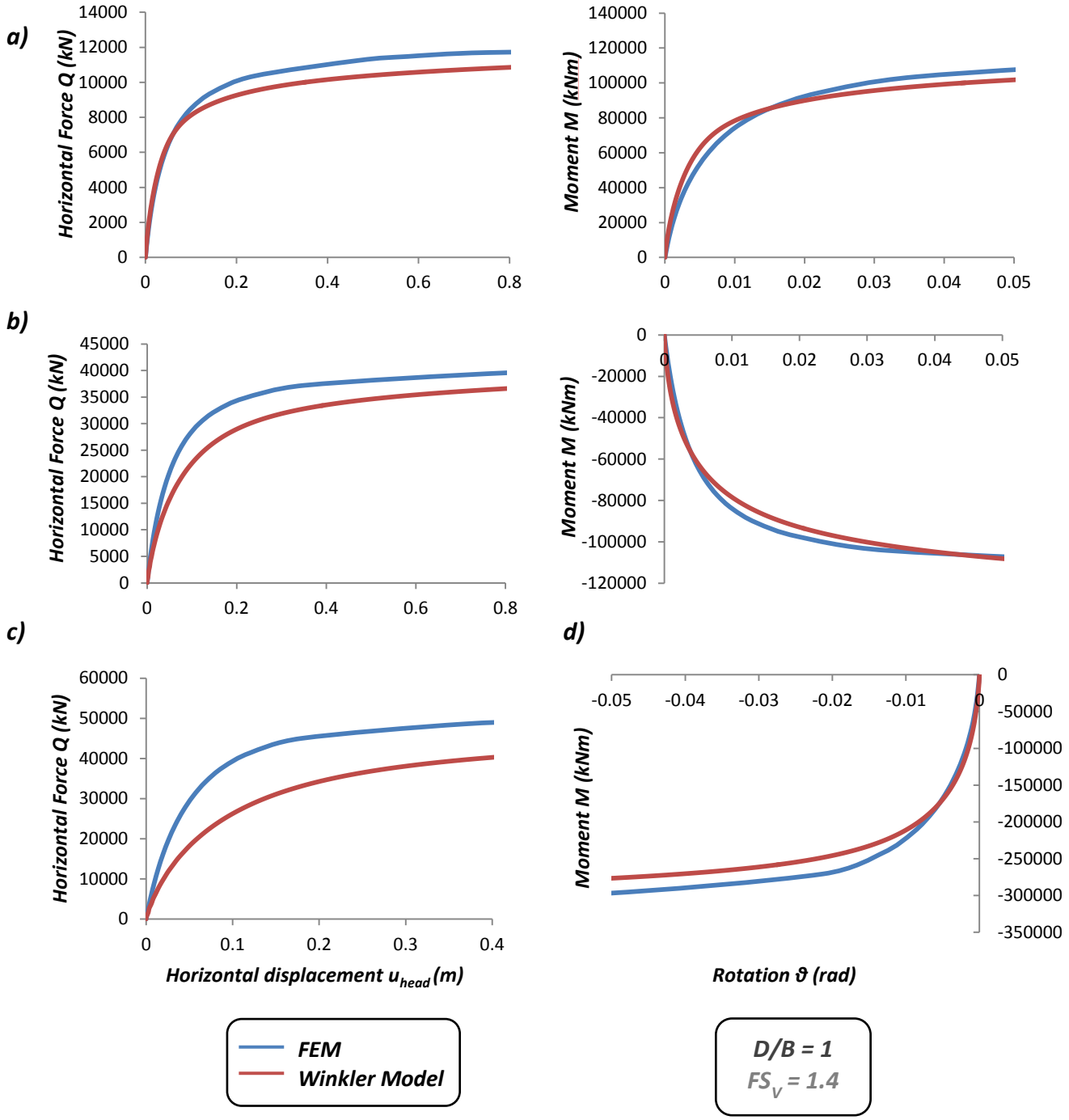

Figure 5.48 *Horizontal force vs horizontal displacement at the head and Moment vs rotation diagrams in the case of a shallow embedded (D/B = 1) caisson foundation characterized by a factor of safety against vertical bearing capacity failure FS_V = 1.4. The curves derived from 3D FE analyses are represented by the blue lines, whereas the curves produced by the Winkler model are represented by the red lines. Figures a) and b) correspond to points in the scoop-slide region of the yield surface (in the first and second quadrant respectively), while figures c) and d) correspond to the points of maximum horizontal and moment capacity*

a)

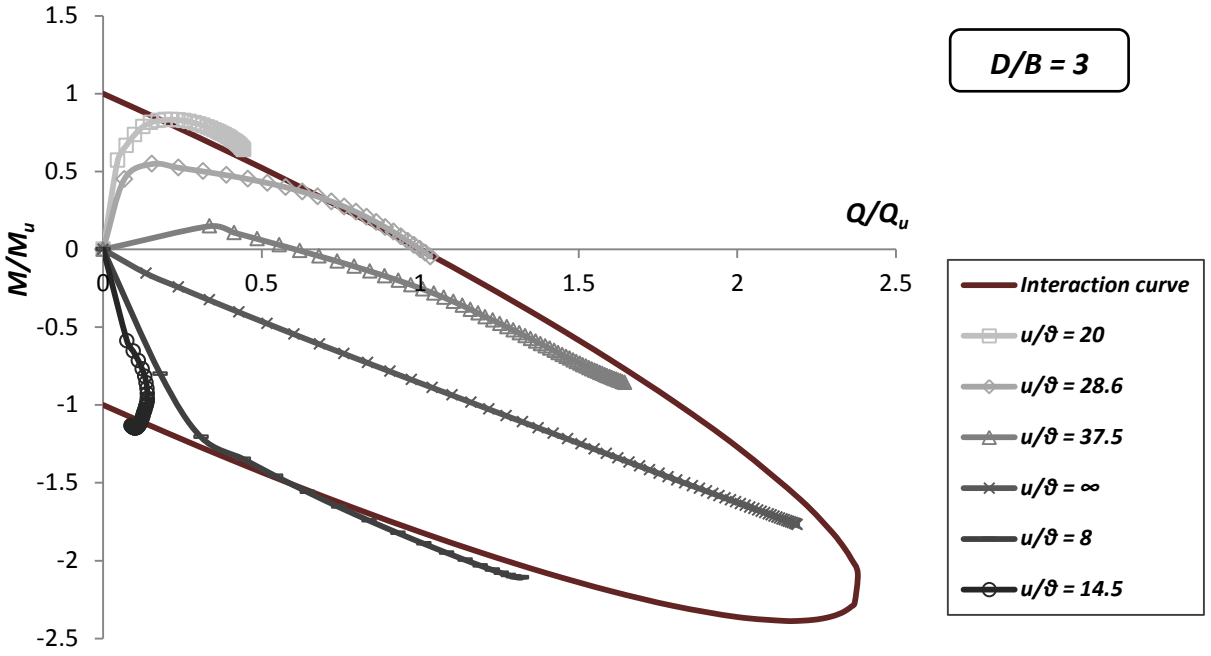
D/B = 3
M/M_u
Q/Q_u
1.5
1
0.5
0
-0.5
-1
-1.5
-2
-2.5
0
0.5
1
1.5
2
2.5
Interaction curve
u/ϑ = 20
u/ϑ = 28.6
u/ϑ = 37.5
u/ϑ = ∞
u/ϑ = 8
u/ϑ = 14.5

b)

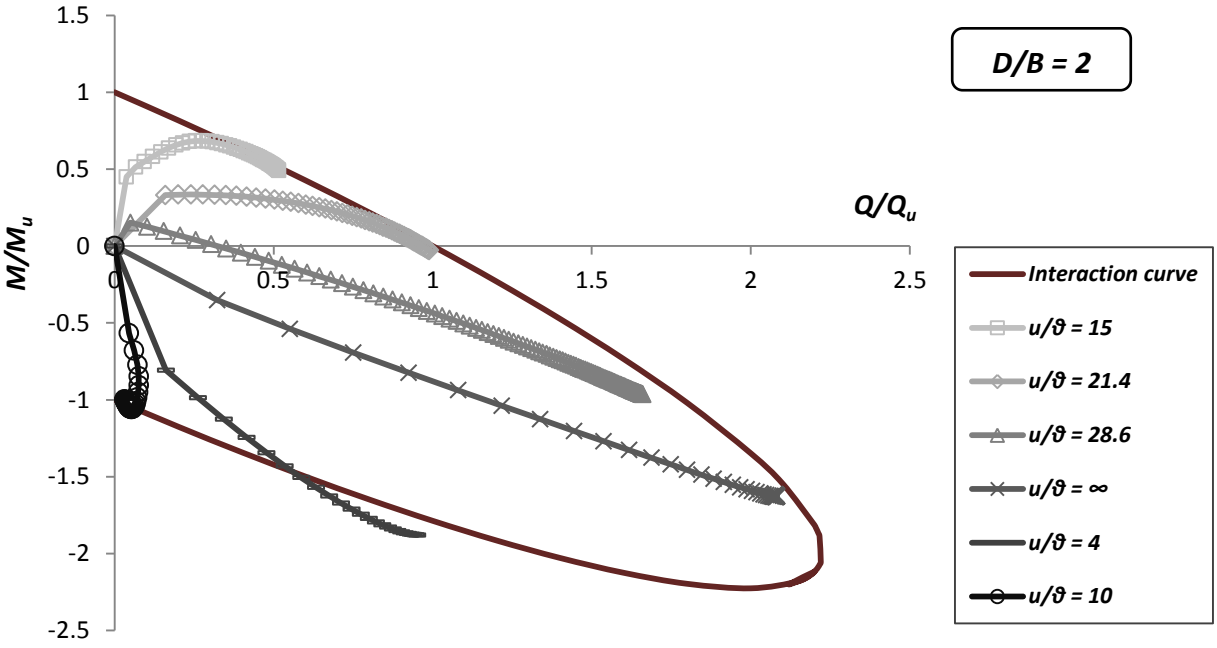
D/B = 2
M/M_u
Q/Q_u
1.5
1
0.5
0
-0.5
-1
-1.5
-2
-2.5
0
0.5
1
1.5
2
2.5
Interaction curve
u/ϑ = 15
u/ϑ = 21.4
u/ϑ = 28.6
u/ϑ = ∞
u/ϑ = 4
u/ϑ = 10

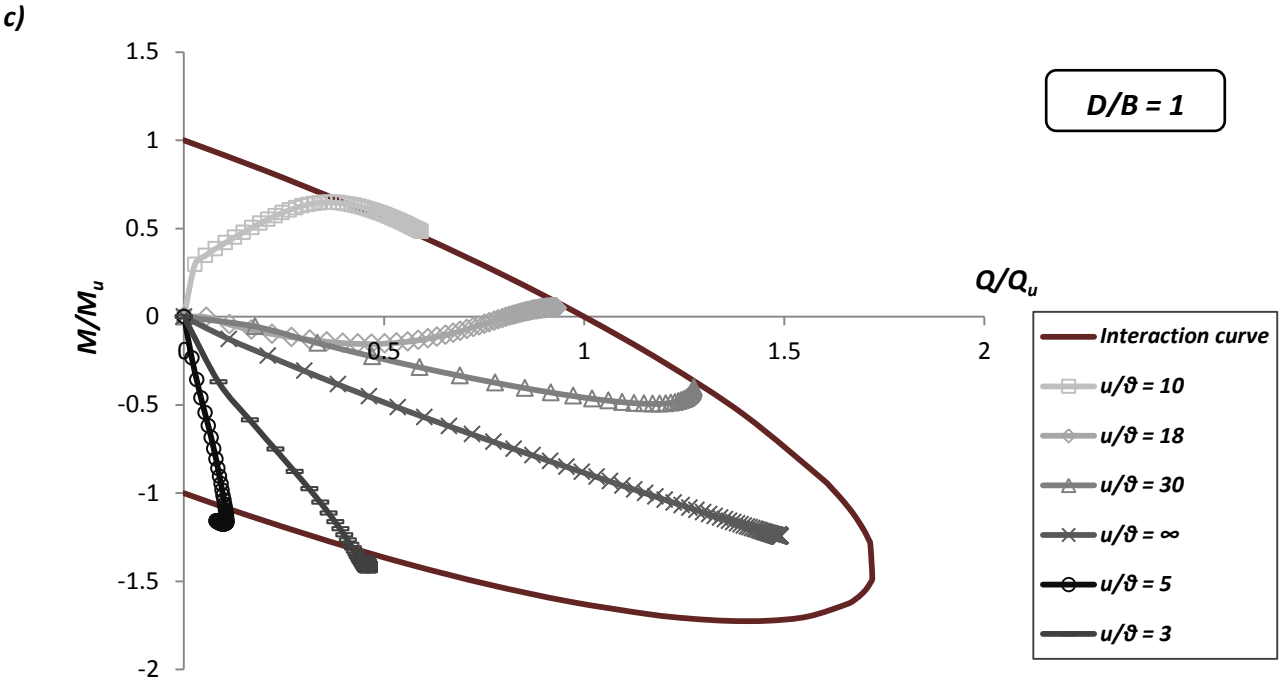

Figure 5.49 *Comparison between swipe tests carried out with the calibrated Winkler model and the interaction curves deduced from FE analyses. Three lightly loaded (FS_V = 5) caisson foundations with embedment ratio: a) D/B = 3, b) D/B = 2 and c) D/B = 1 were considered. The model displays remarkable ability to capture the displacement –controlled response to failure.*

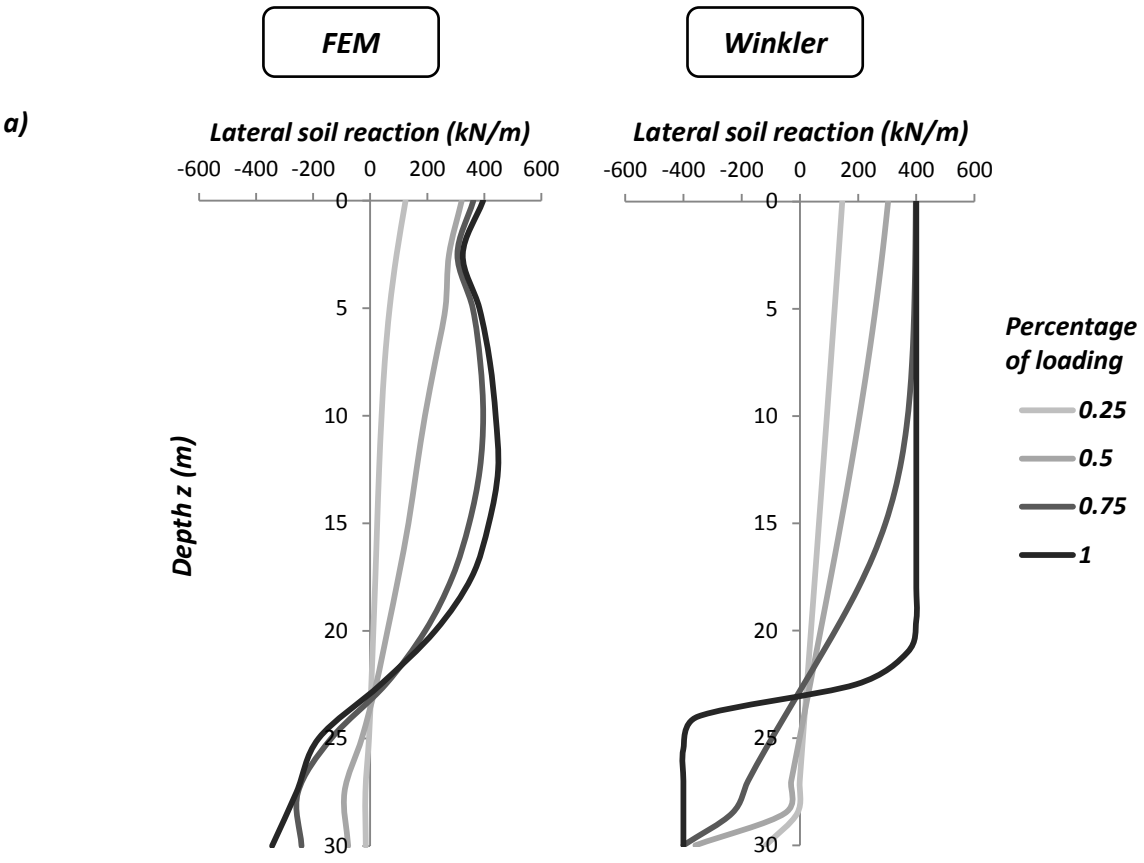

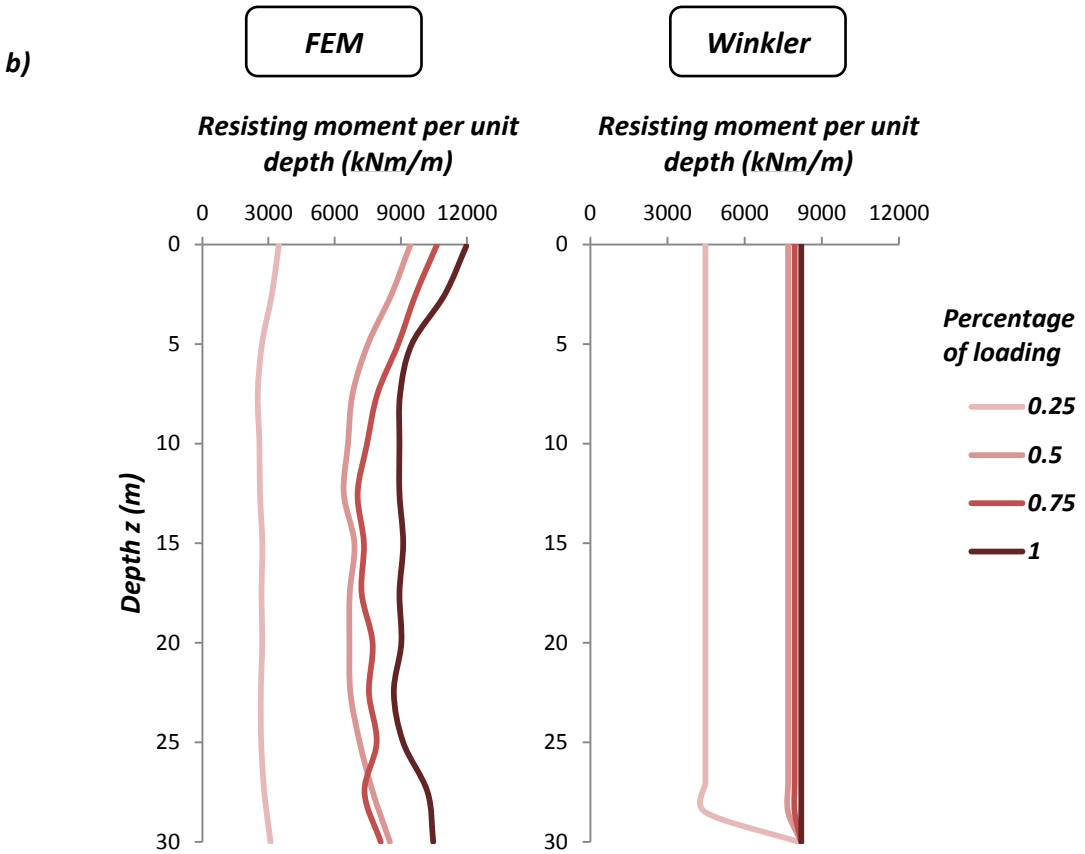

Figure 5.50 *Comparison between the lateral soil reaction (a) and resisting moment per unit depth (b) time – histories as derived from the F analyses and the calibrated Winkler model. This case refers to a caisson foundation with embedment ratio D/B = 3 subject to combined M-Q loading corresponding to the scoop-slide region of the yield surface.*

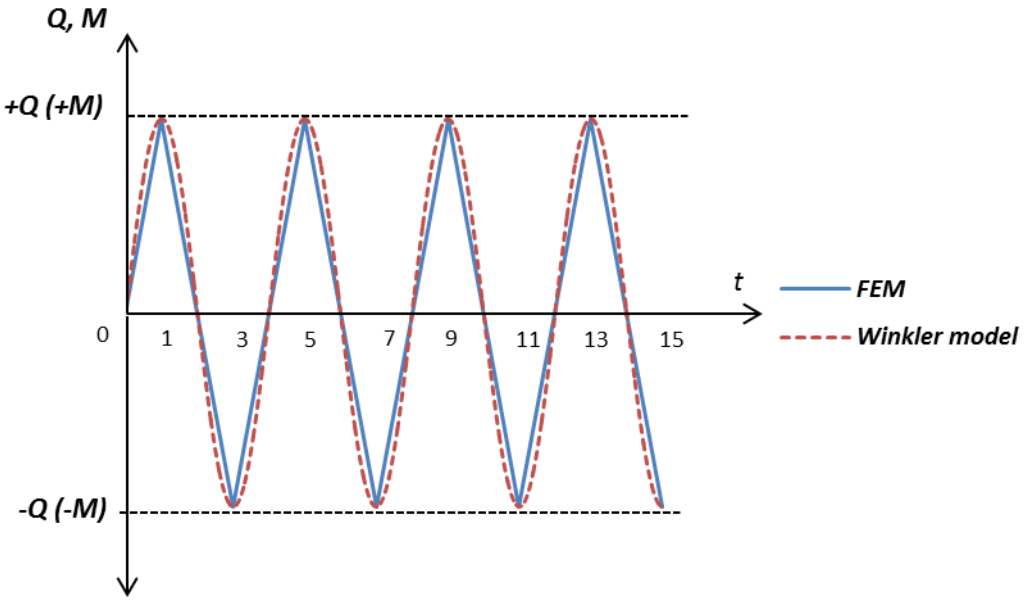

Figure 5.51 *Combined M-Q cyclic loading pattern applied to the head of the caisson foundations. A linear sequence of static steps was applied in the FE analyses, whereas an equivalent sinusoid "static" pattern was applied in the Winkler model for viscosity reasons.*

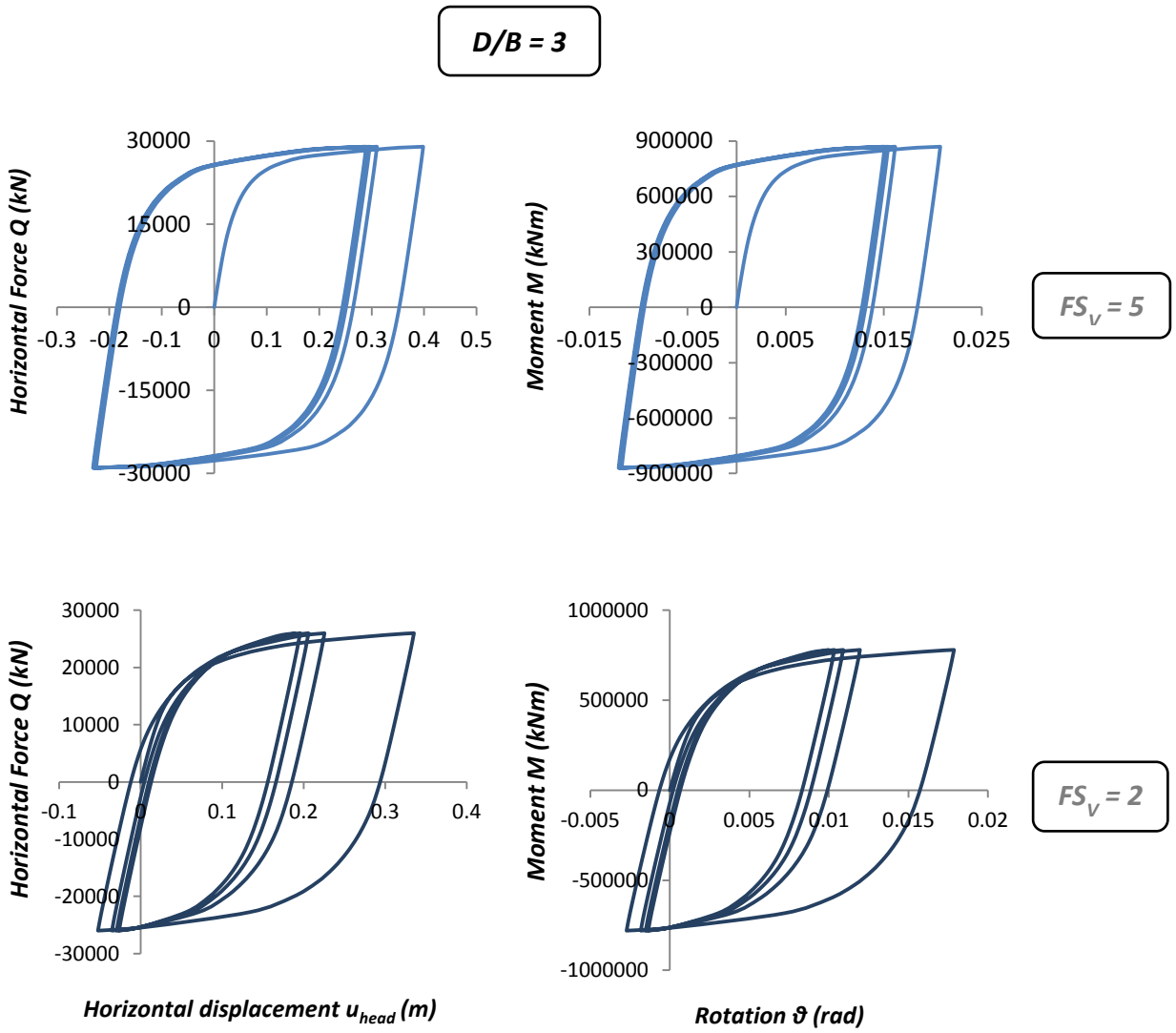

Figure 5.52 *The horizontal force-head displacement and moment-rotation loops for a lightly and a heavily loaded caisson foundation of embedment ratio D/B = 3 under combined M-Q loading corresponding to the 1st quadrant of the scoop slide region. The lightly loaded system ($FS_V = 5$) displays a rather symmetric behavior with limited hardening taking place only in the first cycle of loading. The heavily loaded system ($FS_V = 2$) has a considerably asymmetric response experiencing hardening with decreasing rate.*

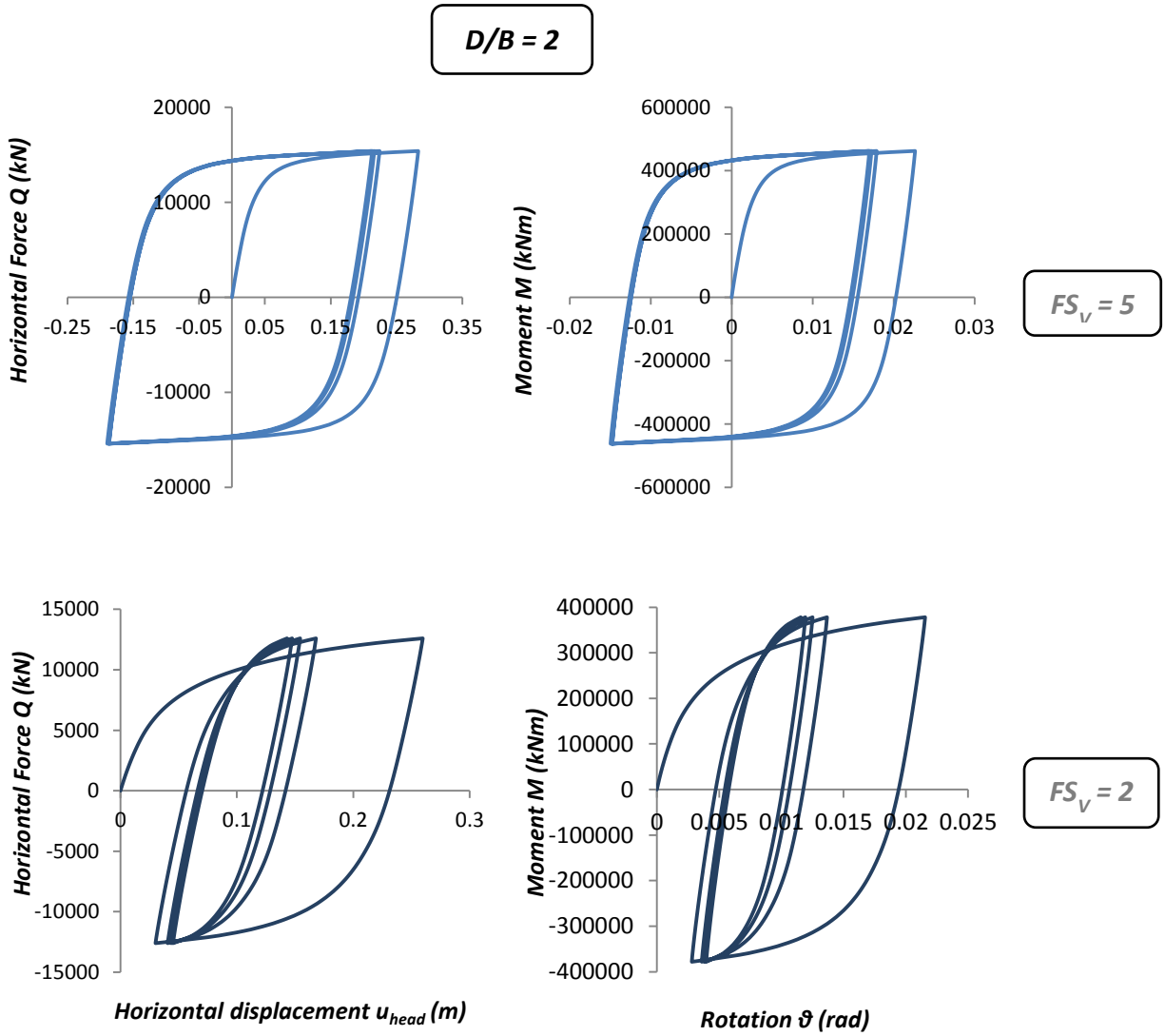

Figure 5.53 *The horizontal force-head displacement and moment-rotation loops for a lightly and a heavily loaded caisson foundation of embedment ratio D/B = 2 under combined M-Q loading corresponding to the 1st quadrant of the scoop slide region. The lightly loaded system (FS_V = 5) displays a rather symmetric behavior with limited hardening taking place only in the first cycle of loading. The heavily loaded system (FS_V = 2) has a considerably asymmetric response experiencing hardening with decreasing rate.*

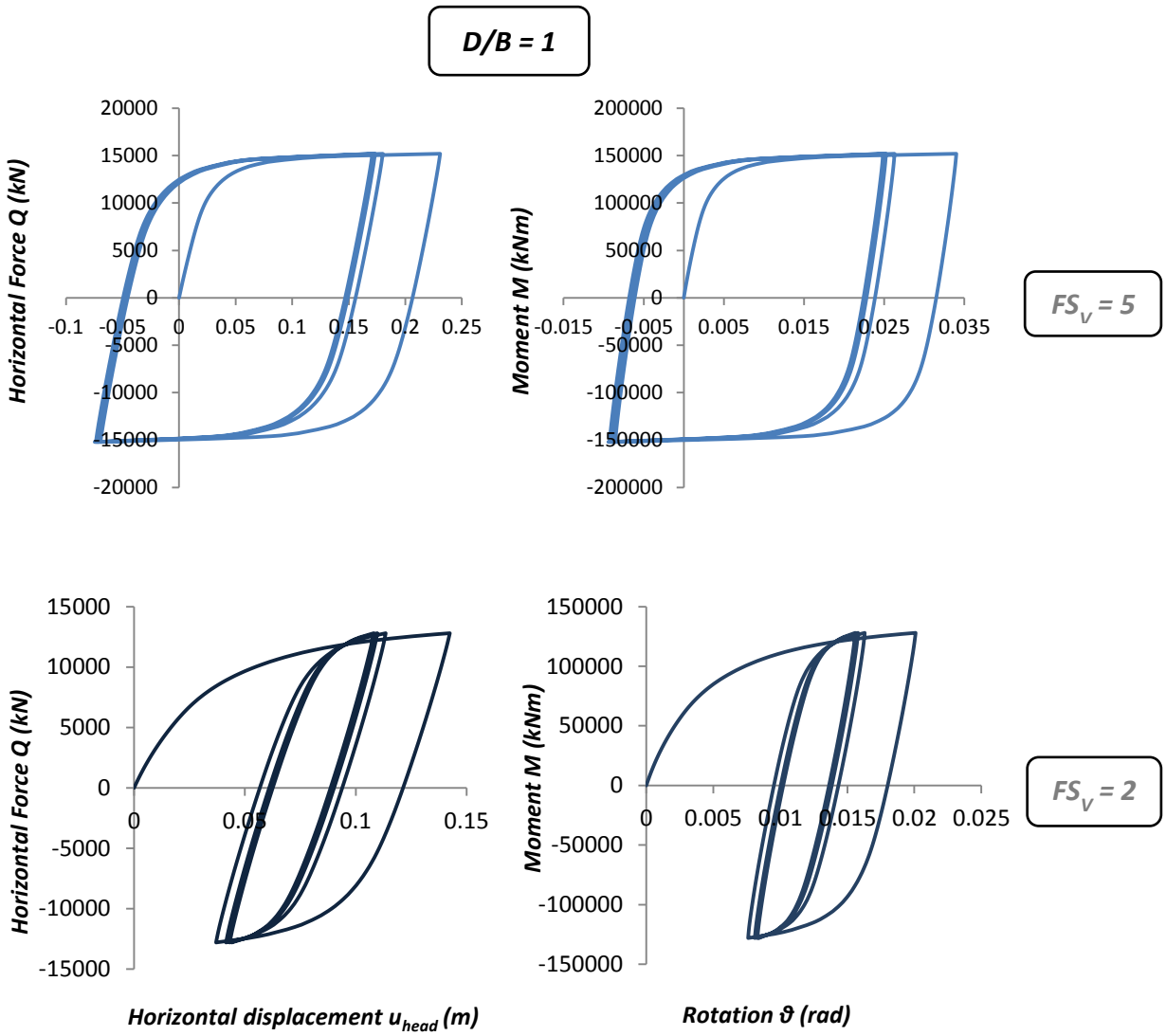

Figure 5.54 *The horizontal force-head displacement and moment-rotation loops for a lightly and a heavily loaded caisson foundation of embedment ratio D/B = 1 under combined M-Q loading corresponding to the 1st quadrant of the scoop slide region. The lightly loaded system (FS_V = 5) displays a more symmetric behavior with limited hardening taking place only in the first cycle of loading. The heavily loaded system (FS_V = 2) has a considerably asymmetric response experiencing hardening with decreasing rate.*

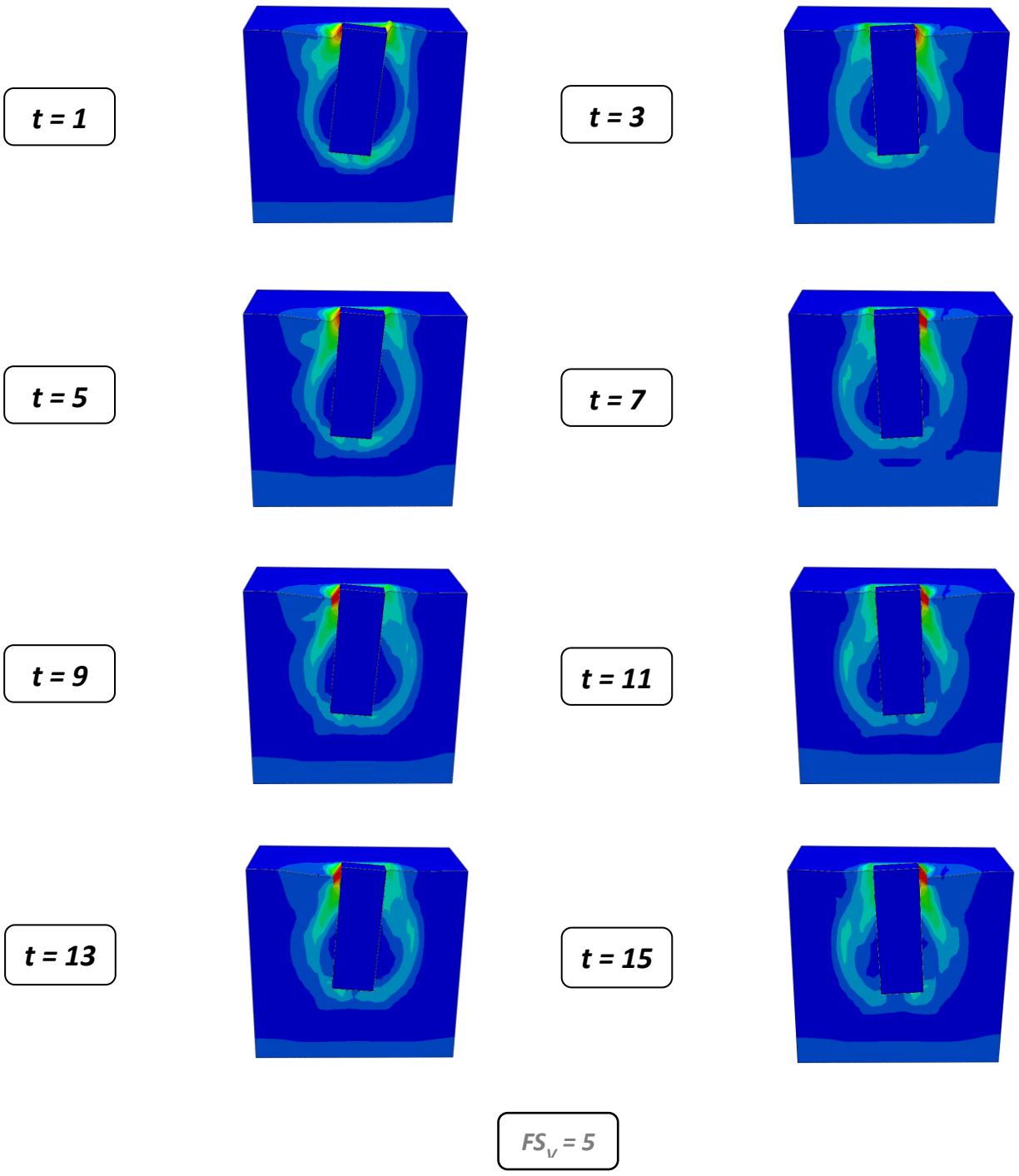

Figure 5.55 *Time history of the plastic strain magnitude contours in the case of a deeply embedded (D/B = 3) foundation subject to cyclic combined M-Q loading at its head for a large factor of safety against vertical loading (FS_V = 5). The absence of considerable vertical load leads to a symmetric response.*

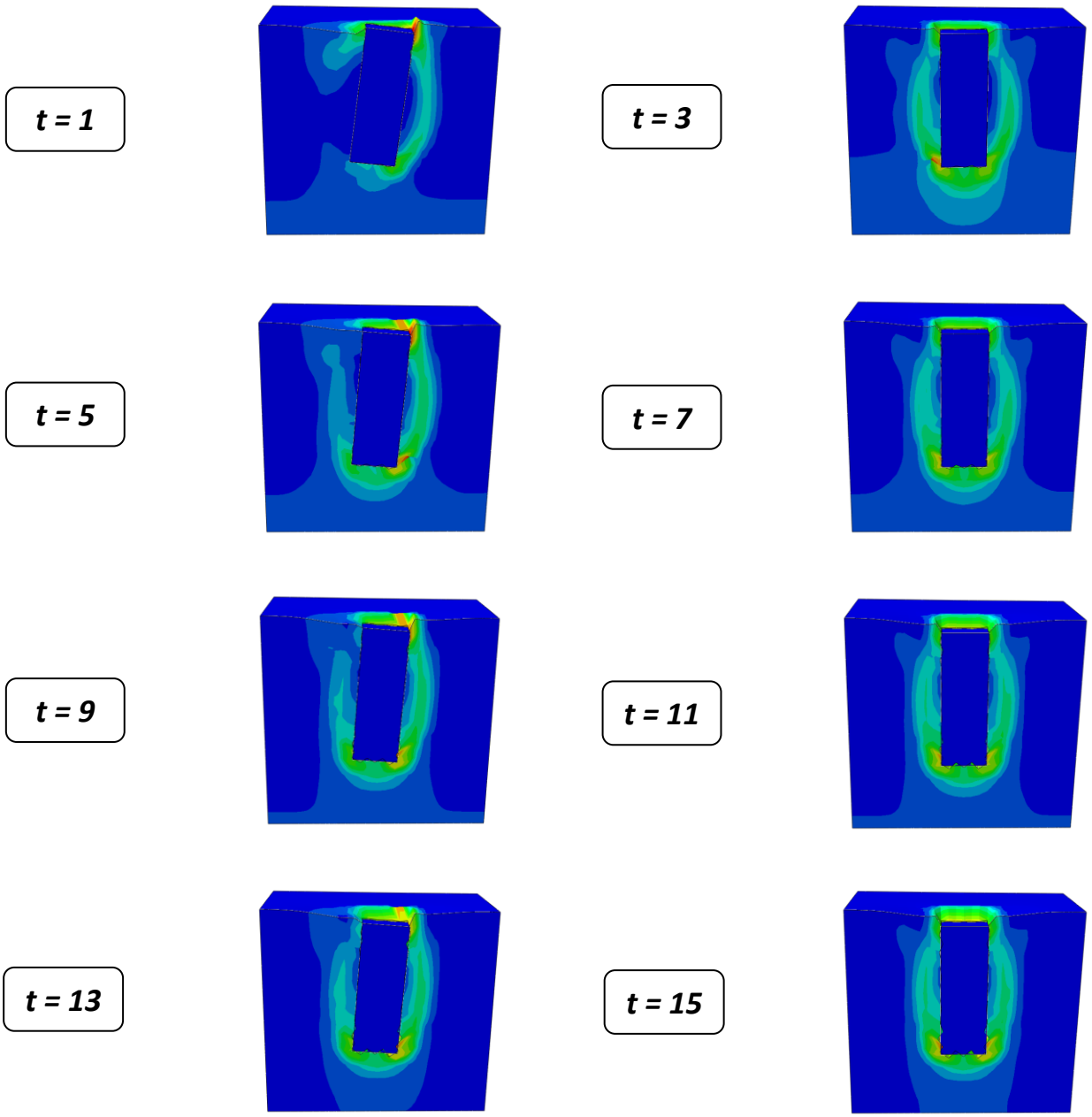

Figure 5.56 *Time history of the plastic strain magnitude contours in the case of a deeply embedded (D/B = 3) foundation subject to cyclic combined M-Q loading at its head for a small factor of safety against vertical loading (FS_V = 2). The presence of considerable vertical load leads to an asymmetric response by trapping the plastification at the side of the caisson in the direction of the first load section.*

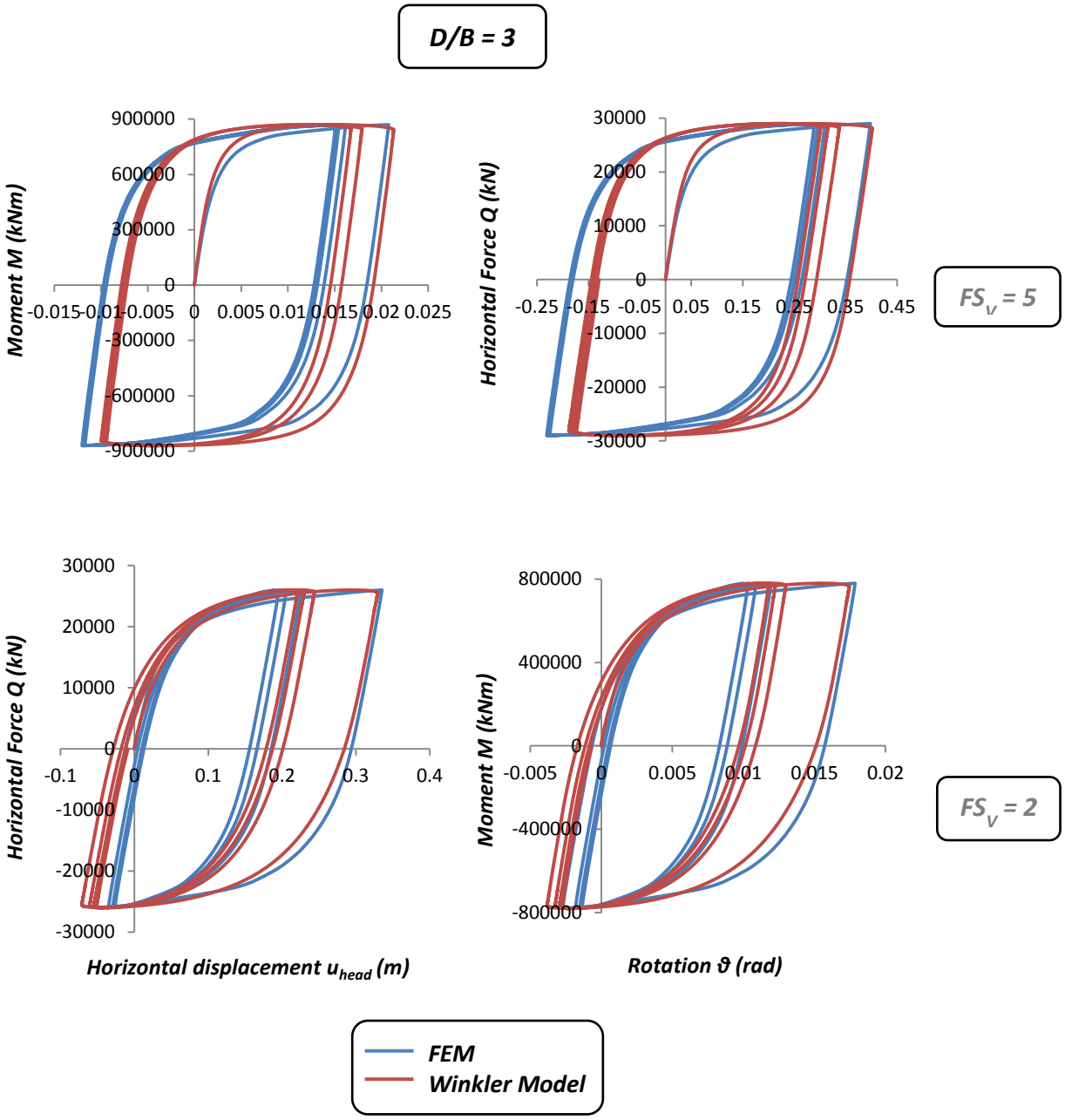

Figure 5.57 *Comparison of the horizontal force – displacement and moment-rotation hysteresis loops derived from the FE analyses and those determined by the calibrated Winkler model, appropriately modified in accordance with Eq. 5.26-5.29. A lightly and a heavily loaded caisson foundation with embedment ratio D/B = 3 is considered in this case. The model satisfactorily captures both types of behaviour, at least in a qualitative fashion.*

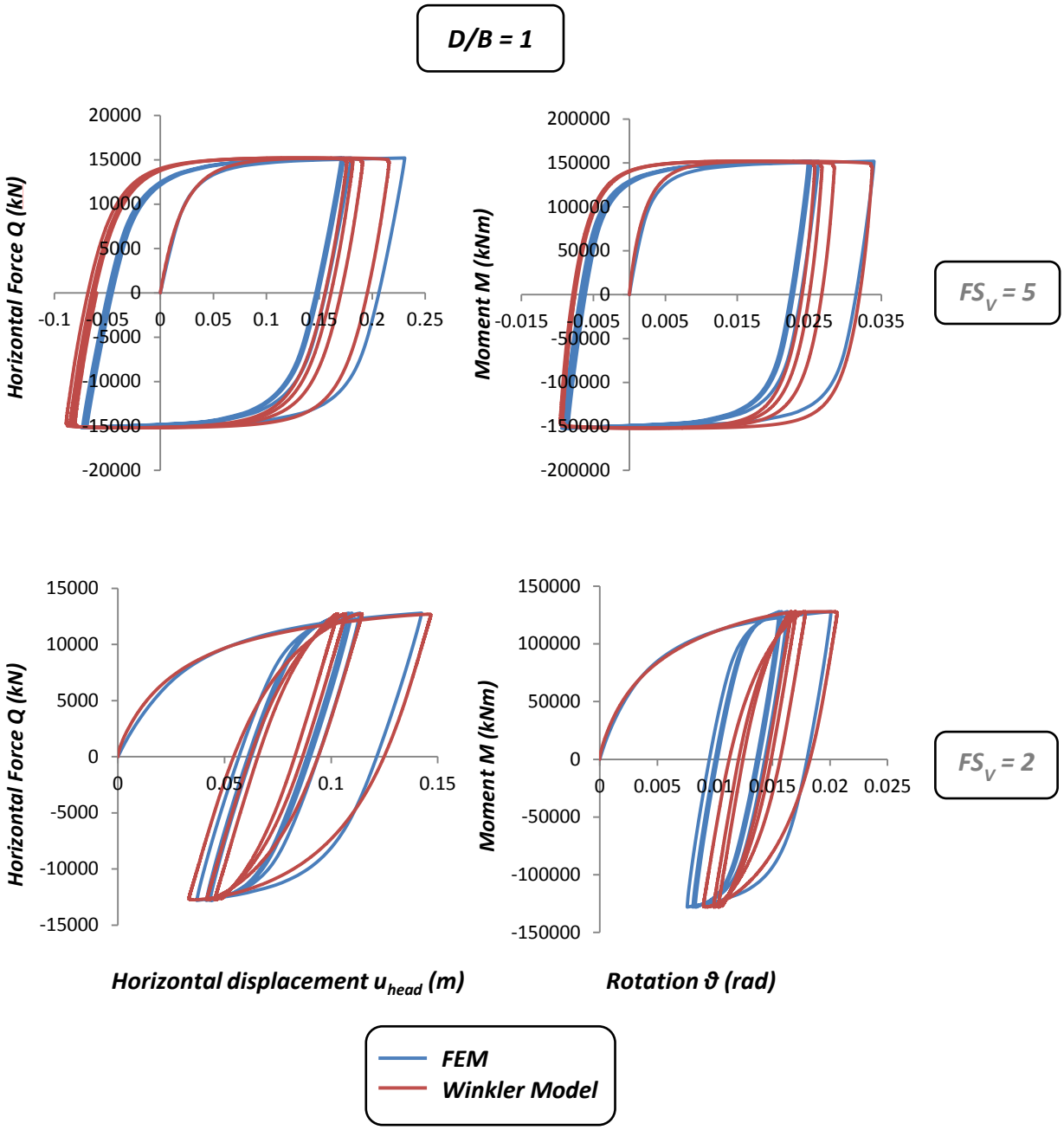

Figure 5.58 *Comparison of the horizontal force – displacement and moment-rotation hysteresis loops derived from the FE analyses and those determined by the calibrated Winkler model, appropriately modified in accordance with Eq. 5.26-5.29. A lightly and a heavily loaded caisson foundation with embedment ratio D/B = 1 is considered in this case. The model satisfactorily captures both types of behaviour, at least in a qualitative fashion.*

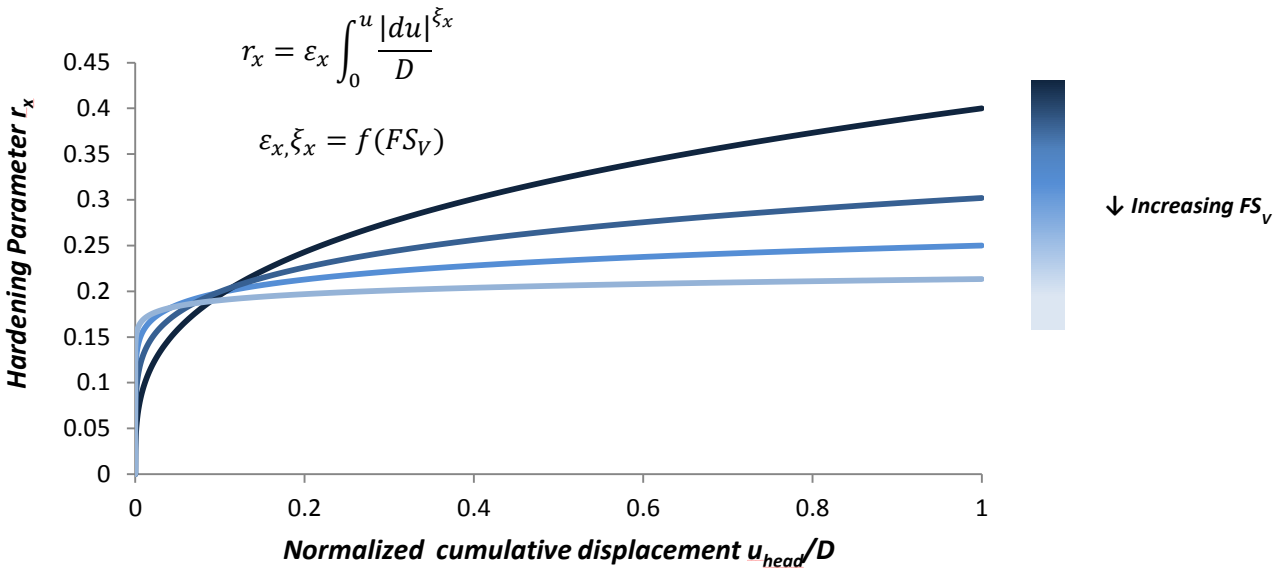

Figure 5.59 *Effect of the factor of safety against vertical bearing capacity failure on the power law of the hardening parameter r_x. As the FS_V decreases, hardening becomes more extensive and is exhibited more gradually with respect to the cumulative displacement. FS_V affects the second hardening parameter r_ϑ in the same fashion with respect to the cumulative rotation.*

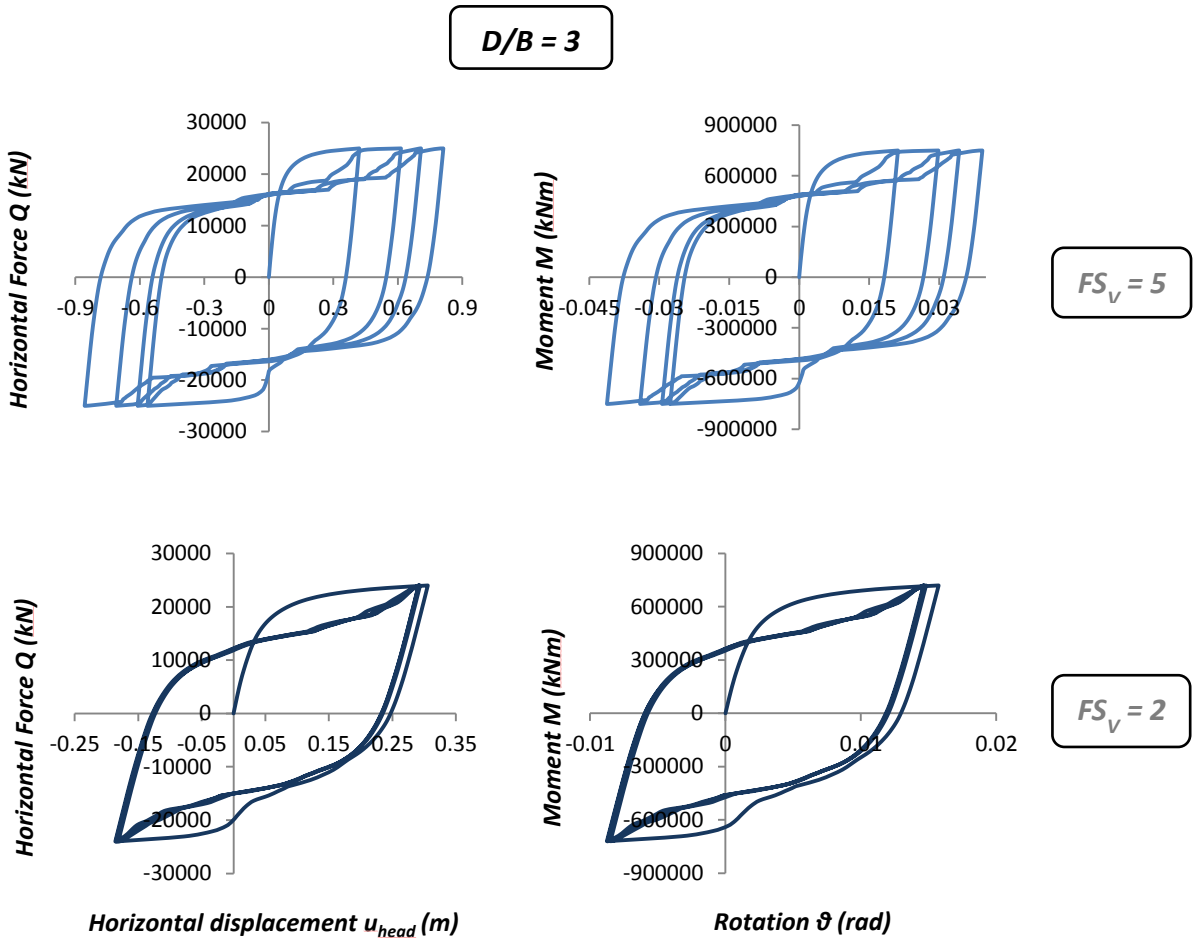

Figure 5.60 *The horizontal force-head displacement and moment-rotation loops for a lightly and a heavily loaded caisson foundation of embedment ratio D/B = 3 under combined M-Q loading corresponding to the 1st quadrant of the scoop slide region. The soil-caisson interface considered is a nonlinear Coulomb one, able to experience gapping and sliding. The lightly loaded system (FS_V = 5) displays a rather asymmetric behavior involving gradual softening. The heavily loaded system (FS_V = 2) has a considerably asymmetric response experiencing slight hardening with decreasing rate.*

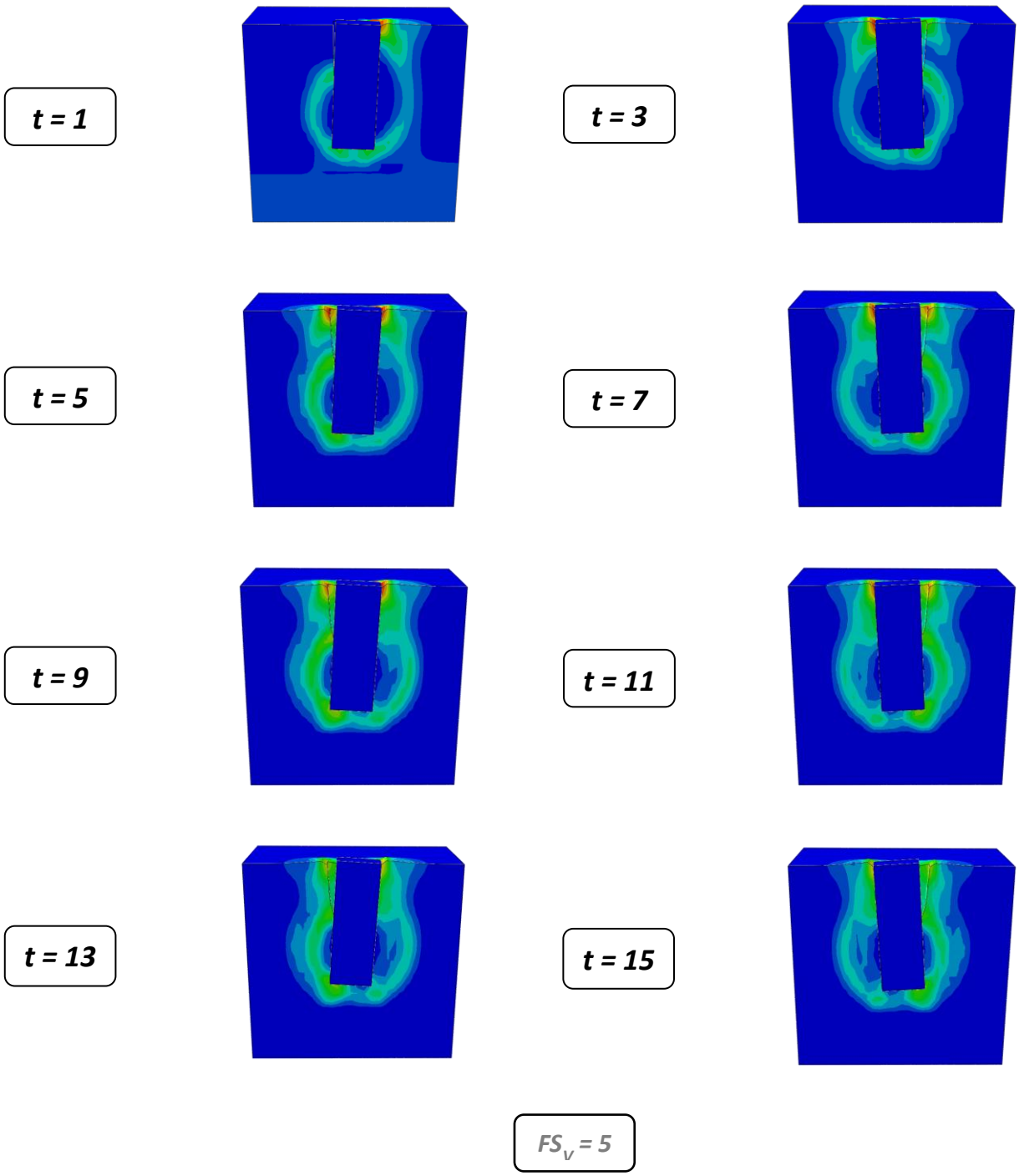

Figure 5.60 *Time history of the plastic strain magnitude contours in the case of a deeply embedded (D/B = 3) foundation subject to cyclic combined M-Q loading at its head for a large factor of safety against vertical loading (FS_V = 5),in which the soil-caisson interface considered is a nonlinear Coulomb one, able to experience sliding and gapping. The response is generally asymmetric. The gap appears to be growing as the number of cycles increases, leading to a macroscopic softening behaviour.*

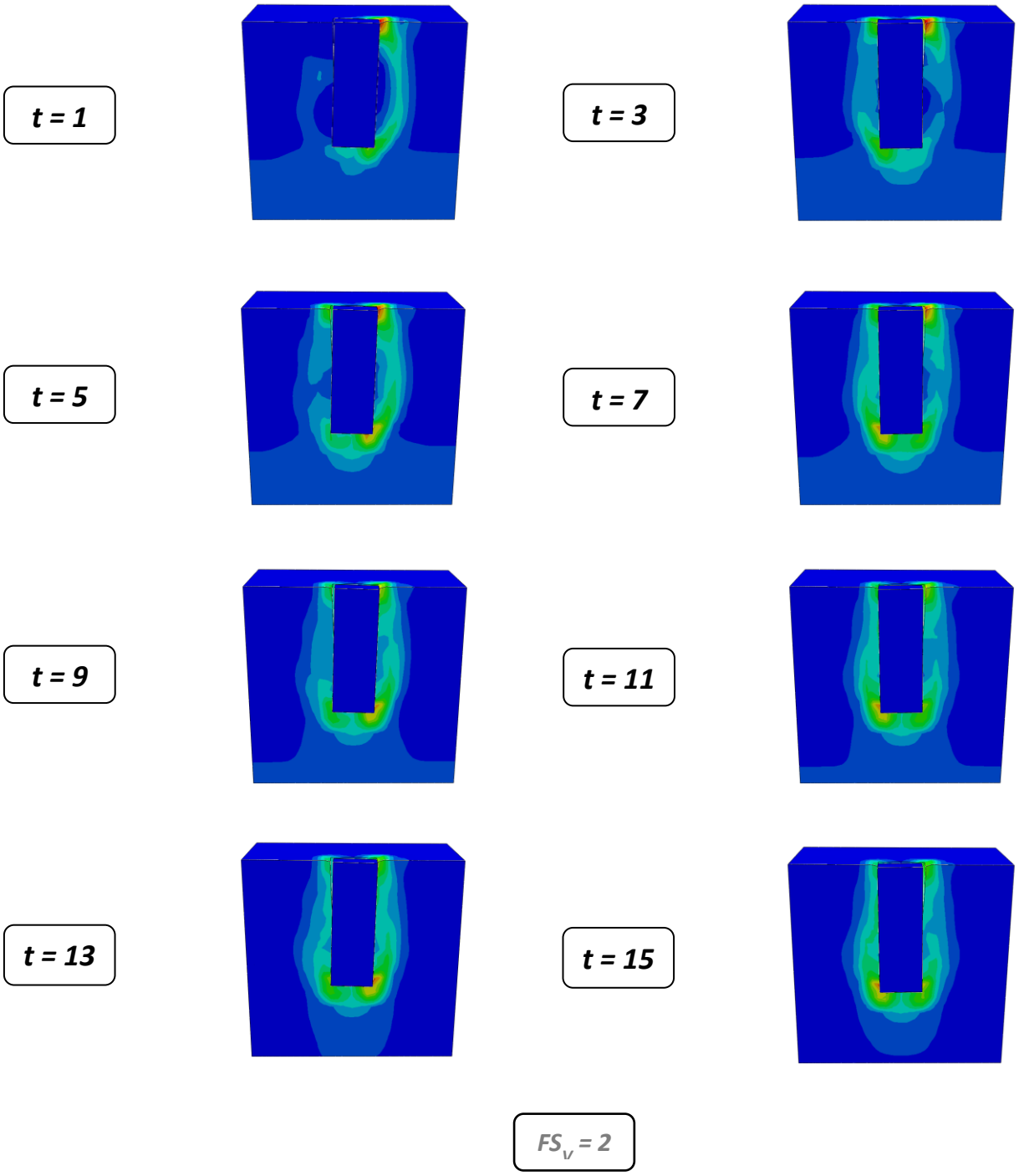

Figure 5.61 *Time history of the plastic strain magnitude contours in the case of a deeply embedded (D/B = 3) foundation subject to cyclic combined M-Q loading at its head for a small factor of safety against vertical loading (FS_V = 2), in which the soil-caisson interface considered is a nonlinear Coulomb one, able to experience sliding and gapping. The response is generally asymmetric. There is no significant detachment taking place, due to the collapse of the plastified soil sidewall.*

CHAPTER 6
Conclusions and Recommendations

6.1. Conclusions

This thesis dealt with the response of caisson foundations resting on a uniform undrained clay profile and subjected to lateral static monotonic and cyclic loading. After developing appropriate Finite Element models for the soil-foundation system, numerous experiments were carried out that served the dual purpose of our work.

Our first aim was to provide insight to the failure envelopes of caisson foundations under combined *M*-*Q*-*N* loading, while emphasizing on the effect of soil-caisson interface nonlinearities on them. Following the work of Gerolymos et al in the case of a bonded interface, we determine analytical expressions that represent these failure envelopes under a more realistic Coulomb interface, able to experience both sliding and gapping. The results can be readily included in a "macro-element" for the lateral response of embedded foundations, recently developed by Gerolymos and Souliotis [*2012*], after proper modification.

Our second aim was to calibrate a sophisticated BWGG Winkler model for the lateral response of caisson foundations developed by Gerolymos and Gazetas [*2006*], thus adding a more microscopic aspect to the intended insight to such foundations. A mathematically-orientated robust calibration methodology is developed that involves the use of genetic algorithm optimization and multilayer neural networks, and is based on numerous FE

experiments. The model's capacity and versatility are tested against lateral static monotonic and cyclic loading.

The important conclusions that were drawn from this thesis are presented below:

- As part of our approach to the failure envelopes of embedded foundations, we first determine the pure horizontal and moment capacities of caisson foundations for three embedment ratios *D/B = 1, 2* and *3* and multiple factors of safety against vertical bearing capacity FS_V *= 1.11, 1.43, 2, 3.33, 5* and ∞ under a bonded soil-caisson interface. The analytical expressions of Gerolymos et al. are assessed against the results and are shown to provide a satisfactory fit. Afterwards, the interface is modified into a sophisticated one able to experience gapping through a nonlinear pressure-overclosure relationship, and sliding through a Coulomb friction law. A series of tests are carried out in order to deduce the equivalent pure capacities by parametrically investigating *D/B* and FS_V in the same fashion as before while introducing the coefficient of friction μ as a third parameter, which takes values *0.1, 0.5, 1* and *2.* The limit values are carefully chosen to correspond to a really smooth and a really rough interface. The results show a totally different effect of the vertical load on the ultimate lateral capacities, with the latter increasing until $FS_V \approx 2$ and then declining to vertical bearing capacity failure ($FS_V = 1$). Finally, we provide equivalent analytical expressions by fitting the numerical results.

- Afterwards, the yield surfaces in the M-Q plane are determined through force-controlled tests for both bonded and nonlinear interface conditions. It appears that the failure envelopes in the case of bonded interface conditions are practically unaffected by the factor of safety against vertical bearing capacity failure and exhibit expansion with increasing *D/B*. The rate of expansion appears to decline for foundations of embedment ratios greater than *1.2*, which can be considered a boundary between shallow and deeply embedded foundations [*Gerolymos et al, 2012*]. On the other hand, in the case of nonlinear interface conditions, FS_V and μ appear to differentiate the shape of the yield locus slightly more, while increasing *D/B* now introduces both an expansion and a rotation of the curve. The rotational aspect is shown to be a result of soil-caisson detachment near the back foot of the foundation. An important observation is that this rotational effect diminishes as *D/B*

approaches *3*, since by then detachment has become limited to the upper part of the foundation and has a limited impact on the ultimate capacity.

- Prior to the analytical representation of the yield surface, we delve into a thorough examination and categorization of the soil deformation mechanisms that develop along the former. Apart from the already referenced *scoop, scoop-slide*, *pure sliding* and *reverse scoop* mechanisms, a new mechanism is suggested governing the region between maximum horizontal and maximum moment capacity in deeply embedded caissons. This mechanism accounts for a generalized (*"diffusive"*) soil failure around the caisson, with no localized shear band being developed except for the base of the caisson. In this narrow region of special interest, the depth of the caisson pivot point rapidly changes from $z = 0$ to $z = \infty$. We assume that an associative flow rule is not applicable in this region, since it is proven to be macroscopically equivalent to the formation of localized failure zone, which is absent here at least in the case of deeply embedded foundations.

- After successfully mapping the yield locus on the M-Q plane, we deal with the analytical representation of the yield loci both in bonded and nonlinear interface conditions. Regarding the former, we limit our work to validating the analytical expressions produced by Gerolymos et al. by comparing them with the numerical results both in normalized and dimensionless *M-Q* terms. Once again, the results are fairly satisfactory. A new expression is determined for the failure envelope in the case of the nonlinear Coulomb interface that can take account for both the expansive and the rotational effect.

- Our analytical approach to the failure surfaces of embedded foundations under nonlinear interface conditions can be incorporated in a recently developed "macro-element" model by Gerolymos and Souliotis [*2012*]. This model incorporates 4 components: a) Elasticity, b) Failure Envelopes, c) Associative plastic flow rule and d) Hardening law. The elastic aspect of the response is unaffected by interface nonlinearities and so is the validity of the associative flow rule, based on the observation that it is equivalent to the development of localized failure zones

throughout the yield surface. The hardening law potentially requires some kind of modification in order to account for the effect of the interface nonlinearities on the elasto-plastic coupling of the response.

- The BWGG Winkler model is examined and compared to the "macro-element" model. Both models may actually be considered as "macro-elements" since they effectively substitute the soil-foundation system with an appropriate nonlinear stiffness matrix able to account for its total behaviour. Their difference lies in the so-called "macro-scale", which represents the macroscopic level of "replacement" of the actual resisting mechanisms that is accomplished by each model. In the Winkler BWGG model, plasticity lies in the soil-reaction level (nonlinear distributed springs), while in the second model it derives from the failure envelopes themselves. Possibly, a more suitable term for the Winkler model would be a "meso-element".

- While, in uniform soil profiles, the "macro-element" model appears to be able to capture the response of embedded foundations in a more realistic fashion due to the consideration of the translational rotational coupling taking place, it loses its advantage over the Winkler model in the case of non-uniform and multilayered soil profiles, which is what is generally faced in practice. In soil profiles with more than 2 distinct layers, the elasticity matrix may only be derived in an approximate fashion through the replacement of the soil with Winkler springs. Hence the two models face the same problem regarding the realistic consideration of the translational-rotational coupling. As for the ultimate capacity in this case, the calibration of the "macro-element" would require numerous FE. On the other hand, the Winkler model can readily account for multi-layered and non-uniform soil profiles by modifying the parameters of the distributed translational and rotational springs. In this sense, it is certainly a more versatile model and offers a more physical approach to the studied problem. Ultimately, the two models can save considerable computational time compared to the conduction of time-consuming 3D Finite Element analyses. Yet, the difference in the computational time of the two models is relatively insignificant.

- A hybrid calibration methodology is developed for the BWGG model in order to determine the ultimate resistance and hardening parameters governing the response of caisson foundations in the case of embedded foundations resting on a uniform undrained layer, with the soil-caisson interface considered bonded. It is based on stress integration from ABAQUS and a dual fit of the model's Horizontal Force–Displacement and Moment-Rotation curves to the equivalent ones derived from FE analyses. The former is used in order to determine the ultimate shear and moment resistance of the base, which are considered uncoupled in this simplified approach, as well as to "help" the 4-parameter (p_y, m_y, n_x, n_r) optimization by providing upper and lower limits. Through integration, the various mechanisms that contribute to the response of caisson foundations are identified and quantified. The above methodology is applied for the same range of FS_V and D/B as before, and for several radial load paths covering the yield locus.

- Driven by the fairly uniform stress patterns determined in ABAQUS and a parametric investigation of the effect of the lateral soil reaction and resisting moment profile on the shape of the deduced failure envelope, we adopt a uniform p_y and m_y profile, ignoring the increase that the confinement appears to introduce even in this uniform profile. In other words, the mean ultimate soil reaction is adopted instead of the local one, "moving" the model upwards in the "macro-scale".

- The ultimate lateral soil reaction is found to no longer be an invariant as considered in the case of piles. The mean ultimate lateral soil reaction changes along the yield locus acquiring its maximum value at the point of maximum horizontal capacity. This variability of p_y with respect to the load angle is attributed to the 3-dimensional response of caisson foundations that derives from their geometry. In fact, this assumption is strengthened by the fact that p_y is even more variable in the case of $D/B = 1$, where the response is fully 3-dimensional. We assume that this is a major deficiency of a two-spring model, in which we are forced to implicitly provide the essential translational-rotational

coupling by rendering the soil reaction as a function of *M/QD.* The resisting moment per unit depth $m_{y,}$ on the other hand, exhibits a limited variability, inverse to that of p_y, exhibiting its lowest value at maximum horizontal capacity. The values of the ultimate lateral soil reaction at its plateau (pure moment) increase as *D/B* increases, whereas the values of the ultimate resisting moment decrease as *D/B* increases. An interesting observation is that at *D/B = 1.2* the contribution of each mechanism is equalized, validating the previous observation that *D/B = 1.2* is indeed a limit value in the behaviour of caisson foundations. Finally, as expected, both the ultimate lateral soil reaction and the ultimate resisting moment decline as the vertical aspect of loading increases, reaching zero resistance for $FS_V = 1.$

- The two hardening parameters display quite the same yet complex trends with respect to each of the variables FS_V, *D/B* and *M/QD.* Two important conclusions can be drawn: *a)* for lightly loaded – deeply embedded foundations, the values of the hardening parameters decline sharply around the point of maximum horizontal capacity, while for lightly loaded – shallow embedded foundations, this trend is not so visible, and b) the values of n_x, n_r decrease as the FS_V decreases, implying that heavily loaded systems have a more coupled elasto-plastic behaviour. The first observation reminds us of the difference in the soil deformation mechanisms deployed by foundations of different embedment ratios at the point of maximum horizontal capacity. On the one hand, the response of deeply embedded caissons reflects the participation of an ever increasing part of the surrounding soil in the resisting mechanism (diffusive failure), while on the other hand, the response of shallow embedded foundations is governed by a formation of a shear band.

- Complicated analytical expressions are deduced for the ultimate resistance parameters, which are yet shown to have a direct relevance with the macroscopic behaviour of the foundation, at least in the case of the major resisting mechanism – the lateral soil reaction. On the other hand, the highly

nonlinear nature of the hardening parameters leads us to train two separate neural networks and incorporate them in the model in Matlab.

- The calibrated model is able to effectively capture the monotonic response of caisson foundations, with the exception of the shallow *D/B = 1* foundation, where the adoption of uncoupled base ultimate capacities has an important impact on the response. Even in that case, however, the validation tests didn't yield an error above 15%. The fact that the major ultimate resistance parameter is expressed as a function of the load angle *M/QD* does not deprive the model of its ability to reproduce displacement-controlled load paths. Through an iterative process, the model calculates the load angle at every step, which is then used to deduce the values of ultimate resistance parameters from the analytical expressions, and the values of the hardening parameters by calling the two neural networks. A series of swipe tests validate this methodology.

- Finally, by modifying the Bouc-Wen differential equations of the model, we incorporate a cyclic hardening parameter r_x (and its rotational spring equivalent r_r), in order to capture the response of caisson foundations under static cyclic combined *M-Q* loading. The Winkler model satisfactorily simulates all basic trends of the response, which is shown to be a plastic shakedown involving hardening at a decreasing rate. In the last section, the effects of geometric nonlinearities at the soil-caisson interface are examined using the same interface as in *Chapter 3*. The response of the lightly loaded system becomes more asymmetric and turns into a macroscopic softening one, due to the formation of gap around the foundation. The system seems to exploit its potential to express these geometric nonlinearities. On the other hand, the heavily loaded system retains its asymmetric response and exhibits a considerably less hardening behavior. The above effects can be taken into account in our model, by introducing a pinching factor h_x in the Bouc-Wen differential equation; yet this work extends beyond the scope of this thesis.

6.2. Recommendations for future research

In this last section, we provide some suggestions for future work on the extensive subject of constitutive modeling of embedded foundations:

- First of all, it is important to examine non-uniform/layered undrained shear strength profiles, since they constitute the majority of the profiles in practice, and deduce equivalent analytical expressions capturing the pure ultimate capacities and the shape of the failure envelope. The ultimate purpose is of course their incorporation in a "macro-element" as the one briefly described in this thesis. The capacity of the BWGG Winkler model to capture different shear strength profiles should also be examined, which will most probably reveal the current advantage of the latter over the macro-element in the case of embedded foundations. This advantage of the Winkler profiles could be exploited in order to calibrate the "macro-element" for these cases, effectively bypassing the time-consuming FE analyses.

- The effect of interface nonlinearities can also be examined from a different perspective e.g that of an S_u oriented slippage law, which would allow a more direct comparison with the case of the bonded interface. In addition, the modification of the "macro-element", mainly in terms of its hardening aspect, should also be studied if the current work on the failure envelopes in the case of interface nonlinearities is to be incorporated in this model.

- In addition, this work should be extended to the study of dynamic problems and especially seismic excitations, justifying the initial adoption of an undrained shear strength profile.

- Future work should perhaps focus on an extension to a 6-spring model, in which additional distributed vertical (shear) springs along the shaft and a concentrated vertical spring on the base are incorporated. This shall pave the way for the

incorporation of a separate surface “macro-element” for the base, rendering the model able to realistically account for both shallow and deeply embedded foundations.

- Finally, it would of particular interest to examine the case of interface nonlinearities, where a Coulomb law is similarly adopted. It is interesting to determine whether the microscopic coupling of the normal and the shear stress can be effectively extended to the soil reaction level. After determining the effect on the ultimate resistance parameters, the model should be extended to capture the cyclic response by appropriately calibrating the pinching factor.

References

ABAQUS 6.1. (2001). Standard user's manual. Rhode Island: Hibbit, Karlsson and Sorensen.

Beredugo YO, Novak M. Coupled horizontal and rocking vibration of embedded footings. Can Geotech J 1972;9(4):477–97.

Bransby, M. F. & Randolph, M. F. (1997). Shallow foundations subject to combined loadings. Proc. 9th Int. Conf. on Computer Methods and Advances in Geomechanics, Wuhan 3, 1947–1952.

Bransby, M. F., Randolph, M. F. (1998). Combined loading of skirted foundations, Geotechnique, 48(5): 637-655.

Bransby, M. F. & Randolph, M. F. (1999a). The effects of embedment on the undrained response of caisson foundations to combined loadings. Soils Found. 39, No. 4, 19–34.

Bransby, M. F. & Randolph, M. F. (1999b). The effect of skirted foundation shape on response to combined V-M-H loadings. Int. J. Offshore Polar Engng 9, No. 3, 214–218.

Chatzigogos, C. T., Figini, R., Pecker, A. and Salençon, J. (2011). A macroelement formulation for shallow foundations on cohesive and frictional soils. Int. J. Numer. Anal. Meth. Geomech. 2011; 35:902–931

Crémer C. Modélisation du comportement non linéaire des fondations superficielles sous séisme. PhD thesis, Laboratoire de Mécanique et de Technologie, ENS – Cachan, France, 2001.

Crémer C, Pecker A, Davenne L. Cyclic macro-element for soil-structure interaction: material and geometrical non linearities. International Journal for Numerical and Analytical Methods in Geomechanics 2001; 25: 1257 – 1284.

Dominguez J. Dynamic stiffness of rectangular foundations. Research Report R78-20. Department of Civil Engineering, Massachusetts Institute of Technology, Cambridge; 1978.

Gadre A, Dobry R. Lateral cyclic loading centrifuge tests on square embedded footing. J Geotech Geoenviron Eng ASCE 1998;124(11): 1128–38.

Gazetas G, Dobry R, Tassoulas JL. Vertical response of arbitrarily shaped embedded foundations. J Geotech Eng ASCE 1985;111(6):750–71.

Gazetas G, Tassoulas J. Horizontal stiffness of arbitrarily shaped embedded foundations. J Geotech Eng ASCE 1987;113(5):440–57.

Gazetas G, Tassoulas JL. Horizontal damping of arbitrarily shaped embedded foundations. J Geotech Eng ASCE 1987;113(5):458–75.

Gazetas G. Formulas and charts for impedances of surface and embedded foundations. J Geotech Eng ASCE 1991;117(9):1363–81.

Gerolymos N, Gazetas G (2006) Winkler model for lateral response of rigid caisson foundations in linear soil. Soil Dynamics and Earthquake Engineering 26 (2006), pp 347–361

Gerolymos N, Gazetas G (2006) Development of Winkler model for static and dynamic response of caisson foundations with soil and interface nonlinearities. Soil Dynamics and Earthquake Engineering 26 (2006), pp 363–376

Gerolymos N, Gazetas G (2006) Static and dynamic response of massive caisson foundations with soil and interface nonlinearities - Validation and results. Soil Dynamics and Earthquake Engineering 26 (2006), pp 377–394

Gerolymos N, Apostolou M and Gazetas G (2005). Neural network analysis of overturning response under near−fault type excitation.

Gerolymos N, Zafeirakos A and Souliotis C (2012). Insight to failure mechanisms of caisson foundations under combined loading: A macro-element approach. Proc. 2nd Int. Conf. on Performance-based design in Earthquake Geotechnical Engineering, Taormina, Italy

Gottardi G, Butterfield R. The displacement of a model rigid surface footing on dense sand under general planar loading. Soils and Foundations 1995; 35(3):71–82.
Gottardi G, Houlsby GT, Butterfield R. Plastic response of circular footings on sand under general planar loading. Géotechnique 1999; 49(4): 453 – 469.

Gourvenec, S. & Randolph, M. F. (2003). Effect of strength nonhomogeneity on the shape and failure envelopes for combined loading of strip and circular foundations on clay. Geotechnique 53, No. 6, 575–586.

Gourvenec, S. "Bearing capacity under combined loading - a study of the effect of shear strength heterogeneity". Proc. , 9th Australian and New Zealand Conference on Geomechanics, Auckland, New Zealand, 2004, pp. 527-533.

Gourvenec, S. (2007). Failure envelopes for offshore shallow foundation under general loading, Geotechnique, 57(9): 715-728.

Gourvenec, S. (2008). Effect of embedment on the undrained capacity of shallow foundations under general loading, Geotechnique, 58(3): 177-185.

Harada T, Kubo K, Katayama T. Dynamic soil–structure interaction analysis by continuum formulation method. Report of the Institute of Industrial Science, vol. 29. The University of Tokyo; 1981 [issue no. 5].

Karabalis DL, Beskos DE. Dynamic response of 3-D embedded foundations by the boundary element method. Comput Methods Appl Mech Eng 1986;56:91–119.

Kausel E, Roesset JM. Dynamic stiffness of circular foundations. J Eng Mech Div ASCE 1975;101(6):770–85.

Martin, C. M. & Houlsby, G. T. (2000). Combined loading of spudcan foundations on clay: laboratory tests. Geotechnique 50, No. 4, 325–338.

Martin, C. M. & Houlsby, G. T. (2001). Combined loading of spudcan foundations on clay: numerical modelling. Geotechnique 51, No. 8, 687–699.

Mitta A, Luco JE. Dynamic response of a square foundation embedded in an elastic half space. Soil Dyn Earthq Eng 1989;8.

Mylonakis G. Elastodynamic model for large-diameter end-bearing shafts. Soil Found. 2001;41(3):31–44.

Nova, R. & Montrasio, L. (1991). Settlements of shallow foundations on sand. Geotechnique 41, No. 2, 243–256.

Roscoe KH, Schofield AN. The stability of short pier foundations on sand. British Welding Journal 1956; August: 343–354.

Roscoe, K. H., Schofield, A. N. (1957). The stability of short pier foundations in sand, discussion, British Welding Journal, January, 12-18.

Saitoh M. Effective seismic motion of caisson and pile foundation. RTRI Rep 2001;46.

Tajimi H. Dynamic analysis of a structure embedded in an elastic stratum. Proceedings of the fourth world conference on earthquake engineering, Santiago, Chile; 1969.

Tassoulas JL. Elements for the numerical analysis of wave motion in layered media. Research Report R81-2. Department of Civil Engineering, Massachusetts Institute of Technology, Cambridge; 1981.

Ticof, J., (1977). "Surface footings on sand under general planar loads", PhD thesis, University of Southampton.

Ukritchon, B., Whittle, A. J. & Sloan, S. W. (1998). Undrained limit analyses for combined loading of strip footings on clay. J. Geotech. Geoenviron. Engng ASCE 124, No. 3, 265–276.

Zaharescu, E. (1961). Sur la stabilite des fondations rigides. Proc. 5th Int. Conf. Soil Mech., Paris 1, 867–871.